# MULTI-FIDELITY REDUCED-ORDER MODELING APPLIED TO FIELDS WITH INCONSISTENT REPRESENTATIONS

A Thesis
Presented to
The Academic Faculty

By

Christian Perron

In Partial Fulfillment
of the Requirements for the Degree
Doctor of Philosophy in the
School of Aerospace Engineering

Georgia Institute of Technology

December 2020

# MULTI-FIDELITY REDUCED-ORDER MODELING APPLIED TO FIELDS WITH INCONSISTENT REPRESENTATIONS

Approved by:


Professor Dimitri N. Mavris
School of Aerospace Engineering
*Georgia Institute of Technology*

Dr. Chung Lee
School of Aerospace Engineering
*Georgia Institute of Technology*

Professor Stephen M. Ruffin
School of Aerospace Engineering
*Georgia Institute of Technology*

Mr. Simon Coggon
Flight Physics Capabilities
*Airbus UK*

Professor Graeme J. Kennedy
School of Aerospace Engineering
*Georgia Institute of Technology*


Date Approved: November 30$^{\text{th}}$, 2020

Essentially all models are wrong, but some are useful

*George E.P. Box*

*À mes parents, Agathe et Luc Perron*

## ACKNOWLEDGMENTS

It feels like not so long ago, I was leaving Canada to begin my journey as a Ph.D. student at Georgia Tech. Throughout my degree, I had the privilege of participating in stimulating research projects, learning from knowledgeable professors, and forming both personal and professional connections. While this dissertation is a personal achievement, it is only made possible through the support of several people in the background to whom I am obliged.

Firstly, I would like to express my gratitude toward my advisor, Prof. Dimitri Mavris, who gave me this unique opportunity and pushed me to my full potential. His patience, compassion, and willingness to go the extra mile for his students made my experience at Georgia Tech a fulfilling one. I have to admit, it took me some time to understand his teachings, but looking back at my journey, his mentoring had a profound impact on the researcher I am today. Thank you, Prof. Mavris, and I hope you can be proud of this dissertation.

Secondly, I would like to acknowledge and thank the members of my thesis committee. In addition to my advisor, these are Prof. Stephen Ruffin, Prof. Graeme Kennedy, Dr. Chung Lee, and Simon Coggon. The comments and suggestions offered by my committee have helped me improve the quality and reach of my research.

Thirdly, I had the privilege of being part of the large ASDL community during my time at Georgia Tech. Learning and working with fellow ASDL students from all around the world exposed me to great minds and expanded my capabilities beyond my expectations. I am also very appreciative of the skills that I developed from working on exciting projects with ASDL research engineers and members of the aerospace industry. It is an honor to be part of the ASDL, and I am thankful for the assistance of all my colleagues.

Finally, I cannot express how thankful I am for the endless support from my family and friends, both here in Atlanta and back at home. A Ph.D. degree is a challenging endeavor, and sharing this burden with them has helped me in more ways than one. I must specifically thank my parents, Agathe and Luc Perron, that stayed behind me this entire time. You knew the importance of this journey to me, and you never wavered in your support. For that, I am endlessly grateful to you both.

## TABLE OF CONTENTS

## LIST OF TABLES

## LIST OF FIGURES

## LIST OF ACRONYMS

**ADODG** Aerodynamic Design Optimization Discussion Group.

**AIAA** American Institute of Aeronautics and Astronautics.

**ANN** Artificial Neural Network.

**CAD** Computer-Aided Design.

**CFD** Computational Fluid Dynamics.

**CRM** Common Research Model.

**DES** Detached-Eddy Simulation.

**DoE** Design of Experiment.

**EGO** Efficient Global Optimization.

**EM-PCA** Expectation-Maximization PCA.

**FEM** Finite Element Method.

**FFD** Free Form Deformation.

**GPOD** Gappy Proper Orthogonal Decomposition.

**GPR** Gaussian Process Regression.

**JST** Jameson-Schmidt-Turkel.

**KLT** Karhunen-Loève Transformation.

**LHS** Latin Hypercube Sampling.

**LLE** Locality Linear Embedding.

**MA-ROM** Manifold Aligned Reduced-Order Model.

**OML** Outer Mold Line.

**PCA** Principal Component Analysis.

**POD** Proper Orthogonal Decomposition.

**RANS** Reynolds-Averaged Navier-Stokes.

**RBF** Radial Basis Function.

**RIC** Relative Information Content.

**RMS** Root-Mean-Square.

**ROM** Reduced-Order Model.

**SVD** Singular Value Decomposition.

**SVR** Support Vector Regression.

**TRMM** Trust Region Management Method.

**VLM** Vortex Lattice Method.

# NOMENCLATURE

## Scalar Variables

| | |
|---|---|
| $b$ | Dimensions of the input space |
| $c$ | Mean aerodynamic chord |
| $d$ | Dimensions of the high-fidelity output space |
| $l$ | Number of validation samples |
| $k$ | Dimensions of the latent space |
| $n$ | Number of high-fidelity samples |
| $n_t$ | Number of high-fidelity test samples |
| $m$ | Number of low-fidelity samples |
| $q$ | Dimensions of low-fidelity output space |
| $s$ | Isotropic scaling factor |
| $\alpha$ | Angle of attack |
| $\beta$ | Scaling parameter in CoKriging model |
| $\lambda$ | Eigenvalue of covariance matrix |
| $\mu$ | Mean of Gaussian process |
| $\tau$ | Multi-fidelity ratio, i.e., $m/n$ |
| $\varepsilon$ | Reconstruction residual |
| $\theta$ | Length scale parameter in correlation function |
| $\sigma$ | Singular value |
| $\sigma^2$ | Variance of Gaussian process |
| $\sigma_n^2$ | Noise variance in correlation function |
| $\Delta$ | Distance parameter in correlation function |
| $M_\infty$ | Freestream Mach number |
| $Re_\infty$ | Freestream Reynolds number |

### Vector and Matrix Variables

| | |
|---|---|
| $\mathbf{p}$ | Vector of input parameters |
| $\mathbf{t}$ | Translation vector |
| $\mathbf{x}$ | High-fidelity output vector |
| $\mathbf{y}$ | Low-fidelity output vector |
| $\mathbf{w}$ | Low-fidelity latent variable vector |
| $\mathbf{z}$ | High-fidelity latent variable vector |
| $\boldsymbol{\phi}$ | Eigenvector of covariance matrix |
| $\boldsymbol{\nu}$ | Eigenvector of kernel matrix |
| $\mathbf{I}$ | Identity matrix |
| $\mathbf{K}$ | Kernel matrix |
| $\mathbf{P}$ | Data matrix of input parameters |
| $\mathbf{Q}$ | Orthonormal transformation matrix |
| $\mathbf{S}$ | Covariance matrix |
| $\mathbf{U}$ | Matrix of left singular vectors |
| $\mathbf{V}$ | Matrix of right singular vectors |
| $\mathbf{W}$ | Data matrix of low-fidelity latent variables |
| $\mathbf{X}$ | Data matrix of high-fidelity output |
| $\mathbf{Y}$ | Data matrix of low-fidelity output |
| $\mathbf{Z}$ | Data matrix of high-fidelity latent variables |
| $\boldsymbol{\Sigma}$ | Diagonal matrix of singular values |
| $\boldsymbol{\Phi}$ | High-fidelity POD basis |
| $\boldsymbol{\Psi}$ | Low-fidelity POD basis |

### Conventions

| | |
|---|---|
| $(\cdot)_k$ | Contains the $k$ most significant variables |
| $(\cdot)_{\text{hi}}$ | Associated with high-fidelity data |
| $(\cdot)_{\text{lo}}$ | Associated with low-fidelity data |
| $(\cdot)_{\text{hi/lo}}$ | High- and low-fidelity data stacked column-wise |
| $(\cdot)_{\text{hi+lo}}$ | High- and low-fidelity data stacked row-wise |

| | |
|---|---|
| $(\cdot)_p$ | Pressure component of aerodynamic coefficient |
| $(\cdot)_{\mathrm{L}}$ | Linked data |
| $(\cdot)_{\mathrm{U}}$ | Unlinked data |
| $(\cdot)_{\mathrm{ML}}$ | Maximum likelihood parameter |
| $(\cdot)_{\mathrm{rc}}$ | Reconstruction component of prediction error |
| $(\cdot)_{\mathrm{rg}}$ | Regression component of prediction error |
| $\widetilde{(\cdot)}$ | Approximation of variable or function |
| $\bar{(\cdot)}$ | Sample mean |
| $(\cdot)^T$ | Transpose of vector or matrix |
| $(\cdot)^*$ | Out-of-sample value |
| $\|\cdot\|_2$ | Euclidean norm |
| $\|\cdot\|_F$ | Frobenius norm |
| $\mathrm{tr}(\cdot)$ | Trace of a matrix |
| $\det(\cdot)$ | Determinant of a matrix |
| $\mathcal{O}(\cdot)$ | Big O notation |

**Aerodynamic Coefficients**

| | |
|---|---|
| $C_D$ | Coefficient of drag |
| $C_L$ | Coefficient of lift |
| $C_F$ | Coefficient of skin friction |
| $C_P$ | Coefficient of pressure |
| $C_N$ | Coefficient of normal force |
| $C_{M,x}$ | Coefficient of root bending moment, i.e., around the wing $x$-axis |
| $C_{M,z}$ | Coefficient of pitching moment, i.e., around the airfoil $z$-axis |

**Miscellaneous**

| | |
|---|---|
| $f(\mathbf{p})$ | Function representing a physical system |
| $g(\mathbf{p})$ | Regression model in non-intrusive ROM |
| $r(\mathbf{p})$ | Correlation function |
| $e(\mathbf{x})$ | Sample prediction error of $\mathbf{x}$ |
| $E(\mathbf{x})$ | Root-mean-square prediction error of $\mathbf{x}$ |

| | |
|---|---|
| $\widehat{E}(\mathbf{x})$ | Normalized root-mean-square prediction error of $\mathbf{x}$ |
| $\delta_{i,j}$ | Kronecker delta |
| $\epsilon(\mathbf{p})$ | Additive correction |
| $\rho(\mathbf{p})$ | Multiplicative correction |
| $\mathcal{M}$ | Mapping from the actual space onto the latent space |
| $\mathcal{M}^{-1}$ | Inverse mapping from the latent space onto the actual space |

## SUMMARY

Our ever-increasing capacity for high-performance computing has progressively elevated the role of physics-based simulations in the conceptual and preliminary phases of aircraft design. This virtualization of the early design process has allowed for additional design freedom and shorter development time while engineers continuously strive for cleaner and quieter aircraft. While modern high-fidelity simulations can provide results with great accuracy, their application is often hindered by their steep computational cost and the limited availability of computing resources. This is especially prohibitive for design problems requiring the analysis of many aircraft configurations and at several flight conditions. To overcome the overwhelming cost of high-fidelity simulations, these are often replaced in practice by cheaper surrogate models generated using a handful of previously obtained solutions. When applied to physics-based results, surrogate models are typically associated with the prediction of integrated quantities. Recently, a new form of surrogate modeling, referred to as Reduced-Order Modeling (ROM), was developed for the prediction of high-dimensional field quantities. In addition to providing physically richer results than conventional surrogate models, this form of approximation is especially relevant for multi-disciplinary applications where the physical quantities exchanged between the disciplines are typically fields.

As with most empirical models, the accuracy of a ROM is contingent on the amount of data used for their construction. While these models offer fast predictions, collecting a sufficiently large dataset to achieve the desired accuracy can be impractical when applied to high-fidelity simulations, especially when considering many design parameters. Hence, the main objective of this dissertation is to improve current ROM methods by requiring less high-fidelity data while maintaining

adequate accuracy. Specifically, we consider a multi-fidelity approach that enhances a few high-fidelity solutions with results from an inexpensive low-fidelity simulation. While various multi-fidelity solutions exist for conventional surrogate models, few are available for reduced-order modeling. A major factor behind the scarcity of multi-fidelity ROMs is that simulations of different fidelity generally produce fields with disparate representations. As a result, this work focuses on this issue and investigate methods to allow the fusion of inconsistent fields.

This dissertation contributes to the field of reduced-order modeling by proposing a multi-fidelity method that employs manifold alignment to find a common low-dimensional representation of two datasets with heterogeneous fields. Once aligned, a single prediction model combines the multi-fidelity datasets with an approach inspired by existing fusion-based multi-fidelity techniques. Therefore, the developed method can combine fields from various models irrespective of their representations. The produced ROM then potentially has better performance than a single-fidelity model trained with the same computational budget.

The viability of the proposed method is validated using two practical problems, i.e., the aerodynamic analysis of a transonic airfoil and a transonic wing. Multiple multi-fidelity scenarios are considered with different fidelity combinations, various model configurations, and inconsistent fields. In many cases, the developed method can effectively provide improved predictions compared to an equivalent single-fidelity approach despite fusing results with inconsistent representations. At worst, when the proposed method is applied to datasets with a large fidelity difference, the accuracy of the resulting ROM tends to that of a single-fidelity model. Also, the results show that the developed method behaves similarly to existing multi-fidelity ROM methods when joining high- and low-fidelity fields with a consistent representation.

# CHAPTER 1
# INTRODUCTION

## 1.1 Numerical Simulations in Aircraft Design

Progress in physical modeling, numerical methods, and high-performance computing have steadily advanced the role of numerical simulations in aerospace engineering. This industry trend is further reinforced by our continuous growth in computer power as predicted by the acclaimed Moore's law [140]. In the past, a lack of computing resources and physically accurate simulations meant that engineers were heavily reliant on experimental facilities, such as wind tunnels, to characterize the performance of a new concept. A significant drawback of an experiment-centric approach is that design modifications often require the construction of a new scaled prototype, which is both a lengthy and costly process. With the current shift towards a more simulation-focused process, an aircraft can remain virtual, and the time between making a design change and assessing its effect is greatly shortened. As a result, more design freedom is available in the early phases of the design process, and the overall development time is reduced. This recent simulation paradigm is exemplified in a lecture made by Airbus in 2008 [43] at the Royal Aeronautical Society, Hamburg Branch, where a reduction of 40% in wind tunnel testing time was claimed for the development of the A350, which was presumably compensated with an increase in simulation time. It should be mentioned that experimental testing remains a key component of any aircraft design process, although its role has been relegated to later design phases when the aircraft concept is more mature and design changes are minor and less frequent.

Also, the rise of numerical simulations in the early phases of aircraft design has enabled a specific class of design activities referred to as *many-query* or *outer-loop*

applications [119, 138]. Loosely speaking, these terms describe any scenarios where a given computational model is evaluated multiple times for different design parameters to achieve some specific goal. For instance, numerical optimization is a type of many-query applications where an optimizer iteratively samples some model to find a set of design parameters that are optimal, subject to some design objective and constraints. Other applications such as design space exploration, uncertainty quantification, inverse design, and sensitivity analysis also fall into this category and are common in aircraft design. These are still areas of active research and the literature contains many examples where these applications have important contributions to the design process [85, 146]. Although many-query applications are not just limited to computational models, they are made possible for aircraft design by the short turnaround time of numerical simulations.

Nonetheless, the vast number of simulations entailed by the many-query context can be problematic in some scenarios. For instance, when performing uncertainty quantification with the Monte Carlo method, the error of the Monte Carlo estimator behaves in $\mathcal{O}(n^{-1/2})$ where $n$ is the number of evaluations [26]. This slow convergence implies that a considerable number of simulations must be carried out to obtain a reasonably small error. As for optimization, using a global algorithm can easily require thousands of iterations to locate the optimum of a function. While the use of a gradient-based algorithm can greatly reduce the computational cost [176, 181], computing the gradient efficiently can be a challenge in itself and the optimizer might converge to a sub-optimal solution. Besides, the overall aircraft design involves multiple disciplines (e.g., aerodynamics, structures, propulsion, etc.) interacting with each other. The use of many-query applications at the vehicle level has the additional constraint of maintaining the consistency between the various physical models [108], further adding to the computational burden. In consequence, many-query applications are often limited in practice to simplified simulations with a relatively low cost.

a) Blended-Wing-Body b) Truss-Braced Wing c) Over-the-Wing Nacelles

**Figure 1.1:** Examples of unconventional aircraft configuration. From left to right, concepts are (a) the NASA N3-X, (b) the Boeing SUGAR Volt, and (c) the Lockheed Martin Hybrid Wing Body.

At the same time, as the aerospace industry continuously strives towards more efficient and cleaner aircraft, aerospace engineers are compelled to use more complex simulations earlier in the design process to meet future demands. Ambitious design objectives can require a radical departure from the conventional tube-and-wing configuration, thus requiring more advanced and tightly intertwined physical modeling. Some of these unconventional aircraft configurations are shown in Figure 1.1 and include the blended-wing-body[94, 100], truss-braced wing [57, 142], and over-the-wing nacelles [16, 49, 69] concepts. For the above reasons, the current engineering trend is to incorporate continuously more physically accurate and realistic models such as Computational Fluid Dynamics (CFD) and Finite Element Method (FEM), in the preliminary and conceptual design phases. These advanced simulations come with a high computational cost and often require many hours, if not days, to solve despite being run on modern supercomputers. When used in conjunction with multi-disciplinary analysis, optimization, or other many-query applications, their long runtime can easily become prohibitive.

## 1.2 Approximation via Surrogate Models

A popular solution to reconcile the need for fast models with the desire for higher accuracy is to replace these high-fidelity simulations with a *surrogate model*, i.e., a cheap-to-evaluate mathematical model designed to mimic the output of a more complex and expensive model. This enables engineers to perform many-query applications at a reasonable cost while partially maintaining the physical accuracy of expensive simulations. In mathematical terms, any physical system can be abstracted as a function $f : \mathbf{p} \mapsto \mathbf{x}$ that maps an input vector $\mathbf{p} \in \mathbb{R}^b$ to an output vector $\mathbf{x} \in \mathbb{R}^d$, where $b$ and $d$ are the dimensions of the input and output spaces respectively. A surrogate model can be defined as a function $\widetilde{f} : \mathbf{p} \mapsto \widetilde{\mathbf{x}}$, where $\widetilde{\mathbf{x}} \in \mathbb{R}^d$ is an estimate of $\mathbf{x}$ that is obtained with a considerably shorter runtime.

Admittedly, despite having a low *evaluation cost*, the *training cost* of a surrogate model, i.e., the cost to create the model itself and gather the data needed for training, can be substantial. In a sense, a surrogate model is a way to trade-off a large upfront computational cost during an *offline* phase to accelerate many evaluations during an *online* phase. This compromise is oftentimes worthwhile in the many-query context, especially since the same model can be reused for a variety of tasks.

In the literature, surrogate models are often implicitly associated with the prediction of scalar quantities (i.e., where $d = 1$). However, some engineering problems require instead the prediction of field quantities (i.e., where $d \gg 1$), which brings additional difficulties and requires a more specialized approach. The following section discusses the similarity, differences, and challenges of both scenarios, which is a key component of the research objective of this dissertation.

### 1.2.1 Prediction of Scalars

In many design problems, the performance of a system can often be summarized by a handful of *global* or *integrated* results, e.g., lift, drag, pitching moment, and gross weight, to name a few. When performing optimization or design space exploration, it is generally sufficient to focus on these few metrics rather than the more detailed solutions of the simulations. For such situations, *data-fit models*[1] (also known as *response surface models*) are surrogate models where the output of interest is a scalar and are well suited for the prediction of integrated quantities. This particular type of surrogate model has been the subject of many reviews over the years, some notable ones being from Forrester and Keane [44], Queipo et al. [122], Yondo et al. [174], and Bhosekar and Ierapetritou [18]. Data-fit models are constructed empirically using a database of results that are generated in an offline phase. The samples of the training data are carefully selected using a Design of Experiment (DoE) [122, 174], such that the information gained from the expensive simulation is maximized and the input space is adequately covered. The prediction of new results (online phase) is then achieved using a form of interpolation or regression with respect to the input parameters. Interestingly, the intrinsic details of the underlying physical modeling are unimportant when constructing a data-fit model. Only the inputs and outputs are relevant such that the underlying high-fidelity model is essentially treated as a *black-box*[2]. This means that data-fit models can indiscriminately replace any simulations, or even experiments, which makes them a highly versatile solution. However, by ignoring the governing physics, data-fit models can sometimes be prone to non-physical results and may have additional difficulties predicting complex phenomena.

The literature on data-fit models can be traced back to the 1950s [22]. Early

[1] Some authors associate the term surrogate model with data-fit models exclusively. In this thesis, a broader definition of the surrogate model is used that includes both data-fit and reduced-order models [40].

[2] The term *black-box* describes a system or function with inputs and outputs that can be observed and interacted with, but whose inner workings are unknown to the user.

applications relied mostly on polynomial regression, a method still widely used in engineering despite its simplicity. Nowadays, more complex methods have become increasingly popular such as Radial Basis Function (RBF) [20, 58] and Kriging[3] [80, 84, 106, 126], of which both use a linear combination of basis functions. It is worth noting that Kriging is a variant of Gaussian Process Regression (GPR) that represents observed values as a combination of random functions following a Gaussian distribution. As a result, Kriging models can also provide an estimate of the error or uncertainty in their predictions, which makes this type of surrogate model particularly appealing for engineering applications. Also, machine learning techniques, such as Support Vector Regression (SVR) [31, 148] and Artificial Neural Network (ANN) [96, 109, 142, 177], can be used as data-fit models and have been used increasingly in recent years. In the case of ANNs, their scalability makes them especially well-suited to applications involving large datasets, a situation becoming more common in engineering with our increasing capacity to generate and store data. Overall, data-fit surrogate modeling is a relatively mature subject and many authors have studied the benefits of this strategy in the context of optimization [28, 45, 71, 75, 76, 127, 128, 129, 130, 131], uncertainty quantification [4, 118, 119, 151], and multi-disciplinary analysis [108, 143, 149].

### 1.2.2 Prediction of Fields

Complex simulations are typically based on a set of governing or conservation laws that are expressed as Partial Differential Equations (PDEs). The raw solution of these equations is the spatial and temporal distribution of some physical quantities from which engineering results are then derived. We define these spatially and temporally varying quantities as physical *fields*. With a few exceptions, these governing equations cannot be solved analytically. Solutions are instead obtained numerically by discretiz-

[3]Named in honor of the geostatistician Daniel G. Krige who pioneered the method.

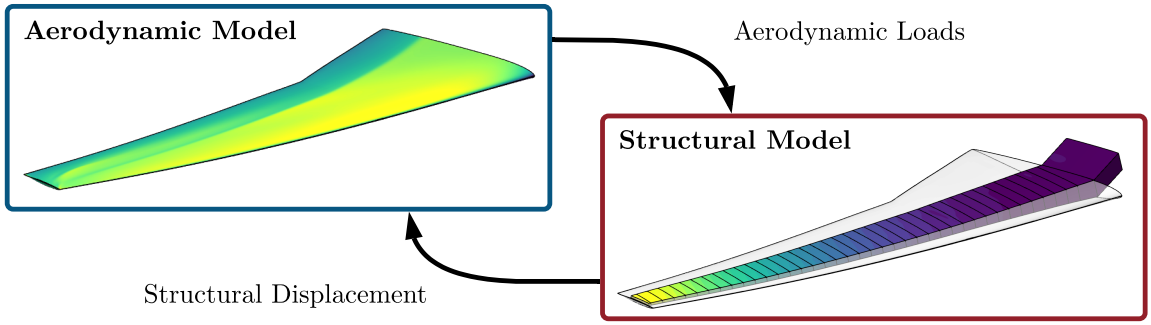


**Figure 1.2:** Demonstration of the multi-disciplinary coupling between the high-dimensional fields of an aerodynamic and a structural model.

ing the PDEs into grids, usually in the form of finite elements or volumes. Therefore, the field solutions of complex simulations are expressed as high-dimensional vectors in practice.

Furthermore, in scenarios involving tightly coupled physical simulations, such as in aeroelastic or aerothermal problems, the field solutions of the individual disciplines act as coupling variables. For instance, consider the notional flexible wing problem shown in Figure 1.2. This problem represents a coupled multi-disciplinary system consisting of a structural and an aerodynamic model. For a given flight condition, the aerodynamic model computes the pressure and shear-stress distribution on the wing. The structural model uses this information to calculate the wing deflection and feeds it back to the aerodynamic model. The aerodynamic loads are then recomputed with the new wing shape that, in turn, updates the structural deformation, and so forth until the solution converges to a consistent aeroelastic shape.

Considering only the aerodynamics, if one were to replace the simulation with a surrogate model, this model would need to predict the aerodynamic load distribution as a function of the wing shape. Assuming a typical CFD grid, this could represent an output with millions of dimensions. Considering the structural simulation instead would produce a similar situation except that the structural displacement field would instead be the output of interest. Typical data-fit models are designed for scalar outputs and are inadequate for such tasks. While it is technically possible to predict

the individual components of a discretized field by an equal number of separate data-fit surrogate models, this approach would be computationally inefficient. It would also disregard completely any spatial or temporal coherence potentially existing within the fields.

A relatively recent solution to field prediction is to employ a Reduced-Order Model (ROM) [98], which is essentially a low-dimensional representation of a physical system. These models assume that the high-dimensional solution of a physical system can be reduced to a small number of fundamental features, thus exploiting the intrinsic structure of the output space. Most ROMs are *projection-based* and the model reduction is achieved by projecting the physical model into a lower-dimensional subspace, also known as *latent space*, that best retains the dominant characteristics of the solution [15]. In other words, a linear combination of dominant features represents the output space of the physical model. While there exist many methods to construct the low-dimensional latent space of a ROM, the most widely used is arguably the Proper Orthogonal Decomposition (POD). Lumley [99] initially introduced this method for the decomposition of turbulent flows into coherent structures. In other fields of science, POD is also closely related to the Karhunen-Loève Transformation (KLT), Singular Value Decomposition (SVD), and Principal Component Analysis (PCA) [74]. The POD basis is extracted empirically from a set of sampled solutions, also known as *snapshots* [144], collected during an offline phase for a range of input parameter values. The POD basis vectors (also known as *POD modes*) are selected such that they best capture the variance of the training data, which equivalently minimizes the reconstruction error of the snapshots (see Bishop [19] for detailed proof). The content of Chapter 3 provides additional details on the POD method.

Although the purpose of ROMs is to predict field results, one should note that predicted fields can still be used to compute integrated quantities at a relatively low cost. For instance, let us consider the prediction of aerodynamic forces and moments

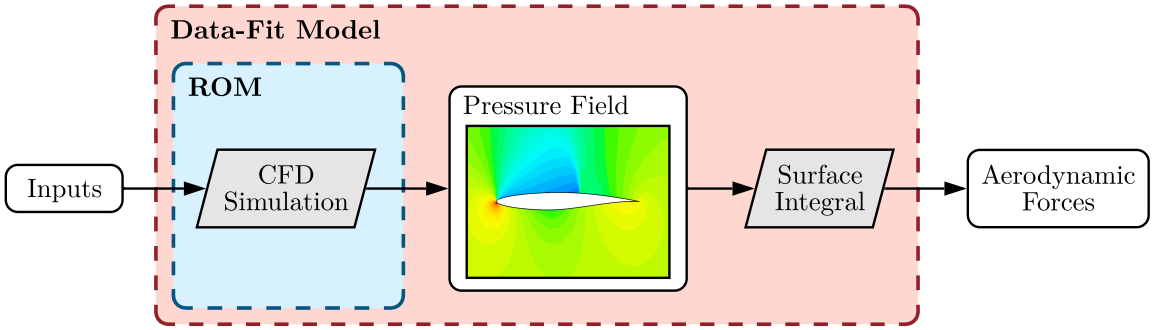


**Figure 1.3:** Notional example of the offline construction of a POD-based ROM.

over an airfoil by using a CFD simulation as illustrated in Figure 1.3. Given a set of design parameters, the raw solution of the CFD code contains the pressure and skin friction fields that are integrated at the airfoil surface to obtain the lift, drag, and pitching moment. A data-fit model would abstract both the CFD simulation and the surface integration such that only the relation between the aerodynamic forces and the design parameters is preserved. On the other hand, a ROM would only replace the CFD code and directly predict the fields of interest. Since the integration step is relatively inexpensive, the aerodynamic forces are then readily computed using the airfoil geometry and the ROM output. Figure 1.3 also highlights that ROM predictions are closer to the underlying simulation and contain richer physics. As a matter of fact, some authors have noted that integrated quantities derived from ROM results are generally more accurate than those predicted via traditional data-fit models [46]. It is also worth noting that with a data-fit model, the prediction of each aerodynamic forces and moments (e.g., lift, drag, etc.) requires a separate surrogate model. With a ROM, the same field prediction can provide all integrated quantities at once.

### 1.2.3 Observations on Surrogate Models

As the design process increasingly leverage physically accurate models for the conceptual and preliminary phases, the more intertwined the various disciplines have

become. In NASA's CFD Visions 2030 study [147], the seamless integration of CFD analysis with multi-disciplinary analyses is identified as one of the key capabilities to be developed. In the same report, the authors also noted that "the use of optimization with multiple disciplines treated using high-fidelity methods is still within the realm of advanced research and is by no means a routine practice." Since the quantities exchanged between coupled simulations are often fields, replacing these individual analyses with cheap approximations necessitate the prediction of field results. While we should not perceive data-fit models as obsolete by any means, the inclusion of surrogate models in future design processes requires the unique capabilities of ROMs. Even in settings requiring the prediction of integrated quantities, the physically richer results of ROMs can potentially improve the prediction. This highlights the importance of reduced-order modeling research for the advancement of aircraft design and is a key motivation for the current dissertation.

## 1.3 Intrusive vs. Non-Intrusive ROMs

When applied to the prediction of fields with respect to some parametrization, we can generally categorize ROM methods as either *intrusive* or *non-intrusive*. In both approaches, the projection-based ROM is constructed in an offline phase as shown in Figure 1.4. During this phase, field solutions are generated from a DoE and are used to uncover the dominant modes present in the data, typically using the POD method. Once the projection basis is identified, new fields are reconstructed by linearly combining the extracted modes as shown in Figure 1.5. As such, the prediction of a new high-dimensional field is reduced to finding the few coefficients of this linear expansion, which are also known as *latent variables* or *latent coordinates*. The main differences between intrusive and non-intrusive methods arise mostly from how these latent variables are obtained.

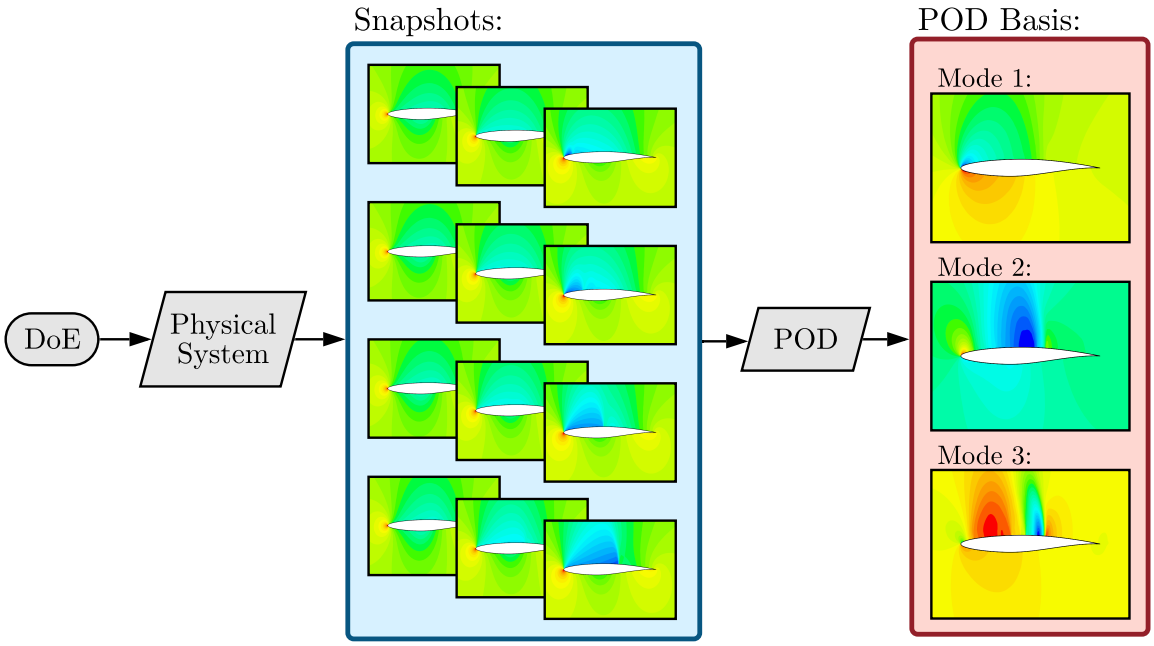


**Figure 1.4:** Notional example of the offline construction of a POD-based ROM.

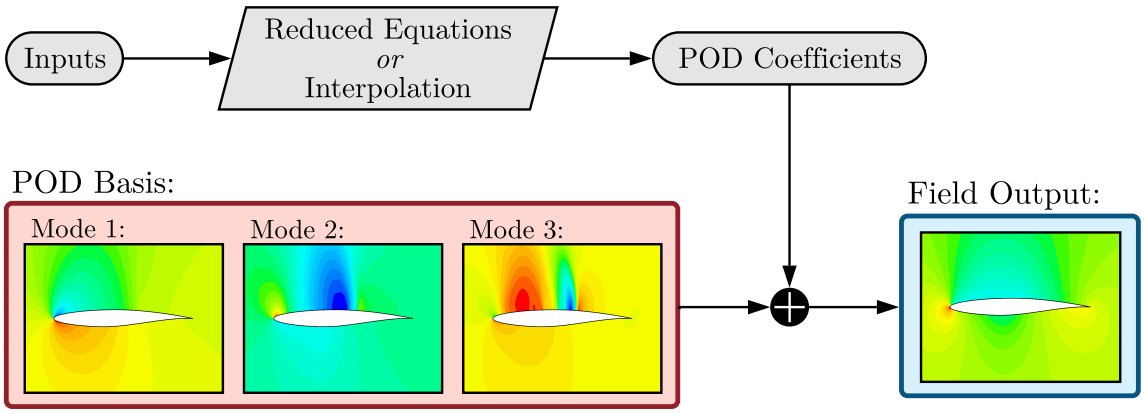


**Figure 1.5:** Notional example of the online prediction of a new field using a POD-based ROM.

With an intrusive approach, the governing equations of the original physical system are projected into the extracted lower-dimensional subspace using a *Galerkin* method [98, 145]. A reduced set of equations is still solved, yet the complexity of the system is greatly reduced. The scientific literature contains multiple examples showing this method applied to problems such as aerodynamic prediction [24, 166, 173] and aeroelastic analysis [6, 7, 95, 155]. The main drawback of intrusive ROMs is that in order to perform the Galerkin projection, the method must have direct access to the discretized equations of the physical system and often requires modification of the simulation source code. Therefore, intrusive methods are restricted to *white-box*[4] simulations, which typically implies open-source or in-house codes. Furthermore, the presence of non-linear terms in the governing equations, which is the case for CFD, poses additional challenges [15].

On the other hand, non-intrusive ROMs represent the sampled data into the extracted latent space and then interpolate between the latent coordinates of those solutions. In other words, non-intrusive methods are a combination of a *dimensionality reduction* (see Section 2.1) method and a regression or interpolation model. New predictions are achieved without solving any system of equations, which means that non-intrusive ROMs can be applied to any high-dimensional fields regardless of what model produced the data, essentially treating the original model as a black-box. In theory, the regression step could use any data-fit models, and some have demonstrated this method using cubic splines [23], RBF [47, 78], Kriging [46, 180], and ANN [68, 117, 152].

### 1.3.1 Observations on Parametric ROMs

In comparison to their intrusive counterpart, non-intrusive ROMs generally tend to be less accurate, especially in scenarios involving strongly non-linear phenomena such

[4]The term *white-box* refers to a system or function whose inner workings are known or available for inspection, i.e., the opposite of a *black-box*.

as shock waves [92] or boundary layer separations. However, their versatility and easier implementation more than compensate for this deficiency since their application is agnostic to the underlying simulation. In the context of replacing expensive simulations in the early design phases, this feature is particularly relevant since a non-intrusive approach is guaranteed to be feasible regardless of the simulation being used, open-source or not. Because non-intrusive methods are disconnected from the governing equations, they are also capable of predicting a subset of a field solution only. For instance, one can construct a non-intrusive ROM to predict the pressure at the surface of a wing only, which is all that is required to compute the aerodynamic loads. This allows for smaller training datasets and even greater adaptability. For the above reasons, this dissertation focuses specifically on non-intrusive ROMs.

## 1.4 Cost and Accuracy Trade-Off of Surrogate Models

As with most empirical methods, the performance of a data-fit model or a POD-based ROM is closely connected to the quality and size of the training data. As a general rule, the more densely sampled is the design space, the more accurate a surrogate model is. In the context of interpolation, the prediction uncertainty at an unobserved point increases the further away it is from the observed data, especially when the point of interest is outside of the convex hull of the data. Likewise with POD, many observations are required to ensure that the extracted POD modes represent the most statistically significant features of the problem. Also, the volume of data required to sample adequately the input space increases exponentially with the number of input parameters, a phenomenon often referred to as the *curse of dimensionality* [65]. Since surrogate models are meant to replace simulations with considerably long runtime, collecting large volumes of data can be a computationally expensive endeavor. One must carefully balance the surrogate model accuracy with its training cost, which is mostly comprised of the computational cost of creating the training

dataset. Generally, the upfront training cost of a surrogate model is entirely offset by its fast execution in many-query settings, especially if more than one design problem can reuse the same surrogate model. However, in some particularly challenging scenarios, i.e., with an expensive physical model and high-dimensional inputs, surrogate modeling might not be a viable option.

To address this issue, researchers have developed methods to mitigate the high training cost of a surrogate model without sacrificing its prediction accuracy. These modeling approaches can generally be divided into two strategies: multi-fidelity modeling and adaptive sampling.

### 1.4.1 Multi-Fidelity Modeling

One way to address the dilemma between accuracy and training costs is to build a surrogate model using more than one source of data. Most engineering problems can be solved using different analysis alternatives with various trade-offs between accuracy and computational cost. In the context of this work, a *high-fidelity* model is a simulation model that is sufficiently detailed for the problem at hand. This will conceivably be a model whose purpose is to capture complex physics and is most likely computationally expensive. In comparison, a *low-fidelity* model is any simplified yet physics-based analysis that sacrifices accuracy for a significant decrease in computing time compared to the high-fidelity model. However, the quality of the results is assumed insufficient for the problem under consideration such that the low-fidelity model is not an adequate substitute for a high-fidelity model. Even though a low-fidelity model is deemed inaccurate, its data potentially share some relation with the data from a high-fidelity model such that useful information can still be exploited. Additionally, with what some low-fidelity data may lack in quality, it can compensate in quantity due to the short evaluation runtime of the low-fidelity model.

Instead of choosing either the high- or the low-fidelity data, a *multi-fidelity sur-*

*rogate model* (also called a *variable-fidelity model*) attempts to combine both sources of information in a synergistic manner [119]. In principle, a multi-fidelity surrogate is generated using a few high-fidelity samples, and many low-fidelity samples to keep the joint sampling cost relatively low. The sparse high-fidelity data establish the accuracy of the surrogate while the dense low-fidelity data provide a useful approximation of the rest of the design space. Loosely speaking, the low-fidelity model is used to fill in the likely large voids unexplored with the high-fidelity model. Assuming the high- and low-fidelity models are related and the latter is substantially faster to evaluate, an accurate surrogate model is obtained at a lower overall computational cost. The concept of a multi-fidelity model is illustrated with a canonical problem in Figure 1.6. In this example, we observe that a single-fidelity model cannot properly capture the complexity of the high-fidelity model due to limited samples. By augmenting the high-fidelity data with some low-fidelity samples, a much better prediction is achieved. It should be mentioned that the current discussion on multi-fidelity surrogate models is limited to scenarios with two levels of fidelity, i.e., one high- and one low-fidelity model. Nonetheless, extending the approach to additional levels of fidelity is usually possible and straightforward [87, 89]. The literature contains many examples of multi-fidelity methods applied to surrogate modeling [62, 64, 80, 88] and surrogate-based optimization [1, 40, 45, 159].

*Types of Model Simplification*

Within a discipline, subject-matter experts are usually aware of multiple simplifications that can be applied to a given simulation to reduce its computational cost. As such, different low-fidelity models can be derived from the same high-fidelity model with varying trade-offs between cost and accuracy.

One possible simplification is to abstract, or even omit, some physical phenomena depending on their influence on the overall solution. For instance, let us consider

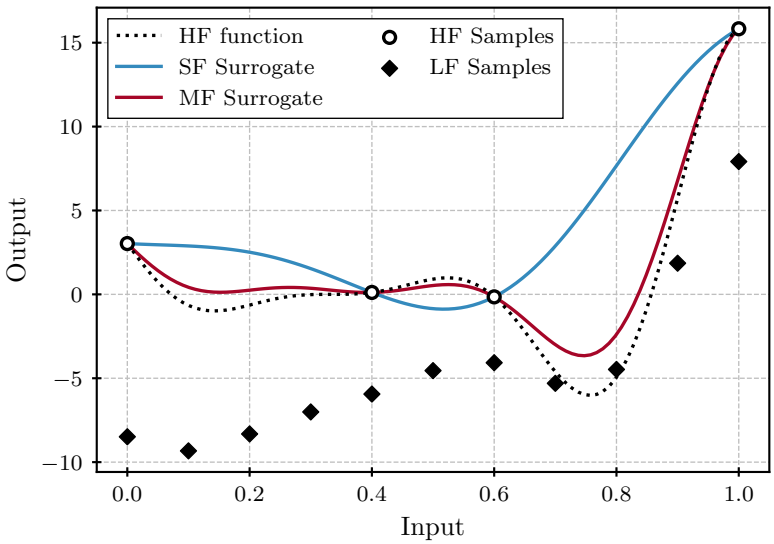


**Figure 1.6:** Comparison of a single- and multi-fidelity surrogate model on a canonical problem. The acronyms in the legend are high-fidelity (HF), low-fidelity (LF), single-fidelity (SF), and multi-fidelity (MF). Inspired from the work of Forrester et al. [45].

the context of aerodynamic analysis. A Reynolds-Averaged Navier-Stokes (RANS) simulation is usually perceived as a high-fidelity model, at least for design purposes. By neglecting viscous phenomena such as turbulence and boundary layers, RANS can be simplified into a more economical inviscid simulation based on the Euler equations. If one further omits non-linear aerodynamic effects such as shock waves, cheaper potential flow methods such as the Vortex Lattice Method (VLM) can be used instead. To put these methods in perspective, a RANS simulation requires a runtime of many hours on a computer cluster. In comparison, a normal desktop computer can solve a VLM simulation in a matter of seconds. However, a VLM model is unable to predict skin friction or wave drag whereas a RANS model can. When designing a transonic transport aircraft, this level of simplification leads to a large error on the cruise performance prediction. A similar hierarchy also exists in structural analyses where, from higher to lower fidelity, a structure can be analyzed using a solid model, a shell model, or a stick-beam model.

In addition to physical modeling, simplifications can be made with respect to the numerical methodology. For simulations relying on a grid discretization, reducing

the grid size will have a strong impact on the computational cost. In general, coarser grids require fewer numerical operations and have a smaller memory footprint, but also reduces the accuracy of the results. Furthermore, most large-scale numerical simulations rely on an iterative solver to obtain a solution. In such cases, the solver iterates until the solution converges and reaches some stopping criteria. By loosening those criteria, the simulation will end in fewer iterations at the expense of an unconverged solution.

*Other Auxiliary Datasets*

Although multi-fidelity models usually imply high-fidelity data supplemented with a low-fidelity dataset, the auxiliary dataset in this context does not necessarily need to be of lower fidelity. In fact, the main requirement is for the auxiliary data to be related to the main dataset, i.e., the high-fidelity, and to be available in larger quantities. A viable alternative to using a lower-fidelity simulation is to take advantage of pre-existing data from a different, yet similar, problem. This data could be from a previous and comparable design problem or be a dataset of a different quantity of interest related to the one being predicted. This scenario can be enticing since the auxiliary data might be readily available and could augment a surrogate model with little additional cost.

Furthermore, some authors have suggested enhancing surrogate models by exploiting gradient information [21, 63, 180]. These approaches have similarities with multi-fidelity methods, although the gradient of the underlying simulation is used as the auxiliary dataset. With the recent progress of adjoint solvers and automatic differentiation [107], the gradient of scalar quantities can be obtained at a reasonably low cost, especially with problems having high-dimensional input spaces. The above techniques usually require specialized codes, and without a fast means of evaluating the gradient, one must then rely on finite differences which can be highly inefficient.

### 1.4.2 Adaptive Sampling

The governing principle of adaptive sampling is that a surrogate model can be improved sequentially to meet some requirements. Each new sample is informed by the previous ones and maximizes the quality of the surrogate model for the least amount of effort. The selection process of the next sample usually takes the form of a sub-optimization problem where some *infill criterion* is optimized. Usually, these infill criteria are formulated such that the next design point offers a balance between *exploration* and *exploitation* [44]. In this context, exploration implies a better capture of the entire design space, while exploitation means an improved accuracy near a potential area of interest, usually an optimum. In the literature some of the most common infill criteria include:

- Probability of Improvement [75]
- Expected Improvement [76]
- Goal Seeking [75]
- Integrated Mean Square Error [65]

It should be noted that the previous criteria assume a stochastic surrogate model such as Kriging. An infill criterion based on the *bumpiness* of the surrogate model response is also available for RBF [20, 58], a deterministic surrogate model.

Typically, adaptive sampling is used in the context of optimization and is a core component of Efficient Global Optimization (EGO) [76], a popular surrogate-based optimization strategy. Adaptive sampling can, moreover, be combined with multi-fidelity modeling [87]. In that context, the selection of the next training sample also considers which fidelity level to query and best improve the multi-fidelity surrogate model. While new samples are usually added sequentially, methods to select multiple infill points at once also exist [59]. This allows the user to parallelize the data

generation and fully utilize the available computing resources.

One of the major limitations of adaptive sampling is that it tends to perform poorly with high-dimensional input spaces [97]. Indeed, a poor surrogate model constructed using a limited number of samples will produce unreliable values for most infill criteria. This is why an initial or *warm-up* dataset with a minimum size is usually provided before beginning the adaptive sampling process. As the number of input variables increases, the size required for the initial dataset grows exponentially, which further illustrates the consequences of the curse of dimensionality. Besides, the sub-optimization problem of adaptive sampling becomes increasingly challenging to solve with higher dimensional input spaces.

### 1.4.3 Observations on Cost Reduction Strategies

In the context of optimization with high-fidelity simulations, multiple studies have shown that adaptive sampling can effectively construct a surrogate model that accurately captures the optimum at a reasonable cost [20, 58, 76, 97]. However, a surrogate model created in such a way is not guaranteed to be reusable in other problems nor is it to be accurate away from the discovered optimum. Also, adaptive sampling is not necessarily suited for applications other than optimization, such as design space exploration, uncertainty quantification, etc. On the other hand, multi-fidelity modeling aims to improve the overall prediction accuracy of the surrogate model. This ability indiscriminately benefits all many-query scenarios including optimization. Furthermore, multi-fidelity methods do not have any inherent limitations with high-dimensional input spaces. Multi-fidelity surrogate models could even be used to improve adaptive sampling in hard problems. From the above observations, we assume that multi-fidelity modeling is a more comprehensive strategy to reduce the training cost of surrogate models for many-query applications.

## 1.5 Challenges of Multi-Fidelity Fields

In the previous section, multi-fidelity methods were established as an effective means of reducing the training cost of a surrogate model while maintaining reasonable accuracy. Many examples can be found in the literature where this strategy was applied to the prediction of scalar quantities [62, 64, 80, 88]. When it comes to the prediction of fields, the multi-fidelity literature is relatively sparse on the subject and only a handful of studies exists (more details in Section 2.5). While the recent introduction of ROMs in engineering problems can partially explain the scarcity of multi-fidelity methods, it is more seemingly due to the inherent difficulty of combining disparate field results. Indeed, simulations of different fidelity levels will likely produce field solutions with dissimilar representations, even though they correspond to the same design problem. Here, we identify and provide examples for three types of inconsistencies associated with field dimensionality, topology, and features.

### 1.5.1 Inconsistent Dimensionalities

As mentioned in Section 1.4.1, a common way of lowering the fidelity of a simulation is to use a coarser discretization. This increases the *discretization error* of the solution in exchange for a substantially lower computational cost. An example of this inconsistency is illustrated in Figure 1.7, where the flow field around an airfoil is discretized with both a coarse and a fine grid. The flow field with the fine grid will have a higher dimensionality than the coarse grid since it contains more cells. Consequently, the two discretized fields do not exist in the same vector space and cannot directly be compared. Differences in grid sizes can also be the result of simulations having different requirements. For instance, the grid for a RANS CFD simulation must be refined near walls to adequately capture large velocity gradients within the boundary layers. This grid refinement is not required for an inviscid CFD simulation

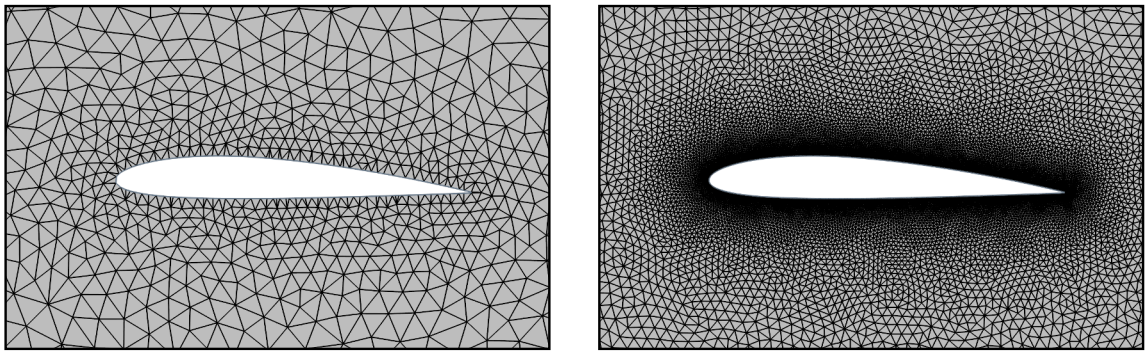

a) Coarse Grid b) Fine Grid

**Figure 1.7:** A coarse (a) and fine (b) discretization for the CFD analysis of a notional airfoil.

since it does not model boundary layers. In fact, the use of closely bunched cells with high aspect ratios and without a correspondingly large flow gradient could potentially have an adverse effect on the numerical solver.

To circumvent inconsistent dimensionalities between high- and low-fidelity solutions, some authors have elected to map all the results onto a common grid, often the coarser one, during a pre-processing step, i.e., before constructing the ROM [12, 14, 105]. Although this approach is not particularly difficult, a drawback of mapping some solutions onto a different grid is the potential introduction of interpolation errors into the results. Besides, if the high-fidelity fields are mapped onto a grid with a coarser discretization, it will degrade the resolution of the high-fidelity solutions.

### 1.5.2 Inconsistent Topologies

In some cases, a lower fidelity simulation requires a simplified geometry. For instance, in aerodynamics, a VLM simulation will represent an aircraft as thin surfaces as demonstrated in Figure 1.8. In comparison, a more complex simulation such as CFD will use the Outer Mold Line (OML) to model the wetted surface of the aircraft. As a consequence, the surface fields of a VLM and CFD analysis, say their surface pressure distribution, are associated respectively with geometries having inconsistent

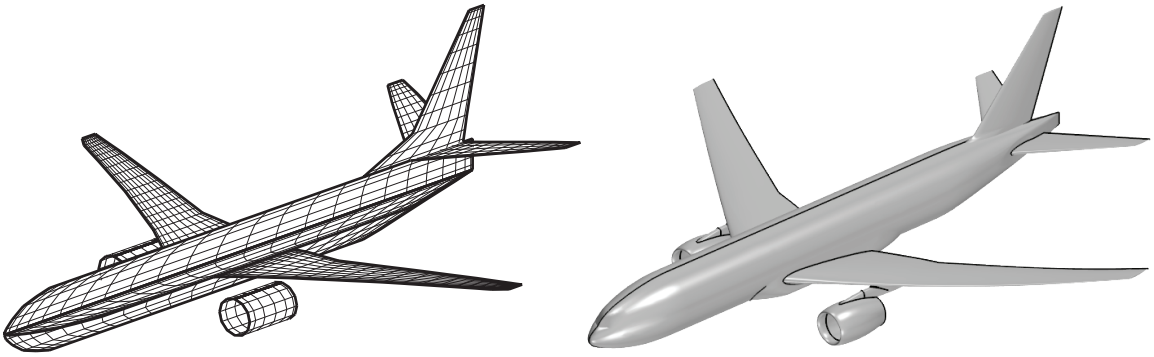

a) Thin surfaces b) Actual geometry

**Figure 1.8:** A thin surface representation (a) of a transport aircraft compared to the OML geometry (b). The aircraft geometries correspond to the NASA Common Research Model [164].

topologies. A similar situation is also common in a structural analysis where the structure of a wing is often simplified by using shell or even beam elements. Even in cases where the dimensionality is the same, fields linked to inconsistent topologies are likely not contained in the same subspace, thus preventing a point by point comparison. Unlike in Section 1.5.1 with inconsistent dimensionalities, mapping field results onto a baseline grid to reconcile inconsistent topologies is not straightforward.

### 1.5.3 Inconsistent Features

As mentioned in Section 1.4.1, an interesting feature of multi-fidelity surrogate models is that the high- and low-fidelity datasets can use different physical quantities, as long as they are related. For example, one could better predict the pitching moment of an airfoil by supplementing it with lift data, assuming the latter is readily available in greater quantity. Therefore, predicting a given field with a different, yet related, one is a reasonable application. Let us consider the skin friction and the surface pressure of a wing as illustrated in Figure 1.9. Let us also assume that both fields are produced by different models and that pressure fields are easier to obtain than skin friction results. A likely cause of this would be that the pressure results are produced by an inviscid

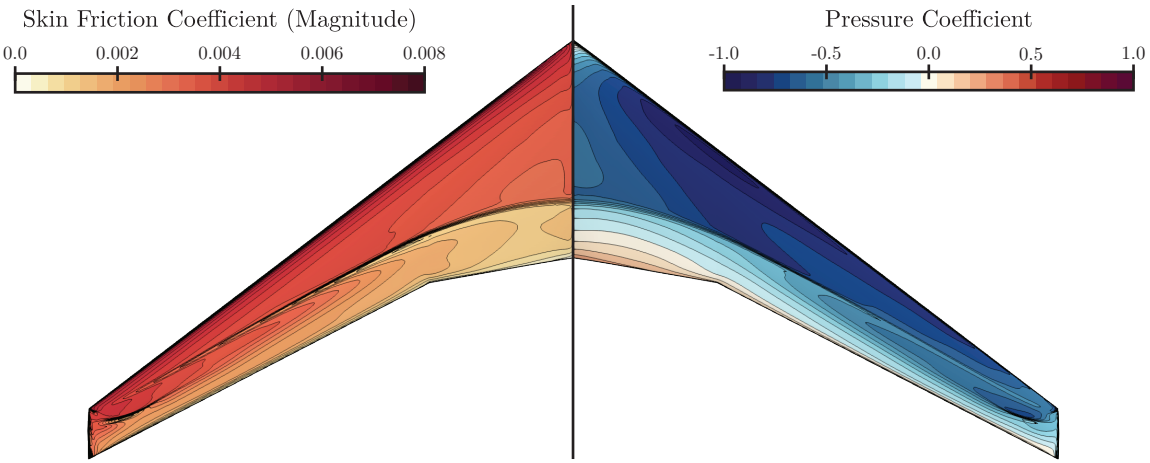


**Figure 1.9:** Distribution of the skin friction coefficient (left) and pressure coefficient (right) over a transonic wing.

simulation while the skin friction is given by a RANS simulation. From Figure 1.9, we can see that both fields share some similarities, yet have slightly different features. Applying POD on these fields will reasonably result in different sets of modes and latent variables, despite potentially having a consistent dimensionality and topology. Consequently, it is not immediately obvious how the skin friction and pressure fields can be combined such that their interrelation can be exploited in a multi-fidelity context.

### 1.5.4 Observations on Multi-Fidelity Fields

Whereas multi-fidelity methods abound for the prediction of scalars, the potential inconsistencies between fields of different fidelity levels result in additional challenges for the multi-fidelity prediction fields. A potential solution is to limit the multi-fidelity combination to simulations using the same representation across all fidelity levels and to rely solely on simpler numerical methods to achieve some computational savings [17, 111, 110]. Alternatively, if the various fields are associated with the same geometry but have inconsistent dimensionalities, one can reasonably interpolate all the multi-fidelity results onto a common grid [12, 14, 105]. The above approaches do

not resolve, however, possible inconsistencies in topologies or features. This leaves many multi-fidelity combinations of high- and low-fidelity simulations incompatible with current multi-fidelity ROM methods. This motivates the development of a multi-fidelity method that could bridge any potential inconsistency in dimensionalities, topologies, and features.

## 1.6 Summary

The conceptual and preliminary phases of aircraft design rely heavily on numerical simulations for many-query applications such as design space exploration, optimization, and uncertainty quantification. At the same time, ambitious design objective and unconventional aircraft configuration motivate the adoption of computationally expensive and high-fidelity models earlier in the design process. In the many-query context, the high computational cost entailed by these high-fidelity simulations is impractical. A generally accepted solution is to approximate them with surrogate models. Whereas surrogate models are conventionally associated with data-fits and the prediction of scalars, a more recent type of model, referred to as ROMs, modify this paradigm by instead predicting field solutions.

This chapter provided an overview of ROMs and outlined their potential benefits for aircraft design, especially in scenarios involving high-fidelity and multi-disciplinary analysis. Intrusive and non-intrusive ROMs methods were compared and our focus on the latter was justified by their greater applicability. This was followed by a discussion on the challenges of surrogate models, such as the potentially large upfront cost of generating the training data. Multi-fidelity methods and adaptive sampling were presented as a means to mitigate large training costs and we argued that the former strategy is more versatile. While well-established multi-fidelity models exist for the prediction of scalar outputs, we discussed the additional difficulties of the multi-fidelity prediction of field quantities. Namely, the multi-fidelity combination of

fields can be afflicted with inconsistencies in field dimensionalities, topologies, and features.

For the sake of clarity, the content of this chapter is structured and summarized into the following key observations:

**Observations 1**

1.1 Many-query applications employing high-fidelity and multi-disciplinary analysis are key enablers for the design of future aircraft.

1.2 The shared variables of multi-disciplinary analysis are often field quantities. Replacing the individual analysis with cheaper approximations requires the unique capabilities of ROMs.

1.3 Even in cases where integrated quantities are required, ROMs can potentially provide better prediction than conventional data-fit models by retaining more physics information in their predictions.

1.4 Compared to intrusive methods, non-intrusive methods are more practical and allow for a broader adoption of ROMs since their construction is independent of the underlying simulation being replaced.

1.5 Although ROMs are fast to evaluate, problems involving expensive simulations and many design parameters can incur a prohibitive upfront training cost.

1.6 Both adaptive sampling and multi-fidelity methods can effectively reduce the training cost of a surrogate model. However, the former is best suited for optimization while the latter can benefit general applications.

1.7 Compared to scalar quantities, the multi-fidelity combination of fields is

considerably more challenging due to potential inconsistencies in dimensionalities, topologies, and features, between results of different models.

1.8 Interpolating fields with different discretization onto a common grid can resolve dimensionality differences. Yet, it can introduce interpolation errors and does not resolve other types of field inconsistencies.

The above observations highlight the importance of non-intrusive ROMs and multi-fidelity methods in a high-fidelity and many-query context. This allows us to premise the following research objective that is the foundation of the current dissertation:

**Research Objective**

To develop or improve a *non-intrusive* and *multi-fidelity* reduced-order modeling method for the purpose of many-query applications, and with an emphasis on combining multi-fidelity fields with *disparate representations*, i.e., fields having inconsistent dimensionalities, topologies, and features.

The remaining chapters of this dissertation are divided as follows:

- **Chapter 2** presents some background information on dimensionality reduction and multi-fidelity modeling. We also review the relevant literature on single- and multi-fidelity ROMs.
- **Chapter 3** describes the proposed multi-fidelity ROM method and provides details on the various numerical techniques that are being leveraged.
- **Chapter 4** outlines the research formulation used to demonstrate the performance of the proposed method with respect to the current objective. This

includes descriptions of the research questions, test cases, and performance metrics, used in the experimental approach.

- **Chapter 5** lays out the experiments used to address the research questions of this work. This is followed by a discussion of the obtained results.
- **Chapter 6** summarizes the contributions and the main findings of this dissertation. Some potential avenues for future research are also explored.

# CHAPTER 2
# BACKGROUND AND LITERATURE

In this chapter, we explore the field of dimensionality reduction, which is a fundamental component of projection-based reduced-order modeling. We then present an extension of dimensionality reduction methods, i.e., manifold alignment, and demonstrate how it can combine fields with disparate representations. This is followed by a brief overview of the current state of the art for multi-fidelity data-fit models. A review of existing non-intrusive ROMs, both single- and multi-fidelity, is then considered, and the gaps with the current approaches are established. The contents of this chapter are then summarized into key observations that are used to formulate the overall hypothesis of this thesis.

## 2.1 Dimensionality Reduction

The efficient analysis of high-dimensional data is a challenging task that goes beyond reduced-order modeling. For example, in image classification, the data to be analyzed is composed of numerous images, which can easily contain thousands or even millions of pixels. This difficulty also extends to signal processing, pattern recognition, image compression, data visualization, etc. As such, *dimensionality reduction* (also known as *feature extraction* or *representation learning*) is a general process from the field of machine learning that attempts to reduce large-scale data into a small and manageable number of dimensions [163]. The overall assumption of dimensionality reduction is that within most high-dimensional datasets, there exists an intrinsic coherence with some dimensions being interdependent. With some clever transformation, the redundant information contained in large-scale data can be removed such that only a handful of relevant dimensions remain. In mathematical terms, given some

high-dimensional dataset $\mathbf{X} = [\mathbf{x}_1, \ldots, \mathbf{x}_n] \in \mathbb{R}^{d \times n}$ containing $n$ samples of dimensionality $d$, there exists an analog low-dimensional dataset $\mathbf{Z} = [\mathbf{z}_1, \ldots, \mathbf{z}_n] \in \mathbb{R}^{k \times n}$ that is a faithful representation of $\mathbf{X}$. Here, we denote $k$ as the *latent* or *effective* dimensionality of the data, where $k \ll d$. The objective of dimensionality reduction is, therefore, to uncover the mapping

$$\mathcal{M} : \mathbf{x} \in \mathbb{R}^d \mapsto \mathbf{z} \in \mathbb{R}^k \tag{2.1}$$

which maps a sample in the *data space* (or *full space*) to a so-called *latent space* (or *reduced space*) of lower dimensionality. One can also consider the latent variable $\mathbf{z}$ as being a set of coordinates on a $k$-dimensional manifold that is embedded in a $d$-dimensional space.

The POD method previously mentioned in Section 1.2.2 and used in many ROMs, is an instance of dimensionality reduction. This method is more commonly referred to as Principal Component Analysis (PCA) in the fields of statistical analysis and machine learning. In this context, the principal components and their coefficients are the counterparts of the POD modes and the POD coefficients. The following discussion will use the term POD instead of PCA to remain consistent with the reduced-order modeling literature, but the reader should note that both methods are equivalent for all practical purposes.

A key difficulty in finding $\mathcal{M}$ is in defining how exactly $\mathbf{Z}$ is representative of $\mathbf{X}$. Indeed, the similarity between the full and reduced spaces can be assessed by several criteria, the choice of which will be dependent on the application and the type of data being reduced. Furthermore, some methods make assumptions regarding the structure of the low-dimensional manifold to alleviate the complexity of the dimensionality reduction task. Figure 2.1 provides a brief taxonomy of some of the most common dimensionality reduction methods found in the literature. We separate these ap-

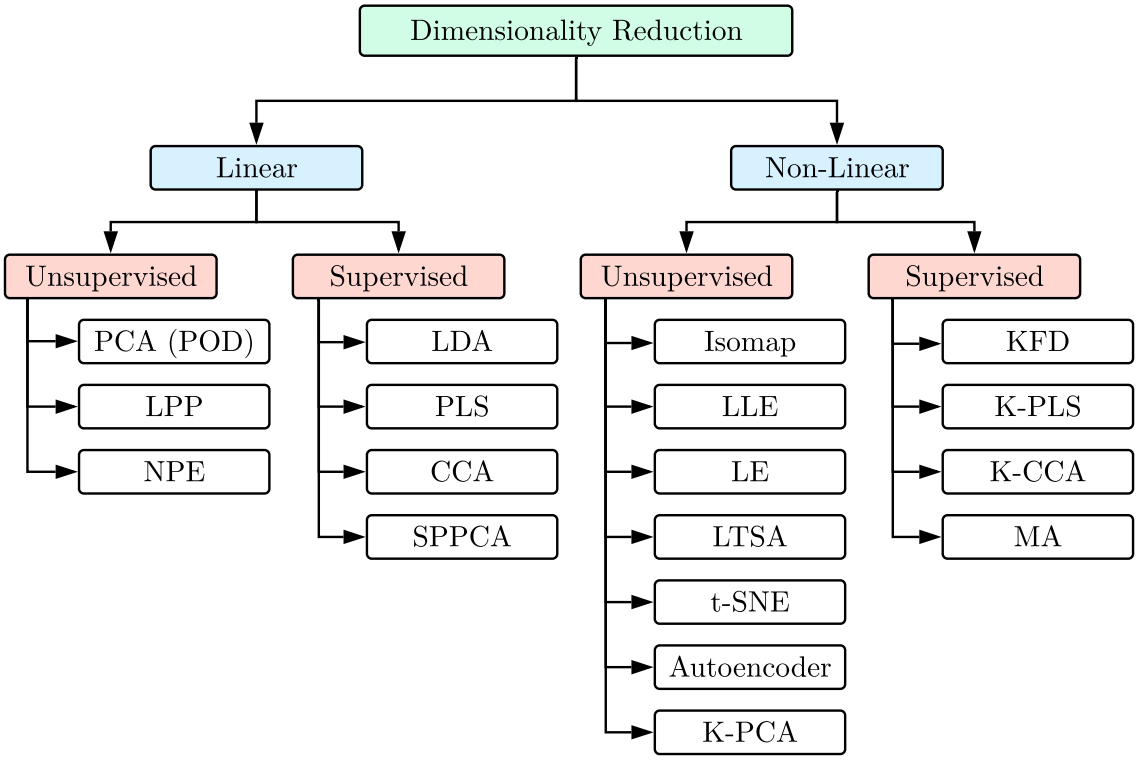


**Figure 2.1:** Taxonomy of some common dimensionality reduction methods. Methods listed are: Principal Component Analysis (PCA) [74], Locality Preserving Projection (LPP) [67], Neighborhood Preserving Embedding (NPE) [66], Linear Discriminant Analysis (LDA) [42], Partial Least Square (PLS) [104], Canonical Correlation Analysis (CCA) [104], Supervised Probabilistic PCA (SPPCA) [175], Isomap [154], Locally Linear Embedding (LLE) [136], Laplacian Eigenmap (LE) [10], Local Tangent Space Alignment (LTSA) [179], T-distributed Stochastic Neighbor Embedding (t-SNE) [103], Autoencoder [37], Kernel PCA (K-PCA) [141], Kernel Fisher Discriminant (KFD) [112], Kernel PLS (K-PLS) [135], Kernel CCA (K-CCA) [70], and Manifold Alignment (MA) [169].

proaches using two overall dichotomies: *linear vs. non-linear* methods and *supervised vs. unsupervised* methods, which are elaborated in the following section.

### 2.1.1 Linear vs. Non-Linear Methods

With a *linear* dimensionality reduction approach, the latent data $\mathbf{Z}$ is obtained with a linear transformation of $\mathbf{X}$. The mapping $\mathcal{M}$ corresponds, in this case, to a projection matrix $\mathbf{\Phi} \in \mathbb{R}^{k \times d}$ that projects vectors from a $d$-dimensional data space onto

a $k$-dimensional latent subspace. The POD method is a well-known instance of linear dimensionality reduction where the mapping and latent variables are given by the principal modes and the corresponding coefficients respectively. In comparison, *non-linear* methods map the data onto a curved manifold, which allows them to outperform linear methods on complex tasks [163]. This is why non-linear dimensionality reduction methods are sometimes referred to as *manifold learning* methods. A linear method can also be made non-linear by applying them in a reproducing kernel Hilbert space using the so-called *kernel trick* [135].

The difference between linear and non-linear methods is made clear in Figure 2.2. In this canonical example, the latent manifold is a two-dimensional sheet warped into a three-dimensional *S-shape*. The linear and non-linear methods used for this demonstration are POD and Isomap [154] respectively. From Figure 2.2a, we see that the linear method simply projects the points onto a two-dimensional plane and the actual curved manifold is not recovered. On the other hand, the results of Figure 2.2b show that the *S-shape* is correctly unraveled into a sheet by the non-linear method, although with some distortions.

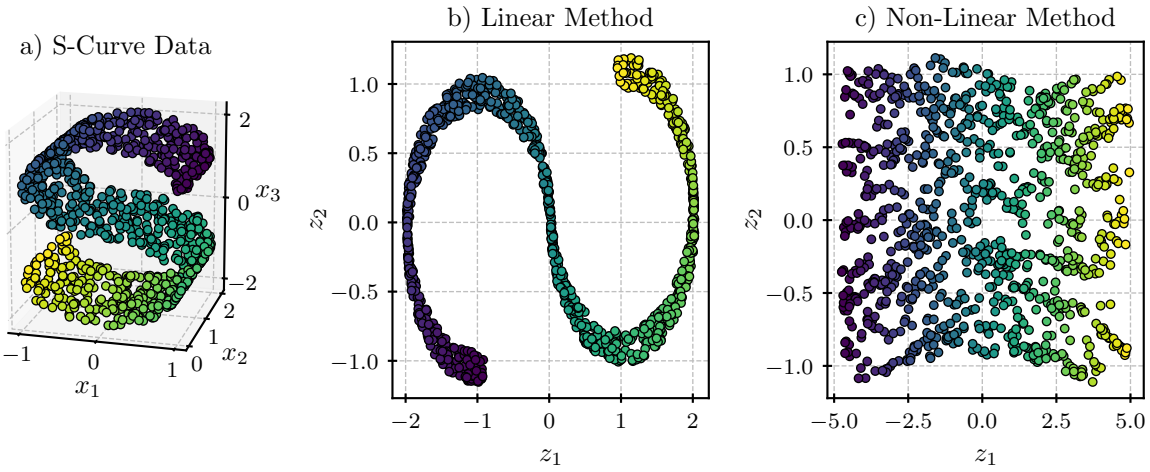


**Figure 2.2:** Demonstration of curved manifold (a) analyzed using a linear (b) and a non-linear (c) dimensionality reduction method. The S-shape is given by $[\sin(z_1), z_2, (\cos(z_1) - 1)\text{sgn}(z_1)]$ where $-3\pi/2 \leq z_1 \leq 3\pi/2$ and $0 \leq z_2 \leq 2$. The linear and non-linear methods correspond to POD and Isomap respectively.

A major drawback of non-linear methods is that most provide the latent variables directly, making the mapping $\mathcal{M}$ implicit. In other words, the correspondence between the full and reduced spaces is known only for the data used for the dimensionality reduction task. The absence of an explicit function for $\mathcal{M}$ means that mapping new points onto the latent space requires the user to repeat the dimensionality reduction or use some approximation. Similarly, the inverse mapping $\mathcal{M}^{-1}$ from the reduced to full space is not available with most non-linear dimensionality reduction techniques. Consequently, the original dataset cannot be easily reconstructed from the reduced data. In the context of a ROM, the reconstruction of the field is a crucial part of the method and the absence of an inverse map can be a major obstacle. The work of Franz et al. [47, 48] is an example of a ROM using a non-linear dimensionality reduction method. More specifically, the authors used Isomap to create an interpolation-based ROM. They solved the inverse mapping issue by using a weighted nearest-neighbor interpolation based on the coordinates in the latent space. The same approach was then used by Decker et al. [36] to construct a non-intrusive ROM using Locality Linear Embedding (LLE) [136] instead, another non-linear dimensionality reduction method.

On the other hand, with linear dimensionality reduction, the mapping is a projection matrix that is given explicitly by the method and defined for any point in the data space. Adding new points to the latent space is then a simple linear transformation and defining the inverse map is relatively straightforward. This is especially effortless if the projection matrix forms an orthonormal basis, in which case, the inverse map $\mathcal{M}^{-1}$ is merely $\mathbf{\Phi}^T$, i.e., the transpose of the original projection.

Furthermore, Van Der Maaten et al. [163] have shown in their review that despite being superior on artificial data sets, non-linear dimensionality reduction does not necessarily surpass linear methods on real-world data. Also, most ROM datasets are *under-sampled*, i.e., the number of samples $n$ is smaller than the dimensionality $d$ of

the field. In this situation, Kokiopoulou et al. [83] have shown that the result of many non-linear methods is, in actuality, a linear subspace. For all the above reasons, the limitations of non-linear dimensionality reduction typically outweigh their theoretical advantages when applied to reduced-order modeling. This explains the popularity of linear methods for ROM, of which, POD is usually the method of choice since it is optimal in terms of reconstruction error (discussed in Section 3.1). In fact, Decker et al. [36] demonstrated recently that POD-based ROMs generally have a lower global prediction error than equivalent non-linear ROMs constructed with either Isomap or LLE. However, the non-linear methods exhibited smaller local errors near discontinuities such as shocks.

### 2.1.2 Supervised vs. Unsupervised Methods

In machine learning terminology, the data used in dimensionality reduction is often *unlabeled*, i.e., is not augmented with some descriptive data, at least in the context of the task. When this is the case, the dimensionality reduction is said to be *unsupervised*. The method identifies the inner structure of the data based on the commonalities existing between each sample. The POD is an example of an unsupervised dimensionality reduction method that identifies the principal subspace using the variance of the data. On the other hand, dimensionality reduction can also be *supervised* such that the data set being reduced is *labeled*, i.e., is associated with some response information. For instance, the data to be reduced can be the high-dimensional inputs to some model and the labels are the corresponding outputs. By considering both the inputs and outputs, a supervised method will define the latent space based on the connection existing between the pair of data instead of the information within the inputs alone. This is particularly advantageous when the dimensionality reduction is ultimately a pre-processing step to a regression or classification task, i.e., other forms of supervised learning.

It should be noted that for reduced-order modeling, the intent is to reduce the dimensionality of some response fields. In comparison, most supervised dimensionality reduction methods are aimed at transforming some input or label datasets with respect to some outputs. As such, ROMs are constructed almost exclusively with unsupervised methods such as POD, Isomap, or LLE.

## 2.2 Manifold Alignment

Dimensionality reduction tasks are typically concerned with the extraction of a lower-dimensional representation of a single high-dimensional dataset. Other situations require instead the analysis of multiple high-dimensional datasets together to learn the potential correspondence existing between them. The goal is then to potentially share and transfer knowledge between these distinct datasets, assuming they are somehow related. The task of matching high-dimensional datasets is often complicated by their heterogeneity, i.e., their different representations, thus preventing a simple side-by-side comparison. However, from the premise that they are related, it follows that these disparate datasets are potentially characterized by a similar low-dimensional representation. Rather than comparing heterogeneous and high-dimensional data in their original state, it is likely much easier to match, or even align, their latent representations.

The purpose of *manifold alignment* [61, 169] is to map disparate, yet related, datasets onto a common latent space, i.e., a shared manifold. This task is a hybrid between unsupervised and supervised dimensionality reduction since the resulting low-dimensional representation should provide correspondences between the datasets, yet still capture their individually dominant features. More formally, let us consider two datasets $\mathbf{X} = [\mathbf{x}_1, \ldots, \mathbf{x}_n] \in \mathbb{R}^{d \times n}$ and $\mathbf{Y} = [\mathbf{y}_1, \ldots, \mathbf{y}_m] \in \mathbb{R}^{q \times m}$ with different features as shown in Figure 2.3, but whose samples are presumed to be embedded on the same latent space. Using the available data, manifold alignment identifies the

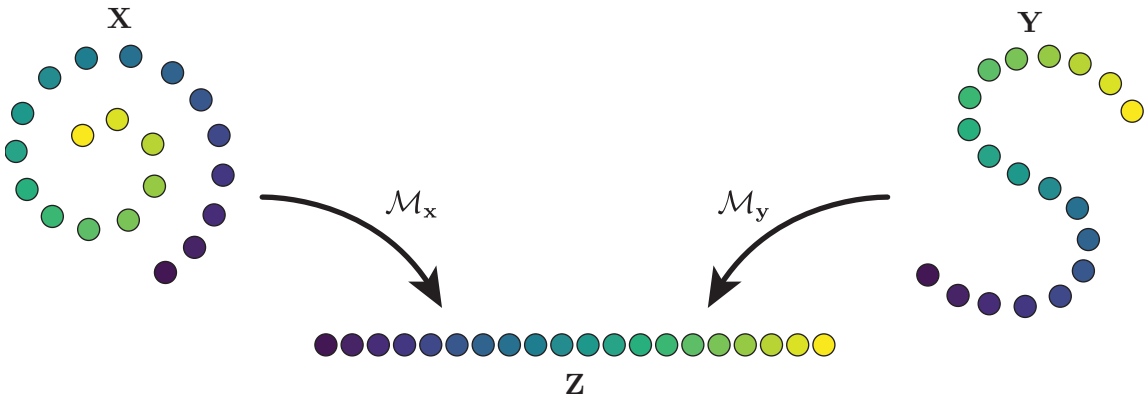


**Figure 2.3:** Example of manifold alignment where two datasets $\mathbf{X}$ and $\mathbf{Y}$ are mapped to a common latent variable $\mathbf{Z}$.

following mappings

$$\mathcal{M}_{\mathbf{x}} : \mathbf{x} \in \mathbb{R}^d \mapsto \mathbf{z} \in \mathbb{R}^k \tag{2.2a}$$

$$\mathcal{M}_{\mathbf{y}} : \mathbf{y} \in \mathbb{R}^q \mapsto \mathbf{z} \in \mathbb{R}^k \tag{2.2b}$$

which transform some high-dimensional quantities $\mathbf{x}$ and $\mathbf{y}$ respectively into a latent variable $\mathbf{z}$ existing on a shared lower dimensional manifold, i.e., where $d \gg k$ and $q \gg k$. Note that for notional samples $\mathbf{x}_i$ and $\mathbf{y}_i$ that are in exact correspondence, the obtained mapping does not necessarily guarantee them to have identical embeddings, i.e., $\mathcal{M}_{\mathbf{x}}(\mathbf{x}_i) \neq \mathcal{M}_{\mathbf{y}}(\mathbf{y}_i)$. Nonetheless, their associated latent variables should exist close to each other on the shared manifold.

The reader is referred to the work of Wang and Mahadevan [170] for a detailed description of manifold alignment and its applications in machine learning. For conciseness, the following section will present two of the forms of manifold alignment that are the most relevant to the current dissertation: *Procrustes Manifold Alignment* and *Semi-Supervised Manifold Alignment*.

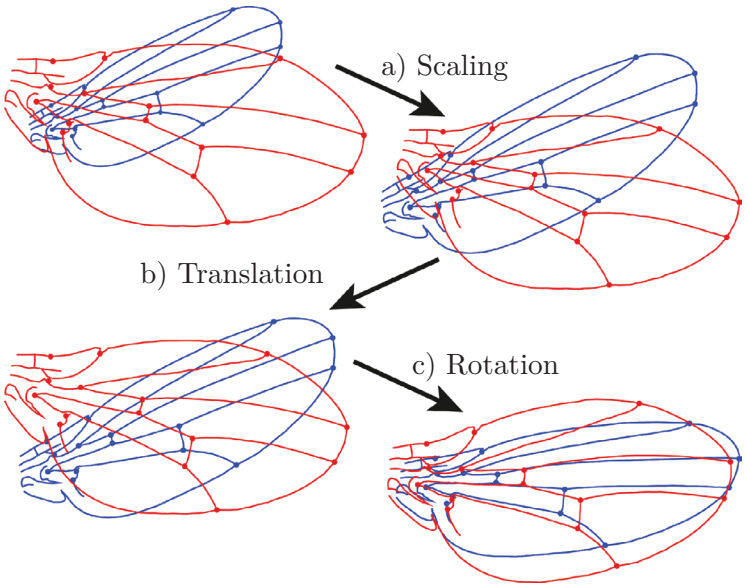


**Figure 2.4:** Example showing the three main steps of the Procrustes analysis, i.e., (a) scaling, (b) translation, (c) rotation. Adapted from Klingenberg [82], distributed under a CC BY 4.0 license.

### 2.2.1 Procrustes Manifold Alignment

The *Procrustes Analysis*[1] [54, 55] is a process in which two different shapes or datasets are aligned using an affine transformation as shown in Figure 2.4. In other words, the method consists of finding the optimal translation, scaling, and rotation, that minimize the Euclidean distances between corresponding points of each dataset. Along similar lines, the *Procrustes Manifold Alignment* method proposed by Wang and Mahadevan [168] attempts to match two dissimilar datasets via a Procrustes analysis of their respective latent representations. This approach is described as a two-step process since the low-dimensional embeddings of the individual datasets are first computed, and then, the manifold alignment is executed. Therefore, the Procrustes manifold alignment must be combined with a conventional dimensionality reduction method as described in Section 2.1.

The transformation performed by the Procrustes analysis is linear. It is known

[1]The name of the method is inspired by the Greek myth of *Procrustes*, a bandit who would either stretch or amputate his victims so their size would match his iron bed.

for any point on both manifolds and preserves the global structure of the data. For this reason, linear dimensionality reduction methods (e.g., POD) that have similar properties are arguably a better combination for the Procrustes manifold alignment. Furthermore, the projection matrix $\mathbf{\Phi}$ produced by a linear dimensionality reduction and the affine transformation of the manifold alignment can easily be combined into a single linear operation. This means that the projection of new samples onto the shared manifold is straightforward. Conversely, the inverse mapping that would allow the reconstruction of a high-dimensional sample of either dataset from its associated latent variable is also easily obtained.

An example of the Procrustes manifold alignment is given by Wang and Mahadevan [168] where it is used to align the 3D structure of proteins. In the same study, the authors also show how their method can be used for the cross-lingual retrieval of documents written in different languages.

### 2.2.2 Semi-Supervised Manifold Alignment

A more complex form of manifold alignment is the *Semi-Supervised Manifold Alignment* that was first introduced by Ham et al. [60, 61] and later developed by Wang and Mahadevan [167, 169]. This method is non-linear in nature and is based on spectral graph theory. As such, semi-supervised manifold alignment shares many similarities with non-linear dimensionality reduction methods such as LLE. The overall idea of this method is to create graphs of the respective datasets where neighboring points are connected with an edge. Then, the individual datasets are joined together by adding edges to points having a correspondence. The embeddings of all the data are obtained by performing a spectral decomposition of the joint graph Laplacian. This approach obtains the shared latent representation of both datasets in a single step, as opposed to the two-step process of the Procrustes manifold alignment.

As with most non-linear dimensionality reduction methods, a significant drawback

of the semi-supervised manifold alignment is the absence of an explicit mapping between the original high-dimensional space and the low-dimensional manifold. Therefore, the entire process must be repeated to map new samples to the manifold, and the reconstruction of latent variables into high-dimensional fields is non-trivial. To mitigate this issue, Wang and Mahadevan [169] developed a linearized version of the algorithm that provides an explicit mapping between the high- and low-dimensional spaces.

The semi-supervised manifold alignment method was used by Ham et al. [61] for the alignment of images belonging to two different sets. This method was also used by Guerrero et al. [56] to improve the classification of magnetic resonance images by combining results with two different resolutions. Furthermore, Liao et al. [93] used semi-supervised alignment to combine hyperspectral and conventional images to provide a visualization of the former with natural colors and finer details.

### 2.2.3 Manifold Alignment and Multi-fidelity Fields

It is worth noting that the contexts of manifold alignment and multi-fidelity modeling share many similarities. In both cases, the objective is to transfer knowledge between different sources of data to improve an overarching task. Loosely speaking, manifold alignment can be perceived as a multi-fidelity extension of dimensionality reduction, especially if applied on high-dimensional datasets having different fidelity levels. Also, its formulation is based on the assumption that the datasets being aligned have different features, meaning that it can readily be applied to field results having disparate representations. Therefore, manifold alignment brings a potential solution to the research objective of the current thesis.

We also note that a fundamental difference between the formulation of the Procrustes and semi-supervised manifold alignment is that the former is a *global* method while the latter is *local* [167]. In other words, the objective of the Procrustes analy-

sis is to minimize the overall discrepancy between two datasets and considers every pairwise combination of samples. On the other hand, the graph-based approach of the semi-supervised method attempts to minimize the local differences among samples within various neighborhoods and never considers the data globally. A common application in machine learning is the classification of data, and in that context, differentiating between points having small differences is critical. For regression tasks, the concern is instead to capture the entire response space and small local errors can be acceptable. As such, the local properties of semi-supervised manifold alignment that clusters similar instances are well suited for classification problems and examples in the literature support this [56, 61, 161, 169]. The global formulation of Procrustes manifold alignment is, in comparison, more in line with regression tasks.

Since reduced-order modeling is akin to a regression task, it follows that Procrustes manifold alignment would be better suited if applied to the construction of a ROM. Furthermore, the extensively used POD method is also perceived as a global approach and offers a more coherent combination with the Procrustes manifold alignment.

## 2.3 Multi-Fidelity Data-Fit Models

Before considering multi-fidelity reduced-order modeling, we briefly review the more exhaustive literature specific to multi-fidelity data-fit models. For clarity, we divide the existing multi-fidelity techniques into two categories: *adaptation-* and *fusion-based* methods. We also briefly mention the additional difficulty of multi-fidelity methods with models having disparate design parametrizations.

### 2.3.1 Adaptation-Based Methods

In an adaptation-based multi-fidelity method, the results from the low-fidelity model are corrected such that they mimic the response of a high-fidelity model. This is achieved by generating a surrogate model of the discrepancies measured between the

high- and low-fidelity results, which is often called a *bridge function* or a *correction function*. The bridge function usually takes the form of either a multiplicative [1, 27] or an additive [30, 40, 153] correction.

Let $f_{\text{hi}} : \mathbf{p} \mapsto x_{\text{hi}}$ be a high-fidelity model predicting a scalar $x_{\text{hi}}$ given some input vector $\mathbf{p} \in \mathbb{R}^b$. Similarly, let $f_{\text{lo}} : \mathbf{p} \mapsto x_{\text{lo}}$ be a low-fidelity counterpart to $f_{\text{hi}}$. Also, let $\mathbf{X}_{\text{hi}} = [x_{\text{hi},1}, \ldots, x_{\text{hi},n}] \in \mathbb{R}^n$ and $\mathbf{X}_{\text{lo}} = [x_{\text{lo},1}, \ldots, x_{\text{lo},n}] \in \mathbb{R}^n$ be datasets of previously sampled solutions for both high- and low-fidelity models. In the multiplicative approach, the multi-fidelity surrogate model is given by

$$\widetilde{f}_{\text{hi}}(\mathbf{p}) = \rho(\mathbf{p})\, f_{\text{lo}}(\mathbf{p}) \tag{2.3}$$

where $\rho(\mathbf{p})$ is a function that predicts the quotient between $\mathbf{X}_{\text{hi}}$ and $\mathbf{X}_{\text{lo}}$. As for the additive correction, the surrogate model is instead

$$\widetilde{f}_{\text{hi}}(\mathbf{p}) = f_{\text{lo}}(\mathbf{p}) + \epsilon(\mathbf{p}) \tag{2.4}$$

where $\epsilon(\mathbf{p})$ is a correction model that is constructed using the differences between $\mathbf{X}_{\text{hi}}$ and $\mathbf{X}_{\text{lo}}$. The additive correction is typically preferred over the multiplicative one since the latter can be singular if $x_{\text{lo}}$ tends to zero. Additionally, the multiplicative and additive approaches can be combined into a hybrid correction [63, 116, 178] that can provide superior results. This correction is given by

$$\widetilde{f}_{\text{hi}}(\mathbf{p}) = \beta f_{\text{lo}}(\mathbf{p}) + \epsilon(\mathbf{p}) \tag{2.5}$$

where $\beta$ is a constant scaling factor which is usually obtained via a least-squares regression. Gano et al. [50, 51] also introduced a hybrid correction that is a weighted combination of the multiplicative and additive corrections.

From the above equations, we see that obtaining an estimate of the high-fidelity

solution with an adaptation-based method usually requires the evaluation of the low-fidelity model. In scenarios where the low-fidelity model is still too expensive to evaluate, a separate surrogate model of the low-fidelity results can substitute for it. The bridge function is then applied to the low-fidelity approximation rather than the physical model. One should note that the different surrogate models forming the adaptation-based methods ($\epsilon(\mathbf{p})$, $\rho(\mathbf{p})$, and $\widetilde{f}_{\text{lo}}(\mathbf{p})$) can essentially be constructed with any type of data-fit methods.

In addition to adapting the low-fidelity model such that its output is consistent with the high-fidelity model, i.e., a zeroth-order correction, one can also use a first-order correction to ensure consistency with the high-fidelity gradient. For instance, Alexandrov et al. [1, 2, 3] developed the Trust Region Management Method (TRMM), an optimization algorithm that uses a quadratic bridge function with first-order consistency, and have shown that matching the gradient of the high-fidelity model is essential for the convergence of the method. Eldred et al. [40] later improved the TRMM by adding a second-order correction to also match the Hessian matrix of the high-fidelity model, which accelerated the optimization process. For a multi-fidelity surrogate model not restricted to optimization, Han et al. [63] developed a gradient-enhanced Kriging model using a hybrid correction and have shown better results than a gradient-free correction method. However, it should be mentioned that the above examples assume that both the high- and low-fidelity models can provide gradient information efficiently.

### 2.3.2 Fusion-Based Methods

When using a multi-fidelity fusion-based method, a single surrogate model combines the information from all levels of fidelity. In doing so, tighter integration of the high- and low-fidelity data is achieved. The resulting multi-fidelity surrogate usually takes

the following form

$$\widetilde{f}_{\text{hi}}(\mathbf{p}) = \beta \widetilde{f}_{\text{lo}}(\mathbf{p}) + \epsilon(\mathbf{p}) \tag{2.6}$$

At first glance, the formulation of Eq. (2.6) appears almost identical to the one of Eq. (2.5) for a hybrid correction except that $f_{\text{lo}}(\mathbf{p})$ is replaced by a surrogate model $\widetilde{f}_{\text{lo}}(\mathbf{p})$. A key difference between both approaches is in how the model is trained. With the adaptation-based method, the scaling factor $\beta$ is chosen such that the scaled difference $\mathbf{X}_{\text{hi}} - \beta\,\mathbf{X}_{\text{lo}}$ is minimized. The resulting discrepancy is then used to train $\epsilon(\mathbf{p})$. With the fusion-based approach, $\beta$ is instead estimated jointly with the training of $\epsilon(\mathbf{p})$ to better predict $\mathbf{X}_{\text{hi}}$. As a result, the obtained $\beta$ tends to improve the smoothness of $\epsilon(\mathbf{p})$, and perhaps counterintuitively, does not generally maximize the agreement between the high- and low-fidelity models. The training process with a fusion-based method is usually achieved via statistical inference, and as such, $\widetilde{f}_{\text{lo}}(\mathbf{p})$ and $\epsilon(\mathbf{p})$ are commonly represented as Gaussian processes, e.g., Kriging models.

Generally speaking, fusion-based methods are considered more accurate than adaptation-based methods [53, 62, 116], although their implementation is typically more involved. A common fusion-based surrogate model is CoKriging, a method initially developed by the geostatistics community [114]. It is essentially an extension of conventional Kriging using auxiliary sources of information. Kennedy and O'Hagan [80] proposed an autoregressive formulation of CoKriging specifically adapted to computer simulations, and more recently, Han et al. [64] suggested a simplified implementation of the method. In the field of aerospace engineering, CoKriging has been successfully applied to various multi-fidelity problems such as airfoil aerodynamic prediction [64, 88], wing aerodynamic optimization [45], the fusion of experimental and computational aerodynamic data [86], and high-pressure compressor optimization [158, 159]. An alternative to CoKriging is Hierarchical Kriging, a method proposed by Han and Görtz [62]. This method offers performances similar to CoKriging but is simpler to implement and provides an error estimation that is more

suitable for optimization.

It is worth noting that a limitation of Kriging and CoKriging models is their poor scaling with a large amount of training samples. For instance, Forester and Keane [44] suggest against Kriging-based models for datasets greater than 500 samples. In these circumstances, it is worth considering other approaches that leverage artificial neural networks such as *Deep Multi-Fidelity Gaussian Processes* [34, 123]. In the context of expensive simulations and limited computational resources, it is reasonable to assume that the training data will be sparse. In which case, conventional Kriging and CoKriging methods should be adequate.

### 2.3.3 Inconsistent Input Parametrizations

Most studies using multi-fidelity surrogate models implicitly assume that both the high- and low-fidelity models share the same design parametrization. More specifically, the input vector $\mathbf{p}$ is assumed to exist in the same vector space for both $f_{\text{hi}}(\mathbf{p})$ and $f_{\text{lo}}(\mathbf{p})$. In some scenarios, however, the high- and low-fidelity models can use slightly different parametrizations. For instance, if the low-fidelity model uses a simplified geometry, some detailed parameters could be accessible only to the high-fidelity model with a more granular geometry description. To resolve this potential issue, Robinson et al. [132, 133, 134] proposed two strategies using space mapping and POD respectively, and applied them to an optimization problem. That being said, the additional difficulties associated with inconsistent input parametrizations are out of the scope of the current dissertation.

## 2.4 Review of Single-Fidelity Non-Intrusive ROM

To better illustrate the current use of single-fidelity and non-intrusive ROMs in the context of aerospace engineering, we briefly present in this section the relevant literature on the subject. More specifically, we set forth a subset of the literature with

a focus on practical applications. The content of Table 2.1 presents the relevant literature with some key information such as the application considered, the number of design parameters $b$, and the size of the training data $n$. Since non-intrusive ROMs essentially combine both a dimensionality reduction and regression model, the methods chosen by the various authors are also listed in Table 2.1.

### 2.4.1 Selection of Models

From Table 2.1, we note that several aerodynamic applications have been studied using non-intrusive ROMs. One exception is the work of Lee et al. [91] that employs the Expectation-Maximization PCA (EM-PCA) [137, 156], a probabilistic variant of PCA. In this study, the authors constructed a ROM to predict engine performance tables generated with an engine cycle analysis code. Due to convergence issues, the generated fields would contain missing data and the EM-PCA is capable of extracting the principal subspace of incomplete datasets. It is worth noting that EM-PCA is closely related to POD, and when applied to complete data, the results of both methods are consistent. We should also mention the work of Franz et al. [47] and Decker et al. [36] that considered both POD and non-linear dimensionality reduction methods (see Section 2.1.1) for the construction of ROMs. Both studies noted that non-linear ROMs could better capture discontinuities such as shocks. Decker et al. also identified that POD-based ROMs generally have a lower prediction error globally at the expense of larger local errors.

With regards to the regression model, Table 2.1 shows that many of the popular data-fit models are used for reduced-order modeling, i.e., Kriging, ANN, RBF, etc. However, there does not seem to be any consensus in the literature concerning the choice of the regression model for non-intrusive ROMs. In fact, Swischuk et al. [152] considered multiple choices of data-fit models including ANN, k-Nearest Neighbor, Decision Tree, and polynomial regression. Interestingly, the authors observed that the

**Table 2.1:** Existing literature on single-fidelity and non-intrusive ROMs applied to industrial applications.

| Authors | Year | Dimensionality Reduction | Regression Model | Application | $b$ | $n$ |
|---|---|---|---|---|---|---|
| Bui-Thanh et al. [23] | 2003 | POD | Cubic Spline | Airfoil Aerodynamics | 2 | 231 |
| Lee et al. [91] | 2011 | EM-PCA | ANN | Engine Cycle Analysis | 6 | 500 |
| Park et al. [117] | 2013 | POD | ANN | Aircraft Aerodynamics | 5 | 10 |
| Franz et al. [47] | 2014 | POD/Isomap | RBF | Airfoil Aerodynamics<br>Wing Aerodynamics | 2<br>2 | 30<br>25 |
| Kato and Funazaki [78] | 2014 | POD | RBF | Turbine Aerodynamics | 4 | 300 |
| Fossati [46] | 2015 | POD | Kriging | Wing Aerodynamics<br>Aircraft Aerodynamics<br>Rotor Aerodynamics | 1<br>2<br>2 | 10<br>85<br>55 |
| Li and Zhang [92] | 2016 | POD | Cubic Spline | Airfoil Aerodynamics | 1 | 100 |
| Ulu et al. [162] | 2016 | POD | ANN | Topology Optimization | 4 | 400 |
| Chen et al. [29] | 2017 | POD | RBF | Airfoil Aerodynamics | 1 | 30 |
| Swischuk et al. [152] | 2019 | POD | See Note* | Composite Panel Analysis<br>Airfoil Aerodynamics | 5<br>2 | 3,000<br>127 |
| Rajaram et al. [124, 125] | 2020 | POD | RBF | Airfoil Aerodynamics | 3 | 1,047 |
| Decker et al. [36] | 2020 | POD/Isomap/LLE | RBF | Airfoil Aerodynamics | 2 | 100 |

*ANN, k-Nearest Neighbor, Decision Tree, and polynomial regression

availability of data in an engineering context is typically much less than in machine learning applications due to the cost of physics-based simulation. When faced with sparse data, simpler approaches such as polynomial regression might be more suited for non-intrusive ROMs than highly expressive models such as ANN.

### 2.4.2 Engineering Applications

We also observe from Table 2.1 that the non-intrusive ROM literature is mostly centered around aerodynamic applications. The likely motivation for this is the arguably higher computational cost and physical complexity of CFD simulations in comparison to other disciplines. As a result, high-fidelity aerodynamic simulations are generally perceived as the bottleneck in the preliminary design process. We further note that many authors in Table 2.1 demonstrated their ROM methodology with the aerodynamic analysis of an airfoil. This is presumably to capture some of the physical complexity of CFD simulations while maintaining an affordable computational cost by using a simpler 2D problem. For the same reason, few studies have applied non-intrusive ROMs to more expensive 3D problems. Among those that do, some make compromises on the fidelity of the simulation. For instance, Park et al. [117] used an inviscid CFD simulation and a coarse grid of only 287,798 cells for the aerodynamic analysis of a fighter aircraft. As for the work of Fossati [46], one of the test cases he used was taken from the fourth AIAA CFD Drag Prediction Workshop [165] and consisted of a fuselage with a wing and horizontal tail. In this case, the chosen grid contained 11 million cells that, despite being a large size, was below average compared to all the grids considered during the AIAA workshop.

Applications of non-intrusive ROMs in disciplines other than aerodynamics can also be found in the literature. For example, Ulu et al. [162] used a ROM to predict the optimal structures generated by a topology optimization solver. In the context of structural analysis, Swischuck et al. [152] predicted the structural state of a com-

posite panel undergoing local degradation with ROMs. Lastly, Lee et al. [91] applied reduced-order modeling to the prediction of engine performance data within a coupled airframe and propulsion sizing environment.

### 2.4.3 Input Dimensionality and Training Cost

From the input space dimensionality $b$ showed in Table 2.1, we notice that many applications in the literature only consider a small number of input parameters. The listed input sizes are between 1 and 6, with a median of 2 and an average of 2.75. Therefore, we note that constructing non-intrusive ROMs with many design parameters is not a common practice in the literature. This is presumably to maintain a reasonable accuracy and avoid excessive training costs as a consequence of the curse of dimensionality, as explained in Section 1.4.

Along the same lines, Table 2.1 also shows that most non-intrusive ROMs are constructed with a relatively low number of training samples $n$. More specifically, the sizes of the training datasets are between 10 and 3,000 for the considered literature, with a median of 100 and an average of 378. We also notice that most applications with many input parameters unsurprisingly have large training datasets, which is consistent with the curse of dimensionality. Yet, it is worth noting that the studies having large training datasets also employ relatively inexpensive physics model to generate the data. For instance, Swischuk et al. [152] used 3,000 training samples to train a ROM for the structural analysis of a composite panel. However, the underlying physical model is relatively coarse. Although the authors did not provide an estimate of the computational cost, an average desktop could likely run a single simulation within a handful of minutes at most. Similarly, Rajaram et al. [125] used a training dataset of 1,047 RANS simulations of an airfoil, and each analysis required roughly 10 minutes to complete using a single CPU. In comparison, studies involving more expensive simulations such as the aerodynamic analysis of a wing, an entire aircraft,

or a helicopter rotor [46], are restricted to smaller training datasets.

The lack of studies in Table 2.1 with many design parameters, large training datasets, and expensive simulations, is an example of the computational cost limitations associated with the training empirical models using high-fidelity data. This relates to the observations made in Section 1.6 and further justify the research objective of this thesis.

## 2.5 Review of Existing Multi-Fidelity ROMs

With the advantages of multi-fidelity methods for data-fit models, many authors understood that a similar strategy could also prove beneficial for non-intrusive ROMs. While the literature on multi-fidelity reduced-order modeling is much sparser than for data-fit models, a handful of authors have successfully combined different levels of fidelity to enhance the prediction of a ROM. This section thus presents a summary of the existing multi-fidelity ROMs methods. As in Section 2.3, we organize the multi-fidelity methods into *adaptation-* and *fusion-based* approaches. The former category implies that a given model corrects the solution of a low-fidelity model into a high-fidelity result, while the latter attempts to fuse the different sources of information into a single prediction model.

### 2.5.1 Adaptation-Based Methods

*Additive Correction*

One of the early attempts at multi-fidelity reduced-order modeling is the work of Malouin et al. [105] who combined the CFD results of a transonic airfoil computed on two different grids. Both fidelity levels used the same simulation setup, except that the high- and low-fidelity models used a fine and coarse grid respectively. Since both simulations produced solutions with inconsistent dimensionalities, the authors interpolated the results of the high-fidelity model onto the low-fidelity grid in a pre-

processing step. The approach proposed by Malouin et al. is to compute the differences between the high- and low-fidelity field solutions and then construct a ROM of the obtained discrepancy fields. The resulting ROM acts as a bridge function between the high- and low-fidelity simulations similarly to the additive correction of Eq. (2.4). To obtain new predictions of the high-fidelity model, the authors would then run the low-fidelity model at the desired design parameters and apply the additive correction calculated from their multi-fidelity ROM.

*GPOD Reconstruction*

Another interesting multi-fidelity ROM approach was suggested by Toal [157], and is based on the Gappy Proper Orthogonal Decomposition (GPOD). Everson and Sirovich [41] originally developed the GPOD method to reconstruct incomplete images. It was later used by Bui-Thanh et al. [23, 25] for the reconstruction of aerodynamic data and the inverse design of airfoils. In his multi-fidelity method, Toal suggests reconstructing a high-fidelity field from a corresponding low-fidelity solution using GPOD, essentially using the output of the low-fidelity model as an input to the ROM.

In short, given a high- and low-fidelity dataset $\mathbf{X}_{\text{hi}} \in \mathbb{R}^{d\times n}$ and $\mathbf{X}_{\text{lo}} \in \mathbb{R}^{q\times n}$ sampled with the same set of parameters, Toal proposed to stack column-wise the solutions of all fidelity levels into a single dataset and find the corresponding POD basis and latent variables. For readers familiar with POD (see Section 3.1 for details), this approach is given by

$$\mathbf{X}_{\text{hi/lo}} = \mathbf{\Phi}_{\text{hi/lo}}\,\mathbf{Z} \tag{2.7}$$

where $\mathbf{Z} \in \mathbb{R}^{k\times n}$ and

$$\mathbf{X}_{\text{hi/lo}} = \begin{bmatrix}\mathbf{X}_{\text{hi}}\\ \mathbf{X}_{\text{lo}}\end{bmatrix} \in \mathbb{R}^{(d+q)\times n} \qquad \mathbf{\Phi}_{\text{hi/lo}} = \begin{bmatrix}\mathbf{\Phi}_{\text{hi}}\\ \mathbf{\Phi}_{\text{lo}}\end{bmatrix} \in \mathbb{R}^{(d+q)\times k} \tag{2.8}$$

Note that the above POD basis is split into $\mathbf{\Phi}_{\text{hi}} \in \mathbb{R}^{d \times k}$ and $\mathbf{\Phi}_{\text{lo}} \in \mathbb{R}^{q \times k}$ for the reconstruction of $\mathbf{X}_{\text{hi}}$ and $\mathbf{X}_{\text{lo}}$ respectively. In Eq. (2.7), the same set of latent variables $\mathbf{Z}$ is used to describe both the high- an low-fidelity samples. As such, Eq. (2.7) can be divided into

$$\mathbf{X}_{\text{hi}} = \mathbf{\Phi}_{\text{hi}} \, \mathbf{Z} \tag{2.9a}$$

$$\mathbf{X}_{\text{lo}} = \mathbf{\Phi}_{\text{lo}} \, \mathbf{Z} \tag{2.9b}$$

Rearranging Eq. (2.9) then provides a mapping between $\mathbf{X}_{\text{hi}}$ and $\mathbf{X}_{\text{lo}}$ such that

$$\mathbf{X}_{\text{hi}} = \mathbf{\Phi}_{\text{hi}} \left( \mathbf{\Phi}_{\text{lo}}^T \, \mathbf{\Phi}_{\text{lo}} \right)^{-1} \mathbf{\Phi}_{\text{lo}}^T \, \mathbf{X}_{\text{lo}} \tag{2.10}$$

In a sense, this GPOD reconstruction method can be viewed as a non-intrusive ROM of the high-fidelity model, where the regression model is a linear mapping and the input space is given by the low-fidelity field. Interestingly, Toal's approach does not require the high- and low-fidelity fields to have consistent representations, i.e., the dimensionality $d$ and $q$ of the high- and low-fidelity dataset respectively need not be the same. This approach was later combined with an adaptive sampling strategy by Benamara et al. [13] to perform a multi-fidelity optimization of a transonic airfoil.

*Latent Variables Mapping*

Recently, Wang et al. [171] introduced a multi-fidelity ROM that maps the latent variables of the low-fidelity data to the latent variables of the high-fidelity results. More specifically, the proposed approach consists of applying POD on both the high- and low-fidelity datasets separately. Then, a data-fit model $g : \mathbf{z}_{\text{lo}} \mapsto \mathbf{z}_{\text{hi}}$ is constructed where $\mathbf{z}_{\text{hi}} \in \mathbb{R}^{k_{\text{hi}}}$ and $\mathbf{z}_{\text{lo}} \in \mathbb{R}^{k_{\text{lo}}}$ are latent variables of the high- and low-fidelity solutions respectively, i.e., $k_{\text{hi}} \neq k_{\text{lo}}$. Note that different dimensionality can be used for $\mathbf{z}_{\text{hi}}$ and $\mathbf{z}_{\text{lo}}$. Afterwards, high-fidelity fields are predicted by obtaining a new

low-fidelity solution at the desired design parameters, computing $\mathbf{z}_{\text{lo}}$ from the low-fidelity POD basis, predicting the associated $\mathbf{z}_{\text{hi}}$ with the trained mapping, and finally, reconstructing the high-fidelity field prediction.

One obvious issue with the method proposed by Wang et al. is that the latent space of the low-fidelity fields can easily contain many POD modes, i.e., have a dimensionality $k_{\text{lo}}$ of 10 or greater. Due to the curse of dimensionality, training the mapping $g$ with a high-dimensional $\mathbf{z}_{\text{lo}}$ can be challenging and costly. In their study, Wang et al. applied this method to the analysis of a lid-driven cavity flow and the transonic flow field around an airfoil. In both test cases, the authors only considered ROMs with at most 14 POD modes for the low-fidelity fields. They also observed a worse multi-fidelity prediction with mappings trained using $\mathbf{z}_{\text{lo}}$ of higher dimensionality. Therefore, this approach seems more suited to problems involving simpler field responses and would likely scale poorly with more complex applications.

### 2.5.2 Fusion-Based Methods

*Common POD Basis*

A simple strategy for the construction of a multi-fidelity ROM is to use the same POD basis for the projection of both the high- and low-fidelity solutions. However, this implicitly imposes that the fields of all fidelity levels must share a common representation. Mifsud et al. [110, 111] used this approach to construct a non-intrusive and multi-fidelity ROM for the prediction of the pressure distribution over a projectile. In their study, the high- and low-fidelity models were both CFD simulations and shared the same grid, yet differed in the numerical scheme used by the solver. More precisely, a combination of third- and second-order accurate schemes were used for the high-fidelity simulation while the low-fidelity used a first-order scheme. Likewise, Bertram et al. [17] also used a common POD basis for the aerodynamic design of a road vehicle. In their work, the application was the CFD analysis of a Volkswagen

Passat with both a RANS simulation and a much more expensive Detached-Eddy Simulation (DES) for the low- and high-fidelity respectively. Once again, both fidelity levels used the same discretization to ensure compatibility between the fields in terms of dimensionality, topology, and features.

To construct the common POD basis, both sets of authors joined together the high- and low-fidelity samples into a single dataset on which the POD was applied. The obtained POD modes would then span the combined latent space of both fidelity levels. For instance, let us consider the datasets $\mathbf{X}_{\text{hi}} \in \mathbb{R}^{d\times n}$ and $\mathbf{X}_{\text{lo}} \in \mathbb{R}^{d\times m}$ containing $n$ high-fidelity samples and $m$ low-fidelity samples respectively. The common POD basis (see Section 3.1 for details) satisfies

$$\mathbf{X}_{\text{hi+lo}} = \mathbf{\Phi}\,\mathbf{Z}_{\text{hi+lo}} \tag{2.11}$$

where $\mathbf{\Phi} \in \mathbb{R}^{d\times k}$ is the shared basis and

$$\mathbf{X}_{\text{hi+lo}} = \begin{bmatrix}\mathbf{X}_{\text{hi}} & \mathbf{X}_{\text{lo}}\end{bmatrix} \in \mathbb{R}^{d\times(n+m)} \qquad \mathbf{Z}_{\text{hi+lo}} = \begin{bmatrix}\mathbf{Z}_{\text{hi}} & \mathbf{Z}_{\text{lo}}\end{bmatrix} \in \mathbb{R}^{k\times(n+m)} \tag{2.12}$$

The POD basis of Eq. (2.11) is subsequently used to project the high- and low-fidelity results into their corresponding latent variables $\mathbf{Z}_{\text{hi}}$ and $\mathbf{Z}_{\text{lo}}$. Each fidelity levels would have different sets of latent variables, yet they would be associated with the same POD modes. Afterwards, a multi-fidelity regression model (e.g., CoKriging) would be trained with both $\mathbf{Z}_{\text{hi}}$ and $\mathbf{Z}_{\text{lo}}$. Given some design parameters, this regression model would predict the corresponding high-fidelity latent variables. These would then be converted into a high-fidelity field using the previously obtained POD basis. Hence, the multi-fidelity ROM produced by this approach combines a multi-fidelity regression model with a common POD basis. In both works by Mifsud et al. and Bertram et al., supplementing the high-fidelity samples with low-fidelity results was shown to improve the predictions of the ROM.

*Extended POD basis*

One issue of executing POD on a dataset indiscriminately comprised of both high- and low-fidelity solutions is that the resulting POD modes will naturally favor the low-fidelity samples since, in most cases, they are available in greater number. Consequently, the computed basis is not guaranteed to provide an optimal reconstruction of the high-fidelity results. In a slight variation of the previous method, Benamara et al. [12, 14] recommended to compute instead the optimal high-fidelity basis given the available data, and extend it with results from the low-fidelity model. The proposed method first computes the high-fidelity basis together with its complementary null space by performing a QR decomposition of the high-fidelity data. The low-fidelity data is subsequently projected onto the null space of the high-fidelity results such that only the information not captured by the initial high-fidelity basis remains. Additional POD modes would then be computed from the projected low-fidelity data and supplement the previously computed high-fidelity basis. This extended basis would be used to transform both the high- and low-fidelity results into their respective latent variables. Similarly to the common POD approach, the multi-fidelity ROM is constructed by combining the extended POD basis with a multi-fidelity regression model trained with both sets of latent variables.

Benamara et al. demonstrated their proposed method with the aerodynamic analysis of a low-pressure compressor. Both fidelity levels used 3D RANS simulations, but the low-fidelity model used a coarser grid than the high-fidelity. As with the common POD basis method, the extended POD basis approach requires a consistent representation among all fidelity levels. Therefore, the authors interpolated the high-fidelity results onto the coarser low-fidelity grid in a pre-processing step. The results of Benamara et al. showed that their multi-fidelity ROM had improved predictions of both the POD basis and the latent variables compared to an equivalent single-fidelity ROM.

### 2.5.3 Observations on Existing Multi-Fidelity ROMs

Here, we note that among the existing multi-fidelity ROM methods, few address the challenges of multi-fidelity fields having inconsistent dimensionalities, topologies, and features. Mifsud et al. [111, 110] and Bertram et al. [17] circumvented the issue by using the same discretization for all fidelity levels. Along similar lines, Malouin et al. [105] and Benamara et al. [12, 14] resolved differences in dimensionalities by interpolating all the results on a common grid but did not provide a solution for fields having inconsistent topologies or features. While the methods proposed by Toal [157] and Wand et al. [171] can technically be applied to any field regardless of their representation, they are adaptation-based methods that require new evaluations of the low-fidelity model to apply their correction. This means that the online evaluation of these multi-fidelity ROMs will only be as fast as the low-fidelity model. This can be problematic in the many-query context unless the lower fidelity simulation is exceptionally cheap. While the low-fidelity model could arguably be replaced by a conventional ROM model, this scenario was considered by neither Toal and Wand et al. The accuracy of the multi-fidelity predictions would also likely be impacted by the correctness of the low-fidelity ROM. As with data-fit models (see Section 2.3), a method that fuses all the data into a single model is likely to outperform an adaptation-based approach. All in all, this literature review support the challenges identified in Section 1.5 with multi-fidelity fields and further motivate the current research.

Nevertheless, the considered multi-fidelity ROM studies show that in the absence of field inconsistencies, it is possible and advantageous to enhance the model predictions by combining fields from different fidelity levels. The fusion-based approaches using a multi-fidelity regression model to combine the latent variables of the different fidelity are of particular interest since the resulting multi-fidelity ROM is self-contained. In other words, a single model tightly integrates the high- and low-fidelity

datasets such that new field predictions can be generated efficiently. Moreover, the literature on multi-fidelity data-fit models suggests that this approach should be superior to an adaptation-based method [53, 62, 116]. We postulate that if one can resolve the differences in representations between the high- and low-fidelity fields such that their latent variables are consistent, a similar fusion-based approach could be used to construct a multi-fidelity ROM.

## 2.6 Summary

To establish the context of this discussion, we first recall the research objective previously defined in Chapter 1 and formulated as:

**Research Objective**

To develop or improve a *non-intrusive* and *multi-fidelity* reduced-order modeling method for the purpose of many-query applications, and with an emphasis on combining multi-fidelity fields with *disparate representations*, i.e., fields having inconsistent dimensionalities, topologies, and features.

For that purpose, this chapter presented some background material of relevant fields such as dimensionality reduction, manifold alignment, and multi-fidelity modeling. The intent was to provide a perspective on the methodological aspects of reduce-order modeling and to identify possible enablers to the current objective. This was followed by a review of the literature on both single- and multi-fidelity non-intrusive ROMs to ascertain the current state of the art and to diagnose the limitations of existing approaches. Here, we condense the key observations of this chapter into the following list:

**Observations 2**

2.1 Linear dimensionality reduction methods, such as POD, are a more convenient option for reduced-order modeling since they can provide an explicit mapping between the full and latent spaces.

2.2 Datasets with disparate dimensionality and features can effectively be compared by using manifold alignment to map them onto a common latent space.

2.3 The Procrustes manifold alignment, a linear and global method, allows for a coherent combination with the popular POD method, which is also linear and global.

2.4 Multi-fidelity data-fit methods with a fusion-based approach, such as CoKriging, are generally superior to those using a simpler adaptation-based method.

2.5 The literature on non-intrusive ROMs establishes the prevalence of POD for model construction. It also illustrates the computational challenges of training models with expensive simulations and many parameters.

2.6 In cases with consistent fields, fusing the latent variables from different fidelity levels using a multi-fidelity regression model can effectively enhance the ROM predictions.

2.7 Some adaptation-based multi-fidelity ROMs can combine inconsistent fields but requires the generation of a new low-fidelity field to apply their correction.

In light of the above observations, we surmise that the challenges of combin-

ing fields with disparate representations can effectively be solved by using manifold alignment. By resolving the inconsistencies and projecting all the datasets onto a common latent space, it enables a fusion-based approach for the multi-fidelity ROM construction as defined in Section 2.5.2. A fusion-based method is preferred over an adaptation-based one since the former allows for tighter integration of the different datasets and should provide superior predictions according to Observation 2.4. It also avoids the need for evaluating the low-fidelity model during online predictions. The discussion from this chapter allows us to define the following overall hypothesis that will guide the development of our methodology:

**Overall Hypothesis**

A non-intrusive and multi-fidelity reduced-order modeling method combining manifold alignment and multi-fidelity regression should match or surpass the predictive performance of existing multi-fidelity ROM methods and provide the capability of fusing high- and low-fidelity fields having different representations.

# CHAPTER 3
# PROPOSED METHOD

Following the formulation of the overall hypothesis in the previous chapter, we outline here the multi-fidelity and non-intrusive ROM method proposed in this work. The developed approach borrows from three distinct numerical methods: *Proper Orthogonal Decomposition*, *Manifold Alignment*, and *Multi-Fidelity Regression*. This chapter first provides the fundamentals of these techniques in the context of multi-fidelity ROMs. Lastly, we demonstrate how the aforementioned methods are combined into a single ROM to address our research objective.

## 3.1 Proper Orthogonal Decomposition

As mentioned previously, the Proper Orthogonal Decomposition (POD) is a linear and unsupervised dimensionality reduction method that is extensively used in projection-based ROMs (see Table 2.1). For all practical purposes, the POD is equivalent to the Principal Component Analysis (PCA), the latter name being preferred in statistical analysis and machine learning. The content of the following section is compatible with either the POD or PCA, but we will use the former name since it is the preferred designation for reduced-order modeling.

### 3.1.1 Formulation

To begin with, consider the data matrix $\mathbf{X} = [\mathbf{x}_1, \ldots, \mathbf{x}_n] \in \mathbb{R}^{d \times n}$ obtained at different input values, whose $j$-th column corresponds to the sample $\mathbf{x}_j \in \mathbb{R}^d$. The sample mean

vector $\overline{\mathbf{x}} \in \mathbb{R}^d$ is then defined as

$$\overline{\mathbf{x}} = \frac{1}{n} \sum_{j=1}^{n} \mathbf{x}_j \tag{3.1}$$

and the sample *covariance matrix* $\mathbf{S} \in \mathbb{R}^{d \times d}$ is given by

$$\mathbf{S} = \frac{1}{n} \sum_{j=1}^{n} (\mathbf{x}_j - \overline{\mathbf{x}}) (\mathbf{x}_j - \overline{\mathbf{x}})^T \tag{3.2}$$

For convenience and without loss of generality, we assume that the results in $\mathbf{X}$ have been centered beforehand such that $\overline{\mathbf{x}} = \mathbf{0}$. Therefore, we will omit the sample mean in the following derivation. Some authors neglect the division by $n$ in Eq. (3.2) such that $\mathbf{S}$ is instead a *scatter matrix*. Using a scatter rather than a covariance matrix is acceptable if one is only interested in the POD basis.

The objective of the POD method is to find basis vectors $\boldsymbol{\phi}_j \in \mathbb{R}^d$ along which the variance of the data is maximum. This essentially assumes that directions of high variance contain more useful information than those of low variance [35]. In mathematical terms, this objective is given by

$$\max_{\boldsymbol{\phi}_j} \frac{\boldsymbol{\phi}_j^T \mathbf{S} \, \boldsymbol{\phi}_j}{\boldsymbol{\phi}_j^T \boldsymbol{\phi}_j} \tag{3.3}$$

which correspond to the optimization of a *Rayleigh quotient* [104]. The solution of (3.3) is given by the following eigenproblem

$$\mathbf{S}\boldsymbol{\phi}_j = \lambda_j \boldsymbol{\phi}_j \quad \text{s.t.} \quad \|\boldsymbol{\phi}_j\| = 1 \tag{3.4}$$

where $\lambda_j$ is the $j$-th eigenvalue of $\mathbf{S}$ in decreasing order and $\boldsymbol{\phi}_j$ is the corresponding eigenvector. Since $\mathbf{S}$ is symmetric and positive semidefinite, all the eigenvalues are real and the corresponding eigenvectors form an orthonormal basis. The objective (3.3)

is maximized when $\boldsymbol{\phi}_j$ is the eigenvector corresponding to the largest $\lambda_j$.

Let $\boldsymbol{\Phi} = [\boldsymbol{\phi}_1, \ldots, \boldsymbol{\phi}_d] \in \mathbb{R}^{d \times d}$ be an orthogonal matrix formed by all the eigenvectors of Eq. (3.4). We define the POD basis $\boldsymbol{\Phi}_k \in \mathbb{R}^{d \times k}$ as a low-rank approximation of $\boldsymbol{\Phi}$ and whose columns are composed of the $\boldsymbol{\phi}_j$ with the $k$-largest eigenvalues, where $k \ll d$. The projection of a sample $\mathbf{x}_j$ onto this reduced subspace is given by

$$\mathbf{z}_j = \boldsymbol{\Phi}_k^T \, \mathbf{x}_j \tag{3.5}$$

where $\mathbf{z}_j \in \mathbb{R}^k$ contains the POD coefficients of the $j$-th sample. Conversely, the approximate reconstruction of the field $\widetilde{\mathbf{x}}_j$ is obtained by

$$\widetilde{\mathbf{x}}_j = \boldsymbol{\Phi}_k \, \mathbf{z}_j \tag{3.6}$$

In this case, $\widetilde{\mathbf{x}}_j$ is an approximation of $\mathbf{x}_j$ since it is reconstructed using only the $k$-first POD modes. If we consider the reconstruction residual $\varepsilon$ defined as

$$\varepsilon = \frac{1}{n} \sum_{j=1}^{n} \|\mathbf{x}_j - \widetilde{\mathbf{x}}_j\|^2 \tag{3.7}$$

it can be shown that the basis vectors which maximize Eq. (3.3) interestingly also minimize $\varepsilon$. As such, the POD basis defines the subspace that provides the optimal reconstruction error in a least-squares sense [19]. In fact, the value of the residual is given by

$$\varepsilon = \sum_{j=k+1}^{d} \lambda_j \tag{3.8}$$

which is simply the sum of the $d - k$ smallest eigenvalues, and whose eigenvectors are orthogonal to the POD basis.

The dimensionality $k$ of the POD subspace can be chosen using the Relative

Information Content (RIC) [120, 166] defined as

$$\text{RIC} = \frac{\sum_{j=1}^{k} \lambda_j}{\sum_{j=1}^{d} \lambda_j} \tag{3.9}$$

The RIC criterion essentially represents the fraction of the total variance captured by the POD basis. The dimension $k$ is selected such that the RIC is greater than some user prescribed threshold. For reduced-order modeling applications, RIC values of 99.9% or higher are fairly common.

### 3.1.2 Dual Form

Note that $\mathbf{S}$ has dimensions $d \times d$ and that the eigendecomposition of this matrix is of complexity $\mathcal{O}(d^3)$. In the context of reduced-order modeling, the fields of interest can have several million dimensions, which would require significant computational resources to apply POD on the data. Additionally, the ROM data are usually under-sampled such that the dimensionality of the field $d$ is much greater than the number of samples $n$. The set of samples then defines a linear subspace whose dimensionality is at most $n - 1$, and applying POD will result in no more than $n - 1$ non-zero eigenvalues. As such, the POD method can be solved more efficiently by considering its *dual* form [19, 35], whereas the solution of Eq. (3.4) corresponds to the *primal* form of the method. This alternative formulation is also referred to as the *method of snapshots* [144].

Consider the matrix $\mathbf{X} \in \mathbb{R}^{d \times n}$ containing the centered data. The primal form of Eq. (3.4) is then rewritten as

$$\frac{1}{n}\mathbf{X}\mathbf{X}^T\boldsymbol{\phi}_j = \lambda_j \boldsymbol{\phi}_j \tag{3.10}$$

Pre-multiplying both sides with $\mathbf{X}^T$ such that

$$\frac{1}{n}\mathbf{X}^T\mathbf{X}(\mathbf{X}^T\boldsymbol{\phi}_j) = \lambda_j(\mathbf{X}^T\boldsymbol{\phi}_j) \tag{3.11}$$

and then substituting $\boldsymbol{\nu}_j = \mathbf{X}^T\boldsymbol{\phi}_j \in \mathbb{R}^n$ and $\mathbf{K} = \mathbf{X}^T\mathbf{X} \in \mathbb{R}^{n\times n}$, gives

$$\frac{1}{n}\mathbf{K}\boldsymbol{\nu}_j = \lambda_i\boldsymbol{\nu}_j \tag{3.12}$$

where $j = 1, \ldots, n$ in this case. We can see from Eq. (3.12) that the matrix $\mathbf{K}$ contains the same $n-1$ non-zero eigenvalues as $\mathbf{S}$ up to a factor $n$. However, this eigenproblem is computed with a complexity of $\mathcal{O}(n^3)$ instead of $\mathcal{O}(d^3)$. For high-dimensional fields, this reformulation represents considerable computational savings. Furthermore, the eigenvectors $\boldsymbol{\phi}_j$ and $\boldsymbol{\nu}_j$ are related. Provided that $\|\boldsymbol{\nu}_j\| = 1$, we can recover $\boldsymbol{\phi}_j$ from $\boldsymbol{\nu}_j$ using

$$\boldsymbol{\phi}_j = \frac{1}{n\lambda_j}\mathbf{X}\boldsymbol{\nu}_j \tag{3.13}$$

It is worth noting that the matrix $\mathbf{K}$ is, in fact, a *Gramian* or *kernel matrix* constructed using a linear kernel function. Consequently, the dual form of POD can be used to make this method non-linear by forming $\mathbf{K}$ using a non-linear kernel function. In the context of machine learning, the resulting dimensionality reduction method is referred to as *kernel PCA* [141].

### 3.1.3 Singular Value Decomposition

The POD method is also closely related to the Singular Value Decomposition (SVD) and many authors use the latter method to compute the POD modes. For instance, let $\mathbf{X} \in \mathbb{R}^{d\times n}$ be a matrix containing the centered data and $d \geq n$. Performing an SVD on $\mathbf{X}$ will result in the following decomposition

$$\mathbf{X} = \mathbf{U}\boldsymbol{\Sigma}\mathbf{V}^T \tag{3.14}$$

where $\mathbf{U} \in \mathbb{R}^{d \times n}$ contains the right singular vectors, $\mathbf{V} \in \mathbb{R}^{n \times n}$ contains the left singular vectors, and $\mathbf{\Sigma} \in \mathbb{R}^{n \times n}$ is a diagonal matrix where the entries $\Sigma_{ii} = \sigma_i$ are called singular values. By construction, both $\mathbf{U}$ and $\mathbf{V}$ are orthonormal bases and $\sigma_i \geq 0 \; \forall i$.

By post-multiplying Eq. (3.14) with $\mathbf{X}^T$, we obtain

$$\mathbf{X}\mathbf{X}^T = \mathbf{U}\mathbf{\Sigma}\mathbf{V}^T \left(\mathbf{U}\mathbf{\Sigma}\mathbf{V}^T\right)^T \tag{3.15}$$

$$= \mathbf{U}\mathbf{\Sigma}^2\mathbf{U}^T \tag{3.16}$$

Compared to Eq. (3.10), we see that the result of Eq. (3.15) is akin to the eigendecomposition of $\mathbf{S}$. More specifically, we can relate the left-singular vectors of $\mathbf{X}$ to its POD modes such that $\mathbf{\Phi} = \mathbf{U}$ and $\lambda_i = \sigma_i^2/n$. Pre-multiplying Eq. (3.14) with $\mathbf{X}^T$ gives instead

$$\mathbf{X}^T\mathbf{X} = \left(\mathbf{U}\mathbf{\Sigma}\mathbf{V}^T\right)^T \mathbf{U}\mathbf{\Sigma}\mathbf{V}^T \tag{3.17}$$

$$= \mathbf{V}\mathbf{\Sigma}^2\mathbf{V}^T \tag{3.18}$$

Comparing the above result with the derivation of Eq. (3.12), we now obtain an equivalence between the right-singular vectors and the eigenvectors of the dual form of the POD.

Although the eigendecomposition of $\mathbf{S}$ and the SVD of $\mathbf{X}$ are mathematically equivalent, practitioners tend to prefer the latter for the calculation of the POD basis. Since SVD algorithms do not explicitly compute the product $\mathbf{X}\mathbf{X}^T$, they are less prone to numerical truncation errors and are considered more stable.

## 3.2 Manifold Alignment

As highlighted previously, the field inconsistencies between the results of different fidelity levels are a major obstacle to the construction of a multi-fidelity ROM, and existing methods do not fully address this challenge (see Section 2.5). We showed in Section 2.2 that disparate datasets can be combined into a common latent space using manifold alignment. Here, we consider the Procrustes manifold alignment for the formulation of the proposed multi-fidelity ROM (see Section 2.2.1). In essence, this method performs a Procrustes analysis on the individual latent coordinates of two or more datasets, thus embedding these results on a shared latent space. Despite having potentially inconsistent representations in the physical space, the latent representation of the different datasets becomes consistent following the alignment.

It is worth noting that this approach is inherently global and linear, and as such, can be combined with the established POD method in a consistent manner. The Procrustes manifold alignment allows us to keep the benefits of the POD while resolving any inconsistencies in the field representations. As it will become evident at the end of this chapter, a ROM constructed with Procrustes manifold alignment is a relatively straightforward multi-fidelity extension to most POD-based ROMs.

### 3.2.1 Multi-Fidelity ROM Context

In the context of a non-intrusive ROM, a new field $\widetilde{\mathbf{x}} \in \mathbb{R}^d$ is generated by first predicting the corresponding latent coordinate $\widetilde{\mathbf{z}} \in \mathbb{R}^k$. Given a design vector $\mathbf{p}$, each component of the latent coordinate is predicted with separate regression models such that $\widetilde{g}_i : \mathbf{p} \mapsto \widetilde{z}_i$, where $\widetilde{z}_i$ is the $i$-component of $\widetilde{\mathbf{z}}$. Here, we treat the components of $\widetilde{\mathbf{z}}$ as independent variables because the POD modes form an orthonormal basis. Considering a single-fidelity ROM, these regression models are trained with a dataset $\mathbf{Z} = [\mathbf{z}_1, \ldots, \mathbf{z}_n] \in \mathbb{R}^{k \times n}$ containing the high-fidelity latent coordinates. Yet, with

a fusion-based multi-fidelity approach similar to the one of Mifsud et al. [110, 111], Bertram et al. [17], and Benamara et al. [12, 14], these regression models must also be trained with the low-fidelity latent coordinates, which we represent with the dataset $\mathbf{W} = [\mathbf{w}_1, \ldots, \mathbf{w}_m] \in \mathbb{R}^{k \times m}$. Because each component of $\widetilde{\mathbf{z}}$ is predicted separately, the datasets $\mathbf{Z}$ and $\mathbf{W}$ must be combined component-wise (i.e., row-wise) for each regression model $\widetilde{g}_i(\mathbf{p})$.

The effectiveness of a multi-fidelity regression model strongly depends on the correlation between the high- and low-fidelity training datasets. Since the high- and low-fidelity fields potentially reside in different latent spaces, the $i$-component of $\mathbf{W}$ is not necessarily the one sharing the highest correlation with the $i$-component of $\mathbf{Z}$. In other words, the coefficients of the $i$-th POD mode of the high-fidelity dataset is not guaranteed to vary jointly with the ones of the $i$-th low-fidelity mode, and a different mode might offer a better correlation. As a result, even though $\mathbf{Z}$ and $\mathbf{W}$ are presumably related, naively fusing these datasets component-wise can result in a set of regression models $\widetilde{g}_i(\mathbf{p})$ that cannot fully leverage the additional information contained within the low-fidelity dataset. The goal of the Procrustes manifold alignment is thus to harmonize the variations of the high- and low-fidelity latent variables. We achieve this by transforming $\mathbf{W}$ such that each component of the low-fidelity latent coordinates best matches the corresponding high-fidelity one. The aligned version of $\mathbf{W}$ can then be fused with $\mathbf{Z}$ component-wise in a manner that maximizes the effectiveness of each multi-fidelity regression model $g_i(\mathbf{p})$. The benefits of the Procrustes manifold alignment in the context of a multi-fidelity ROM is demonstrated later in Section 5.5.1 with a simple experiment.

### 3.2.2 Formulation

Consider the data matrices $\mathbf{X} = [\mathbf{x}_1, \ldots, \mathbf{x}_n] \in \mathbb{R}^{d \times n}$ whose columns are high-fidelity results $\mathbf{x}_j \in \mathbb{R}^d$, where $j = 1, \ldots, n$. The high-fidelity data are complemented with

a low-fidelity dataset $\mathbf{Y} = [\mathbf{y}_1, \ldots, \mathbf{y}_m] \in \mathbb{R}^{q \times m}$ containing low-fidelity solutions $\mathbf{y}_j \in \mathbb{R}^q$, where $j = 1, \ldots, m$. In the multi-fidelity context, we expect that low-fidelity data are available in greater numbers than high-fidelity results such that $m > n$. We also assume that the representations of $\mathbf{x}_j$ and $\mathbf{y}_j$ are not necessarily consistent such that $d \neq q$. Additionally, let the $n$ first solutions $\mathbf{x}_j$ and $\mathbf{y}_j$ have a pair-wise correspondence, i.e., where $\mathbf{y}_j$ and $\mathbf{x}_j$ are generated with the same design parameter values. The last $m - n$ columns of $\mathbf{Y}$ are then low-fidelity samples that are not related to any high-fidelity field. The low-fidelity results are thus partitioned into $\mathbf{Y} = [\mathbf{Y}_\mathrm{L}, \mathbf{Y}_\mathrm{U}]$, where $\mathbf{Y}_\mathrm{L} \in \mathbb{R}^{q \times n}$ contains the solutions *linked* to $\mathbf{X}$, while $\mathbf{Y}_\mathrm{U} \in \mathbb{R}^{q \times (m-n)}$ holds the *unlinked* data.

Following the methodology of Wang and Mahadevan [168], the Procrustes manifold alignment can be divided into three main steps: learning the individual embeddings, finding the optimal alignment, and mapping the data onto the shared manifold. These are detailed as follows:

*Step 1: Learning the Individual Embeddings*

The first step of the Procrustes manifold alignment is to find the low-dimensional latent representation (or embeddings) of the individual datasets. As a result, we define $\mathbf{Z} = [\mathbf{z}_1, \ldots, \mathbf{z}_n] \in \mathbb{R}^{k \times n}$ and $\mathbf{W} = [\mathbf{w}_1, \ldots, \mathbf{w}_m] \in \mathbb{R}^{k \times m}$ as the $k$-dimensional latent variables of $\mathbf{X}$ and $\mathbf{Y}$ respectively, i.e., the high- and low-fidelity datasets. As previously, we partition the low-fidelity data into $\mathbf{W} = [\mathbf{W}_\mathrm{L}, \mathbf{W}_\mathrm{U}]$ where $\mathbf{W}_\mathrm{L} \in \mathbb{R}^{k \times n}$ are latent variables linked to $\mathbf{Z}$ and $\mathbf{W}_\mathrm{U} \in \mathbb{R}^{k \times (m-n)}$ are unlinked latent variables.

For the proposed method, the embeddings $\mathbf{Z}$ and $\mathbf{W}$ are learned via the POD method. These latent variables are given by the following projections

$$\mathbf{Z} = \mathbf{\Phi}_k^T \mathbf{X} \tag{3.19}$$

$$\mathbf{W} = \mathbf{\Psi}_k^T \mathbf{Y} \tag{3.20}$$

where $\mathbf{\Phi}_k \in \mathbb{R}^{d\times k}$ and $\mathbf{\Psi}_k \in \mathbb{R}^{q\times k}$ are orthonormal bases formed by the $k$-first POD modes of $\mathbf{X}$ and $\mathbf{Y}$ respectively. At this stage, the dimensionality of $\mathbf{Z}$ and $\mathbf{W}$ is the same, but both datasets do not necessarily reside on a common manifold.

*Step 2: Finding the Optimal Alignment*

Once both low-dimensional embeddings are identified, the following step is to perform a Procrustes analysis and find an affine transformation (i.e., translation, scaling, rotation, and reflection) that would optimally align $\mathbf{W}_\mathrm{L}$ with $\mathbf{Z}$. More specifically, we seek the transformation which minimizes the following objective

$$\min_{s,\mathbf{t},\mathbf{Q}} \quad \|\mathbf{Z} - s\mathbf{Q}(\mathbf{W}_\mathrm{L} - \mathbf{t})\|_F \quad \text{s.t.} \quad \mathbf{Q}^T\mathbf{Q} = \mathbf{I} \tag{3.21}$$

where $s$ is an isotropic scaling factor, $\mathbf{t} \in \mathbb{R}^k$ is a translation vector, and $\mathbf{Q} \in \mathbb{R}^{k\times k}$ is an orthogonal transformation matrix. Note that if $\det(\mathbf{Q}) = 1$, the transformation of $\mathbf{Q}$ represents a rotation and if $\det(\mathbf{Q}) = -1$, it is instead the combination of a rotation and a reflection [54].

The optimal translation is obtained by shifting both $\mathbf{Z}$ and $\mathbf{W}_\mathrm{L}$ such that their centroids are at the origin. Since we assume that $\mathbf{X}$ and $\mathbf{Y}$ have been centered prior to the POD (see Section 3.1.1), the mean of $\mathbf{Z}$ and $\mathbf{W}$ are both zero. However, the dataset $\mathbf{W}_\mathrm{L}$, as a subset of $\mathbf{W}$, is not necessarily centered. The optimal translation vector for the linked data is thus given by

$$\mathbf{t} = \frac{1}{n}\sum_{j=1}^{n} \mathbf{w}_j = \mathbf{0} \tag{3.22}$$

Before evaluating remaining variables, we first compute the following decomposition

$$\mathbf{U}\mathbf{\Sigma}\mathbf{V}^T = \mathrm{SVD}\left(\mathbf{W}_\mathrm{L}'\mathbf{Z}^T\right) \tag{3.23}$$

where $\mathbf{W}'_{\mathrm{L}} = \mathbf{W}_{\mathrm{L}} - \mathbf{t}$ contains the shifted low-fidelity latent variables. It can be shown [33] that the optimal orthogonal transformation matrix is given by

$$\mathbf{Q} = \mathbf{V}\mathbf{U}^T \tag{3.24}$$

and the optimal isotropic scaling factor is obtained as follows

$$s = \frac{\mathrm{tr}(\mathbf{\Sigma})}{\mathrm{tr}\left(\mathbf{W}'_{\mathrm{L}}(\mathbf{W}'_{\mathrm{L}})^T\right)} \tag{3.25}$$

*Step 3: Mapping the Data onto the Shared Manifold*

Having used the linked dataset $\mathbf{W}_{\mathrm{L}}$ to identify the optimal affine transformation, the final step is to apply it to all the low-fidelity latent variables $\mathbf{W}$, i.e., both the linked and unlinked data. The aligned latent variables are thus given by

$$\mathbf{Z}_{\mathrm{lo}} = s\,\mathbf{Q}\,(\mathbf{W} - \mathbf{t}) \tag{3.26}$$

where $\mathbf{Z}_{\mathrm{lo}} \in \mathbb{R}^{k\times m}$ contains the latent variables of the low-fidelity data projected onto the high-fidelity manifold. For the sake of consistency, the set of high-fidelity variables $\mathbf{Z}$ is referred to as $\mathbf{Z}_{\mathrm{hi}}$ from here onward. With this transformed representation, both the high- and low-fidelity data are represented in the same latent space such that they can be easily compared and fused into a multi-fidelity model. Also, the mappings of Eq. (3.19) along with the transformation of Eq. (3.26) can be readily combined to allow the projection of new low-fidelity samples onto the shared manifold.

### 3.2.3 Datasets with Different Latent Dimensionality

In the previous section, we have assumed that the dimensionality of the high- and low-fidelity latent variables $\mathbf{Z}$ and $\mathbf{W}$ was identical. However, due to a greater amount of data, the dimensionality of $\mathbf{W}$ can conceivably be larger than $\mathbf{Z}$ in some cases.

The algorithm of Section 3.2.2 can still be applied in such an event, thus making use of all the information available. The manifold alignment then becomes a *projection Procrustes problem* [54, 55] such that $\mathbf{Q}$ is instead an orthonormal projection matrix. In the opposite scenario where the latent dimensionality of $\mathbf{W}$ is less than $\mathbf{Z}$, the current algorithm can also be used by artificially extending the dimensionality of $\mathbf{W}$. This is achieved by padding the missing dimensions of $\mathbf{W}$ with zero vectors. Note that in such a case, the information transfer from the low- to the high-fidelity data will likely be weaker.

## 3.3 Multi-Fidelity Regression

The purpose of the regression model inside a non-intrusive ROM is to predict coordinates in the latent space given a set of new design parameters. These coordinates, together with some previously extracted POD modes, are used to reconstruct the high-dimensional field results. In mathematical terms, new field predictions are obtained with

$$\widetilde{\mathbf{x}} = \sum_{i=1}^{k} \boldsymbol{\phi}_i \, \widetilde{g}_i(\mathbf{p}) \tag{3.27}$$

where $\widetilde{\mathbf{x}} \in \mathbb{R}^d$ is a field prediction, $\boldsymbol{\phi}_i$ is the $i$-th POD mode, and $\widetilde{g}_i : \mathbf{p} \mapsto \widetilde{z}_i$ is a regression model predicting the $i$-th coordinate $\tilde{z}_i$ in the POD latent space. With a $k$-dimensional latent space, a set of $k$ regression models $\widetilde{\mathbf{g}}(\mathbf{p}) = [\widetilde{g}_1(\mathbf{p}), \ldots, \widetilde{g}_k(\mathbf{p})]$ are trained to predict all $k$ components of a latent variable $\mathbf{z} \in \mathbb{R}^k$. Since the latent space coordinates are all orthogonal to each other, each model $\widetilde{g}_i(\mathbf{p})$ can be trained independently.

In practice, $\widetilde{g}_i(\mathbf{p})$ can be constructed with any type of data-fit model and one of the popular options for single-fidelity ROM is Kriging [46, 180]. However, for a multi-fidelity ROM with a fusion-based approach, the regression model must be able to incorporate the information of both high- and low-fidelity results, i.e., $\mathbf{Z}_{\text{hi}}$ and $\mathbf{Z}_{\text{lo}}$

in the context of manifold alignment. As noted in Section 2.3, the current state of the art for multi-fidelity data-fit model is CoKriging [80], a multi-fidelity extension of Kriging. This section first provides an overview of the Kriging formulation which is then used to introduce the CoKriging prediction model.

### 3.3.1 Kriging Formulation

As noted in Section 1.2.1, Kriging is a very popular interpolation model that was first introduced by Krige [84] in the field of geostatistics, and is equivalent to Gaussian Process Regression (GPR) for all practical purposes. In this approach, we represent the output of some deterministic function as the realization of a random process. The Kriging model is then constructed such that predictions are a linear combination of previous observations and the prediction error is unbiased.

Consider the function $g : \mathbf{p} \mapsto z$ which maps some design parameters $\mathbf{p} \in \mathbb{R}^b$ to some scalar output $z$. We represent this function as a stochastic process such that

$$g(\mathbf{p}) = \mu + \epsilon(\mathbf{p}) \tag{3.28}$$

where $\mu$ is an estimated mean and $\epsilon(\mathbf{p})$ is a stationary random process. We assume that $\epsilon(\mathbf{p})$ is normally distributed with a zero mean and a covariance given by

$$\mathrm{Cov}\left[\epsilon(\mathbf{p}), \epsilon(\mathbf{p}')\right] = \sigma^2 \, r\left(\mathbf{p}, \mathbf{p}'\right) \tag{3.29}$$

where $\sigma^2$ is the process variance, and $r(\mathbf{p}, \mathbf{p}')$ is a correlation or kernel function. Assuming that $g(\mathbf{p})$ is continuous, one can reasonably expect that two observations $z_i$ and $z_j$ made close to each other, i.e., where $\|\mathbf{p}_i - \mathbf{p}_j\| \to 0$, will have similar values. As such, the correlation function represents the spatial dependence between two coordinates in the parameter space. This function should tend to one when $\mathbf{p}_i$ and $\mathbf{p}_j$ coincide, and to zero when $\|\mathbf{p}_i - \mathbf{p}_j\| \to \infty$. Some popular choices of correlation

functions [126] include

- *Squared-Exponential Function*

$$r\left(\mathbf{p}_i, \mathbf{p}_j\right) = \exp(-\Delta^2) \tag{3.30}$$

- *Matérn 3/2 Function*

$$r\left(\mathbf{p}_i, \mathbf{p}_j\right) = (1 + \sqrt{3}\Delta)\exp(-\sqrt{3}\Delta) \tag{3.31}$$

- *Matérn 5/2 Function*

$$r\left(\mathbf{p}_i, \mathbf{p}_j\right) = \left(1 + \sqrt{5}\Delta + \frac{5}{3}\Delta^2\right)\exp(-\sqrt{5}\Delta) \tag{3.32}$$

where

$$\Delta = \sqrt{\sum_{k=1}^{b} \frac{(p_{i,k} - p_{j,k})}{\theta_k}} \tag{3.33}$$

Note that the parameters $\theta_k$ used to compute the distance $\Delta$ between two parameters are the *length scales* of the correlation function and are determined through the training process. Loosely speaking, the choice of $\theta_k$ will affect how fast the correlation between $\mathbf{p}_i$ and $\mathbf{p}_j$ drops off. When the data are noisy, one can also append a noise term to the correlation function such that

$$r_n\left(\mathbf{p}_i, \mathbf{p}_j\right) = r\left(\mathbf{p}_i, \mathbf{p}_j\right) + \sigma_n^2\,\delta_{i,j} \tag{3.34}$$

where $\sigma_n^2$ is the noise variance and $\delta_{i,j}$ is the Kronecker delta, which is one if $i = j$ and zero otherwise. Even if the data do not contain any noise, the variable $\sigma_n^2$ can still be used as a regularization parameter to prevent overfitting and increase the robustness of the prediction. The value of the noise can be set to a known value or determined

through the training process together with $\theta_k$.

Suppose the function $g(\mathbf{p})$ is sampled with the following set of design parameters $\mathbf{P} = [\mathbf{p}_1, \ldots, \mathbf{p}_n] \in \mathbb{R}^{b \times n}$ such that the set of observations $\mathbf{Z} = [z_1, \ldots, z_n] \in \mathbb{R}^n$ is collected. With an adequate choice of correlation function, the Kriging predictor $g(\mathbf{p})$ is then given by the expected value of Eq. (3.28) conditioned by the observations in $\mathbf{Z}$. As demonstrated by Rasmussen and Williams [126], this predictor is formulated as

$$\widetilde{g}(\mathbf{p}) = \mu + \mathbf{r}(\mathbf{p})^T \mathbf{R}^{-1}(\mathbf{Z} - \mu\mathbf{1}) \tag{3.35}$$

where

$$\mathbf{r}(\mathbf{p}) = \begin{bmatrix} r(\mathbf{p}_1, \mathbf{p}) \\ \vdots \\ r(\mathbf{p}_n, \mathbf{p}) \end{bmatrix} \in \mathbb{R}^n \qquad \mathbf{R} = \begin{bmatrix} r(\mathbf{p}_1, \mathbf{p}_1) & \ldots & r(\mathbf{p}_1, \mathbf{p}_n) \\ \vdots & \ddots & \vdots \\ r(\mathbf{p}_n, \mathbf{p}_1) & \ldots & r(\mathbf{p}_n, \mathbf{p}_n) \end{bmatrix} \in \mathbb{R}^{n \times n} \tag{3.36}$$

The term $\mathbf{R}^{-1}(\mathbf{Z} - \mu\mathbf{1})$ in Eq. (3.35) solely depends on the observed values and only needs to be computed once. Therefore, for simplicity, the Kriging predictor can be reformulated as

$$\widetilde{g}(\mathbf{p}) = \mu + \mathbf{w}^T \mathbf{r}(\mathbf{p}) \tag{3.37}$$

where $\mathbf{w} \in \mathbb{R}^n$ is a weight vector defined as

$$\mathbf{w} = \mathbf{R}^{-1}(\mathbf{Z} - \mu\mathbf{1}) \tag{3.38}$$

One salient feature of the stochastic formulation of a Kriging model is that, in addition to providing the expected value of $g(\mathbf{p})$, it can also estimate the variance of the prediction. This information can then serve as an assessment of the prediction accuracy or be used in the context of adaptive sampling and surrogate-based optimization [76]. As showed by Jones [75], the prediction variance can be evaluated with

$$\text{var}\left(\widetilde{g}(\mathbf{p})\right) = \sigma^2 \left[1 - \mathbf{r}(\mathbf{p})^T \mathbf{R}^{-1} \mathbf{r}(\mathbf{p}) + \frac{(1 - \mathbf{r}(\mathbf{p})^T \mathbf{R}^{-1} \mathbf{r}(\mathbf{p}))^2}{\mathbf{1}^T \mathbf{R}^{-1} \mathbf{1}}\right] \tag{3.39}$$

### 3.3.2 Maximum Likelihood Estimation

For a Kriging model to provide the best possible predictions, one must select adequate values for the model parameters $\mu$, $\sigma^2$, $\sigma_n^2$, and $\theta_k$. These quantities are referred to as the *hyper-parameters* of the Kriging model and are determined during the training process. The most popular method for doing so is to choose the hyper-parameters that maximize the likelihood of the random process given the observed data [106]. This is loosely equivalent to finding the hyper-parameters that are the most consistent with the available information.

Without going into the details of the derivation [126], the logarithm of the likelihood function is given by

$$\log\ P(\mathbf{z}|\mu, \sigma^2, \theta_k) = -\frac{n}{2}\log(2\pi\sigma^2) - \frac{1}{2}\log(|\mathbf{R}|) - \frac{(\mathbf{Z} - \mu\mathbf{1})^T \mathbf{R}^{-1} (\mathbf{Z} - \mu\mathbf{1})}{2\sigma^2} \tag{3.40}$$

The optimal values of $\mu$ and $\sigma^2$ are obtained by computing the derivatives of Eq. (3.40) with respect those parameters and setting them to zero. As such, their maximum likelihood estimate is given by

$$\mu_{\text{ML}} = \frac{\mathbf{1}^T \mathbf{R}^{-1} \mathbf{Z}}{\mathbf{1}^T \mathbf{R}^{-1} \mathbf{1}} \tag{3.41}$$

$$\sigma^2_{\text{ML}} = \frac{(\mathbf{Z} - \mu_{\text{ML}}\mathbf{1})^T \mathbf{R}^{-1} (\mathbf{Z} - \mu_{\text{ML}}\mathbf{1})}{n} \tag{3.42}$$

Substituting $\mu_{\text{ML}}$ and $\sigma^2_{\text{ML}}$ into Eq. (3.40) and omitting the constant terms results in the *concentrated log-likelihood* function [75] defined as

$$-\frac{n}{2}\log(\sigma^2_{\text{ML}}) - \frac{1}{2}\log(|\mathbf{R}|) \tag{3.43}$$

A closed-form solution for the optimal length-scales $\theta_k$ and the noise $\sigma_n^2$ unfortunately does not exist. The estimation of these hyper-parameters requires instead the numerical optimization of Eq. (3.43). This can be achieved efficiently with a gradient-based optimization method. An analytical expression for the gradient of Eq. (3.43) with respect to $\theta_k$ and $\sigma_n^2$ is given by Toal et al. [160]. Ollar et al. [115] also suggested a gradient-based hyper-parameter optimization method that includes a constraint on the condition number of the correlation matrix $\mathbf{R}$ to prevent the Kriging model from becoming ill-conditioned. However, the likelihood function is non-convex and can have multiple maxima. It is customary to repeat the hyper-parameter optimization several times with different random initialization in an attempt to find globally optimal values.

### 3.3.3 CoKriging Formulation

The Kriging formulation presented in Section 3.3.1 assumed that the mean $\mu$, also known as the trend, of the random process is constant throughout the parameter space. However, the Kriging model can also be augmented with a mean having a spatial dependence. For instance, the method known as *universal Kriging* [172] uses a general polynomial to represent the mean of the model. Alternatively, an auxiliary non-linear function can also represent the mean, and this approach is referred to as *Kriging with external drift* [172].

In the context of multi-fidelity surrogate models, *CoKriging* [80] is a multi-fidelity variation of Kriging where the mean of the high-fidelity random process is given by a second random process representing some low-fidelity data. In other words, CoKriging is equivalent to a Kriging model of the high-fidelity data, but where the mean follows a separate Kriging model of some low-fidelity observations. Given some high-fidelity observations $\mathbf{Z}_{\text{hi}} = [z_{\text{hi},1}, \ldots, z_{\text{hi},n}] \in \mathbb{R}^n$ corresponding to the set of parameters $\mathbf{P} = [\mathbf{p}_1, \ldots, \mathbf{p}_n] \in \mathbb{R}^{b \times n}$, the formulation of the CoKriging predictor is

given by

$$\widetilde{g}_{\text{hi}}(\mathbf{p}) = \beta\, \widetilde{g}_{\text{lo}}(\mathbf{p}) + \mathbf{r}(\mathbf{p})^T \mathbf{R}^{-1}(\mathbf{Z}_{\text{hi}} - \beta\, \mathbf{Z}_{\text{lo}}) \tag{3.44}$$

where $\beta$ is a scaling factor, and $\widetilde{g}_{\text{lo}}(\mathbf{p})$ is a low-fidelity Kriging model. Also, the vector $\mathbf{Z}_{\text{lo}} \in \mathbb{R}^n$ contains low-fidelity observations obtained at the same design parameters as $\mathbf{Z}_{\text{hi}}$. If the low-fidelity samples do not coincide with every high-fidelity observation, it is admissible to replace $\mathbf{Z}_{\text{lo}}$ with the estimations $\widetilde{\mathbf{Z}}_{\text{lo}} = [\widetilde{g}_{\text{lo}}(\mathbf{p}_1), \ldots, \widetilde{g}_{\text{lo}}(\mathbf{p}_n)] \in \mathbb{R}^n$ produced by the low-fidelity Kriging model [62].

The mean model $\widetilde{g}_{\text{lo}}(\mathbf{p})$ in Eq. (3.44) only depends on the low-fidelity observations and can be trained prior to the CoKriging model [80]. As with any multi-fidelity methodology, we assume that the low-fidelity observations are available in greater quantity and that they are related to the high-fidelity samples. For simplicity, most authors use the same correlation function for both $\widetilde{g}_{\text{lo}}(\mathbf{p})$ and $\widetilde{g}_{\text{hi}}(\mathbf{p})$, but each model has their own set of optimal hyper-parameters.

As for conventional Kriging models, the hyper-parameters of CoKriging models are typically obtained using maximum likelihood estimations. In which case, the optimal values of $\beta$ and $\sigma^2$ are given by

$$\beta_{\text{ML}} = \frac{\mathbf{Z}_{\text{lo}}^T\, \mathbf{R}^{-1} \mathbf{Z}_{\text{hi}}}{\mathbf{Z}_{\text{lo}}^T\, \mathbf{R}^{-1} \mathbf{Z}_{\text{lo}}} \tag{3.45}$$

$$\sigma^2_{\text{ML}} = \frac{(\mathbf{Z}_{\text{hi}} - \beta_{\text{ML}}\, \mathbf{Z}_{\text{lo}})^T\, \mathbf{R}^{-1} (\mathbf{Z}_{\text{hi}} - \beta_{\text{ML}}\, \mathbf{Z}_{\text{lo}})}{n} \tag{3.46}$$

The optimal value of the length-scales $\theta_k$ and noise $\sigma_n^2$ of the correlation function are then estimated by numerically optimizing the concentrated log-likelihood function of Eq. (3.43). This can once again be done with a gradient-based approach with random restarts.

## 3.4 Multi-Fidelity ROM with Manifold Alignment

Having described the fundamentals of the POD, Procrustes manifold alignment, and multi-fidelity regression, we now demonstrate how these methods are integrated into a non-intrusive ROM that utilizes multi-fidelity information, potentially from heterogeneous data. We refer to this proposed multi-fidelity ROM as Manifold Aligned Reduced-Order Model (MA-ROM), which is illustrated in Figure 3.1. We denote the high- and low-fidelity models as $f_x : \mathbf{p} \mapsto \mathbf{x}$ and $f_y : \mathbf{p} \mapsto \mathbf{y}$ respectively, where $\mathbf{x} \in \mathbb{R}^d$ and $\mathbf{y} \in \mathbb{R}^q$ are high- and low-fidelity fields, and $\mathbf{p} \in \mathbb{R}^b$ is a $b$-dimensional vector of design parameters common to both models. We also assume that the sample sizes $n$ and $m$ for the high- and low-fidelity datasets respectively are such that low-fidelity results are available in greater numbers, i.e., $n < m$. Note that no assumptions are made regarding the dimensions or the topology of the fields, thus allowing the high- and low-fidelity datasets to be heterogeneous.

As with most surrogate models, the methodology of MA-ROM is divided into two phases: an *offline* phase to train the model and an *online* phase to make new predictions. For the offline phase, the overall process is given by the following steps:

**Step 1 - Generate Linked Data:** Select a set of $n$ distinct designs $\mathbf{P}_\mathrm{L} = [\mathbf{p}_1, \ldots, \mathbf{p}_n] \in \mathbb{R}^{b \times n}$ for the linked data. Then, sample both $f_x$ and $f_y$ to generate the matrices $\mathbf{X}$ and $\mathbf{Y}_\mathrm{L}$, which form the linked multi-fidelity datasets.

**Step 2 - Generate Unlinked Data:** Select a set of $m - n$ additional designs $\mathbf{P}_\mathrm{U} = [\mathbf{p}_{n+1}, \ldots, \mathbf{p}_m] \in \mathbb{R}^{b \times (m-n)}$ for the unlinked data. Ideally, $\mathbf{P}_\mathrm{U}$ should not repeat points in $\mathbf{P}_\mathrm{L}$. Then, sample only $f_y$ with $\mathbf{P}_\mathrm{U}$ to generate the matrix $\mathbf{Y}_\mathrm{U}$, which is the unlinked dataset.

**Step 3 - Align Manifolds:** Apply the Procrustes manifold alignment on $\mathbf{X}$, $\mathbf{Y}_\mathrm{L}$, and $\mathbf{Y}_\mathrm{U}$, to obtain high- and low-fidelity latent variables $\mathbf{Z}_\mathrm{hi}$ and

$\mathbf{Z}_{\text{lo}}$. This is divided into the following three sub-steps:

(a) Extract the high- and low-fidelity POD modes, i.e., $\mathbf{\Phi}_k$ and $\mathbf{\Psi}_k$, as well as their latent variables $\mathbf{Z}_{\text{hi}}$ and $\mathbf{W}$.

(b) Perform the Procrustes analysis of $\mathbf{Z}_{\text{hi}}$ and $\mathbf{W}_{\text{L}}$ to evaluate the optimal scaling $s$, translation $\mathbf{t}$, and orthonormal projection $\mathbf{Q}$.

(c) Apply the optimal transformation to $\mathbf{W}$ such that $\mathbf{Z}_{\text{lo}}$ contains the embeddings of $\mathbf{Y}$ onto the shared manifold.

**Step 4 - Fit Regression Model:** Train a set of $k$ multi-fidelity regression models $\widetilde{\mathbf{g}}(\mathbf{p}) = [\widetilde{g}_1(\mathbf{p}), \ldots, \widetilde{g}_k(\mathbf{p})]$ using CoKriging. These models combine the information from both $\mathbf{Z}_{\text{hi}}$ and $\mathbf{Z}_{\text{lo}}$, together with their associated design parameters $\mathbf{P} = [\mathbf{P}_{\text{L}}, \mathbf{P}_{\text{U}}] \in \mathbb{R}^{b \times m}$.

In Steps 1 and 2, the design parameters for the training data can be selected using a Design of Experiment (DoE). For models based on computer experiments, Santner et al. [139] recommend using *space-filling* designs. Popular options include Latin Hypercube Sampling (LHS), quasi-random sequences (e.g., Sobol or Halton sequence), and Maximum Projection Design [77]. Also, in Step 3, the computation of $\mathbf{\Psi}_k$ is required to obtain $\mathbf{W}$, but the low-fidelity modes are not needed for the online predictions of the ROM and can be safely be discarded. As for the online phase, the process is identical to most projection-based ROM and is described by the following steps:

**Step 5 - Predict Latent Variable:** Given an out-of-sample design parameter $\mathbf{p}^*$, predict the corresponding latent variable $\widetilde{\mathbf{z}}^*$ using $\widetilde{\mathbf{g}}(\mathbf{p})$.

**Step 6 - Reconstruct Field:** Using $\mathbf{\Phi}_k$ together with Eq. (3.6), compute the predicted value of the new high-fidelity field $\widetilde{\mathbf{x}}^*$ given $\widetilde{\mathbf{z}}^*$.

Before proceeding forward, we highlight the salient features of the novel MA-ROM method:

- By reducing the dimensionality of $\mathbf{X}$ and $\mathbf{Y}$ separately and then aligning both subspaces, both sets of solutions do not need to be consistent in terms of dimensionality or topology. Therefore, the proposed method does not require any pre-processing and is agnostic to the representation of the individual fields. Although, the low- and high-fidelity fields must still be somewhat interrelated for any multi-fidelity model to be effective.

- Since all the high- and low-fidelity solutions are projected onto the same latent space, the number of samples available for the training of the regression models $\widetilde{\mathbf{g}}(\mathbf{p})$ can be relatively larger. This will aid in reducing the prediction error of new latent space coordinates, especially for problems where the number of design parameters is large.

- During manifold alignment, the POD modes $\mathbf{\Phi}_k$ of the high-fidelity data are left untouched, and as such, MA-ROM will not improve the accuracy of the dimensionality reduction in terms of reconstruction error (see Eq. (4.4)). Consequently, the proposed approach will mostly benefit situations where the prediction error of a non-intrusive ROMs is dominated by the accuracy of the underlying regression model (see Eq. (4.5)). We will demonstrate in Chapter 5 that this is often the case in practice.

**Offline Phase:**

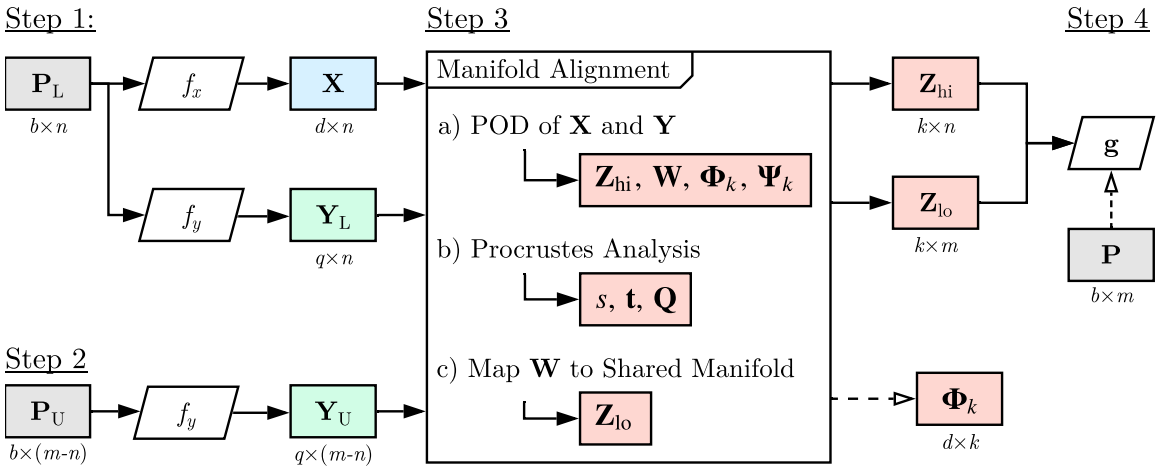


**Online Phase:**

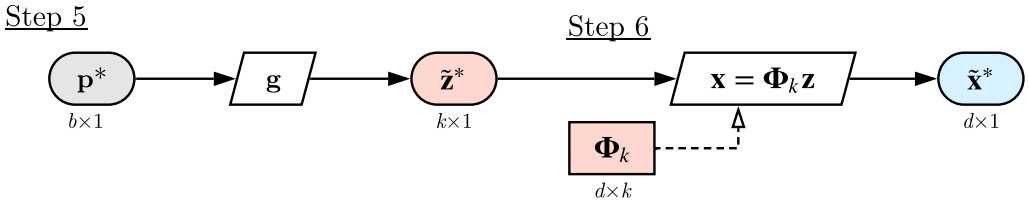


**Figure 3.1:** Flowchart of the proposed MA-ROM method. This process is broken down into an offline (training) and online (prediction) phase.

# CHAPTER 4
# RESEARCH FORMULATION

We have previously established in Chapter 1 the need for cheap-to-evaluate and non-intrusive ROMs for advanced aircraft design, and we have shown the benefits that a multi-fidelity modeling approach can offer. The unresolved challenges associated with the multi-fidelity combination of fields have led to the overall research objective of this dissertation that we repeat here for convenience:

**Research Objective**

To develop or improve a *non-intrusive* and *multi-fidelity* reduced-order modeling method for the purpose of many-query applications, and with an emphasis on combining multi-fidelity fields with *disparate representations*, i.e., fields having inconsistent dimensionalities, topologies, and features.

After reviewing the literature on dimensionality reduction, multi-fidelity methods, and reduced-order modeling in Chapter 2, we have determined that the above objective could be addressed using manifold alignment, and in particular, using the Procrustes manifold alignment method outlined in Chapter 3. Together with a multi-fidelity regression model, the proposed approach would extend the capability of existing multi-fidelity ROMs to fuse fields having disparate representation. As such, the overall hypothesis of this research was formulated as:

**Overall Hypothesis**

A non-intrusive and multi-fidelity reduced-order modeling method combining manifold alignment and multi-fidelity regression should match or surpass the predictive performance of existing multi-fidelity ROM methods and provide the capability of fusing high- and low-fidelity fields having different representations.

The purpose of the current chapter is to identify the unresolved questions concerning the applicability of the Manifold Aligned Reduced-Order Model (MA-ROM) in the context of aircraft design. This is followed by an experimental plan designed to address these questions and verify the overall hypothesis. The results from this process will then ultimately demonstrate if the overall objective of this thesis has been adequately met.

## 4.1 Research Questions

In the following section, we detail the research questions that this dissertation will address. The purpose of these questions is to gain some insight into the strengths and weaknesses of the proposed method, and to support the viability of MA-ROM for engineering applications.

### 4.1.1 Multi-Fidelity Performance

The overarching goal of any multi-fidelity model is to provide improved predictions at a lower overall training cost when compared to an equivalent single-fidelity approach (see Section 1.4.1). This typically implies a more accurate model for a given computational budget, or conversely, the same precision at a lower overall training cost. As such, the first research question is simply given by:

**Research Question 1**

Compared to an equivalent single-fidelity ROM, can the proposed multi-fidelity method improve the overall performance of the model, in terms of accuracy and training cost, by augmenting high-fidelity data with low-fidelity results?

Here, the accuracy of a model is defined as some prediction error measured on some previously unseen designs, i.e., a testing dataset. As for the training cost, it refers to the computational cost required to generate the training data for the surrogate model. For the multi-fidelity approach, this includes the cost of both the high- and low-fidelity datasets. Multi-fidelity models should require more samples overall, but since the low-fidelity simulation is assumed to be much cheaper than the high-fidelity, the added cost should be relatively small. One could also consider the computational cost of training the model itself, but this effort is typically insignificant when compared to the evaluation cost of high-fidelity simulations. These accuracy and cost metrics are defined in more detail in Section 4.3.

From the literature, it is generally accepted that multi-fidelity models require the high- and low-fidelity results to be related. As such, their performance mainly depends on two factors: the ratio of high- and low-fidelity data, and the level of affinity existing between the high- and low-fidelity models [158]. Loosely speaking, the accuracy of a multi-fidelity model is mostly obtained from the high-fidelity data, while the low-fidelity results provide the general trend. The accuracy of a multi-fidelity model is further improved by adding high-fidelity than low-fidelity results in equal numbers. Although, since they can be more easily generated, the potentially greater number of low-fidelity samples compensates for their lower accuracy. Therefore, the balance between accuracy and cost of a multi-fidelity model will depend on the proportion of high- and low-fidelity results in the training data. As for the effect of the high- and low-fidelity interrelation, it is worth noting that not all low-fidelity models are

equal. Low-fidelity simulations that are further away from the high-fidelity model in terms of assumptions and discretization tend to offer more computational savings, but also have a weaker correlation to the high-fidelity results. The strength of this correlation will then affect how much low-fidelity information the multi-fidelity model can leverage for the high-fidelity prediction. In fact, if the high- and low-fidelity results are completely unrelated, the multi-fidelity model can potentially offer worse predictions than a single-fidelity approach. Consequently, the accuracy and cost of a multi-fidelity model also depend on the fidelity of the auxiliary dataset. From the above discussion, we can then formulate the following hypothesis for the first research question:

**Hypothesis 1.1**

Similarly to multi-fidelity data-fit models, the performance of a MA-ROM, in terms of accuracy and training costs, should be superior to an equivalent single-fidelity model. Furthermore, the performance improvement between a multi- and single-fidelity model, if any, should depend on the ratio of high- and low-fidelity results, and the fidelity difference between both sources of data.

Also, as mentioned in Section 1.4, the accuracy of any surrogate model, both single- and multi-fidelity, tends to be negatively affected by the number of design parameters due to the curse of dimensionality. Nonetheless, a multi-fidelity approach should still be able to improve the prediction of a surrogate model despite having a high-dimensional input space. We expect the relative improvement offered by the proposed multi-fidelity method over a single-fidelity ROM to be preserved with many design variables.

**Hypothesis 1.2**

Similarly to multi-fidelity data-fit models, the relative benefits of a MA-ROM compared to an equivalent single-fidelity ROM, in terms of cost and accuracy, should be preserved in situations with many design parameters.

### 4.1.2 Effect of Field Inconsistencies

We previously outlined in Section 1.5 the unique challenges associated with the multi-fidelity combination of fields. Namely, field solutions produced by simulations of varying fidelity can possibly have inconsistent representations in terms of dimensionality, topology, and features. These difficulties are at the core of the current research objective, and the MA-ROM method was developed specifically to overcome potential inconsistency issues. However, the consequences, if any, of combining solutions having different representations on the performance of a multi-fidelity ROM is unclear. This motivates our second research question that is given as:

**Research Question 2**

Is the multi-fidelity performance of the proposed MA-ROM method affected by inconsistencies between the high- and low-fidelity field representations in terms of dimensionality, topology, and feature?

Recall that the cornerstone of the proposed approach is the Procrustes manifold alignment method. As detailed in Section 3.2, this method consists of individually projecting the high- and low-fidelity fields into their respective latent space, and then, linearly align these subspaces to minimize the discrepancies between their latent coordinates. Since both datasets are independently projected, their respective bases can be selected to account for their individual field representation. The high- and

low-fidelity solutions are only combined in the latent space after differences in dimensionality, topology, and features have been removed by the dimensionality reduction. Consequently, the performance of MA-ROM will ultimately depend on the interrelation between the high- and low-fidelity latent variables, but should not be contingent on the original representation of these datasets. We should mention that differences in fidelity levels should still affect the performance of the proposed multi-fidelity ROM as mentioned in Hypothesis 1.1. As such, our hypothesis for the second research question is:

**Hypothesis 2**

Aside from differences in terms of fidelity levels, inconsistencies between the field representations of the high- and low-fidelity results should not directly affect the performance of the MA-ROM method since the multi-fidelity datasets are fused after being projected onto a shared latent space.

### 4.1.3 Comparison with Existing Multi-fidelity Methods

As presented in Section 2.5, other authors have previously proposed multi-fidelity methods for non-intrusive ROMs. These techniques are listed in Table 4.1 for convenience. Here, we distinguish between *adaptation-* and *fusion-based* methods. In the former case, a high-fidelity prediction is obtained by correcting the results from a low-fidelity simulation. This implies that a new low-fidelity field must be produced before estimating the high-fidelity result. This can either be achieved by evaluating the low-fidelity simulation directly if it is sufficiently inexpensive, or by using the prediction of a separate ROM trained on the low-fidelity results only. On the other hand, in fusion-based methods, both high- and low-fidelity data are combined into a self-contained predictive model. We also note that, except for the GPOD method

**Table 4.1:** Existing literature on single-fidelity and non-intrusive ROMs applied to industrial applications.

| Multi-Fidelity Method | Type | Requires Consistent Fields |
|---|---|---|
| Additive Correction [105] | Adaptation | ✓ |
| GPOD Reconstruction [157] | Adaptation | ✗ |
| Common POD Basis [111] | Fusion | ✓ |
| Extended POD Basis [12] | Fusion | ✓ |

of Toal [157], the existing multi-fidelity ROM methods require the representation of high- and low-fidelity fields to be consistent.

While the proposed MA-ROM method has been developed specifically to address the challenges of combining disparate fields, it can also conceivably be applied to problems where the training data fortuitously have a consistent representation. For instance, the high- and low-fidelity models can share the same discretization, or all the results can be conveniently mapped to a common grid. For such scenarios, the benefits of the proposed method, if any, are not immediately apparent, and the other multi-fidelity approaches of Table 4.1 are potential alternatives. One can then reasonably ask if the MA-ROM remains a viable multi-fidelity approach in situations where field inconsistencies are absent. As such, the third research question of this dissertation is formulated as follows:

**Research Question 3**

In situations where high- and low-fidelity results have a consistent field representation, is the performance of the MA-ROM method comparable to other multi-fidelity ROM methods existing in the literature?

As mentioned previously, the manifold alignment within MA-ROM aims to minimize the discrepancies between the high- and low-fidelity latent variables prior to the

training of the multi-fidelity regression model. This process can be applied to any two sets of latent variables regardless of how they were obtained from their respective high-dimensional field results. The Procrustes manifold alignment can equally be applied to multi-fidelity fields with either consistent or inconsistent representation as long as there exists a relation between them. Also, if the high- and low-fidelity results are related such that their latent representations are inherently aligned, then the Procrustes alignment would not modify the data, and at worst, be superfluous. Therefore, it is reasonable to expect that the MA-ROM method would perform as well with consistent multi-fidelity fields than with inconsistent ones, assuming their interrelation remains similar.

When compared to the other multi-fidelity methods present in the literature, the MA-ROM method shares many similarities with the fusion-based approach of Mifsud et al. [110, 111] and Benamara et al. [12, 14]. These methods also combine the high- and low-fidelity results in the latent space and make new predictions using a multi-fidelity regression model. However, MA-ROM use individually optimal bases for both datasets and then apply manifold alignment to combine the results in a common subspace. In comparison, the fusion-based methods of Table 4.1 use a common basis to project both the high- and low-fidelity datasets into a shared latent space. These approaches are built on the implicit assumption that both high- and low-fidelity data have nearly identical features, and consequently, are embedded in similar subspaces. In scenarios where this assumption is indeed correct, the manifold alignment in MA-ROM becomes unnecessary and the resulting model has a formulation essentially equivalent to the other fusion-based approaches. Therefore, the MA-ROM method is likely to perform at least as well as the Common and Extended POD methods of Table 4.1 in a situation without field inconsistencies.

In light of the above observations, our hypothesis associated with the third research question is formulated as follows:

**Hypothesis 3**

In problems involving high- and low-fidelity results with a consistent field representation, the MA-ROM method should perform comparably to existing fusion-based multi-fidelity ROM methods on the basis that their formulations are alike.

## 4.2 Description of the Test Cases

To address the research questions of the previous section, we define two practical test cases that will provide insights into the proposed multi-fidelity ROM. More specifically, the MA-ROM method is applied to the aerodynamic analysis of a transonic airfoil and a transonic wing. These test cases are meant to represent real engineering problems that can be encountered in early aircraft design.

### 4.2.1 Transonic Airfoil

Despite being a relatively simple problem, the aerodynamic analysis of an airfoil involves essentially the same governing equations as that of a complete aircraft. Indeed, the two-dimensional CFD simulation of an airfoil can exhibit complex physical phenomena such as boundary layers, flow separation, shock waves, etc. Field results with a complexity representative of large-scale simulations can be generated at a substantially lower cost, making this test case ideal for exploratory studies. This explains why many existing ROM studies focusing on engineering problems also use the aerodynamic analysis of an airfoil as their main use case (see Table 2.1).

*Geometry*

The airfoil geometry used for this thesis corresponds to the RAE 2822, which is presented in Figure 4.1. This airfoil is designed for transonic flow conditions, and as such, is representative of the airfoils used for civil transport aircraft. The choice of

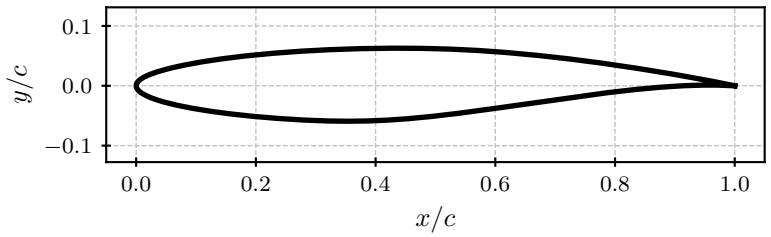


**Figure 4.1:** The RAE 2822 transonic airfoil [32]. The dimensions shown are normalized by the airfoil chord.

the RAE 2822 is motivated by the availability of experimental data [32], which we used to validate our CFD methodology. This airfoil has been the subject of many CFD studies and is the initial geometry of the second benchmark problem defined by the AIAA Aerodynamic Design Optimization Discussion Group (ADODG) [8, 90, 121].

*Simulation Setup*

We use a compressible CFD simulation of the RAE 2822 to analyze the flow field around this airfoil in transonic conditions. The simulations are performed using the open-source SU2 code[1] [39], and we solve for the turbulent flow field using the Reynolds-Averaged Navier-Stokes (RANS) equations and the Spalart-Allmaras turbulence model [150]. The Jameson-Schmidt-Turkel (JST) scheme [72] is used for the spatial discretization, and the steady-state solution is obtained using a backward Euler scheme. The fluid domain around the airfoil is discretized using a structured O-grid topology extruded using a hyperbolic solver, an example of which is shown in Figure 4.2. The distance between the far-field of the fluid domain and the airfoil surface is roughly 100 times the airfoil chord.

A brief grid convergence study is performed to evaluate the accuracy of the discretization, and the obtained aerodynamic coefficients are compared to both experimental and numerical results from Cook et al. [32] and Lee et al. [90] respectively.

[1]The simulations of this thesis use the release 7.0.0 of the SU2 code.

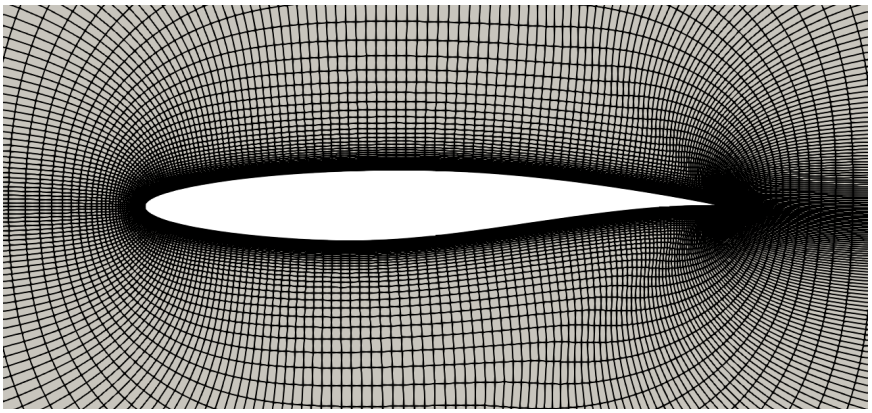

**Figure 4.2:** Baseline O-grid (41,796 nodes) of the RAE 2822 generated using a hyperbolic solver.

This comparison considers a freestream Mach number of $M_\infty = 0.73$ and Reynolds number of $Re_\infty = 6.5 \times 10^6$ that correspond to Case 9 of the experimental campaign performed by Cook et al. The results of the grid convergence study are reported in Table 4.2 and presented graphically in Figure 4.3 for the normal force coefficient $C_N$ and the pitching moment coefficient $C_{M_z}$. Note that the wind tunnel experiment of the RAE 2822 originally used an angle of attack of $\alpha = 3.19°$ whereas the CFD simulations use $\alpha = 2.79°$ to account for the walls interference [52]. The data in Figure 4.3 show that the $C_N$ results asymptotically converge from the coarse to the fine grid to a value close to the reference results. The $C_{M,z}$ results of the current setup converge to a pitching moment that is higher than the experimental value, but this offset is consistent with the CFD result of Lee et al. As for the drag coefficient $C_D$, the results on the finest grid is within less than a drag count of the reference values. All in all, the current CFD setup provides aerodynamic coefficients having a good agreement with previous experimental and numerical studies.

*Parametrization*

The angle of attack and the airfoil shape are considered as the design parameters for this test case. The airfoil shape is parametrized using a Free Form Deformation

**Table 4.2:** Grid convergence study of the RAE 2822 CFD with comparison to experimental [32] and numerical [90] results from the literature. The flow conditions correspond to Case 9 of the experimental campaign ($Re_\infty = 6.5\times10^6$ and $M_\infty = 0.73$).

| Cases | Grid Size | $\alpha$ [deg] | $C_N$ | $C_{M,z}$ | $C_D$ [$10^4$] |
|---|---|---|---|---|---|
| Fine | 166,536 | 2.79 | 0.806 | -0.089 | 165.9 |
| Baseline | 41,796 | 2.79 | 0.787 | -0.085 | 162.6 |
| Coarse | 10,530 | 2.79 | 0.765 | -0.082 | 167.7 |
| Cook et al. [32] | N/A* | 2.79† | 0.803 | -0.099 | 168.0 |
| Lee et al. [90] | 12,067,328 | 2.79 | 0.802 | -0.091 | 167.0 |

*Experimental results

†Value corrected for wind tunnel walls interference

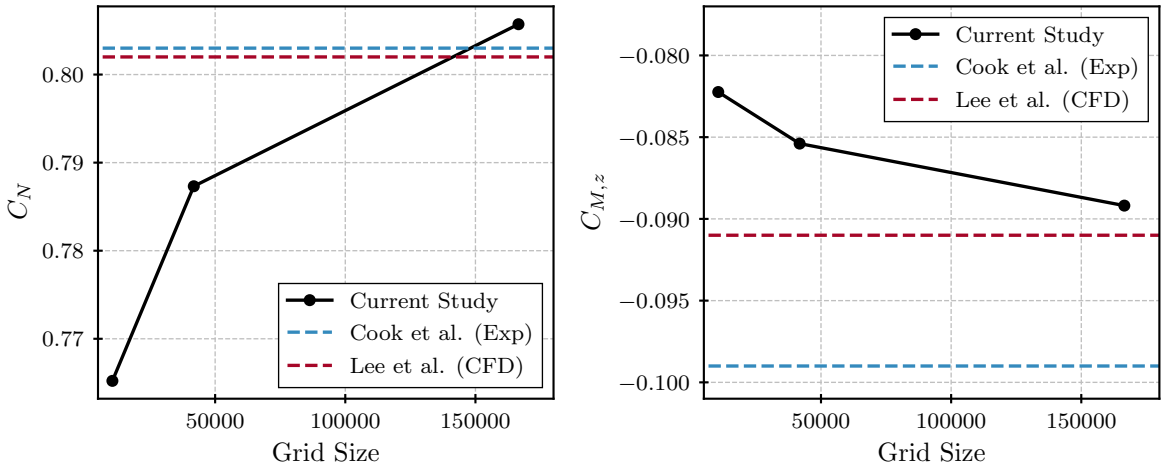


**Figure 4.3:** Grid convergence of the $C_N$ and $C_{M,z}$ values for the RAE 2822 test case with comparison to previous experimental [32] and numerical [90] studies. The flow conditions correspond to Case 9 of the experimental campaign ($Re_\infty = 6.5 \times 10^6$ and $M_\infty = 0.73$).

(FFD) [81] approach as illustrated in Figure 4.4. This type of parametrization encloses a geometry into an FFD volume (or box), which is a simple rectangle in this use case. The FFD volume essentially acts as a flexible rubber-like material, and by displacing the boundary nodes of the FFD volume, the geometry within is subsequently deformed. With this technique, geometries of any complexity can easily be modified without the need for CAD software. Once the new airfoil geometry is generated, the deformation is propagated into the rest of the flow field grid using a linear elasticity approach [38]. It is worth noting that the tools required for this FFD parametrization and grid deformation are all included in the SU2 code suite.

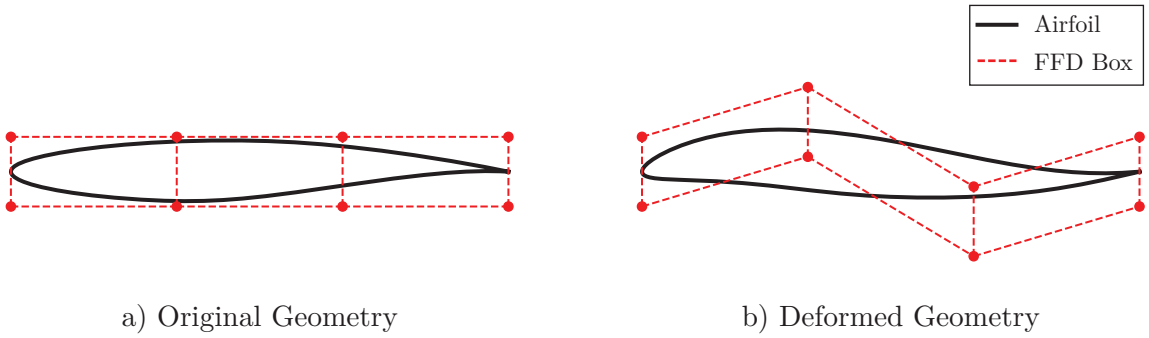


a) Original Geometry b) Deformed Geometry

**Figure 4.4:** Free form deformation of the RAE 2822 airfoil using a $4 \times 2$ FFD volume. The airfoil deformation is exaggerated for demonstration purposes.

In this test case, the input space dimensionality $b$ is varied between 3 and 9 design parameters as shown in Table 4.3. Each of the design parametrizations includes the angle of attack and a flexible number of FFD control points. To prevent the FFD deformation from affecting the angle of attack of the airfoil, we fix the nodes at the leading and trailing edge. We also limit the FFD control points to move along the vertical axis only. In all of the parametrizations, the angle of attack is varied between $0°$ and $4°$, while the FFD control point displacements are limited to $\pm 0.03$ chord length. For example, the parametrization with $b = 5$ ($\alpha$ plus 4 FFD control points) is illustrated in Figure 4.4.

**Table 4.3:** Design parametrizations for the RAE 2822 airfoil. Note, only vertical movement of the FFD control points are considered and the control points at the airfoil leading and trailing edge are kept fixed.

| $b$ | Parametrization | Size of FFD box |
|---|---|---|
| 3 | $\alpha + 2$ FFD control points | $3 \times 2$ |
| 5 | $\alpha + 4$ FFD control points | $4 \times 2$ |
| 7 | $\alpha + 6$ FFD control points | $5 \times 2$ |
| 9 | $\alpha + 8$ FFD control points | $6 \times 2$ |

*Fidelity Levels*

The main purpose of a multi-fidelity model is to combine expensive simulation results with a cheaper auxiliary source of data to obtain an accurate model at a lower overall cost. The present study considers the following datasets of different fidelity levels and computational costs:

**A1 -** RANS CFD simulation using a baseline grid (41,796 nodes);

**A2 -** RANS CFD simulation using a coarse grid (10,530 nodes);

**A3 -** Inviscid CFD simulation using a coarse grid without near-wall refinement (8,910 nodes).

For all the ROMs used in this study, the fidelity A1 is used as the high-fidelity model and combined with one of the other fidelity levels to construct a multi-fidelity model. Table 4.4 provides a comparison of the computational cost required to generate samples for each fidelity levels. These costs represent the time to converge the corresponding simulations with the reference flow conditions and an undeformed airfoil geometry using an Intel Xeon Gold 6248 CPU. It is worth noting that the execution times of the fidelity A2 and A3 are roughly 6.8 and 10.8 times shorter than A1 respectively. These computational savings are achieved by using a coarser

**Table 4.4:** Description of the various fidelity levels for the RAE 2822 test case.

| Fidelity | Physics Model | Grid Size | Cost/Sample [CPU-min]* |
|---|---|---|---|
| A1 | RANS | 41,796 | 8.191 |
| A2 | RANS | 10,530 | 1.201 |
| A3 | Inviscid | 8,910 | 0.760 |

*CPU times are based on an Intel Xeon Gold 6248 CPU

discretization, and in the case of A3, a simplified physical model. The above datasets all use grids of different sizes, and thus, have inconsistent dimensionality. For the A3 fidelity, the features of the flow field should also be inconsistent with those of A1 due to the absence of viscous effects.

### 4.2.2 Transonic Wing

While the general characteristics of the MA-ROM method can be assessed with the analysis of a simple airfoil, the low computational cost of this simulation, even with a fine grid, is unlikely to necessitate a multi-fidelity approach in an industrial setting. The proposed method is intended to be used in situations where the training cost is prohibitive from an aircraft design perspective. Hence, this second use case considers the analysis of a transonic wing to demonstrate the relevance of MA-ROM for large-scale problems representative of an industrial design process. Although this test case does not consider the entire airframe, the wing is usually the component responsible for most of the flow complexity and at the center of any aerodynamic design. Also, the computational cost of a wing CFD simulation is still orders of magnitude greater than that of the two-dimensional analysis of an airfoil. Repeatedly sampling this high-fidelity model can require days of effort on a specialized cluster, and the promises of multi-fidelity modeling can represent a substantial cost reduction.

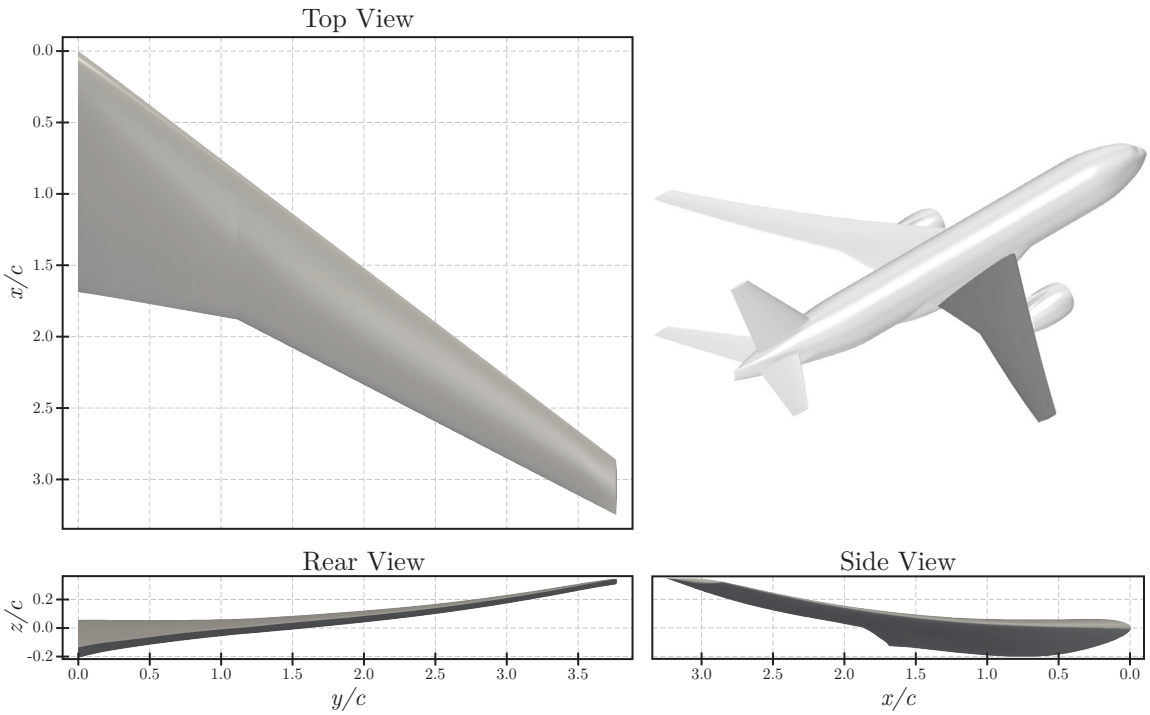


**Figure 4.5:** Top, rear, and side view of the CRM wing as defined by the ADODG. The dimensions provided are normalized by the mean aerodynamic chord whose value is 275.8 in. The top right isometric view shows the wing in context of the full aircraft configuration.

*Geometry*

The geometry considered for this test case is the wing of the NASA Common Research Model (CRM) [164] and is shown in Figure 4.5. The CRM is a transonic transport aircraft geometry specifically designed to provide a relevant and challenging problem for academia and the development of aerodynamic prediction methods. Similar to the airfoil test case, the CRM wing is also part of the suite of benchmark problems defined by the ADODG, and multiple researchers have published numerical results on this geometry [8, 90, 100, 101, 102].

*Solver Setup*

The CFD simulation setup for the CRM wing follows a very similar approach to that of the RAE 2822 airfoil described previously. The open-source SU2 code is

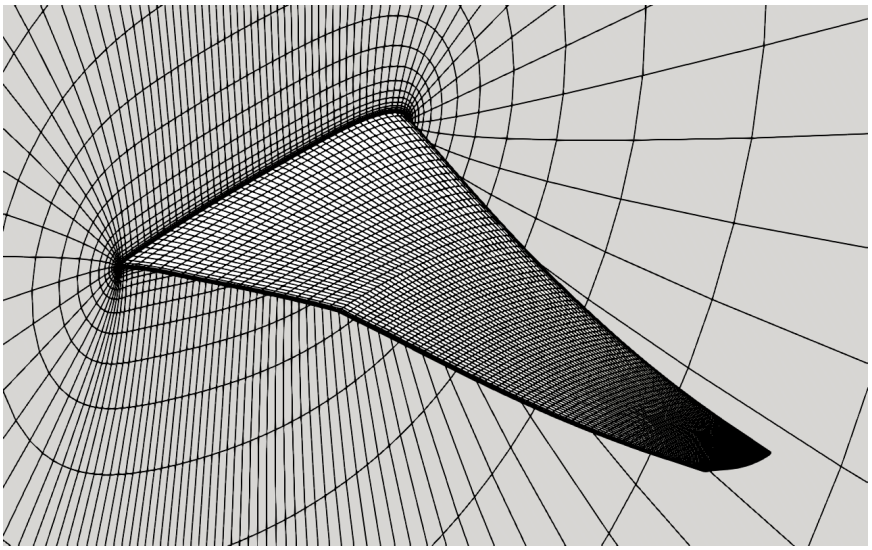

**Figure 4.6:** Coarse grid (450K nodes) of the CRM wing surface and symmetry plane.

used once again to solve the steady-state RANS equations together with the Spalart-Allmaras turbulence model, the JST convection scheme, and the backward Euler scheme. For the discretization of the fluid domain, we use the grids provided by the Multidisciplinary Design Optimization Laboratory [113] of the University of Michigan as part of the ADODG benchmark case. These consist of multi-block structured grids of various sizes that were previously used by Lyu et al. [102] for a multilevel RANS-based aerodynamic shape optimization of the CRM wing. An example of the smallest grid size is presented in Figure 4.6. Since SU2 is an unstructured CFD code, these structured grids are converted to an unstructured data format before being used.

To validate the current CFD setup, simulations of the CRM wing are evaluated on each grid size, and the obtained results are compared to those of Lyu et al. [101]. These simulations are evaluated at a fixed lift coefficient of $C_L = 0.5$ and at a freestream condition of $Re_\infty = 5 \times 10^6$ and $M_\infty = 0.85$. The validation results are presented in Table 4.5 and the convergence of the drag coefficient $C_D$ is shown graphically in Figure 4.7. Overall, we observe a good agreement between the current and the published results. The largest disagreement is observed with the coarser grid (450K nodes) where the angle of attack $\alpha$ and drag coefficient $C_D$ discrepancies are

**Table 4.5:** Grid convergence study of the CRM wing CFD and comparison to previously published CFD results [101]. The flow conditions correspond to $Re_\infty = 5 \times 10^6$ and $M_\infty = 0.85$.

| Grid Level | Grid Size | $C_L$ | Current Study | | Lyu et al. [101] | |
|---|---|---|---|---|---|---|
| | | | $\alpha$ [deg] | $C_D$ [$10^4$] | $\alpha$ [deg] | $C_D$ [$10^4$] |
| Fine | 28,835,840 | 0.50 | 2.219 | 199.1 | 2.210 | 199.7 |
| Baseline | 3,604,480 | 0.50 | 2.239 | 202.5 | 2.184 | 201.7 |
| Coarse | 450,560 | 0.50 | 2.340 | 216.8 | 2.194 | 211.1 |

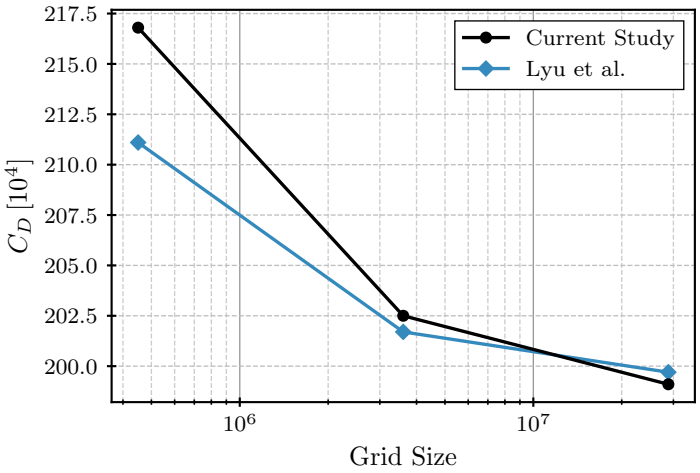


**Figure 4.7:** Grid convergence of $C_D$ values for the CRM wing test case with comparison to previously published CFD results [101]. The flow conditions correspond to $C_L = 0.5$, $Re_\infty = 5 \times 10^6$, and $M_\infty = 0.85$.

0.15° and 5.7 drag counts respectively. These discrepancies are reduced to only 0.009° and 0.6 drag counts respectively on the finest grid (28.8M nodes).

In addition to CFD simulations, the CRM wing is also analyzed with a Vortex Lattice Method (VLM) [79]. These simulations are performed with the aerodynamic module of the open-source OpenAeroStruct code [73]. The VLM is based on the potential flow equations and uses a flattened representation of the wing (see Figure 1.8 for an example). Compared to RANS simulations, VLM models use simplified physical assumptions that make them unable to predict either viscous effects or shocks. However, because of their simplicity, typical desktop computers can easily compute

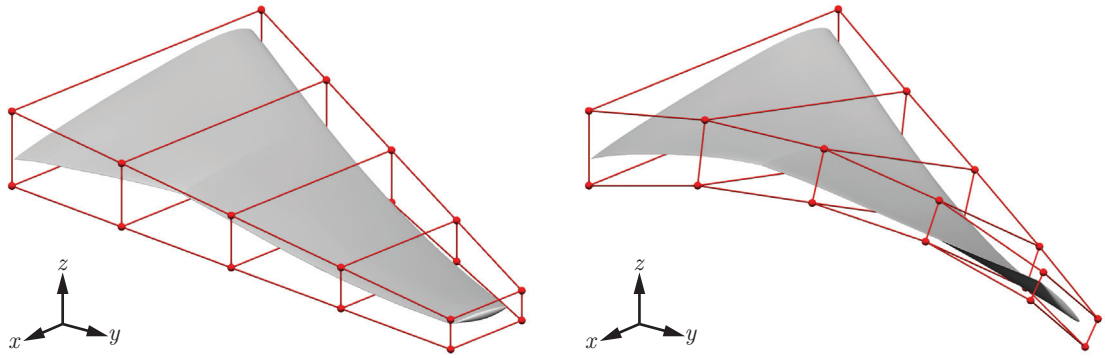


a) Original Geometry b) Deformed Geometry

**Figure 4.8:** Twist deformation of the CRM wing using a $2 \times 5 \times 2$ FFD volume. The wing deformation is exaggerated for demonstration purposes.

VLM simulations in the order of minutes. This type of aerodynamic analysis is usually perceived as a low-fidelity model.

*Parametrization*

The shape of the CRM wing is modified by changing its twist distribution. As with the RAE 2822 test case, the wing twist is parametrized using the FFD method. However, instead of displacing each point individually, all the control points of a given cross-section are rotated in unison in order to modify the wing twist. This rotation is centered around the local quarter-chord line of the wing as shown in Figure 4.8. For this dissertation, two twist parametrizations are considered with numbers of design parameters $b = 2$ and $b = 5$ respectively. The first parametrization modifies the twist at both the root and tip of the wing using a $2 \times 2 \times 2$ FFD box. The second parametrization uses instead a $2 \times 5 \times 2$ FFD box with a total of 5 twist stations distributed equally between the wing root and tip (see Figure 4.8). In both design parametrizations, the twist modifications are limited to $\pm 2°$ and $\pm 5°$ at the wing root and tip respectively, with a linear variation in between. Also, the flow conditions are kept fixed at $\alpha = 2°$, $Re_\infty = 5 \times 10^6$, and $M_\infty = 0.85$.

*Fidelity Levels*

To provide the MA-ROM method with results of different fidelity, three fidelity levels are defined for the CRM wing with varying accuracy and cost. The levels are the following:

**W1 -** RANS CFD simulation using a baseline grid (3.6M nodes);

**W2 -** RANS CFD simulation using a coarse grid (450K nodes);

**W3 -** VLM simulation using a thin wing representation (5,015 vortex panels).

The W1 fidelity level is considered the high-fidelity level and the other two fidelity are used as an auxiliary source of data for multi-fidelity modeling. The computational costs of these fidelity levels have been measured on an Intel Xeon E5-2698 CPU and are listed in Table 4.6. This table also provides the grid sizes of these simulations that are in part responsible for the computational cost differences between the levels. For the sake of completeness, the discretization of the CRM wing surface is also made available since this experiment will focus on the prediction of aerodynamic loads.

The W2 and W3 levels are 28 and 17,000 times faster respectively to evaluate than the W1 level, which represents a much larger relative cost difference between the fidelity levels compared to the RAE 2822 test case. It should also be mentioned that the grids of each fidelity levels are of different sizes such that their field results have inconsistent dimensionalities. In the case of the W3 fidelity level, the computed fields also have an inconsistent topology with respect to the other two fidelity levels since the CRM wing is represented as a thin surface in a VLM simulation. In transonic flow conditions, a RANS simulation will likely display shocks while a VLM analysis will not, thus making the results from W1 and W3 fidelity further inconsistent in terms of field features. For the above reasons, the combination of the W1 and W3 fidelity levels represents arguably an extreme multi-fidelity scenario for the MA-ROM

**Table 4.6:** Description of the various fidelity levels for the CRM wing test case.

| Fidelity | Physics | Grid Size | | Cost/Sample [CPU-hr]* |
|---|---|---|---|---|
| | | Volume | Surface | |
| W1 | RANS | $3.6 \times 10^6$ | 45,177 | 91.20 |
| W2 | RANS | $450 \times 10^3$ | 11,325 | 3.233 |
| W3 | VLM | - | 4,872† | $5.37 \times 10^{-3}$ |

*CPU times are based on an Intel Xeon E5-2698 CPU

†Number of vortex panels in the VLM model

method, and we do not expect it to perform strongly. Nonetheless, the W1 and W3 fidelity combination is included in this experiment to demonstrate the lower bound of the multi-fidelity performance of the proposed method.

## 4.3 Model Performance Metrics

The performance of the proposed multi-fidelity method is assessed by comparing its accuracy and training cost to an equivalent single-fidelity model. The following section defines the metrics used in this dissertation to quantify the accuracy and cost of single- and multi-fidelity ROMs.

### 4.3.1 Field Prediction Error

The main metric to quantify the accuracy of a surrogate model is the *field prediction error* that represents the differences between the actual and predicted fields. Given a design sample not used during the training phase of the model and with an exact solution $\mathbf{x}_j \in \mathbb{R}^d$, we define the sample prediction error as

$$e(\mathbf{x})_j = \|\mathbf{x}_j^* - \widetilde{\mathbf{x}}_j\|_2 \tag{4.1}$$

where $\widetilde{\mathbf{x}}_j \in \mathbb{R}^d$ is the ROM prediction corresponding to $\mathbf{x}_j^*$. Here, we use the $L^2$-norm of the error field to provide an integrated measure of the prediction error for a given sample. Let us then consider a verification dataset containing $n_t$ test samples, the global prediction error of the model is computed using the Root-Mean-Square (RMS) of Eq. (4.1) such that

$$E(\mathbf{x}) = \sqrt{\frac{\sum_{j=1}^{n_t} \|\mathbf{x}_j^* - \widetilde{\mathbf{x}}_j\|_2^2}{n_t}} \tag{4.2}$$

Note that the magnitude of $E(\mathbf{x})$ is dependent on the field quantity being considered. To compare errors between different design problems, we also define a normalized prediction error given by

$$\widehat{E}(\mathbf{x}) = \frac{E(\mathbf{x})}{\sqrt{\sum_{j=1}^{n_t} \|\mathbf{x}_j^* - \overline{\mathbf{x}}\|_2^2 / n_t}} \tag{4.3}$$

It is worth noting that the normalization term used in Eq. (4.3) is essentially the total standard deviation of the testing dataset. As a result, the definition of $\widehat{E}(\mathbf{x})$ represents the ratio between the variation of $\mathbf{x}$ unexplained by the ROM and the total variation of the data.

Recognizing that a non-intrusive ROM is essentially a combination between a dimensionality reduction model and a regression model, we decompose the prediction error into a *reconstruction* and a *regression* component. We define the reconstruction error as the discrepancy linked to the mapping between the latent and physical spaces, or in the case of POD, the error associated with the accuracy of the POD basis. Loosely speaking, it represents the information lost due to the compression of the high-dimensional data into a handful of latent variables. The RMS of the reconstruction error is given by

$$E_{\text{rc}}(\mathbf{x}) = \sqrt{\frac{\sum_{j=1}^{n_t} \|(\mathbf{I} - \boldsymbol{\Phi}_k \boldsymbol{\Phi}_k^T)\mathbf{x}_j^*\|_2^2}{n_t}} \tag{4.4}$$

Note that $E_{\text{rc}}(\mathbf{x})$ is different from the reconstruction residual $\varepsilon$ defined in Eq. (3.7).

The former is computed from previously unseen data, while the latter is associated with the training dataset.

As for the regression error, it is characterized as the discrepancies in the latent space between the actual and predicted latent coordinates. In other words, it is caused by the inaccuracies of the underlying regression models $\mathbf{g}(\mathbf{p})$. We define the RMS of the regression error as

$$E_{\mathrm{rg}}(\mathbf{x}) = \sqrt{\frac{\sum_{j=1}^{n_t} \|\boldsymbol{\Phi}_k(\boldsymbol{\Phi}_k^T \mathbf{x}_j^* - \widetilde{\mathbf{z}}_j)\|_2^2}{n_t}} \tag{4.5}$$

where $\widetilde{\mathbf{z}}_j$ is the predicted latent space coordinates corresponding to $\mathbf{x}_j^*$.

One can also view the reconstruction and regression errors as being the components of the prediction error that are respectively perpendicular and aligned with the POD subspace. Since both of these components are orthogonal to each other, it can be shown that $E_{\mathrm{rc}}(\mathbf{x})$ and $E_{\mathrm{rg}}(\mathbf{x})$ can be combined into $E(\mathbf{x})$ as follows

$$E(\mathbf{x}) = \sqrt{E_{\mathrm{rc}}(\mathbf{x})^2 + E_{\mathrm{rg}}(\mathbf{x})^2} \tag{4.6}$$

For additional details, the above relation is demonstrated in Appendix A.

### 4.3.2 Integrated Scalar Error

While the main purpose of a ROM is to predict fields, its result can also be used to compute other integrated quantities as previously mentioned in Section 1.2.2. For example, in aerodynamic problems, one can integrate the pressure and skin friction distributions into aerodynamic coefficients. In addition to considering the errors of predicted fields, it is worth taking into account the consequences of these inaccuracies on derived quantities. For the current test cases, these are aerodynamic quantities such as lift, drag, and pitching moment.

Let us consider the lift coefficient $C_L$, we quantify the prediction error of this

integrated quantity with

$$E(C_L) = \sqrt{\frac{\sum_{j=1}^{n_t} \left( C^*_{L,j} - \widetilde{C}_{L,j} \right)^2}{n_t}} \tag{4.7}$$

where $C^*_{L,j}$ is the lift coefficient of the $j$-th test sample computed with the actual CFD solution, while $\widetilde{C}_{L,j}$ is the corresponding coefficient obtained from the predicted field. The formulation of Eq. (4.7) also applies to other aerodynamic quantities such as the drag coefficient $C_D$ or the pitching moment $C_{Mz}$. For the transonic wing test case, the root bending moment $C_{My}$ is also of interest since it has a direct impact on the structural design.

It should be mentioned that the above aerodynamic coefficient can be decomposed into their pressure and skin friction contributions. For instance, the drag coefficient $C_D$ can be divided into $C_{Dp}$ and $C_{Df}$ for its pressure and friction components respectively. This decomposition facilitates the error quantification associated with either the pressure and skin friction distributions.

### 4.3.3 Computational Training Cost

Recall that the computational cost of a surrogate model can be separated into its evaluation and training costs. The former designates the cost of predicting new results and should be negligible. Therefore, we focus on the training component that itself can be divided into the cost of making the model and the cost of generating the training data. Depending on the size of the data, the modeling choices, and the computer hardware being used, creating a ROM can take anywhere from less than a minute to a few hours. In comparison, a single CFD simulation will require a handful of hours to complete on a cluster composed of multiple CPUs, meaning that a dataset of tens of cases can take days. The data generation is responsible for nearly all of the upfront training cost of a ROM, at least in practical engineering problems. In

the context of this dissertation, we focus on the data generation cost when referring to the training cost of a ROM, omitting the costs of creating the model itself. Note that for a multi-fidelity model, the training cost is the compounded cost of generating both the high- and low-fidelity datasets.

The generation of training data is typically a parallelizable task. For one, the individual simulations can be distributed over many CPUs to accelerate their completion. For another, each case in a DoE need not be run sequentially, and one can batch multiple simulations together if the computing resources are available. Consequently, the actual time (or *wall-time*) to complete all the simulations is highly dependent on how the process is parallelized. A more meaningful measure of the training cost is the CPU time, usually in CPU-hr, which is the total amount of computational time used by each processing unit involved. The CPU time can then be divided by the number of CPUs available to obtain an estimate of the wall-time, neglecting any performance loss from the parallelization. For the current thesis, since the simulation time of each design within a DoE varies, a constant cost is assumed for each sample of the airfoil and wing use cases. The corresponding CPU times were presented in Tables 4.4 and 4.6 respectively. The total training cost of ROMs in this study is then taken as the number of training samples times the constant cost per sample.

Although we mostly use the CPU time to quantify the computational cost of a model, it is worth mentioning that one can also give a monetary value to this metric. Computing facilities typically define a rate in \$/CPU-hr that incorporates various operational factors such as equipment acquisition, energy costs, server utilization, etc. For instance, at the time of this writing, some compute-optimized nodes can be rented from the Amazon Web Services for prices starting at \$0.034 per CPU-hr [5]. When considering a large scale and high-fidelity simulation, generating a sizable training dataset can easily amount to thousands of dollars.

# CHAPTER 5
# EXPERIMENTS AND RESULTS

Having outlined the research formulation of this work, the following chapter presents experiments to answer our research questions and discusses the obtained results. More specifically, we first study the multi-fidelity performance of the MA-ROM method using the RAE 2822 airfoil and the CRM wing test cases. This is followed by an investigation of the effect of inconsistent representations on the accuracy of the proposed method. Finally, predictions of the MA-ROM method and existing multi-fidelity ROM methods are compared on applications with consistent high- and low-fidelity fields.

## 5.1 Experiment 1: Multi-Fidelity Performance with Transonic Airfoil

The goal of the following experiments is to assess the multi-fidelity performance, in terms of accuracy and cost, of the MA-ROM method using the RAE 2822 test case. As discussed in Section 4.2.1, we use the RAE 2822 geometry since it is representative of the aerodynamic design seen on modern transonic aircraft. Despite being a 2D problem with a relatively low computational cost, the CFD analysis of a transonic airfoil exhibits the same complex physics observed in larger-scale problems. Also, the low cost of this test case facilitates the data generation and allows us to explore many model configurations with different training datasets, design parametrizations, and fidelity combinations. For these reasons, other authors have also considered this airfoil in their work on reduced-order modeling (see Table 2.1).

The results of these experiments are intended to answer Research Question 1 and to corroborate the related Hypotheses 1.1 and 1.2. To cover many training scenarios, this section presents and discusses the prediction error and training cost of various

MA-ROM configurations, i.e., with different sizes of training data, ratios of high- and low-fidelity results, choices of fidelity levels, numbers of design parameters, etc. We then compare the performance of MA-ROM and an equivalent single-fidelity ROM to verify if the proposed method can truly provide improved predictions at a lower overall cost.

### 5.1.1 Problem Setup

To measure the model accuracy, large datasets of 2,500 CFD simulations of the RAE 2822 airfoil are compiled for each fidelity levels listed in Table 4.4 and each parametrization listed in Table 4.3. These samples are selected using a LHS design. For a given model configuration, a subset of $n$ training cases is randomly selected from the dataset of the A1 fidelity level and is used to train a conventional ROM. For the training of a MA-ROM, the same $n$ cases and an additional $m - n$ cases are selected from one of the auxiliary datasets corresponding to the A2 or A3 fidelity level. For the single-fidelity ROM, values of $n$ ranging from 10 to 1,000 are evaluated. As for the multi-fidelity MA-ROM, the value of $m$ is scaled proportionally with $n$ via the multi-fidelity ratio $\tau = m/n$. Ratios of $\tau = 2$, 4, and 8, are considered together with the limit $m \leq 1,200$.

Once the training is complete, we then use the remaining cases from the high-fidelity dataset as a testing set to measure the prediction error for both the ROM and MA-ROM models. Since each CFD dataset contains 2,500 samples and at most 1,000 are used for the training, the created models are tested with a minimum of 1,500 test samples. This process is repeated at least 100 times for each model configuration with different training and testing sets, and the average prediction error is recorded for each configuration. These repetitions are to ensure the presented results are not biased toward a specific selection of training samples, but rather provide a general expectation of the ROM and MA-ROM performance.

Also, when applying the POD on both the high- and low-fidelity datasets, the criterion RIC $\geq$ 99.9999% (see Eq. (3.9)) is used for all the models to select the number of POD modes $k$. This high RIC value ensures that the generated single- and multi-fidelity ROMs fully exploit the information available in the provided data and keep the training error to a minimum, even if this results in slightly larger models. Note that choosing a high RIC is common in the ROM literature and some authors even elect to preserve all the POD modes [47], essentially resulting in RIC = 100%.

### 5.1.2 Prediction of Pressure Field

In this section, we present the results regarding the field prediction error of MA-ROM. More specifically, we examine the metric $\widehat{E}(C_P)$, i.e., the normalized field prediction error of the coefficient of pressure $C_P$ in the two-dimensional flow field surrounding the RAE 2822. We first focus on the field solutions for an airfoil parametrization with three design parameters, i.e., with $b = 3$. Section 5.1.4 later considers scenarios with higher-dimensional inputs. The averaged $\widehat{E}(C_P)$ for the single-fidelity ROM and the MA-ROM methods as a function of $n$ and the total training cost are shown in Figures 5.1 and 5.2. The former figure shows the multi-fidelity results joining the A1 (baseline RANS CFD) and A2 (coarse RANS CFD) fidelity levels, while the latter presents the results of combining the data of the A1 and A3 (coarse inviscid CFD) fidelity levels.

For all considered model configurations, Figures 5.1 and 5.2 shows an exponential decrease in $\widehat{E}(C_P)$ as we provide more training data. We observe that augmenting the high-fidelity data with either of the lower-fidelity datasets yields a consistent reduction in $\widehat{E}(C_P)$ for a given $n$ in all multi-fidelity cases. We further note that increasing $\tau$ improves the accuracy of the multi-fidelity method, although it appears that this improvement slowly stalls with increasing $\tau$. Comparing Figures 5.1 and 5.2 side-by-side, we observe that the overall performance of MA-ROM is higher when

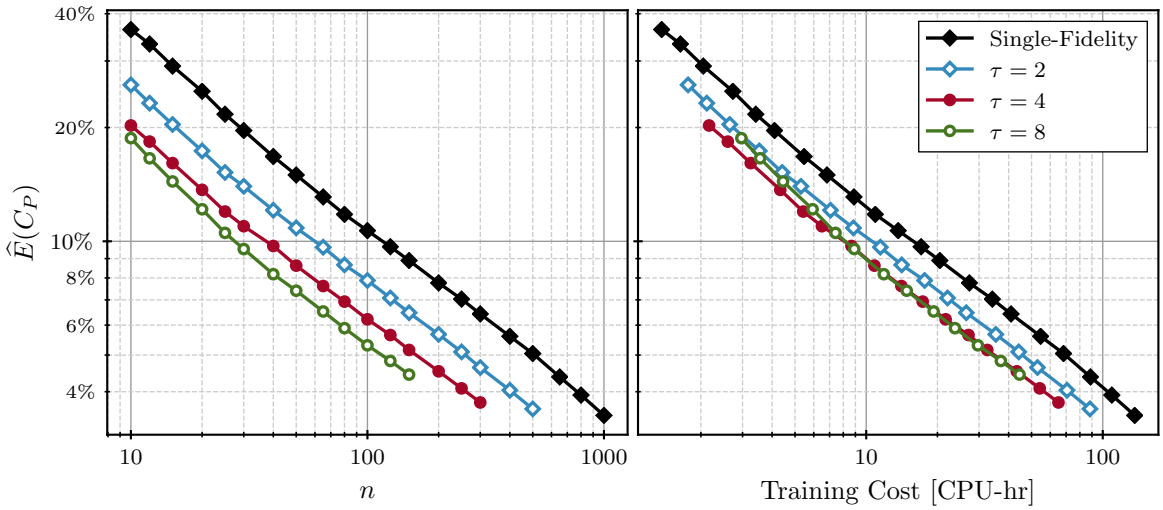


**Figure 5.1:** Normalized prediction error of the RAE 2822 flow field $C_P$ distribution for the A1 + A2 fidelity combination, and the $b = 3$ parametrization.

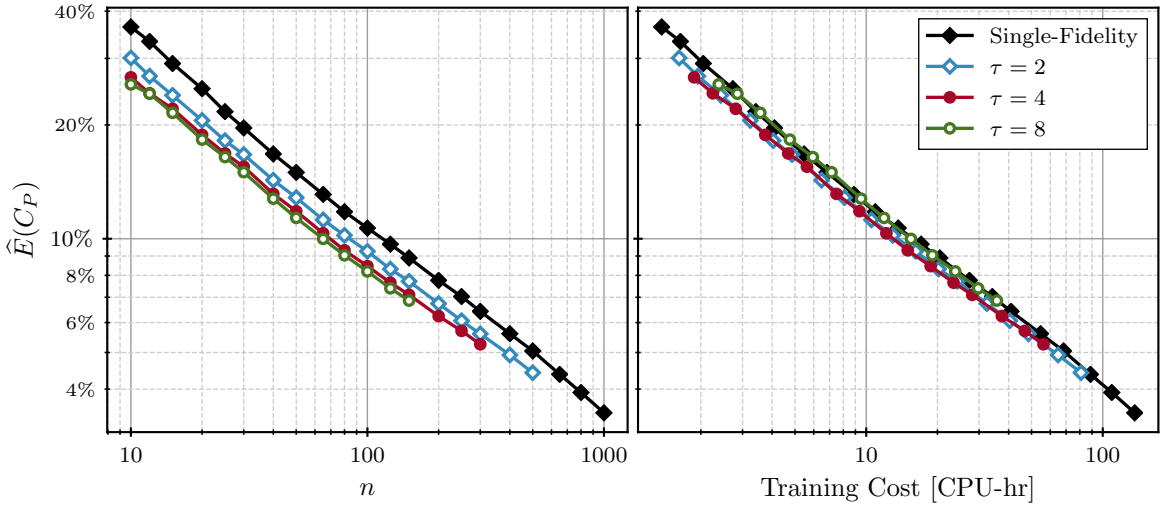


**Figure 5.2:** Normalized prediction error of the RAE 2822 flow field $C_P$ distribution for the A1 + A3 fidelity combination, and the $b = 3$ parametrization.

augmenting the high-fidelity results with the A2 rather than the A3 fidelity level. When compared to the A2 fidelity, a simpler physical model and coarser grid are used for the aerodynamic analysis of the RAE 2822 with the A3 fidelity level. Its connection with the high-fidelity data is expected to be weaker, and in turn, hinders the multi-fidelity performance of MA-ROM. Nonetheless, the overall performance of the MA-ROM method combining both the A1 and A3 fidelity levels remains better than a conventional ROM model using the A1 fidelity level alone.

To understand better the effects of the proposed multi-fidelity method, Table 5.1 offers a closer look at some of the results shown in Figure 5.1. For the current test case, we see from Table 5.1 that for a conventional ROM, the normalized regression error $\widehat{E}_{\text{rg}}(C_P)$ is the dominant contributor to $\widehat{E}(C_P)$. Although high for small $n$, the reconstruction error $\widehat{E}_{\text{rc}}(C_P)$ is quickly reduced by increasing the training data size which allows for additional and more accurate POD modes. This is consistent with the high RIC criterion chosen for this study. As discussed in Section 3.4, a MA-ROM trained with a comparable number of high-fidelity data, say $n = 100$, will rely on an equivalent POD basis for the high-fidelity field reconstruction. It will accordingly have a similar $\widehat{E}_{\text{rc}}(C_P)$ than a single-fidelity model. However, the governing idea of MA-ROM is to enrich the latent space with low-fidelity data to improve the prediction of the latent space coordinates. The results of Table 5.1 support this statement and indeed show a clear reduction in $\widehat{E}_{\text{rg}}(C_P)$ with additional low-fidelity data. In contrast, $\widehat{E}_{\text{rc}}(C_P)$ remain more or less the same, yet at a low value.

In practice, the availability of training data is limited by the amount of computing resources at one's disposal. Figures 5.1 and 5.2 also provide the prediction errors of the MA-ROM method as a function of the computational cost to generate the training data, taking into account the size of both the high- and low-fidelity datasets. The training cost is measured in terms of CPU time and uses the cost per sample listed in Table 4.4. With the A2 data as the low-fidelity fields, the results of Figure 5.1 indicate

**Table 5.1:** Detailed breakdown of the $C_P$ field prediction error for the RAE 2822 test case and the $b = 3$ parametrization.

| Fidelity | $n$ | $\tau$ | $m$ | $k$ | $\widehat{E}(C_P)$ | $\widehat{E}_{\mathrm{rc}}(C_P)$ | $\widehat{E}_{\mathrm{rg}}(C_P)$ |
|---|---|---|---|---|---|---|---|
| A1 | 10 | - | - | 9 | 36.3% | 16.2% | 32.4% |
| | 100 | | | 58 | 10.7% | 1.06% | 10.6% |
| | 1000 | | | 92 | 3.46% | 0.14% | 3.46% |
| A1 + A2 | 100 | 2 | 200 | 58 | 7.88% | 1.11% | 7.80% |
| | | 4 | 400 | 58 | 6.22% | 1.10% | 6.11% |
| | | 8 | 800 | 58 | 5.31% | 1.10% | 5.19% |
| A1 + A3 | 100 | 2 | 200 | 58 | 9.26% | 1.12% | 9.19% |
| | | 4 | 400 | 58 | 8.46% | 1.07% | 8.39% |
| | | 8 | 800 | 58 | 8.20% | 1.10% | 8.12% |

that the MA-ROM method can provide a significant reduction in the training cost over a single-fidelity approach for a prescribed $\widehat{E}(C_P)$. As for the data of Figure 5.1, we once again observe that the A3 fidelity level offers a more modest multi-fidelity improvement. In both cases, the cost of multi-fidelity models with $\tau = 8$ seems to be similar or worse than models with $\tau = 4$. This suggests there is a practical limit to the amount of information that the low-fidelity data can convey to the high-fidelity predictions.

To better establish the potential cost savings that the MA-ROM method can offer, Table 5.2 compares the total training cost of both single-fidelity ROMs and MA-ROMs for a target $\widehat{E}(C_P)$ value. These costs are estimated via a log-linear interpolation of the results of Figures 5.1 and 5.2. The values in Table 5.2 show that with $\tau = 4$, a MA-ROM fusing the A1 and A2 fidelity levels requires 68% less high-fidelity samples than an equivalently accurate ROM using the A1 data only. This translates into 49% less CPU time for the multi-fidelity model. Using the A3 in place of the A2 fidelity level, the cost savings for $\tau = 4$ are cut down to 18% less CPU time for the

same target $\widehat{E}(C_P)$. It is worth noting that with the A1 + A2 results, there are no appreciable benefits of using $\tau$ values greater than four. In fact, with the A1 and A3 fidelity combination, the results with $\tau = 8$ are noticeably worse than with $\tau = 4$. Turning around the comparison, Table 5.3 presents the estimated $\widehat{E}(C_P)$ for a target training cost. In this scenario, the data shows that for an equivalent CPU time, the $C_P$ field predicted by a single-fidelity ROM trained with the A1 fidelity only is up to 29% less accurate than a MA-ROM enhanced with the A2 fidelity level. Even with the A3 rather than the A2 fidelity level, the multi-fidelity ROM offers up to 8.7% better predictions given the same computational budget. Once again, the results of Table 5.3 indicates that for the current application, there is little to no benefit in using $\tau > 4$.

To complement the previous results, Figure 5.3a offers a visualization of the actual $C_P$ field of the RAE 2822 for a notional design point. This solution is compared to the field predicted by a single-fidelity ROM with $n = 100$ in Figure 5.3b together with the discrepancy field between the actual and predicted results. Figures 5.3c and 5.3d then provide the corresponding visualizations for MA-ROMs trained with the same $n$ high-fidelity samples and with $m = 400$ additional low-fidelity results. The former figure uses the A2 fidelity level for the low-fidelity data, while the latter uses the A3 fidelity level. We should note that the test sample selected for these visualizations have a sample prediction error comparable to the average results of Table 5.1 for a similar model configuration. If the reader is interested in visualizing the results for the test samples having the lowest and highest error, these are made available in Appendix B.1. From the aforementioned figures, we observe that the single- and multi-fidelity ROMs can reproduce the pressure field around the RAE 2822 with reasonable accuracy. A glance at the error fields of Figure 5.3 also reveals that the majority of the field prediction error is concentrated near a strong shock on the airfoil's upper surface in all the considered scenarios. It is a known fact that POD-based

**Table 5.2:** Estimated training cost of single- and multi-fidelity ROMs given a target prediction error. Results are for the RAE 2822 test case with a $b = 3$ parametrization. Results in parentheses indicate percent change with respect to an equivalent single-fidelity ROM.

| Target $\widehat{E}(C_P)$ | $b$ | Fidelity | $\tau$ | $n$ | CPU-hr |
|---|---|---|---|---|---|
| 10% | 3 | A1 | - | 116 | 15.8 |
| 10% | 3 | A1 + A2 | 2 | 60 ($\downarrow$ 48%) | 10.6 ($\downarrow$ 33%) |
| | | | 4 | 37 ($\downarrow$ 68%) | 8.01 ($\downarrow$ 49%) |
| | | | 8 | 27 ($\downarrow$ 77%) | 8.01 ($\downarrow$ 49%) |
| 10% | 3 | A1 + A3 | 2 | 84 ($\downarrow$ 28%) | 13.6 ($\downarrow$ 14%) |
| | | | 4 | 69 ($\downarrow$ 41%) | 12.9 ($\downarrow$ 18%) |
| | | | 8 | 65 ($\downarrow$ 44%) | 15.5 ($\downarrow$ 2.4%) |

**Table 5.3:** Estimated prediction error of single- and multi-fidelity ROMs given a target training cost. Results are for the RAE 2822 test case with a $b = 3$ parametrization. Results in parentheses indicate percent change with respect to an equivalent single-fidelity ROM.

| Target CPU-hr | $b$ | Fidelity | $\tau$ | $n$ | $\widehat{E}(C_P)$ |
|---|---|---|---|---|---|
| 20 | 3 | A1 | - | 147 | 8.99% |
| 20 | 3 | A1 + A2 | 2 | 113 | 7.42% ($\downarrow$ 17%) |
| | | | 4 | 92 | 6.46% ($\downarrow$ 28%) |
| | | | 8 | 67 | 6.41% ($\downarrow$ 29%) |
| 20 | 3 | A1 + A3 | 2 | 124 | 8.36% ($\downarrow$ 7.0%) |
| | | | 4 | 107 | 8.21% ($\downarrow$ 8.7%) |
| | | | 8 | 84 | 8.84% ($\downarrow$ 1.6%) |

ROMs tend to struggle with the prediction of discontinuities such as shock waves [92], and the current visualizations support this. Despite this limitation, predictions from the proposed MA-ROM method offer an error field that is both narrower and of lower intensity near this discontinuity, thus capturing the shock more accurately. We also note that the error field for the MA-ROM method using the A1 + A2 fidelity combination is lower than with the same method using the A1 + A3 fidelity level. This is consistent with the previously discussed results of Figures 5.1 and 5.2. On the whole, the visualizations of Figure 5.3 provide a qualitative validation of the main observations of this experiment.

### 5.1.3 Prediction of Aerodynamic Coefficients

To investigate further the accuracy of the proposed MA-ROM method, the following experiment provides the integrated error of the RAE 2822 aerodynamic coefficients. These coefficients are calculated from the integration of the pressure fields predicted previously in Section 5.1.2 at the airfoil surface for both single- and multi-fidelity ROMs. Namely, we consider the pressure component of the lift, drag, and pitching coefficients, i.e., $C_{Lp}$, $C_{Dp}$, and $C_{Mz,p}$. As in Section 5.1.2, the following multi-fidelity results consider both the A1 + A2 and A1 + A3 fidelity combinations with the $b = 3$ parametrization of the airfoil geometry. It is worth noting that in the current experiment, our single- and multi-fidelity ROMs predict the pressure of the entire flow field, while only the surface results are integrated into aerodynamic coefficients. Therefore, the models are not specifically optimized for accurate surface predictions. In practice, one could instead train a ROM to predict the surface pressure only for more accurate estimates of $C_{Lp}$, $C_{Dp}$, and $C_{Mz,p}$. This is unnecessary for the current study since we are interested in measuring the relative improvement of MA-ROM over a single-fidelity model.

The $C_{Lp}$, $C_{Dp}$, and $C_{Mz,p}$, errors as a function of the amount of training samples $n$

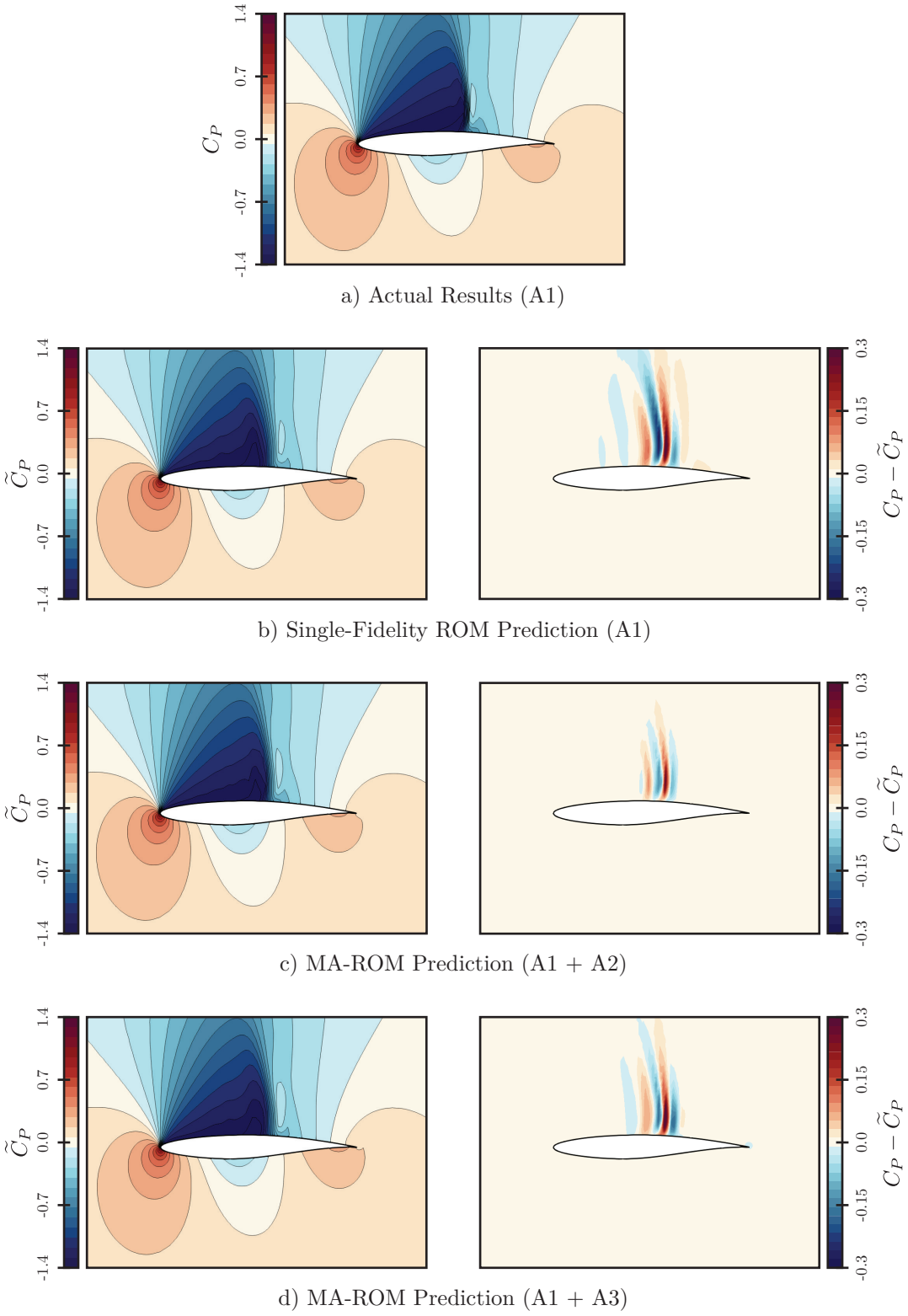


**Figure 5.3:** Comparison of the predicted $C_P$ field (left) and its error (right) with respect to the actual solution for both single- and multi-fidelity ROMs. Results are for the RAE 2822 test case with $n = 100$, $\tau = 4$ (MA-ROM only), and $b = 3$.

**Table 5.4:** Global statistics of the aerodynamic coefficients computed from the A1 fidelity results for the RAE 2822 test case with a $b = 3$ parametrization.

| | $C_{Lp}$ | $C_{Dp}\,[10^4]$ | $C_{Mz,p}$ |
|---|---|---|---|
| Mean | 0.6122 | 92.39 | -0.2426 |
| Minimum | 0.0542 | 20.67 | -0.3558 |
| Maximum | 1.0155 | 334.0 | -0.1242 |
| Std. Deviation | 0.2200 | 75.88 | 0.0713 |

and the multi-fidelity ratio $\tau$ are shown in Figures 5.4, 5.5, and 5.6 respectively. For each of these figures, the left and right sides display the results for the A1 + A2 and A1 + A3 fidelity combinations. To provide some perspective regarding the physical meaning of these results, Table 5.4 presents some key statistics regarding the lift and drag from the CFD dataset of 2,500 cases used for both the training and testing of the single- and multi-fidelity ROMs. From the left side of Figures 5.4 to 5.6, we note that the MA-ROMs combining the A1 and A2 fidelity can better predict the aerodynamic coefficients of the RAE 2822 airfoil than single-fidelity ROMs with the same number of high-fidelity samples. Unlike for the field prediction error, the relative multi-fidelity improvement of the method is not constant with $n$ and tends to be larger for small training datasets. At large $n$, the error trends appear to converge to the single-fidelity errors. Admittedly, at that point, the evaluation error for either $C_{Lp}$, $C_{Dp}$, and $C_{Mz,p}$, becomes reasonably small, at least for design purposes. As with the prediction of the $C_P$ field, the values of $E(C_{Lp})$, $E(C_{Dp})$, and $E(C_{Mz,p})$, are improved when the MA-ROMs are provided with more low-fidelity data, although there is no significant benefit of using more than $\tau = 4$. Regarding the A1 and A3 fidelity combination, the results presented on the right side of the aforementioned figures indicate that the data from the A3 fidelity level do not appreciably improve the computation of the RAE 2822 aerodynamic coefficients. While the values of $E(C_{Lp})$, $E(C_{Dp})$, and

$E(C_{Mz,p})$, are barely smaller than those of a single-fidelity model at small $n$, the multi-fidelity improvement quickly becomes negligible with additional training data. For large $n$, the MA-ROM error with the A1 + A3 fidelity combination is even slightly worse than that of a conventional ROM.

For additional insights on the multi-fidelity prediction of $C_{Lp}$, $C_{Dp}$, and $C_{Mz,p}$, some of the results of Figures 5.4, 5.5, and 5.6, are detailed in Table 5.5. We can see that with $\tau = 4$ and the A1 + A2 fidelity combination, the prediction error on the lift is reduced by 80% at $n = 10$. For the same configuration, the errors on the drag and pitching moment are reduced by 59% and 69% respectively. However, this impressive improvement is reduced to 15%, 39%, and 23% for $C_{Lp}$, $C_{Dp}$, and $C_{Mzp}$ respectively at $n = 300$. In comparison, the multi-fidelity performance of the MA-ROM method with the A1 + A3 fidelity combination is overall weaker than with the A1 + A2 combination. The multi-fidelity results for $n = 300$ are up to 17% worse than for a single-fidelity ROM trained with the same high-fidelity samples. We should note that in the same situation, the results of Section 5.1.2 showed that the $C_P$ predictions of the MA-ROM method were actually better than those of a single-fidelity ROM. However, the results of Table 5.5 demonstrates that the higher accuracy of the $C_P$ field prediction does not necessarily guarantee a more precise integration of the field into aerodynamic coefficients.

### 5.1.4 Effect of Input Space Dimensionality

Having demonstrated the effectiveness of MA-ROM on a parametrization with three design parameters, the following section extends the previous analysis to applications with higher-dimensional input spaces. As such, the proposed multi-fidelity method is applied to the RAE 2822 test case with input space dimensionalities $b = 5$, 7, and 9. The additional design parameters are obtained by adding more control points to the FFD box surrounding the geometry (see Section 4.2.1). For conciseness, we focus on

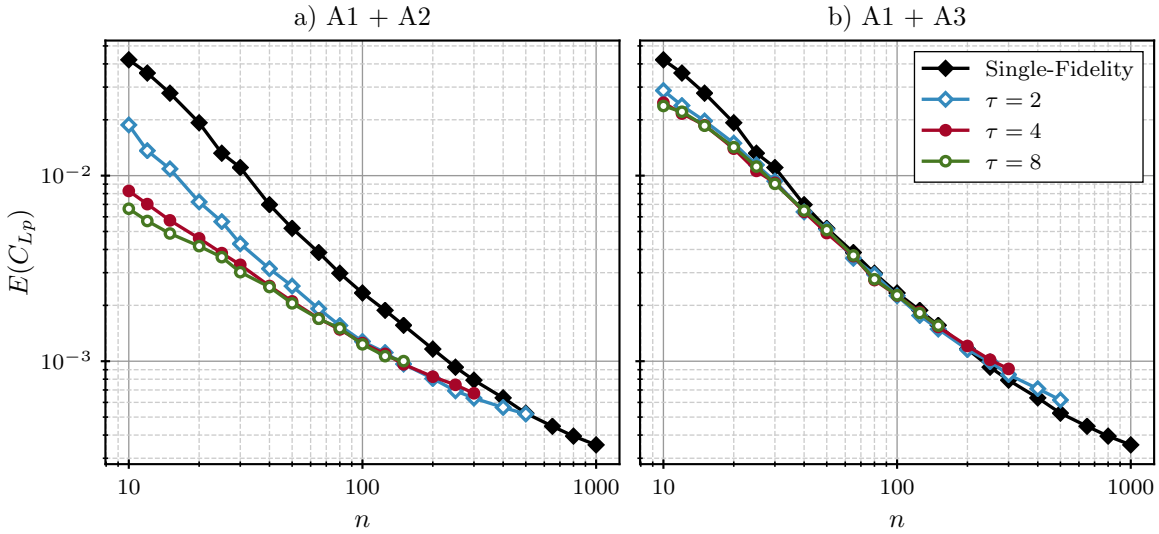


**Figure 5.4:** Lift coefficient errors computed from MA-ROM predictions of the RAE 2822 airfoil surface pressure for the A1 + A2 (a) and A1 + A3 (b) fidelity combinations, and the $b = 3$ parametrization.

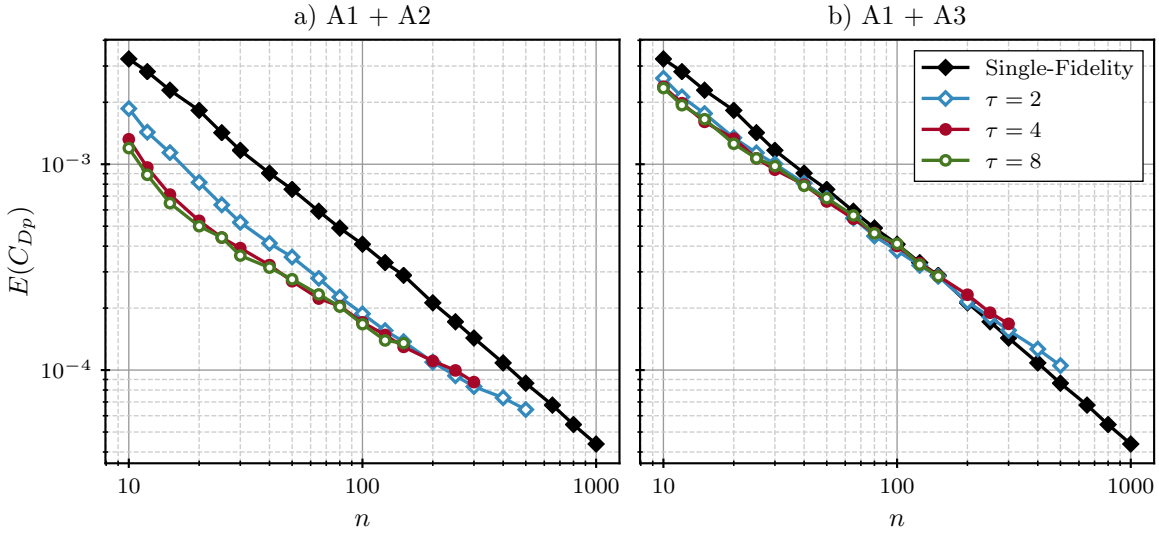


**Figure 5.5:** Drag coefficient errors computed from MA-ROM predictions of the RAE 2822 airfoil surface pressure for the A1 + A2 (a) and A1 + A3 (b) fidelity combinations, and the $b = 3$ parametrization.

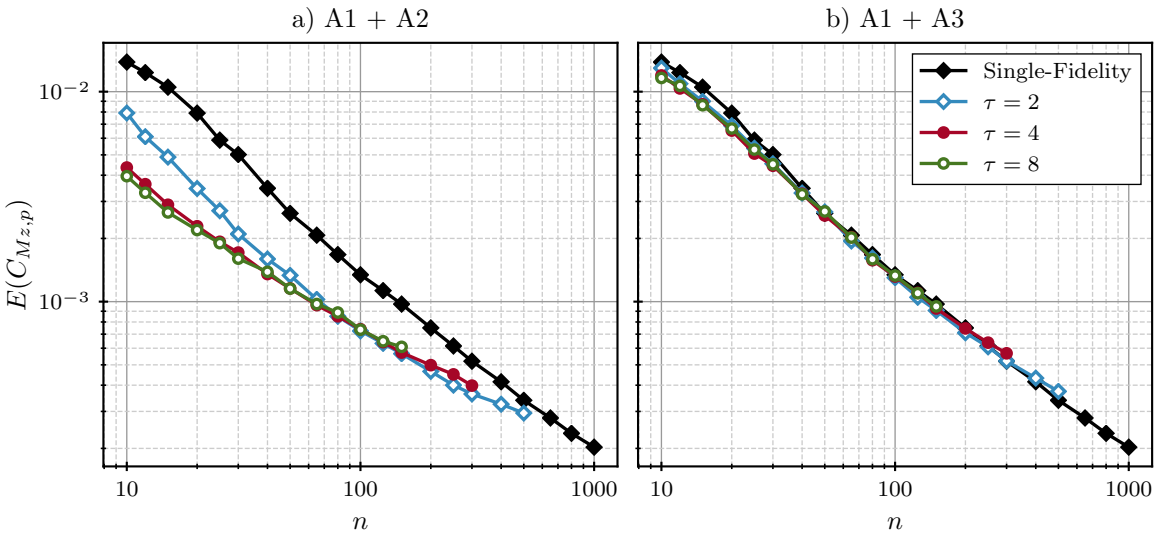


**Figure 5.6:** Pitching moment coefficient errors computed from MA-ROM predictions of the RAE 2822 airfoil surface pressure for the A1 + A2 (a) and A1 + A3 (b) fidelity combinations, and the $b = 3$ parametrization.

**Table 5.5:** Detailed aerodynamic coefficient errors computed from ROM and MA-ROM predictions of the RAE 2822 airfoil $C_P$ distribution for the $b = 3$ parametrization. Results in parentheses indicate percent change with respect to an equivalent single-fidelity ROM.

| Fidelity | $\tau$ | $n$ | $E(C_{Lp})$ [$10^3$] | $E(C_{Dp})$ [$10^4$] | $E(C_{Mz,p})$ [$10^3$] |
|---|---|---|---|---|---|
| A1 | - | 10 | 42.09 | 32.47 | 13.83 |
| | | 100 | 2.332 | 4.087 | 1.342 |
| | | 300 | 0.790 | 1.431 | 0.520 |
| A1 + A2 | 4 | 10 | 8.269 (↓ 80%) | 13.218 (↓ 59%) | 4.352 (↓ 69%) |
| | | 100 | 1.252 (↓ 46%) | 1.705 (↓ 58%) | 0.739 (↓ 45%) |
| | | 300 | 0.672 (↓ 15%) | 0.874 (↓ 39%) | 0.398 (↓ 23%) |
| A1 + A3 | 4 | 10 | 24.71 (↓ 41%) | 23.802 (↓ 27%) | 11.95 (↓ 14%) |
| | | 100 | 2.262 (↓ 3.0%) | 4.007 (↓ 2.0%) | 1.317 (↓ 1.9%) |
| | | 300 | 0.909 (↑ 15%) | 1.677 (↑ 17%) | 0.567 (↑ 9.1%) |

the multi-fidelity combination of the A1 and A2 fidelity only.

The results in Figure 5.7 show the accuracy and cost trade-off of the MA-ROM method when applied to a design problem with 5 to 9 design parameters. Compared to Figure 5.1, we observe an all-around increase in $\widehat{E}(C_P)$ as we consider more design parameters. A slower decrease in the error when adding more training data is also observed for all the presented results. This degradation of both the ROM and MA-ROM performance is consistent with how empirical models generally behave with higher-dimensional input spaces and the so-called *curse of dimensionality*. That being said, the proposed multi-fidelity ROM method continues to provide a substantial reduction in the prediction error compared to an equivalent single-fidelity model. Examining Figures 5.7a, 5.7b, and 5.7c together, we observe a nearly identical trend between $\widehat{E}(C_P)$ and $n$ despite the error magnitude being different on each figure. These trends are also generally equivalent or slightly better than those observed in Figure 5.1 with $b = 3$.

In Figures 5.7b and 5.7c, we further notice an unusually high prediction error for the single-fidelity models at very low $n$ that is not observed on Figures 5.7a and 5.1. This behavior is likely due to the input space having a similar size to the training dataset which leads to *overfitting*. In essence, overfitting occurs in surrogate models when not enough available data are available to support the model complexity such that small variations in the response are mistakenly interpreted as being significant [19]. To resolve this issue, practitioners must either provide more training data or resort to a less expressive model. Interestingly, the multi-fidelity results of Figure 5.7 do not display the same error spike at low $n$ since the models are trained with an effectively larger dataset that includes both high- and low-fidelity data.

For additional insights on the accuracy and cost trade-off of MA-ROM with a larger input space, Tables 5.6 and 5.7 estimate the error and cost reductions that can be achieved for some target accuracy or computational budget. These estimates

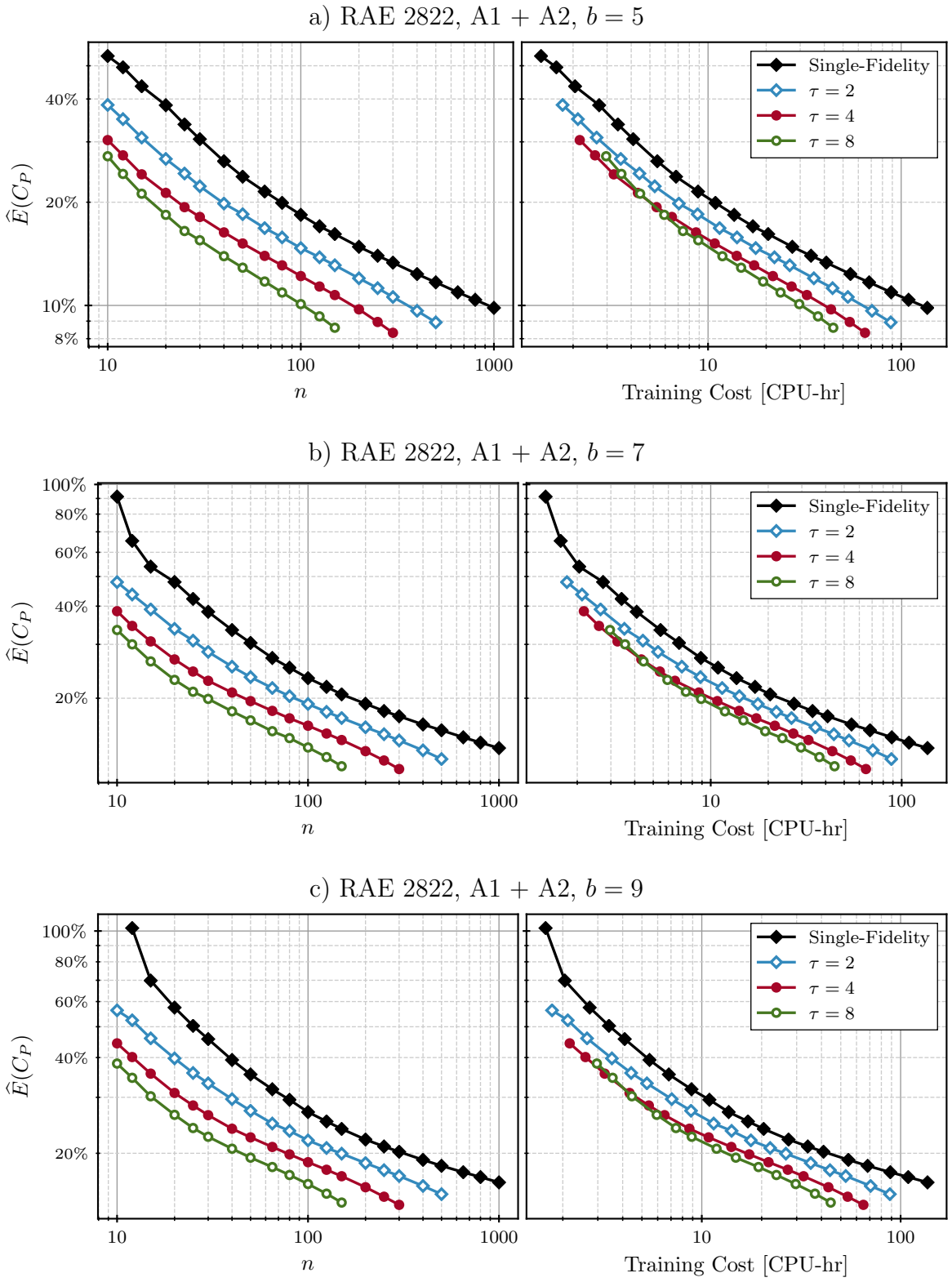


**Figure 5.7:** Normalized prediction error of the RAE 2822 flow field $C_P$ distribution for the A1 + A2 fidelity combination, and the $b = 5$ (a), $b = 7$ (b), and $b = 9$ (c) parametrizations.

are limited to $\tau = 4$ and are obtained from the results of Figure 5.7 via a simple log-linear interpolation. With a target $\widehat{E}(C_P)$ of 15% and $b = 5$, Table 5.6 shows that augmenting the A1 fidelity level with the results of the A2 fidelity can lower the required number of high-fidelity training samples by 73% and consequently decrease the CPU time by 57% when compared to an equivalent single-fidelity model. Almost identical results are also observed for model configurations having higher input dimensionalities and a larger target error to account for the curse of dimensionality. In comparison, Table 5.2 presented a reduction in the cost of 49% for a similar scenario, but with 3 design parameters and a target error of 10%. Fixing the computational budget instead, Table 5.7 shows that when the MA-ROM method is applied to the high-dimensional input cases, a 20% to 23% reduction in the field prediction error can be achieved when compared to an equivalent single-fidelity ROM. This is slightly lower than the 28% presented in Table 5.3 for similar circumstances, yet for $b = 3$.

On the whole, this experiment shows that the accuracy of the MA-ROM method is negatively affected by the addition of more design parameters, as most empirical models are due to the curse of dimensionality. Nevertheless, the relative improvement that the multi-fidelity method offers over an equivalent single-fidelity ROM remains strong, despite the additional design parameters. The percent reduction in both prediction error and training cost witnessed for $b = 9$ are loosely on par with those observed for $b = 3$. Therefore, the proposed MA-ROM method can effectively mitigate the adverse effects of the curse of dimensionality.

### 5.1.5 Summary

The main outcome of this experiment is that the MA-ROM method applied to the RAE 2822 test case has been shown to yield improved performance, in terms of accuracy and training cost, when compared to an equivalent single-fidelity ROM. For instance, by combining the A1 and A2 fidelity levels, the results of this section show

**Table 5.6:** Estimated training cost of single- and multi-fidelity ROMs given a target prediction error. Results are for the RAE 2822 test case with a $b = 5$, 7, and 9 parametrizations. Results in parentheses indicate percent change with respect to an equivalent single-fidelity ROM.

| Target $\widehat{E}(C_P)$ | $b$ | Fidelity | $\tau$ | $n$ | CPU-hr |
|---|---|---|---|---|---|
| 15% | 5 | A1 | - | 192 | 26.2 |
| | | A1+A2 | 4 | 52 ($\downarrow$ 73%) | 11.3 ($\downarrow$ 57%) |
| 20% | 7 | A1 | - | 169 | 23.1 |
| | | A1+A2 | 4 | 46 ($\downarrow$ 73%) | 10.0 ($\downarrow$ 57%) |
| 25% | 9 | A1 | - | 128 | 17.5 |
| | | A1+A2 | 4 | 35 ($\downarrow$ 73%) | 7.58 ($\downarrow$ 57%) |

**Table 5.7:** Estimated prediction error single- and multi-fidelity ROMs given a target training cost. Results are for the RAE 2822 test case with a $b = 5$, 7, and 9 parametrizations. Results in parentheses indicate percent change with respect to an equivalent single-fidelity ROM.

| Target CPU-hr | $b$ | Fidelity | $\tau$ | $n$ | $\widehat{E}(C_P)$ |
|---|---|---|---|---|---|
| 20 | 5 | A1 | - | 147 | 16.3% |
| | | A1+A2 | 4 | 92 | 12.5% ($\downarrow$ 23%) |
| 20 | 7 | A1 | - | 147 | 20.7% |
| | | A1+A2 | 4 | 92 | 16.6% ($\downarrow$ 20%) |
| 20 | 9 | A1 | - | 147 | 24.0% |
| | | A1+A2 | 4 | 92 | 19.1% ($\downarrow$ 20%) |

that multi-fidelity ROMs using the proposed method can be trained with up to 57% fewer computational resources while maintaining the same field prediction accuracy than a conventional ROM. Equivalently, if we fix the computational budget, using the MA-ROM method can reduce the field prediction error by up to 29%. The improved field prediction of the multi-fidelity method also allows for more accurate estimations of integrated aerodynamic coefficients for the lift, drag, and pitching moment of the airfoil. These positive results for both the $C_P$ field and the aerodynamic predictions provide strong evidence for our Hypothesis 1.1. Furthermore, the multi-fidelity benefits of the MA-ROM method were shown to be scalable to applications with additional design parameters. The overall performance of the multi-fidelity ROM would still be negatively affected by a higher-dimensional design space, but the relative improvement compared to a single-fidelity approach would remain more or less the same. This supports our Hypothesis 1.2 stating that the multi-fidelity improvement of the MA-ROM method should be preserved in situations with many design parameters.

While the above results are encouraging, there exist some caveats, and this experiment has also highlighted some potential limitations of the proposed multi-fidelity ROM. For one, as with any multi-fidelity methods, the fidelity of the auxiliary data will affects the performance of MA-ROM. Multi-fidelity ROMs trained using the A2 fidelity level for the auxiliary data offer noticeably better training cost and accuracy than equivalent models trained with the A3 fidelity level. In some scenarios, the MA-ROMs leveraging the A1 + A3 fidelity combination would even perform worse than single-fidelity models training with the A1 data only. For another, given a fixed high-fidelity dataset, adding low-fidelity data will improve the model predictions, but only up to a point. This experiment considered multi-fidelity ratios $\tau$ from 2 to 8, and in most cases, little to no improvement is observed with MA-ROM models using $\tau > 4$. Roughly speaking, this indicates that the amount of information transferable from the low- to the high-fidelity data can become saturated. Ultimately, the lack

of high-fidelity data cannot be entirely remedied with an abundance of low-fidelity results.

## 5.2 Experiment 2: Multi-Fidelity Performance with Transonic Wing

To complement the results of Experiment 1, the following section examines the multi-fidelity performance of the MA-ROM method applied to the CRM wing test case. As mentioned previously in Section 4.2.2, NASA has designed the CRM to be representative of a modern transport aircraft [164], which makes this test case relevant for industrial applications. We focus here on only the wing of the CRM since it is the component that contributes the most to the aerodynamic design of an aircraft. This test case considers a twist parametrization of the wing since twist modifications are relatively frequent during the design process due to uncertainties in the aerodynamic loads and the structural sizing. Also, compared to the previous experiments using the RAE 2822 airfoil, the aerodynamic analysis of the CRM wing requires CFD simulations with a scale and computational cost more representative of an industrial application of reduced-order modeling. Therefore, the secondary purpose of this study is to demonstrate the viability of the proposed method on a realistic design problem.

As in the previous section, multi-fidelity ROMs of the CRM wing are trained with different configurations of training data sizes, fidelity combinations, and parametrizations. The benefits of the proposed method, in terms of accuracy and cost, are then assessed by comparing the results of MA-ROMs and equivalent single-fidelity ROMs. As with Section 5.1, the goal of this experiment is to provide answers to Research Question 1 and to verify the associated Hypotheses 1.1 and 1.2.

### 5.2.1 Problem Setup

The single-fidelity ROMs of the following experiments are trained using a dataset of 400 CFD simulations for the W1 fidelity level. From this data, a subset of $n$

training samples is randomly selected, and the $m - n$ remaining results are used for validation purposes. We consider values of $n$ between 10 and 300 samples that guarantee a minimum of 100 samples for the measurement of the model prediction errors. For the multi-fidelity ROMs, two additional datasets of 1,500 simulations are compiled for both the W2 and W3 fidelity levels. Given a fixed multi-fidelity ratio $\tau$, the high-fidelity data is augmented with $m$ additional samples selected from these datasets. As in Section 5.1.1, the above process is repeated at least 100 times for each model configuration, and the averaged results are reported. These repetitions are to ensure that the evaluation metrics for a given model configuration are not dependent on the specific subset of the training data used. Also, for both single- and multi-fidelity ROMs, the numbers of POD modes are selected using a RIC criterion of at least 99.9999%.

### 5.2.2 Prediction of Surface Pressure Field

We begin this experiment by applying the MA-ROM method to the pressure field prediction of the CRM wing. Unlike the RAE 2822 test case, we only consider the pressure distribution at the wing surface rather than the entire flow field. Most design applications are simply concerned with the prediction of the aerodynamic performance and loads, and these only depend on the surface pressure and shear-stress distributions. Although ROMs are capable of modeling the entire flow field, we focus here on the surface results for the sake of practicality. We present in Figures 5.8 and 5.9 the normalized prediction error $\widehat{E}(C_P)$ of the CRM wing $C_P$ distribution obtained with both the proposed MA-ROM method and a single-fidelity approach. In the first figure, the multi-fidelity ROMs are augmented with the W2 (coarse RANS CFD) fidelity results to better predict solutions of the W1 (baseline RANS CFD) fidelity level. The second figure uses the W3 (VLM) fidelity level as the auxiliary dataset instead. In both cases, the results are for the CRM wing with the $b = 2$

parametrization, i.e., the root and tip twist.

From Figure 5.8, we observe that the predictions from all MA-ROMs using the W1 + W2 fidelity combination are more accurate than those of single-fidelity ROMs at comparable $n$ values. We also note that most of the reductions in $\widehat{E}(C_P)$ are achieved with $\tau = 2$, meaning that the MA-ROM method is quickly saturated with low-fidelity information. Compared to the results of the RAE 2822 test case of Section 5.1.2, the multi-fidelity improvement offered by the proposed method appears overall weaker in the current scenario. However, the cost difference between the W1 and W2 fidelity of the CRM wing problem is relatively larger than the corresponding fidelity levels for the RAE 2822 test case. As a result, the addition of low-fidelity results has a lesser impact on the compounded training cost of the MA-ROM method.

As for the results of Figure 5.9, we see that the accuracy of MA-ROMs with the W1 + W3 fidelity combination and conventional ROMs are more or less the same. This suggests that the results from the W3 fidelity level constitute a poor auxiliary dataset for the field predictions of the W1 fidelity level. It should be noted that the VLM approach used in the W3 fidelity level contains many simplifications that the RANS CFD simulation of the W1 fidelity level does not. For instance, the VLM is based on the potential flow assumption, does not capture shocks, and uses a simplified thin surface representation of the wing. The W1 and W3 levels are very distant in terms of model fidelity and represent an extreme multi-fidelity scenario. With that in mind, the poor multi-fidelity performance displayed in Figure 5.9 is not entirely surprising. These results show that a poor choice of low-fidelity data will, at worse, make the prediction accuracy of the MA-ROM method similar to that of a single-fidelity method. Although, the exceptionally small computational cost of the VLM method is such that the additional low-fidelity samples barely affect the total training cost of the multi-fidelity models.

For a deeper analysis of Figures 5.8 and 5.9, some of the previous prediction errors

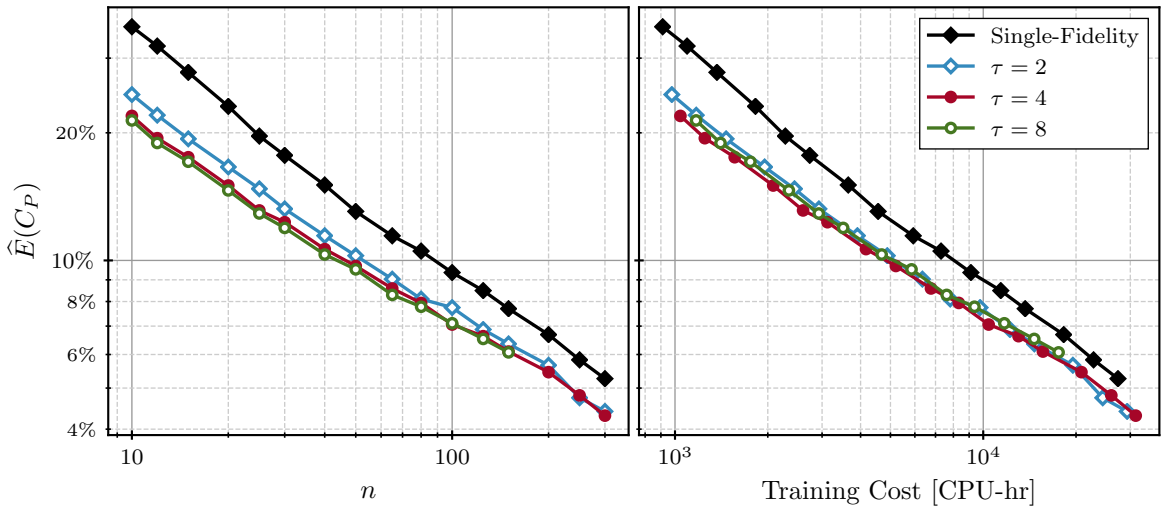


**Figure 5.8:** Normalized prediction error of the CRM wing surface $C_P$ for the W1 + W2 fidelity combination, and the $b = 2$ parametrization.

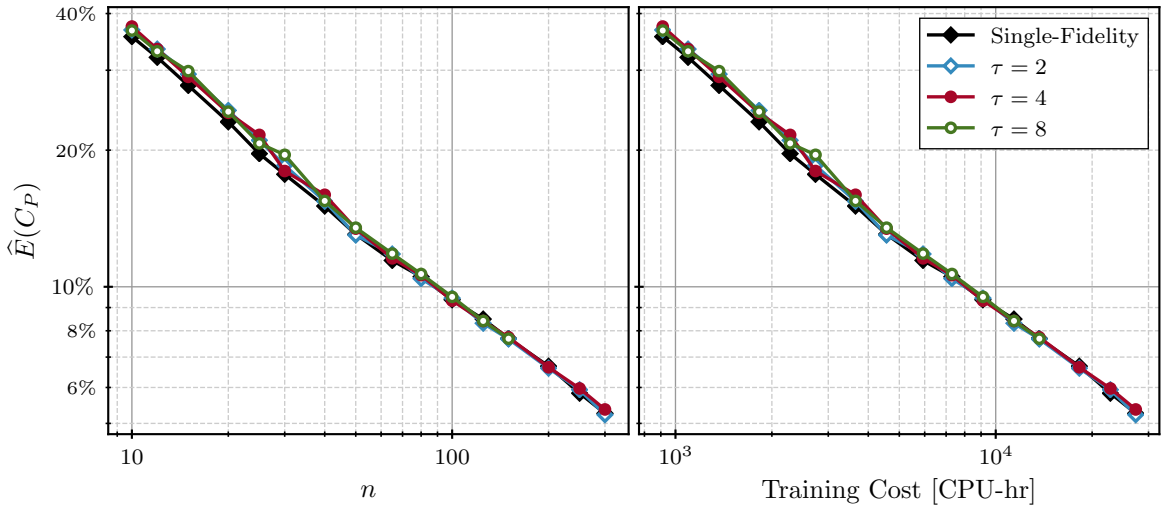


**Figure 5.9:** Normalized prediction error of the CRM wing surface $C_P$ for the W1 + W3 fidelity combination, and the $b = 2$ parametrization.

**Table 5.8:** Detailed breakdown of the flow field $C_P$ prediction error for the CRM wing test case and the $b = 2$ parametrization.

| Fidelity | $n$ | $\tau$ | $m$ | $k$ | $\widehat{E}(C_P)$ | $\widehat{E}_{\text{rc}}(C_P)$ | $\widehat{E}_{\text{rg}}(C_P)$ |
|---|---|---|---|---|---|---|---|
| W1 | 10 | - | - | 9 | 35.6% | 20.7% | 28.7% |
| | 100 | | | 92 | 9.36% | 4.55% | 8.18% |
| | 300 | | | 218 | 5.26% | 1.72% | 4.96% |
| W1 + W2 | 100 | 2 | 200 | 92 | 7.74% | 4.65% | 6.18% |
| | | 4 | 400 | 92 | 7.06% | 4.47% | 5.46% |
| | | 8 | 800 | 92 | 7.11% | 4.53% | 5.47% |
| W1 + W3 | 100 | 2 | 200 | 92 | 9.44% | 4.53% | 8.28% |
| | | 4 | 400 | 92 | 9.32% | 4.49% | 8.16% |
| | | 8 | 800 | 92 | 9.50% | 4.58% | 8.32% |

are broken down into $\widehat{E}_{\text{rc}}(C_P)$ and $\widehat{E}_{\text{rg}}(C_P)$, i.e., the reconstruction and regression errors, and are listed in Table 5.8. As with the results of Table 5.1, the data in Table 5.8 show that $\widehat{E}_{\text{rg}}(C_P)$ is once again the largest contributor to the overall error. The results for the W1 + W2 fidelity combination demonstrate that the MA-ROM method only operates on the regression component of the error as detailed in Section 3.4. In contrast with the RAE 2822 use case, the values of $\widehat{E}_{\text{rc}}(C_P)$ and $\widehat{E}_{\text{rg}}(C_P)$ are relatively closer to each other. This smaller gap between $\widehat{E}_{\text{rc}}(C_P)$ and $\widehat{E}_{\text{rg}}(C_P)$ implies that the potential for improvement using the proposed multi-fidelity method is consequently lower. This is likely the cause behind the weaker performance of the MA-ROM in the current scenario than the previous airfoil problem.

From the above results, the multi-fidelity performance of MA-ROM on the current test case is quantified by setting a target prediction error and comparing the training cost to a single-fidelity model. This is achieved with a log-linear interpolation of the results of Figures 5.8 and 5.9, and the estimated costs are presented in Table 5.9. Given a target error of 10% and $\tau = 4$, we see that the MA-ROM method with the

W1 + W2 fidelity combination requires 48% less high-fidelity training samples, and consequently, 40% less computing resources. Increasing $\tau$ to 8 allows the multi-fidelity model to use a smaller $n$, but the additional low-fidelity samples result in a smaller cost reduction in the end. As for the W1 + W3 fidelity combination, we observe that the training cost of the MA-ROM method tends to be slightly larger than that of a single-fidelity ROM with the same prediction error. In a similar manner, Table 5.10 presents the prediction error of the MA-ROM for a fixed computational budget. In this scenario, the multi-fidelity combination of the W1 and W2 fidelity levels improve the model accuracy by up to 20% compared to a similar single-fidelity ROM. However, the lowest error is observed at $\tau = 4$, and the results at $\tau = 8$ are slightly worse. Considering instead the W1 + W3 fidelity combination, we establish once again from Table 5.10 that incorporating VLM results into the multi-fidelity model produces virtually no advantage compared to without any low-fidelity results.

Finally, the visualizations of Figures 5.10 and 5.11 provide together a qualitative evaluation of the multi-fidelity performance of the MA-ROM method with the CRM wing test case. More specifically, Figure 5.10 displays the actual $C_P$ distribution over the wing at a notional design point. For the sake of completeness, the results on both the upper and lower surfaces of the wing are shown. However, we focus on the former since most of the interesting flow features are on the upper surface of the current design. Figure 5.11 then presents the predicted $\widetilde{C}_P$ obtained with a single-fidelity ROM, a MA-ROM using the W2 fidelity level as the low-fidelity model, and a MA-ROM using the W3 level instead. These models are generated using the same $n = 100$ high-fidelity samples, and the multi-fidelity models are trained with $m = 400$ additional low-fidelity results. As with Figure 5.3, the sample selected for these visualizations corresponds to a wing design with a sample prediction error on par with the average results presented in Table 5.8. The field predictions for the test samples with both the lowest and highest errors are not shown here for conciseness

**Table 5.9:** Estimated training cost of single- and multi-fidelity ROMs given a target prediction error. Results are for the CRM wing test case with a $b = 2$ parametrization. Results in parentheses indicate percent change with respect to an equivalent single-fidelity ROM.

| Target $\widehat{E}(C_P)$ | $b$ | Fidelity | $\tau$ | $n$ | CPU-hr |
|---|---|---|---|---|---|
| 10% | 2 | W1 | | 88 | 8026 |
| 10% | 2 | W1 + W2 | 2 | 53 ($\downarrow$ 40%) | 5176 ($\downarrow$ 36%) |
| | | | 4 | 46 ($\downarrow$ 48%) | 4790 ($\downarrow$ 40%) |
| | | | 8 | 44 ($\downarrow$ 50%) | 5151 ($\downarrow$ 36%) |
| 10% | 2 | W1 + W3 | 2 | 88 (0.0%) | 8027 (0.0%) |
| | | | 4 | 89 ($\uparrow$ 1.1%) | 8119 ($\uparrow$ 1.2%) |
| | | | 8 | 91 ($\uparrow$ 3.4%) | 8303 ($\uparrow$ 3.5%) |

**Table 5.10:** Estimated prediction error of single- and multi-fidelity ROMs given a target training cost. Results are for the CRM wing test case with a $b = 2$ parametrization. Results in parentheses indicate percent change with respect to an equivalent single-fidelity ROM.

| Target CPU-hr | $b$ | Fidelity | $\tau$ | $n$ | $\widehat{E}(C_P)$ |
|---|---|---|---|---|---|
| 10,000 | 2 | W1 | | 110 | 8.99% |
| 10,000 | 2 | W1 + W2 | 2 | 102 | 7.65% ($\downarrow$ 15%) |
| | | | 4 | 96 | 7.21% ($\downarrow$ 20%) |
| | | | 8 | 85 | 7.57% ($\downarrow$ 16%) |
| 10,000 | 2 | W1 + W3 | 2 | 110 | 8.96% ($\downarrow$ 0.4%) |
| | | | 4 | 110 | 8.93% ($\downarrow$ 0.6%) |
| | | | 8 | 110 | 9.04% ($\uparrow$ 0.5%) |

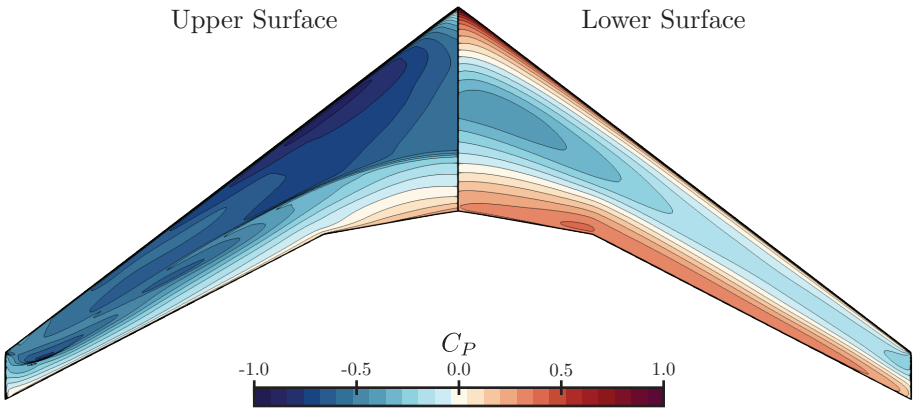


**Figure 5.10:** Actual $C_P$ field over the CRM wing upper (left) and lower(right) surfaces for the CRM wing test case with the $b = 2$ parametrization and the W1 fidelity level.

and are presented in Appendix B.2 instead. All in all, the field results of Figure 5.11 are an adequate prediction of the actual $C_P$ field of Figure 5.10. As with Figure 5.3 for the RAE 2822 test case, the spikes in the error fields are correlated with the presence of shocks on the upper surface of the CRM wing. The MA-ROM results with the W1 and W2 fidelity levels show a sharper shock capturing that is associated with an appreciable reduction of the error field. On the other hand, the results of Figures 5.11a and 5.11c for the single-fidelity ROM and the MA-ROM with the W1 + W3 fidelity combinations respectively are visually equivalent. This is in line with the previous observations made for the CRM wing test case.

### 5.2.3 Prediction of Aerodynamic Coefficients

In addition to the field prediction error, the following experiment considers the error on integrated scalar quantities computed from the field predictions of the MA-ROM method for the CRM wing test case. More specifically, we examine the accuracy of $C_{Lp}$, $C_{Dp}$, and $C_{Mx,p}$, i.e., the pressure component of the lift, drag, and root bending moment coefficients, computed from the predicted $C_P$ distribution over the wing surface. These aerodynamic coefficient errors are computed from the results of MA-ROM augmented with both the W2 and W3 fidelity levels. They are then compared

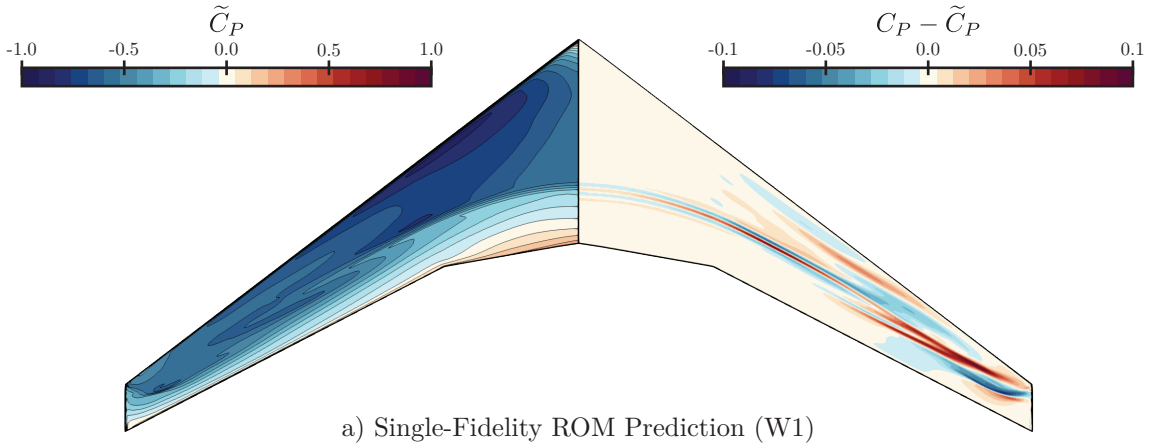


a) Single-Fidelity ROM Prediction (W1)

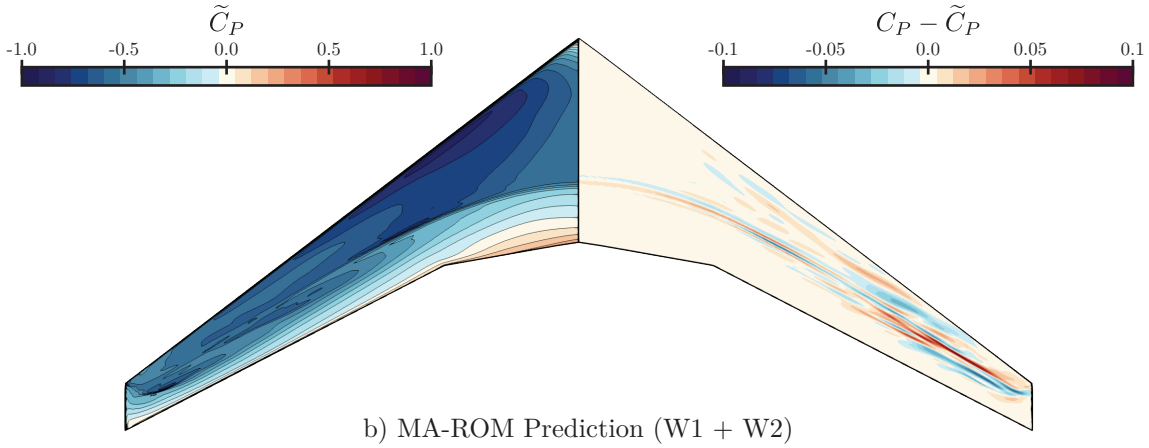


b) MA-ROM Prediction (W1 + W2)

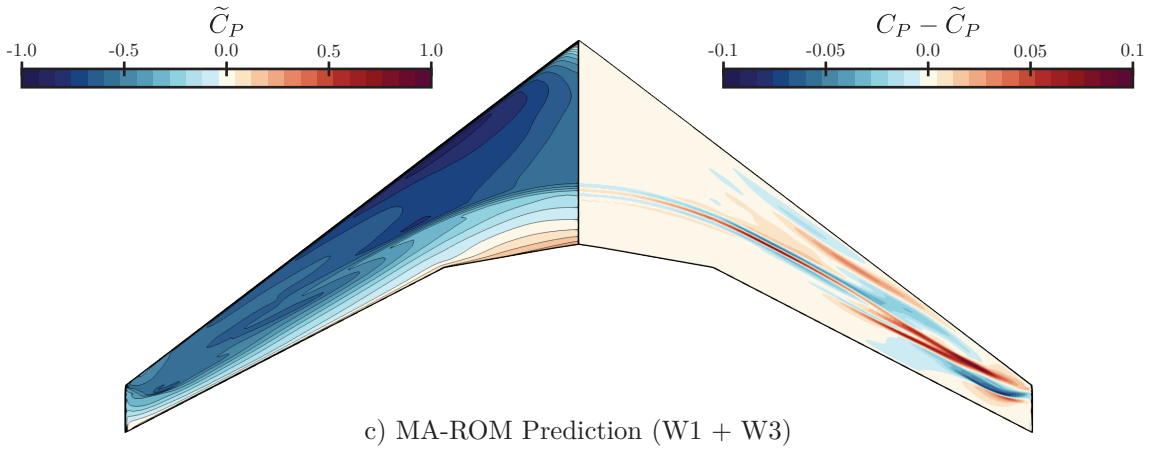


c) MA-ROM Prediction (W1 + W3)

**Figure 5.11:** Comparison of the predicted $C_P$ field (left) of the CRM upper surface and its error (right) with respect to the actual solution (see Figure 5.10) for both single- and multi-fidelity ROMs. Results are for the CRM wing test case with $n = 100$, $\tau = 4$ (MA-ROM only), and $b = 2$.

to the errors of an equivalent single-fidelity ROM. We focus on the root bending moment instead of the pitching moment since the former is an important metric for structural sizing and gives some insights regarding the benefits of the current work on aero-structural problems. The values of $E(C_{Lp})$ from the MA-ROM predictions using the W1 + W2 and the W1 + W3 fidelity combinations are presented in Figure 5.12. These results are followed in Figures 5.13 and 5.14 by the $E(C_{Dp})$ and $E(C_{Mx,p})$ values respectively for the same multi-fidelity combinations. To give some context regarding the significance of these errors, Table 5.11 provide the distributions of $C_{Lp}$, $C_{Dp}$, and $C_{Mx,p}$, computed from the high-fidelity training dataset.

Compared to the single-fidelity errors, the left side of Figures 5.12 to 5.14 show that $E(C_{Lp})$, $E(C_{Dp})$, and $E(C_{Mx,p})$, are effectively reduced by the proposed multi-fidelity method when using the W1 + W2 fidelity combination. As with the $C_P$ field prediction of Figure 5.8, using $\tau$ values greater than two do not improve significantly the computation of aerodynamic coefficients with the MA-ROM method. We also note that the multi-fidelity approach produces a stronger reduction in the errors for $C_{Lp}$ and $C_{Mx,p}$ than for $C_{Dp}$. Moreover, the error reduction offered by the MA-ROM method is larger for small $n$ values and becomes negligible with larger high-fidelity training datasets. A similar trend was also observed in Figure 5.4 for the RAE 2822 airfoil test case. Comparing the trends of Figures 5.12 and 5.14, we note that $E(C_{Mx,p})$ results are similar to those of $E(C_{Lp})$. Since the root bending moment is essentially the span-wise integration of the wing sectional lift distribution, it makes sense for the errors of these two quantities to be related. Regarding the W1 + W3 fidelity combination, the right sides of Figures 5.12 to 5.14 suggest that for the CRM wing test case, the proposed method augmented with the W3 fidelity level does not provide any appreciable benefits over a conventional single-fidelity ROM for the computation of all aerodynamic coefficients. This is consistent with the results of Section 5.2.2 regarding the $C_P$ prediction over the CRM wing using the same multi-fidelity combination.

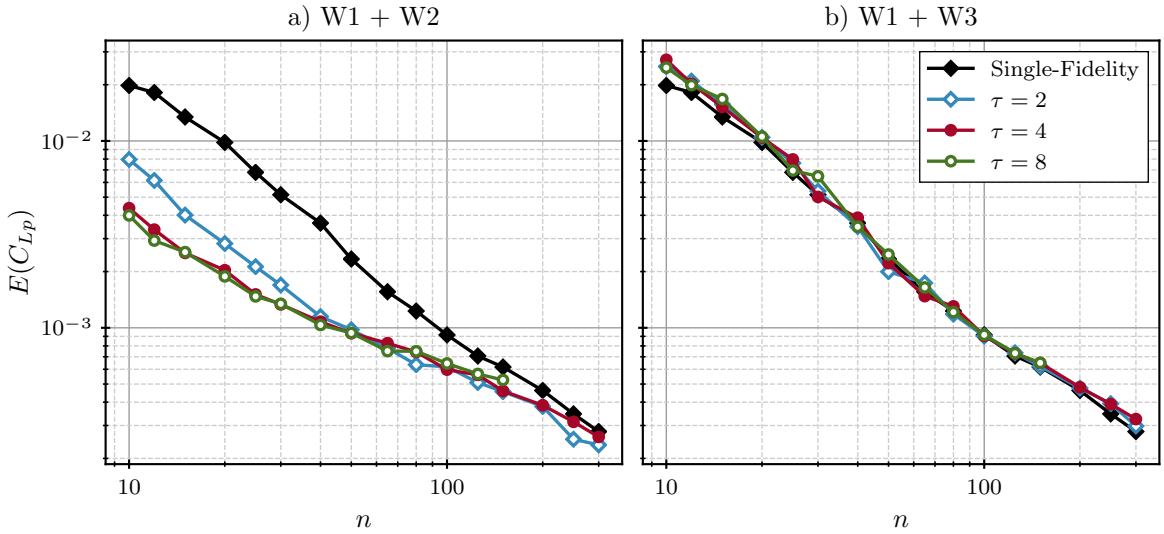


**Figure 5.12:** Lift coefficient errors computed from MA-ROM predictions of the CRM wing surface pressure for the W1 + W2 (a) and W1 + W3 (b) fidelity combinations, and the $b = 2$ parametrization.

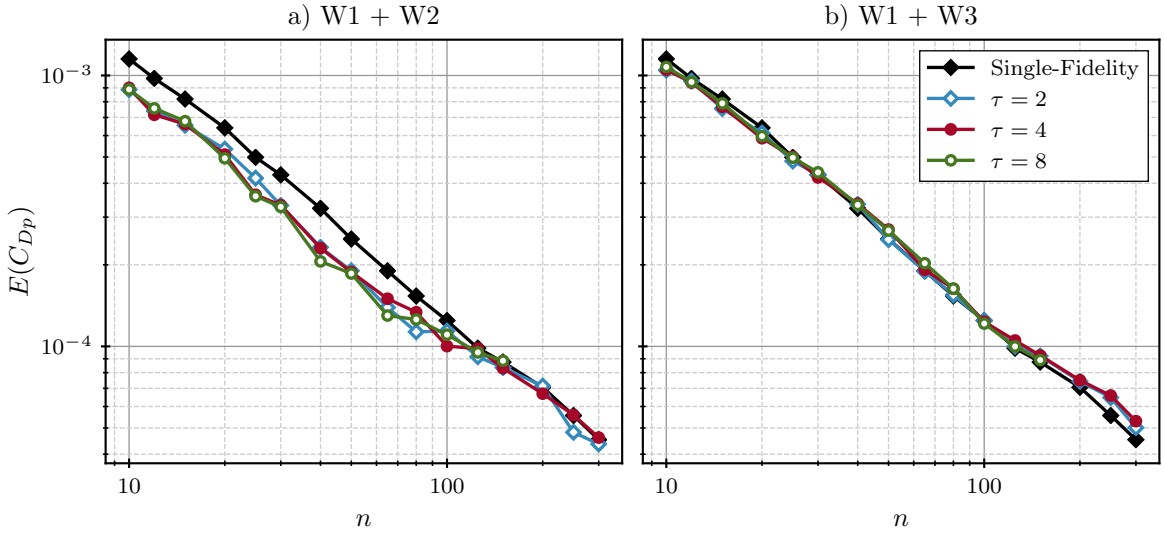


**Figure 5.13:** Drag coefficient errors computed from MA-ROM predictions of the CRM wing surface pressure for the W1 + W2 (a) and W1 + W3 (b) fidelity combinations, and the $b = 2$ parametrization.

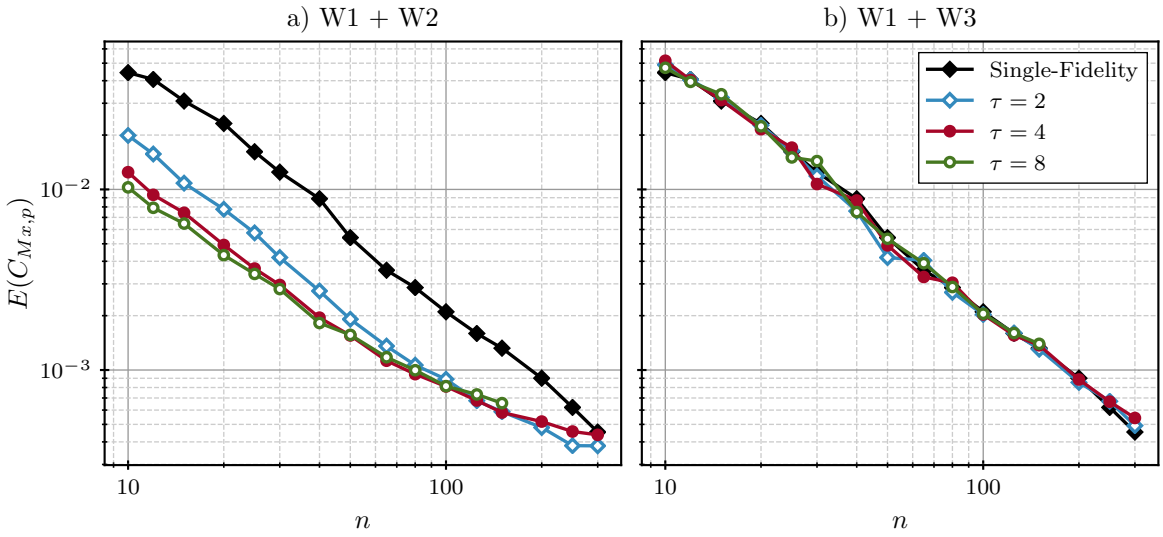


**Figure 5.14:** Root bending moment coefficient errors computed from MA-ROM predictions of the CRM wing surface pressure for the W1 + W2 (a) and W1 + W3 (b) fidelity combinations, and the $b = 2$ parametrization.

**Table 5.11:** Global statistics of the aerodynamic coefficients computed from the W1 fidelity results for the CRM wing test case with a $b = 2$ parametrization.

| | $C_{Lp}$ | $C_{Dp}\,[10^4]$ | $C_{Mx,p}$ |
|---|---|---|---|
| Mean | 0.4049 | 132.5 | 0.6269 |
| Minimum | 0.0603 | 33.58 | 0.0243 |
| Maximum | 0.7246 | 631.9 | 1.1059 |
| Std. Deviation | 0.1612 | 110.3 | 0.2543 |

To provide a more detailed analysis of the above errors, a small selection of the errors in Figures 5.12 to 5.14 are enumerated in Table 5.12. From the inspection of these results, we remark that with the W1 + W2 fidelity combination and $\tau = 4$, the reduction in $E(C_{Lp})$ offered by the MA-ROM method relative to the single-fidelity results varies from 78% at $n = 10$ to only 6% at $n = 300$. The $E(C_{Mx,p})$ values for the root bending moment follow a similar trend, and reduction from 72% to 3.5% are observed over the same interval. For the drag coefficient, the results indicate a weaker relative reduction in $E(C_{Dp})$ that goes from a 22% decrease to a 2% increase in similar circumstances. Similarly to the RAE 2822 airfoil test case, the results of Table 5.12 demonstrate that the multi-fidelity performance of the MA-ROM method regarding the evaluations of integrated aerodynamic coefficients is better for small training datasets. As for the W1 and W3 multi-fidelity combination, we see from Table 5.12 that the overall performance of the MA-ROM method is worse than a single-fidelity method. Recall that the W1 fidelity level uses a RANS simulation to generate the CRM wing aerodynamic data while the W3 level uses a VLM simulation. As discussed in Section 5.2.2, the poor performance of the MA-ROM method for this specific fidelity combination is attributed to the large discrepancy between the physical assumptions of both modeling approaches.

### 5.2.4 Effect of Input Space Dimensionality

We continue the analysis of the accuracy and training cost of the MA-ROM by examining a parametrization with a larger number of design variables. Namely, we consider a parametrization of the CRM wing twist controlled at 5 span-wise stations, i.e., $b = 5$, distributed uniformly from root to tip (see Section 4.2.2). Recall that the parametrization of Sections 5.2.2 and 5.2.3 consisted of only 2 twist stations, i.e., $b = 2$. Due to the poor performance of the MA-ROM method with the W1 + W3 fidelity combination observed previously, we focus here on the W1 and W2 multi-

**Table 5.12:** Detailed aerodynamic coefficient errors computed from ROM and MA-ROM predictions of the CRM wing $C_P$ distribution for the $b = 2$ parametrization. Results in parentheses indicate percent change with respect to an equivalent single-fidelity ROM.

| Fidelity | $\tau$ | $n$ | $E(C_{Lp})\,[10^3]$ | $E(C_{Dp})\,[10^4]$ | $E(C_{Mx,p})\,[10^3]$ |
|---|---|---|---|---|---|
| W1 | - | 10 | 19.81 | 11.51 | 44.33 |
| | | 100 | 0.916 | 1.246 | 2.100 |
| | | 300 | 0.278 | 0.452 | 0.453 |
| W1 + W2 | 4 | 10 | 4.369 (↓ 78%) | 9.005 (↓ 22%) | 12.46 (↓ 72%) |
| | | 100 | 0.597 (↓ 35%) | 1.002 (↓ 20%) | 0.811 (↓ 61%) |
| | | 300 | 0.261 (↓ 6.4%) | 0.461 (↑ 1.8%) | 0.438 (↓ 3.5%) |
| W1 + W3 | 4 | 10 | 27.19 (↑ 37%) | 10.51 (↓ 8.7%) | 51.57 (↑ 16%) |
| | | 100 | 0.906 (↓ 1.1%) | 1.233 (↓ 1.0%) | 2.031 (↓ 3.3%) |
| | | 300 | 0.325 (↑ 17%) | 0.530 (↑ 17%) | 0.543 (↑ 20%) |

fidelity combination only.

The field prediction errors for the $C_P$ distribution over the wing as a function of $n$, $\tau$, and the training cost, are shown in Figure 5.15. From this figure, we see that the $\widehat{E}(C_P)$ is globally larger than in Section 5.2.2 for all combinations of $n$ and $\tau$, as expected of design problems with a higher-dimensional input space. However, when compared to the results in Figure 5.8 for $b = 2$, we remark that the MA-ROM method provides a much stronger reduction in prediction errors than a single-fidelity method in the current test case with $b = 5$. Previously, with the $b = 2$ parametrization we observed no appreciable benefits of setting $\tau$ to values higher than four. In the current problem, the results of Figure 5.15 suggests that incorporating more low-fidelity data in the training of the MA-ROM method continues to improve the performance of the multi-fidelity ROM with $\tau = 8$ and possibly beyond. In fact, for cases at higher $n$, the differences in $\widehat{E}(C_P)$ between the single- and multi-fidelity ROM tend to increase

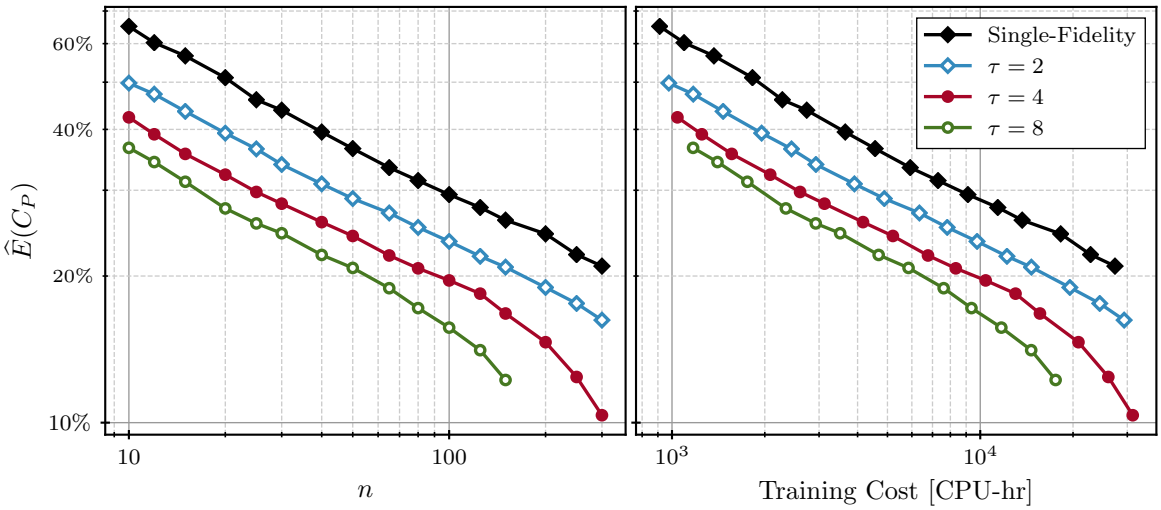


**Figure 5.15:** Normalized prediction error of the CRM wing surface $C_P$ for the W1 + W2 fidelity combination and the $b = 5$ parametrization.

with larger $\tau$. All in all, the relative performance of the MA-ROM method applied to the CRM wing use case appears to be positively affected by the larger input space dimensionality. In comparison, the performance of the proposed method was more or less the same with increasing $b$ values with the RAE 2822 airfoil test case.

To quantify the accuracy and training cost trade-off of the MA-ROM method for the CRM wing with $b = 5$, we evaluate the training cost of the method given some desired error threshold, or similarly, the achievable accuracy for a fixed computational budget. These estimates are obtained from the results of Figure 5.15 and are presented in Tables 5.13 and 5.14 respectively. These estimated costs and errors are also compared to the prediction error and training cost of an equivalent single-fidelity ROM. From Table 5.13, we see that the MA-ROM method with $\tau = 2$ requires 53% less high-fidelity training samples than an equivalent single-fidelity model, and in turn, results in a 49% reduction in CPU time. With $\tau = 8$, the compounded CPU time to produce the high- and low-fidelity training data is reduced by 78% instead. By fixing the desired training cost, Table 5.14 shows that the proposed multi-fidelity method can provide a model accuracy between 18% and 42% superior to a single-fidelity ROM. When compared to Tables 5.9 and 5.10, these results reaffirm that the

**Table 5.13:** Estimated training cost of single- and multi-fidelity ROMs given a target prediction error. Results are for the CRM wing test case with the $b = 5$ parametrization. Results in parentheses indicate percent change with respect to an equivalent single-fidelity ROM.

| Target $\widehat{E}(C_P)$ | $b$ | Fidelity | $\tau$ | $n$ | CPU-hr |
|---|---|---|---|---|---|
| 30% | 5 | W1 | | 93 | 8482 |
| | | | 2 | 44 ($\downarrow$ 53%) | 4297 ($\downarrow$ 49%) |
| 30% | 5 | W1 + W2 | 4 | 24 ($\downarrow$ 74%) | 2499 ($\downarrow$ 71%) |
| | | | 8 | 16 ($\downarrow$ 83%) | 1873 ($\downarrow$ 78%) |

**Table 5.14:** Estimated prediction error of single- and multi-fidelity ROMs given a target training cost. Results are for the CRM wing test case with the $b = 5$ parametrization. Results in parentheses indicate percent change with respect to an equivalent single-fidelity ROM.

| Target CPU-hr | $b$ | Fidelity | $\tau$ | $n$ | $\widehat{E}(C_P)$ |
|---|---|---|---|---|---|
| 10,000 | 2 | W1 | | 110 | 28.7% |
| | | | 5 | 102 | 23.4% ($\downarrow$ 18%) |
| 10,000 | 5 | W1 + W2 | 4 | 96 | 19.8% ($\downarrow$ 31%) |
| | | | 8 | 85 | 16.7% ($\downarrow$ 42%) |

multi-fidelity benefits of the MA-ROM method are greater with $b = 5$ design variables than with $b = 2$.

To investigate further the multi-fidelity performance of the MA-ROM method with the $b = 5$ parametrization of the CRM wing, Table 5.15 provides a breakdown of some of the results from Figure 5.15 in terms of the reconstruction and regression errors. Compared to the results of Table 5.8 for $b = 2$, both $\widehat{E}_{\text{rc}}(C_P)$ and $\widehat{E}_{\text{rg}}(C_P)$ are generally larger in the current problem. However, we note that the gap between $\widehat{E}_{\text{rc}}(C_P)$ and $\widehat{E}_{\text{rg}}(C_P)$ is larger for $b = 5$ than it was for $b = 2$. For instance, if we consider the error breakdown for the single-fidelity ROM, Table 5.8 shows a difference of roughly

**Table 5.15:** Detailed breakdown of the flow field $C_P$ prediction error for the CRM wing test case and the $b = 5$ parametrization.

| Fidelity | $n$ | $\tau$ | $m$ | $k$ | $\widehat{E}(C_P)$ | $\widehat{E}_{\text{rc}}(C_P)$ | $\widehat{E}_{\text{rg}}(C_P)$ |
|---|---|---|---|---|---|---|---|
| W1 | 10 | - | - | 9 | 65.1% | 30.5% | 57.0% |
| | 100 | | | 98 | 29.4% | 7.74% | 28.3% |
| | 300 | | | 274 | 21.0% | 3.04% | 20.7% |
| W1 + W2 | 100 | 2 | 200 | 98 | 23.6% | 7.63% | 22.3% |
| | | 4 | 400 | 98 | 19.6% | 7.55% | 18.1% |
| | | 8 | 800 | 98 | 15.7% | 7.60% | 13.7% |

4% between the reconstruction and regression errors with $b = 2$. Assuming $n = 100$, this represents approximately half of the total prediction error. For the $b = 5$ cases, Table 5.15 reveal that for the same single-fidelity approach, the difference between $\widehat{E}_{\text{rc}}(C_P)$ and $\widehat{E}_{\text{rg}}(C_P)$ is around 20% and represent a bigger fraction of $\widehat{E}(C_P)$. As mentioned previously, the MA-ROM method is formulated to reduce the regression component of the prediction error by providing low-fidelity latent coordinates to the regression model within the ROM. Since $\widehat{E}_{\text{rg}}(C_P)$ is larger relative to $\widehat{E}_{\text{rc}}(C_P)$ for $b = 5$, it follows that the potential for improvement is larger when using the MA-ROM method. This would explain why the proposed multi-fidelity method performs better with the higher-dimensional parametrization of the CRM wing.

### 5.2.5 Summary

While we established in Experiment 1 that the MA-ROM method can effectively reduce the training cost of a ROM, the current experiment demonstrated that the method is also applicable to problems of larger scales such as the aerodynamic analysis of a transonic wing. By applying MA-ROM to the prediction of the pressure distribution over the CRM wing, the results of this experiment show that a cost reduction of up to 78% compared to an equally accurate single-fidelity model is attainable.

These same results alternatively establish that for a given amount of CPU time, the proposed multi-fidelity method could reduce the field prediction error by up to 42%. This higher accuracy of the predicted field can subsequently improve the prediction of some integrated quantities such as the lift, drag, or root bending moment. In short, the results of this section together with the observations previously made in Experiment 1 further support our Hypothesis 1.1 concerning the multi-fidelity performance of the MA-ROM method.

The application of MA-ROM to the CRM wing use case has also highlighted some additional characteristics of the proposed method. For instance, by augmenting the results from a RANS CFD simulation with VLM data, i.e., the W1 + W3 fidelity combination, we demonstrated the consequence of using MA-ROM with fidelity levels that are too far apart from each other. The results show that in this extreme scenario, the performance of MA-ROM is essentially comparable to a single-fidelity ROM, thus negating any benefits from the multi-fidelity approach. This indicates that the source of the low-fidelity data must be chosen with some considerations and that there is a practical lower limit to its fidelity level.

Furthermore, the current experiment establishes the importance of the regression error on the overall performance of MA-ROM. In cases where the gap between the reconstruction and regression errors was the largest, the proposed multi-fidelity method was shown to excel in both accuracy and training costs. This behavior can be directly linked to the formulation of MA-ROM centered around enhancing the prediction of high-fidelity latent coordinates using aligned low-fidelity data. Therefore, the proposed multi-fidelity method is better suited for ROM problems dominated by regression errors. We also note that with the CRM wing test case, the dimensionality of the parametrization affected the gap between the reconstruction and regression errors. In the context of Hypothesis 1.2, this shows that there is an indirect dependence between the input dimensionality and the multi-fidelity performance of the

MA-ROM method. However, the use of a higher-dimensional parametrization had a positive effect on the multi-fidelity method and still suggests that its application is scalable to larger input spaces.

## 5.3 Experiment 3: Effect of Field Inconsistencies

The salient feature of the MA-ROM method is its ability to combine fields of different fidelity levels and potentially with disparate representations. These inconsistent representations represent a difficulty unique to multi-fidelity ROMs and can be caused by differences in terms of dimensionality, topology, and field features. In this section, we verify if the proposed multi-fidelity method can truly resolve differences in field representation and investigate the effect of these inconsistencies on the accuracy of the model. The outcome of this experiment is aimed at addressing Research Question 2 and validating the related Hypothesis 2. This section presents and discusses three distinct experiments associated with each type of field inconsistency considered. As with Experiments 1 and 2, we consider here the transonic airfoil and wing test cases due to their physical complexity and their relevance for industrial applications.

### 5.3.1 Experiment 3.1: Inconsistent Dimensionalities

Among the considered field inconsistencies, differences in terms of dimensionality are perhaps the most common in the context of multi-fidelity simulations. Indeed, given a complex physics-based simulation solving some discretized governing equations, one of the more convenient ways of reducing the computational cost is to use a coarser grid, albeit at the expense of reduced accuracy. Also, simulations of different fidelity naturally tend to have different grid requirements.

It is worth noting that all of the fidelity levels in both the transonic airfoil and the transonic wing test cases have inconsistent grid sizes (see Tables 4.4 and 4.6). Consequently, all of the previous MA-ROM results of Sections 5.1 and 5.2 involved

the combination of fields having disparate dimensionalities. These experiments were performed without any pre-processing that would ensure a consistent dimensionality among all the training datasets. While the results of Sections 5.1 and 5.2 demonstrated that the MA-ROM method can successfully combine multi-fidelity fields into a more accurate and cheaper model, they also establish that it can do so with fields having inconsistent dimensionalities. For instance, the results of Table 5.3 show that for a computation budget of 20 CPU-hr, the MA-ROM method with the A1 + A2 fidelity combination can generate results up to 29% more accurate than an equivalent single-fidelity ROM despite the grid of the A2 fidelity being roughly four times smaller than the A1 fidelity.

To assess clearly the impact of inconsistent field dimensionalities on the performance of MA-ROM, we perform an additional experiment where the proposed method is applied to multi-fidelity fields with consistent grid size. These results are then compared to the prediction of an equivalent multi-fidelity model trained with fields having inconsistent dimensionalities. Any differences in the model accuracies would represent the potential effect of inconsistent dimensionalities on the multi-fidelity performance of MA-ROM.

*Problem Setup*

For this experiment, we select the RAE 2822 test cases with the A1 + A2 fidelity combination that was previously evaluated in Section 5.1.2. The simulations of the A1 and A2 fidelity levels use grids with 41,796 and 10,530 nodes respectively. To make the results of these two fidelity levels consistent in terms of dimensionality, the solutions of the A1 fidelity level are interpolated onto the coarser grid of the A2 level using a weighted linear interpolation. This pre-processing step is done using the interpolation schemes available in the Paraview visualization software [9]. For clarity, we denote the interpolated results of the A1 fidelity as A1-I.

The accuracy of the MA-ROMs using either the A1 or A1-I fidelity levels is then compared in terms of the $C_P$ normalized field prediction error. The value of $\widehat{E}(C_P)$ is obtained using the approach described in Section 5.1.1. As with previous experiments, the error values presented here are an average of at least 100 unique models trained with different subsets of the available high- and low-fidelity data. We also consider both the $b = 3$ and 5 design parametrizations of the airfoil.

*Results*

The field prediction error of the MA-ROM method applied to fields with and without consistent grid sizes are shown in Figures 5.16 and 5.17 as a function of $n$ and $\tau$. These figures present results for cases with $b = 3$ and 5 design parameters respectively. We note that the $\widehat{E}(C_P)$ values for MA-ROMs trained with the A1 + A2 fidelity combination are identical to the results presented in Section 5.1 for the same model configuration. From Figure 5.16, we see that using A1-I instead of A1 fidelity level with the MA-ROM method, i.e., by interpolating the high-fidelity results on the coarse low-fidelity grid, did not have any visible effect on the multi-fidelity performance of the method. This observation also applies to the results of Figure 5.17 with a higher-dimensional parametrization. Despite the overall higher prediction error due to the additional design parameters, the multi-fidelity results with the A1-I + A2 fidelity combination appear to match exactly those for the A1 + A2 combination.

Since there is no visible differences in Figures 5.16 and 5.17 between cases with and without consistent dimensionalities, the results from the above figures for $n = 100$ are enumerated in Table 5.16. From this table, we note that the accuracies of multi-fidelity ROMs trained with either the A1 + A2 or the A1-I + A2 fidelity combinations are indeed closely similar. The $\widehat{E}(C_P)$ values of cases with similar $b$, $n$, and $\tau$, are within less than 0.05% of each other. Therefore, the results of Table 5.16 together with the trends of Figures 5.16 and 5.17 verify that the MA-ROM method is essentially

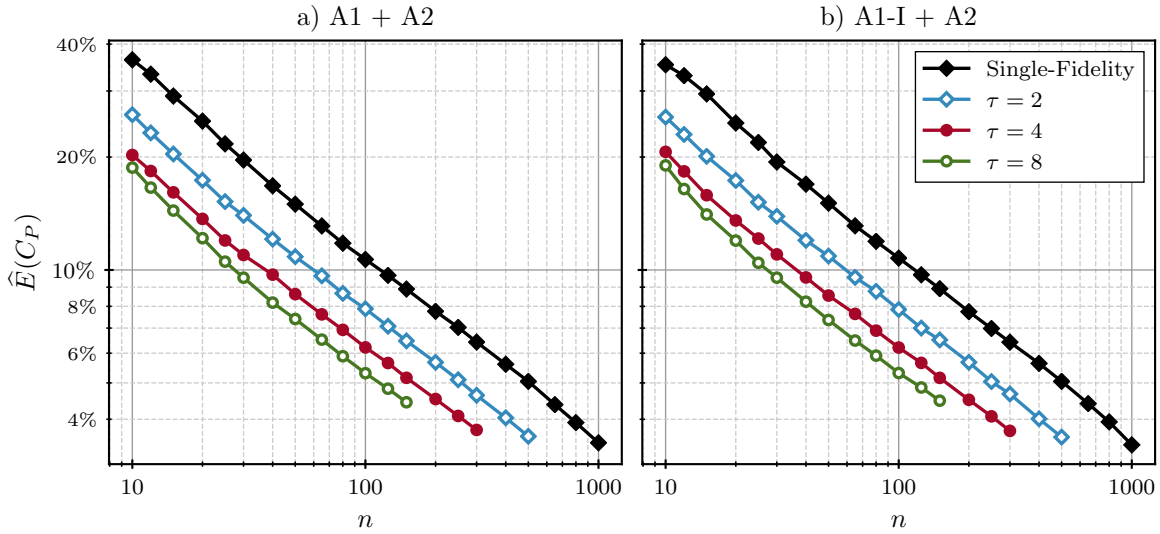


**Figure 5.16:** Field prediction errors of MA-ROMs generated with and without inconsistent dimensionalities. Models are trained with the A1 + A2 (a) and A1-I + A2 (b) fidelity combinations for the RAE 2822 test case and with $b = 3$.

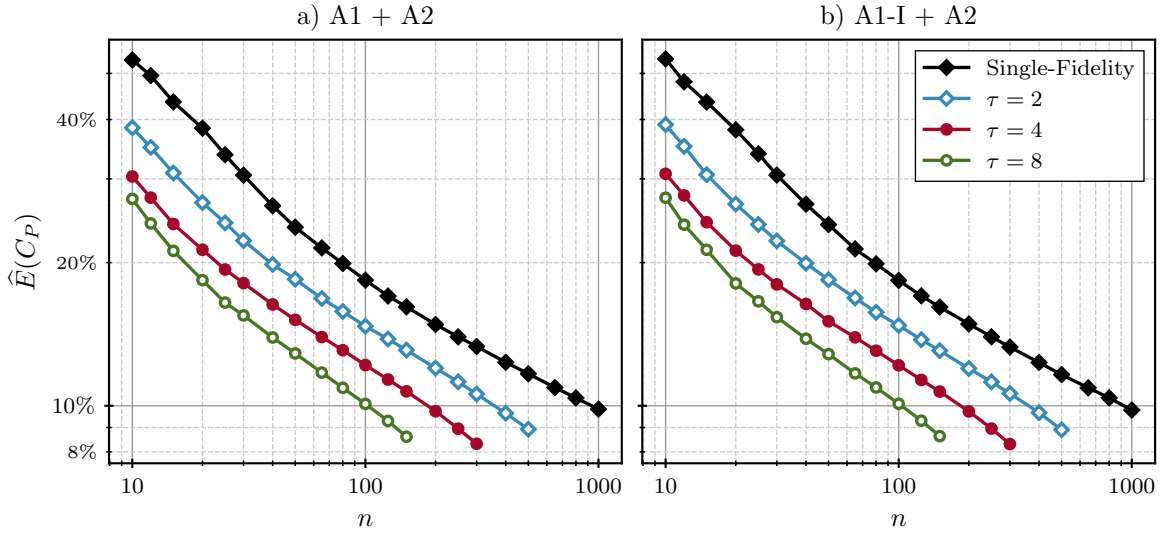


**Figure 5.17:** Field prediction errors of MA-ROMs generated with and without inconsistent dimensionalities. Models are trained with the A1 + A2 (a) and A1-I + A2 (b) fidelity combinations for the RAE 2822 test case and with $b = 5$.

**Table 5.16:** Tabulated $\widehat{E}(C_P)$ of MA-ROMs trained with and without inconsistent dimensionalities. Models are trained with the A1 + A2 and A1-I + A2 fidelity combinations for the RAE 2822 test case.

| $b$ | Fidelity | $n$ | $\tau$ | $m$ | $\widehat{E}(C_P)$ |
|---|---|---|---|---|---|
| 3 | A1 | 100 | - | - | 10.67% |
| 3 | A1 + A2 | 100 | 2 | 200 | 7.878% |
| | | | 4 | 400 | 6.218% |
| | | | 8 | 800 | 5.306% |
| 3 | A1-I + A2 | 100 | 2 | 200 | 7.845% |
| | | | 4 | 400 | 6.212% |
| | | | 8 | 800 | 5.313% |
| 5 | A1 | 100 | - | - | 18.37% |
| 5 | A1 + A2 | 100 | 2 | 200 | 14.70% |
| | | | 4 | 400 | 12.18% |
| | | | 8 | 800 | 10.09% |
| 5 | A1-I + A2 | 100 | 2 | 200 | 14.75% |
| | | | 4 | 400 | 12.17% |
| | | | 8 | 800 | 10.10% |

insensitive to differences in dimensionality between the multi-fidelity fields. That is not to say that the fidelity of the individual datasets is irrelevant, but rather that for a given fidelity combination, interpolating results with inconsistent discretization on a common grid is redundant. This is advantageous from a practical standpoint since no additional pre-processing is required before applying the MA-ROM method on a given multi-fidelity dataset.

### 5.3.2 Experiment 3.2: Inconsistent Topologies

As explained in Section 1.5.2, fields with inconsistent topologies can be the result of using a simplified geometry for the low-fidelity simulation. For instance, a CFD and a VLM simulation of an aircraft will produce solutions having different topologies since the former considers the vehicle OML while the latter uses a thin surface representation of the geometry (see Figure 1.8). In Section 5.2.2, we considered a similar scenario where the MA-ROM method combines the solutions from a RANS CFD and a VLM simulation, i.e., the W1 and W3 fidelity levels. We demonstrated that the proposed method could indeed combine these two datasets despite their inconsistent topologies, but the accuracy of the resulting models did not show any improvement over an equivalent single-fidelity level. However, this poor multi-fidelity performance was attributed to the large fidelity gap between the W1 and W3 levels rather than the disparate topologies of the fields.

To fully establish the capability of MA-ROM to combine solutions with inconsistent topologies, we consider here an experiment where the proposed method is applied on fields having disparate topologies, but without a large difference in fidelity levels. The resulting multi-fidelity ROM is then compared to a model trained with fields of similar fidelity, but with consistent topologies.

*Problem Setup*

As with Section 5.1.2, this experiment considers the prediction of the $C_P$ field of the RAE 2822 airfoil test cases and the A1 + A2 fidelity combinations. Although the A1 and A2 fidelity levels use grids of different sizes, they both consider the same airfoil geometry and the same fluid domain, making their topology consistent. We also note that the results of Section 5.1.2 show that the A1 and A2 levels are sufficiently close in terms of model fidelity that the MA-ROM method can provide an appreciable reduction in terms of prediction errors and training costs when compared

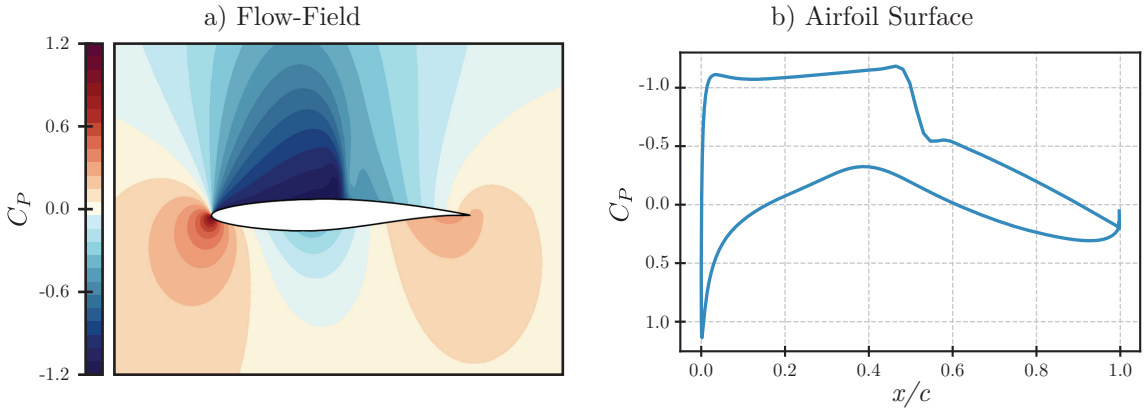


**Figure 5.18:** Comparison between the flow field (a) and surface (b) $C_P$ distribution for the RAE 2822 test case.

to an equivalent single-fidelity ROM.

Besides, we define a new scenario where the MA-ROM method predicts the flow field $C_P$ of the A1 fidelity level augmented with the A2 level, but where the low-fidelity results are the $C_P$ distributions at the airfoil surface only. In other words, instead of using the entire flow field solution from the A2 fidelity level, only the results at the airfoil surface are used to augment the multi-fidelity models, which we refer to as the A2-S fidelity level. The A1 and A2-S fidelity levels use inconsistent topologies since the former considers the entire flow field while the latter only considers the surface $C_P$ distribution. At the same time, the fidelity gap between the A1 and A2-S levels is the same as for the A1 + A2 fidelity combination, and was shown to be adequate for the MA-ROM method. Figure 5.18 illustrates both the flow field and surface $C_P$ distribution of the RAE 2822 airfoil. Although both pressure fields have fundamentally different representations, a clear relationship exists between the features of Figures 5.18a and 5.18b that the proposed method can exploit. We also note that scenarios can occur in practice where aerodynamic results are only available at the airfoil surface. For instance, in wind tunnel experiments, pressure results are typically limited to measurements at the geometry surface obtained using embedded pressure taps.

If the proposed method can truly combine fields with inconsistent topologies, then the prediction error of a model trained with the A1 + A2-S fidelity combination should be equivalent to the error of a model trained with the A1 + A2 combination. For this experiment, the accuracy of the different MA-ROMs is assessed once more using the normalized field prediction of the $C_P$ field. The value of $\widehat{E}(C_P)$ is obtained following the methodology described previously in Section 5.1.1. Also, this experiment considers both the $b = 3$ and 5 parametrizations of the RAE 2822.

*Results*

Figures 5.19 and 5.20 present the values of $\widehat{E}(C_P)$ as a function of the number of high-fidelity training samples and the multi-fidelity ratio $\tau$. The former figure shows the results for the $b = 3$ parametrization while the latter considers the $b = 5$ parametrization. The left plots of these figures give the field prediction errors of the MA-ROM method combining the A1 + A2 fidelity levels and the right plots contain the errors for the A1 + A2-S fidelity combination, i.e., with inconsistent topologies. We also include the results of a conventional single-fidelity ROM for reference purposes. Comparing side by side the errors of Figures 5.19a and 5.19b for the $b = 3$ cases, we see that augmenting the proposed multi-fidelity method with either the low-fidelity flow field or surface $C_P$ distribution, i.e., the A2 and A2-S fidelity levels, essentially produces the same model accuracy. Looking closer, one can discern some small differences between individual points, but those variations are small and would likely have a negligible impact in practice. Considering instead the results of Figure 5.20 for the $b = 5$ cases, we observe that the value of $\widehat{E}(C_P)$ is overall higher due to the additional design parameters, but the error trends with both the A1 + A2 and A1 + A2-S fidelity combinations are again more or less the same.

In an attempt to better quantify the differences between MA-ROMs augmented with either the A2 or A2-S fidelity levels, Table 5.17 contains error values from Fig-

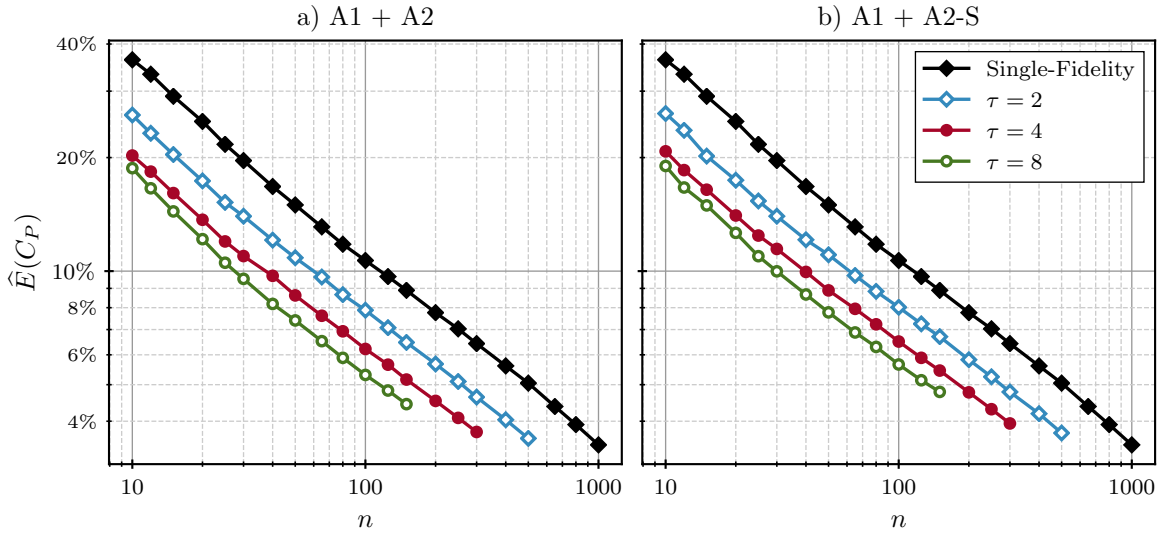


**Figure 5.19:** Field prediction errors of MA-ROMs generated with and without inconsistent topologies. Models are trained with the A1 + A2 (a) and A1 + A2-S (b) fidelity combinations for the RAE 2822 test case and with $b = 3$.

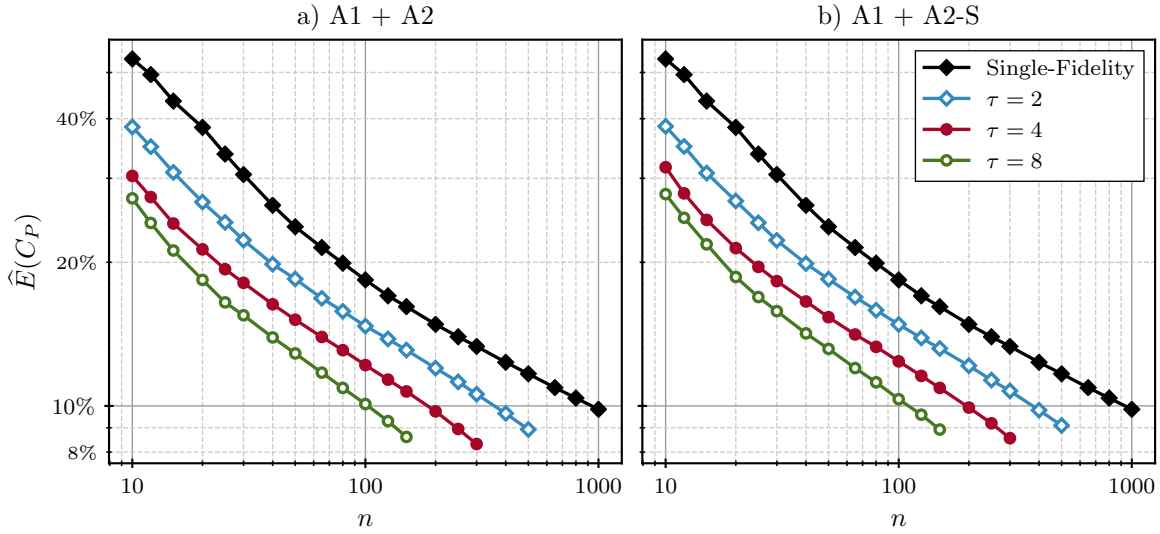


**Figure 5.20:** Field prediction errors of MA-ROMs generated with and without inconsistent topologies. Models are trained with the A1 + A2 (a) and A1 + A2-S (b) fidelity combinations for the RAE 2822 test case and with $b = 5$.

ures 5.19 and 5.20 for $n = 100$. For a given parameter $b$, the results of Table 5.17 show that the normalized prediction errors between multi-fidelity ROMs trained with either the A2 and A2-S fidelity levels are within 0.3% of each other, with the latter being slightly higher. These differences in $\widehat{E}(C_P)$ are relatively small when compared to the error reduction of roughly 3% to 8% that the multi-fidelity models offer over single-fidelity ROMs trained with the same high-fidelity samples. Therefore, the above results demonstrate that the MA-ROM method is capable of combining multi-fidelity fields with inconsistent topologies. As long as the fields being combined are adequately related, differences in terms of topology do not appear to have a significant impact on the multi-fidelity performance of the proposed method.

### 5.3.3 Experiment 3.3: Inconsistent Features

Differences in the field features is the third and last type of field inconsistency considered in this work. In the context of POD-based ROMs, this inconsistency arises when comparing field results having distinct POD modes despite having potentially consistent dimensionality and topology. Even though these fields exist in different subspaces, their variation in terms of latent coordinates can still be related, and a multi-fidelity method can exploit this connection. For example, one can consider the $C_F$ and $C_P$, i.e., skin friction and pressure coefficient, over the CRM wing shown in Figure 5.21. Both of these fields have unmistakably different distributions, but it is reasonable to assume that they can vary in a coordinated manner. The following section presents an experiment designed to assess the effect of inconsistent flow features on the multi-fidelity performance of the MA-ROM method.

#### *Problem Setup*

The effect of inconsistent features is evaluated by using the MA-ROM method to combine solutions with different physical quantities. More specifically, we consider

**Table 5.17:** Tabulated $\widehat{E}(C_P)$ of MA-ROMs trained with and without inconsistent topologies. Models are trained with the A1 + A2 and A1 + A2-S fidelity combinations for the RAE 2822 test case.

| $b$ | Fidelity | $n$ | $\tau$ | $m$ | $\widehat{E}(C_P)$ |
|---|---|---|---|---|---|
| 3 | A1 | 100 | - | - | 10.67% |
| 3 | A1 + A2 | 100 | 2 | 200 | 7.878% |
| | | | 4 | 400 | 6.218% |
| | | | 8 | 800 | 5.306% |
| 3 | A1 + A2-S | 100 | 2 | 200 | 8.020% |
| | | | 4 | 400 | 6.506% |
| | | | 8 | 800 | 5.656% |
| 5 | A1 | 100 | - | - | 18.37% |
| 5 | A1 + A2 | 100 | 2 | 200 | 14.70% |
| | | | 4 | 400 | 12.18% |
| | | | 8 | 800 | 10.09% |
| 5 | A1 + A2-S | 100 | 2 | 200 | 14.82% |
| | | | 4 | 400 | 12.40% |
| | | | 8 | 800 | 10.33% |

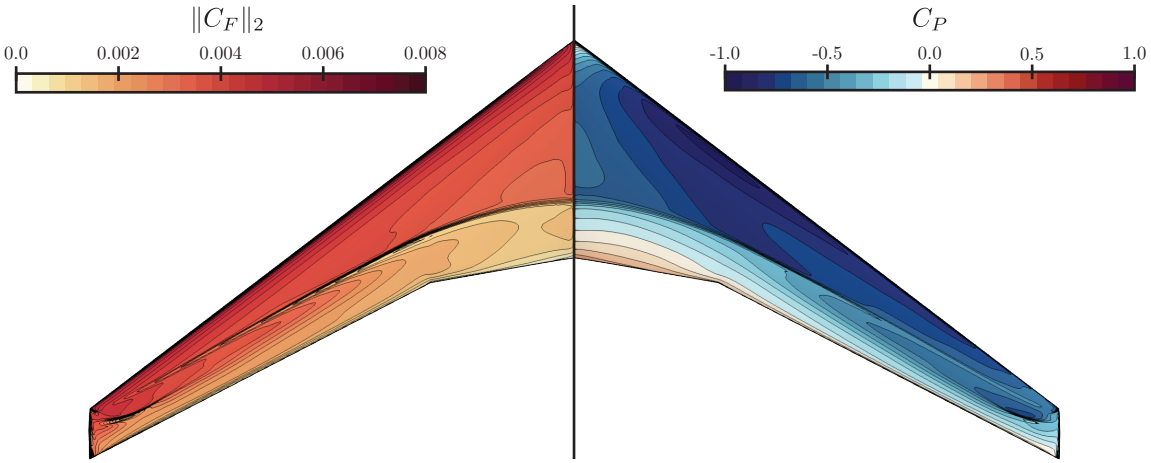


**Figure 5.21:** Distribution of the $C_F$ magnitude (left) and $C_P$ (right) distributions over the CRM wing test case.

a scenario where the high-fidelity solutions to be predicted are the $C_F$ distributions over the CRM wing, while the low-fidelity results are the corresponding $C_P$ distributions. The same topology is used for both the high- and low-fidelity data, but they differ in terms of field features as illustrated in Figure 5.21. In practice, this multi-fidelity scenario could represent a situation where the low-fidelity results are given by an inviscid CFD simulation such that the skin friction distribution is not immediately available. Alternatively, the low-fidelity fields could come from experimental results where the pressure distribution over the CRM wing is obtained with embedded pressure taps or with a pressure-sensitive paint [11]. This experiment also has the advantage of demonstrating the predictive capability of the MA-ROM method on a physical quantity other than the pressure field.

The accuracies of multi-fidelity ROMs trained with the $C_F$ and $C_P$ fields are then compared to models constructed using an equivalent multi-fidelity combination, but where the $C_F$ distribution is used for both the high- and low-fidelity data, i.e., with consistent field features. The high- and low-fidelity results are obtained from the solutions of the W1 and W2 fidelity levels, and we use the suffixes $C_P$ and $C_F$ to denote which field is being used for a given set of results. If the MA-ROM method can

properly fuse multi-fidelity fields with inconsistent features, then the field prediction error of models trained with either the W1-$C_F$ + W2-$C_F$ and the W1-$C_F$ + W2-$C_P$ fidelity combination should be similar. For the sake of thoroughness, we consider the results of both the $b = 2$ and 5 design parametrizations. The field prediction error of the trained models are computed in the same manner described in Section 5.2.1 with the exception that the field of interest is the $C_F$ distribution and the corresponding normalized error is $\widehat{E}(C_F)$.

*Results*

The normalized prediction errors of the $C_F$ distribution over the CRM wing are displayed in Figures 5.22 and 5.23 for $b = 2$ and 5 respectively. These figures compare the $\widehat{E}(C_F)$ values of MA-ROMs augmented with either the W2-$C_F$ or the W2-$C_P$, i.e., the low-fidelity $C_F$ and $C_P$ fields, as a function of $n$ and $\tau$. From Figure 5.22a, we see that the proposed multi-fidelity method with the W1-$C_F$ + W2-$C_F$ fidelity combination can effectively improve the prediction of the $C_F$ field for all the cases considered. Compared to the prediction of the $C_P$ field, the current $\widehat{E}(C_F)$ values are overall higher than the $\widehat{E}(C_P)$ values shown in Figure 5.8. Yet, the relative reduction in error offered by MA-ROM is more or less the same for cases with an equivalent model configuration. As for supplementing the $C_F$ field prediction with low-fidelity $C_P$ solutions, the results of Figure 5.22b show that the MA-ROM method with the W1-$C_F$ + W2-$C_P$ fidelity combination has reduced errors compared to an equivalent single-fidelity ROM. Therefore, the multi-fidelity method can leverage the auxiliary results to improve the model prediction despite the high- and low-fidelity fields representing different physical quantities and having disparate features. However, comparing Figures 5.22a and 5.22b, we note that the multi-fidelity performance offered by the W1-$C_F$ + W2-$C_P$ fidelity combination is weaker than for the W1-$C_F$ + W2-$C_F$ combination. In other words, the MA-ROM method performs worse when the high-

and low-fidelity results represent different quantities of interest, yet better than a single-fidelity ROM.

Looking instead at Figure 5.23, we note that the higher number of design parameters causes the prediction error to be generally higher. As observed in Section 5.2.4, the results also show that the MA-ROM method performs generally better with the more granular parametrization of the CRM wing. Both the results using the W1-$C_F$ + W2-$C_F$ and the W1-$C_F$ + W2-$C_F$ fidelity combinations display a stronger decrease in $\widehat{E}(C_F)$ compared to a single-fidelity ROM, and this effect increases with larger $\tau$. Nevertheless, comparing Figures 5.23a and 5.23b side-by-side show us that the prediction error with the W1-$C_F$ + W2-$C_F$ fidelity combination is overall lower than the W1-$C_F$ + W2-$C_P$ combination. This is consistent with the trends observed in Figure 5.22 for cases with $b = 2$.

To provide a closer look on the above results, Table 5.23 present the numerical values of the results from Figures 5.22 and 5.23 for cases with $n = 100$. From that table, we observe that when compared to a single-fidelity model, the MA-ROM errors with $b = 2$ are up to 14.9% and 9.85% lower using the W1-$C_F$ + W2-$C_F$ and W1-$C_F$ + W2-$C_P$ fidelity combinations respectively. Considering instead the $b = 5$ parametrization, the error reduction becomes 38.1% and 25.9% for the same fidelity combinations. Therefore, augmenting the prediction of the $C_F$ field using low-fidelity $C_P$ solutions can still provide a viable improvement to the model accuracy. At the very least, this experiment shows that the applicability of the proposed method is not restricted to the multi-fidelity combination of fields having consistent features. The results suggest that the high- and low-fidelity datasets should have a similar set of features, but even in cases where this is not possible, the MA-ROM method is still a viable solution.

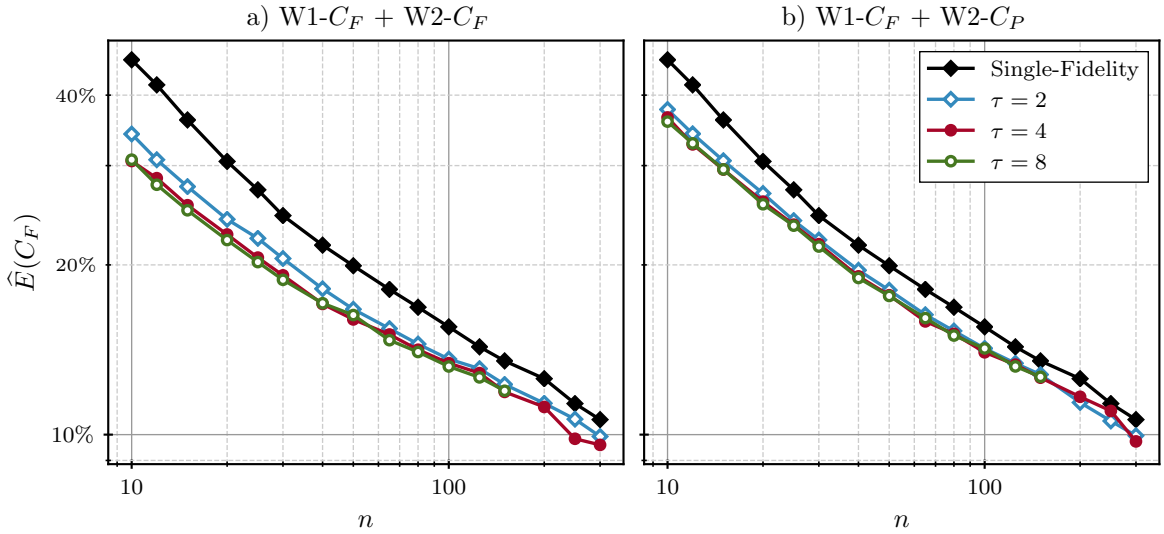


**Figure 5.22:** Field prediction errors of MA-ROMs generated with and without inconsistent field features. Models are trained with the W1-$C_F$ + W2-$C_F$ and W1-$C_F$ + W2-$C_P$ fidelity combinations for the CRM wing test case and with $b = 2$.

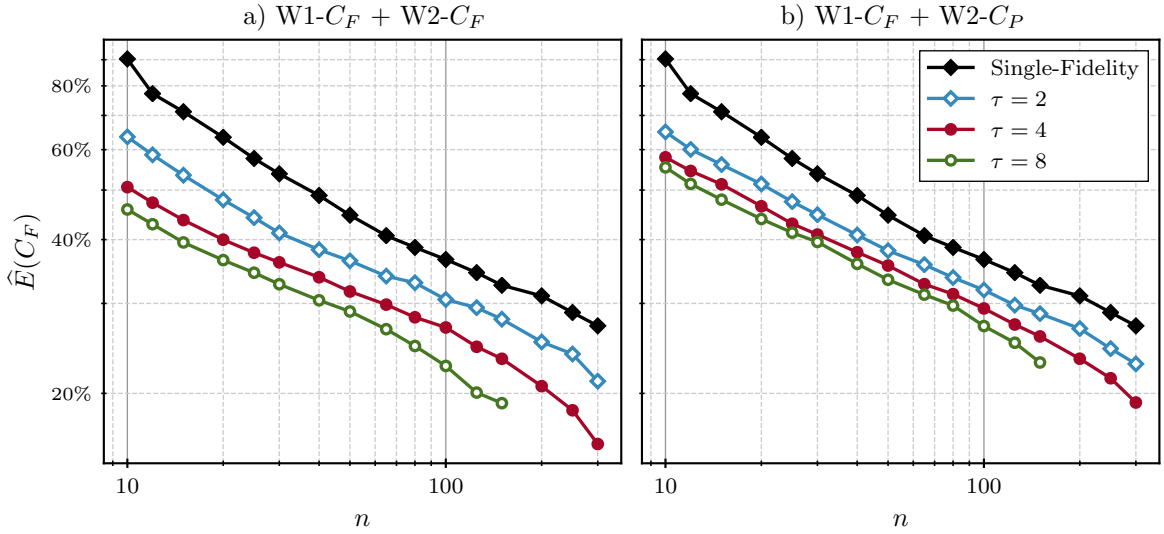


**Figure 5.23:** Field prediction errors of MA-ROMs generated with and without inconsistent field features. Models are trained with the W1-$C_F$ + W2-$C_F$ and W1-$C_F$ + W2-$C_P$ fidelity combinations for the CRM wing test case and with $b = 5$.

**Table 5.18:** Tabulated $\widehat{E}(C_P)$ of MA-ROMs trained with and without inconsistent field features. Models are trained with the W1-$C_F$ + W2-$C_F$ and W1-$C_F$ + W2-$C_P$ fidelity combinations for the CRM wing test case.

| $b$ | Fidelity | $n$ | $\tau$ | $m$ | $\widehat{E}(C_P)$ |
|---|---|---|---|---|---|
| 2 | W1-$C_F$ | 100 | - | - | 15.53% |
| 2 | W1-$C_F$ + W2-$C_F$ | 100 | 2 | 200 | 13.62% |
| | | | 4 | 400 | 13.39% |
| | | | 8 | 800 | 13.21% |
| 2 | W1-$C_F$ + W2-$C_P$ | 100 | 2 | 200 | 14.22% |
| | | | 4 | 400 | 14.00% |
| | | | 8 | 800 | 14.22% |
| 5 | W1-$C_F$ | 100 | - | - | 36.58% |
| 5 | W1-$C_F$ + W2-$C_F$ | 100 | 2 | 200 | 30.53% |
| | | | 4 | 400 | 26.92% |
| | | | 8 | 800 | 22.63% |
| 5 | W1-$C_F$ + W2-$C_P$ | 100 | 2 | 200 | 31.87% |
| | | | 4 | 400 | 29.33% |
| | | | 8 | 800 | 27.09% |

### 5.3.4 Summary

This section investigated the capability of the MA-ROM method to combine multi-fidelity fields with disparate representations. We assessed the effect of inconsistent dimensionalities, topologies, and features, on the predictive performance of the method beyond any differences in terms of model fidelity. Specifically, we performed experiments combining multi-fidelity datasets where each type of field inconsistency is introduced individually. The field prediction error of a MA-ROM with a given field inconsistency was then compared to the results of an equivalent model trained on data of the same fidelity levels, yet without the inconsistency of interest.

We tested the capability of the MA-ROM method to fuse fields with inconsistent dimensionalities by considering two sets of multi-fidelity fields: one with the high- and low-fidelity solutions having different grid sizes, and one with the high-fidelity results interpolated onto the low-fidelity grid. We demonstrated in Experiment 3.1 that the proposed method can combine fields where the high- and low-fidelity results have different discretizations, and this does not produce any adverse effect on the performance of the MA-ROM method. This implies that if the high- and low-fidelity simulations use different grids, their results can be combined as is, i.e., without the need for additional pre-processing. Although, one can still decide to do so for reasons other than the accuracy of the multi-fidelity method. As for differences in terms of field topology, Experiment 3.2 used the MA-ROM method to augment the prediction of the flow field $C_P$ around an airfoil with low-fidelity results at the airfoil surface only. The obtained results suggest that the MA-ROM method can combine fields with disparate topologies and, as long as their affinity is sufficiently high, this will not have a significant impact on the performance of the method. Therefore, the proposed method is a viable option to combine the solution of simulations applied to different geometries or computational domain. Finally, regarding inconsistencies in terms of field features, we considered in Experiment 3.3 a scenario where the $C_P$

distribution over the CRM wing is used as an auxiliary dataset for the prediction of the $C_F$ field. Despite the high- and low-fidelity results representing different physical quantities and having distinct features, the MA-ROM method was still able to fuse both datasets and provide a superior accuracy than an equivalent single-fidelity ROM. However, when compared to models trained with $C_F$ field results for both the high- and low-fidelity data, the data show that using multi-fidelity fields with inconsistent features incurs a penalty on the overall performance of the proposed method.

In short, the outcome of the above experiments establishes that the MA-ROM method can effectively fuse multi-fidelity fields without any restrictions on their dimensionality, topology, or set of features. This flexibility enables the use of the MA-ROM method for a wide spectrum of multi-fidelity applications. For the most part, this supports our Hypothesis 2 stating that field inconsistencies will not handicap the performance of the proposed method as long as the high- and low-fidelity data are adequately related. One exception is the multi-fidelity combination of fields with inconsistent features. While the proposed method can still leverage the information of fields with different POD modes, it performs better when the training data has consistent field features.

## 5.4 Experiment 4: Comparison with Existing Multi-fidelity Methods

We have identified in Section 2.5 a handful of existing multi-fidelity reduced-order modeling method capable of combining fields of various fidelity into an improved model. Unlike the MA-ROM method developed in this work, most of the current methods cannot readily fuse multi-fidelity fields with disparate representations. As such, the subsequent section outlines experiments that compare the performance of the proposed method to other multi-fidelity methods available in the literature. Since the existing multi-fidelity models are naturally divided into fusion- and adaptation-based methods, separate comparisons are made for these two categories. The outcome

of this experiment is meant to highlight the pros and cons of MA-ROM in the context of the current state of the art. This is directly related to the Research Question 3 and the associated Hypothesis 3.

For the sake of convenience, the existing multi-fidelity reduced-order modeling methods presented previously in Section 2.5 are summarized here. For the fusion-based methods, these are:

- **Common POD** [111]: The high- and low-fidelity results are joined into a single large dataset on which the POD is performed, and the obtained basis is used to project all the fields onto a common latent space. A multi-fidelity regression model is then used to combine the high- and low-fidelity latent variables.

- **Extended POD** [12]: The POD basis of the low-fidelity results is projected onto the null space of the POD basis of the high-fidelity results to extend the latter. The extended basis is then used to compute the high- and low-fidelity results that are both used to train a multi-fidelity regression model.

As for the adaptation-based methods, these are the following:

- **Additive Correction** [105]: The differences between the high- and low-fidelity results are computed, and a correction ROM is trained from the resulting discrepancy fields. High-fidelity predictions are then made by applying the ROM correction over the corresponding solutions generated by the low-fidelity model or a surrogate of it.

- **GPOD Reconstruction** [157]: The $d$-dimensional high-fidelity fields and the $q$-dimensional low-fidelity solutions are stacked such that they form a set of vectors with $d + q$ dimensions. Using the GPOD method, a high-fidelity result is then approximately reconstructed using a corresponding low-fidelity solution, essentially treating the high-fidelity field as missing values.

In Section 2.5, we also presented the latent variable mapping method of Wang et al. [171]. This method consists of using the POD coefficients of the low-fidelity data as input parameters for the regression model of the high-fidelity latent coordinates. However, the CFD solutions in this work can require upward of 50 POD modes to capture properly the main features of the fields. Considering that the accuracy of a surrogate model quickly deteriorates with the dimensionality of the input space, the method proposed by Wang et al. is unlikely to perform well with that many low-fidelity coefficients. In fact, the authors only considered ten or less low-fidelity POD modes in their work. For the above reason, the following experiments ignore the latent variable mapping method.

### 5.4.1 Problem Setup

To compare the accuracy of all the multi-fidelity ROM methods, we once again use the RAE 2822 airfoil test case. More specifically, we focus on the airfoil problem parametrized with $b = 3$ design parameters. Similar to previous experiments, we select the transonic airfoil test case due to the availability of challenging physics and its relevance to aerodynamic design. As in Section 5.1, the field quantity predicted by the ROMs is the $C_P$ distribution within the flow domain surrounding the airfoil. For the high-fidelity results, we use the A1 fidelity level, and the low-fidelity data is provided by either the A2 or A3 fidelity levels. Since the multi-fidelity fields of the RAE 2822 test case all have different discretizations, the high-fidelity results are interpolated onto the low-fidelity grids during a pre-processing step. In other words, for the cases with the A1 + A2 fidelity combination, all the results are mapped onto the coarse RANS grid described in Table 4.4 (10,530 nodes). The same goes for the A1 + A3 fidelity combination except that the inviscid grid (8,910 nodes) of Table 4.4 is used instead. As with the experiment of Section 5.3.1, the interpolated fields are processed using the Paraview visualization software.

Following a methodology similar to Section 5.1.1, the accuracy of the various multi-fidelity ROMs is quantified using the $\widehat{E}(C_P)$ metric, i.e., the normalized prediction error of the $C_P$ field. The multi-fidelity models are trained with $n$ high-fidelity results and $m = \tau \times n$, where $n$ is ranging between 10 and 300 samples and the multi-fidelity ratio is fixed to $\tau = 4$. We also assume a RIC of 99.9999% when computing the POD basis of the various ROM methods. A total of 2,500 cases are available for each fidelity level, and the solutions not considered for the training are used to compute $\widehat{E}(C_P)$ instead. As in all the previous experiments, at least 100 distinct models are trained for every $n$ value and ROM method, each using a different random subset of the CFD database. The presented error is then an average of all the trained models such that the results are not biased toward a specific training and verification set. The prediction errors of a conventional single-fidelity ROM are also computed for reference purposes.

To ensure a fair comparison between the MA-ROM and the other multi-fidelity ROM methods, similar regression models are used for each method that requires one. Single- and multi-fidelity regressions are performed using Kriging and CoKriging models trained using the maximum likelihood criterion as described in Section 3.3. We also note that for the adaptation-based multi-fidelity ROM method, predictions of the high-fidelity results require corresponding low-fidelity solutions. Since the online evaluation of the low-fidelity model can incur a prohibitive computational cost in a many-query context, one can alternatively use the predictions of a ROM trained using the low-fidelity results only. In that case, the low-fidelity ROM is a conventional single-fidelity model trained with $m$ samples and replacing entirely the low-fidelity simulation. This allows the multi-fidelity ROM to be evaluated quickly, but the resulting model must contend with the added inaccuracies of the low-fidelity ROM. For thoroughness, this experiment considers both scenarios for the adaptation-based methods, i.e., using the actual low-fidelity solutions or the predictions of a low-fidelity

ROM.

### 5.4.2 Comparison With Fusion-Based Methods

The prediction errors of the proposed MA-ROM method and the existing fusion-based multi-fidelity ROM are presented in Figures 5.24 and 5.25 for the A1 + A2 and the A1 + A3 fidelity combinations respectively. Both of these figures contain results based on the RAE 2822 test case with $\tau = 4$ and $b = 3$. Looking first at Figure 5.24, we observe that the $\widehat{E}(C_P)$ values with respect to $n$ for the Common and Extended POD methods follow a trend similar to the MA-ROM method. The prediction errors for the Common POD method are lower than for the MA-ROM method with few training samples, and the reverse is seen at larger $n$ values. As for the Extended POD method, its results closely follow the other two methods, yet its prediction error is overall higher. Nevertheless, all the multi-fidelity ROM methods of Figure 5.24 display a substantial reduction in $\widehat{E}(C_P)$ compared to a single-fidelity ROM trained with the same number of high-fidelity samples. This shows that for the current test case and fidelity combination, i.e., RANS CFD simulations using a baseline and coarse grids, the multi-fidelity performance of the MA-ROM method is comparable to the other fusion-based methods. As discussed in Section 4.1.3, this outcome is expected since the formulation of the MA-ROM method owes much to the works of Mifsud et al. [110] and Benamara et al. [12].

Focusing instead on Figure 5.25 for the A1 + A3 fidelity combination, we note that the $\widehat{E}(C_P)$ results for the Common and Extended POD methods are not significantly lower than those for a conventional single-fidelity ROM. In comparison, the prediction errors for the MA-ROM method is still noticeably better than the errors of a single-fidelity model, although not as low as in Figure 5.24. Therefore, the MA-ROM is clearly superior to the other two fusion-based multi-fidelity ROM methods in the current scenario. The lackluster performance of the Common and Extended POD

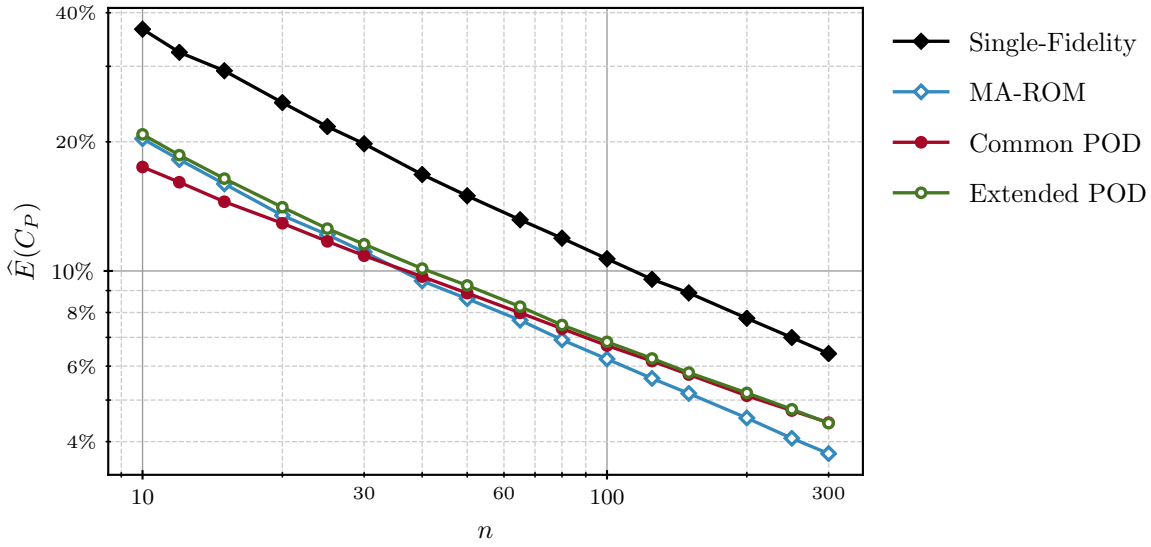


**Figure 5.24:** Field prediction error of the MA-ROM method compared to existing fusion-based multi-fidelity ROM methods. Results correspond to the RAE test case with the A1 + A2 fidelity combinations, $\tau = 4$, and $b = 3$.

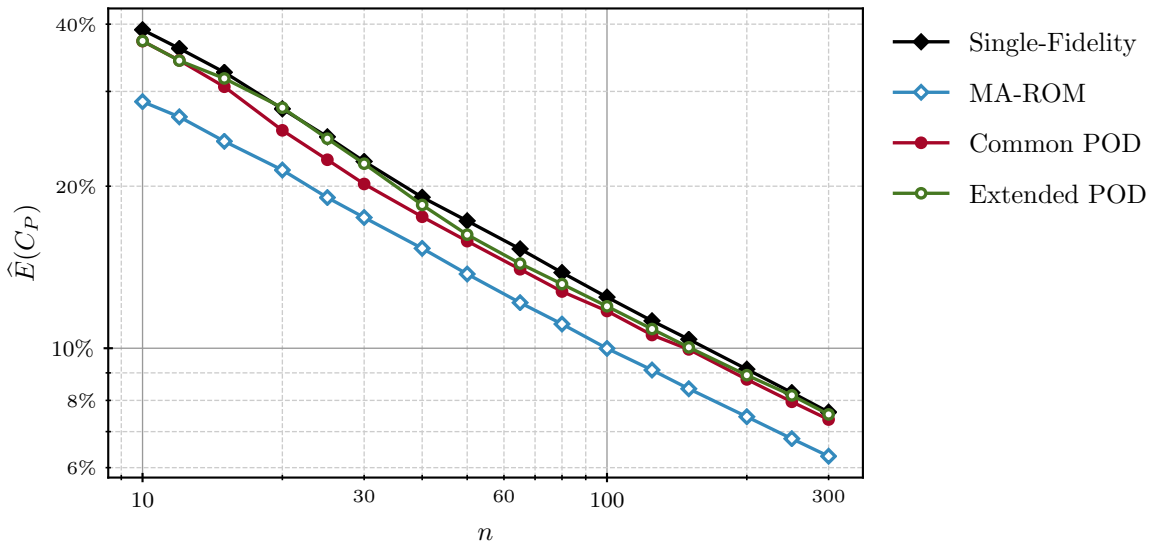


**Figure 5.25:** Field prediction error of the MA-ROM method compared to existing fusion-based multi-fidelity ROM methods. Results correspond to the RAE test case with the A1 + A3 fidelity combinations, $\tau = 4$, and $b = 3$..

methods is explained by the fact that a single POD basis is used to project both the high- and low-fidelity data. This assumes that the computed latent space is representative of both fidelity levels at once. With the A1 + A2 fidelity combination, this assumption is reasonable since both the high- and low-fidelity models are RANS CFD simulations, and differences in flow features should be reasonably small. Considering instead the A1 + A3 fidelity combination, the high- and low-fidelity solutions use different physics models, i.e., RANS and inviscid CFD, such that the principal features of both datasets are less likely to be overlapping. By then forcing the same projection basis on both datasets, the correspondence between the high- and low-fidelity latent variables ends up being suboptimal for the multi-fidelity regression model. The MA-ROM method avoids that issue by optimally aligning the high- and low-fidelity latent variables with a Procrustes analysis before training the regression model. The results of Figure 5.25 establish that the existing fusion-based methods struggle more with challenging fidelity combinations than the proposed MA-ROM method.

To provide additional insights regarding the differences between the MA-ROM, Common POD, and Extended POD methods, Table 5.19 presents a breakdown of the prediction errors of Figures 5.24 and 5.25. Namely, these errors are expressed in terms of their reconstruction and regression components, i.e., $\widehat{E}_{\text{rc}}(C_P)$ and $\widehat{E}_{\text{rg}}(C_P)$ respectively. The results of this table show that for both the A1 + A2 and the A1 + A3 fidelity combinations, the Common and Extended POD methods have lower reconstruction errors than the proposed method globally. Unlike the MA-ROM method, the existing fusion-based methods compute the POD modes using both the high- and low-fidelity data. This results in a more accurate projection basis and lower $\widehat{E}_{\text{rc}}(C_P)$ values. As for the regression errors, the $\widehat{E}_{\text{rg}}(C_P)$ results are lower for the MA-ROM method, which directly highlights the benefit of the manifold alignment. Since the reconstruction and regression errors have a similar order of magnitude with sparse training samples, the lower $\widehat{E}_{\text{rc}}(C_P)$ of the Common POD method explains why it

**Table 5.19:** Tabulated $\widehat{E}(C_P)$ of MA-ROMs trained with and without inconsistent dimensionalities. Models are trained with the A1 + A2 and A1-I + A2 fidelity combinations for the RAE 2822 test case.

| Fidelity | Method | $\tau$ | $n$ | $\widehat{E}(C_P)$ | $\widehat{E}_{\text{rc}}(C_P)$ | $\widehat{E}_{\text{rg}}(C_P)$ |
|---|---|---|---|---|---|---|
| A1 + A2 | MA-ROM | 4 | 10 | 20.3% | 16.0% | 12.4% |
| | | | 100 | 6.23% | 0.90% | 6.16% |
| | | | 300 | 3.75% | 0.24% | 3.74% |
| A1 + A2 | Common POD | 4 | 10 | 17.5% | 2.94% | 17.2% |
| | | | 100 | 6.70% | 0.47% | 6.68% |
| | | | 300 | 4.43% | 0.26% | 4.42% |
| A1 + A2 | Extended POD | 4 | 10 | 20.8% | 2.88% | 20.62% |
| | | | 100 | 6.83% | 0.38% | 6.82% |
| | | | 300 | 4.42% | 0.17% | 4.41% |
| A1 + A3 | MA-ROM | 4 | 10 | 28.7% | 18.2% | 22.2% |
| | | | 100 | 10.0% | 1.01% | 9.94% |
| | | | 300 | 6.30% | 0.26% | 6.29% |
| A1 + A3 | Common POD | 4 | 10 | 37.2% | 5.18% | 36.8% |
| | | | 100 | 11.7% | 0.66% | 11.7% |
| | | | 300 | 7.37% | 0.31% | 7.36% |
| A1 + A3 | Extended POD | 4 | 10 | 37.2% | 5.17% | 36.9% |
| | | | 100 | 12.0% | 0.56% | 12.0% |
| | | | 300 | 7.53% | 0.21% | 7.53% |

is superior to the MA-ROM method for smaller $n$. However, the reconstruction error rapidly becomes small with larger $n$ values, while the regression error remains substantial. Because of this, the MA-ROM method offers lower prediction errors when we provide more training samples. The consequence of using separate POD bases for the high- and low-fidelity datasets in the MA-ROM method is a slightly higher $\widehat{E}_{\text{rc}}(C_P)$ when compared to existing fusion-based methods. This drawback is easily compensated by a reduced $\widehat{E}_{\text{rg}}(C_P)$ and the capability of combining fields with inconsistent representations.

### 5.4.3 Comparison With Adaptation-Based Methods

We show in Figure 5.26 the field prediction errors of the MA-ROM method compared to those of existing adaptation-based methods combining RANS CFD solutions computed with a baseline and coarse grid, i.e., the A1 + A2 fidelity combination. For the Additive Correction and the GPOD Reconstruction methods, the solid lines represent cases where the adaptation-based methods are applied to the exact low-fidelity solutions. The dashed lines of the same colors are instead results where the high-fidelity predictions are based on low-fidelity solutions approximated by a ROM of the low-fidelity training data, which we denote as LF-ROM. The results of Figure 5.26 reveal that the standard Additive Correction method (i.e., without the LF-ROM) performs better than the proposed MA-ROM method for $n <= 100$. For cases where this method is combined with a low-fidelity ROM to circumvent the costly evaluation of the low-fidelity simulation (i.e., with the LF-ROM), the $\widehat{E}(C_P)$ values are instead higher than those of the MA-ROM method for $n >= 30$. Since a separate ROM provides the low-fidelity solutions, the prediction errors are compounded with the errors of the Additive Correction itself, thus degrading the overall performance of the method. We should note that the many-query context requires fast evaluations and would likely necessitate the use of a low-fidelity ROM for adaptation-based methods.

In which case, the MA-ROM method would be a better candidate than the Additive Correction method for the current multi-fidelity problem.

As for the GPOD Reconstruction, Figure 5.26 shows that for small $n$ values, this multi-fidelity method offers better predictions compared to a single-fidelity ROM. However, this improvement disappears with larger training datasets. Reconstructing the high-fidelity results from the LF-ROM predictions rather than the exact low-fidelity solutions results in lower $\widehat{E}(C_P)$, yet the GPOD Reconstruction method is still inferior to the other multi-fidelity methods. We should mention that the GPOD method is meant to reconstruct datasets with randomly missing entries [41]. In the context of a multi-fidelity ROM, the high- and low-fidelity fields are assumed to be two parts of the same solution where the high-fidelity entries are always assumed to be missing, which is not random. Therefore, the formulation of the GPOD Reconstruction method is not ideal for multi-fidelity applications.

In a similar way to Figure 5.26, the results of Figure 5.27 compares the performance of the MA-ROM and existing adaptation-based methods, yet is applied to the A1 + A3 fidelity combination instead of the A1 + A2 combination. As mentioned in Section 5.4.2, this is a more challenging multi-fidelity problem since the high- and low-fidelity simulations are based on different governing equations, i.e., RANS and Euler equations. Consequently, the flow features between corresponding cases of the different fidelity levels are not necessarily aligned and hinder the accuracy of the multi-fidelity methods. The results of Figure 5.27 show that for the current fidelity combination, the field prediction errors of both the Additive Correction and the GPOD Reconstruction are actually worse than those of a conventional single-fidelity ROM trained with the same number of high-fidelity samples. In other words, the addition of low-fidelity data to the adaptation-based methods degrades their accuracy rather than improving it for the A1 + A3 fidelity combination. Recall that in similar circumstances, the fusion-based multi-fidelity methods also performed poorly

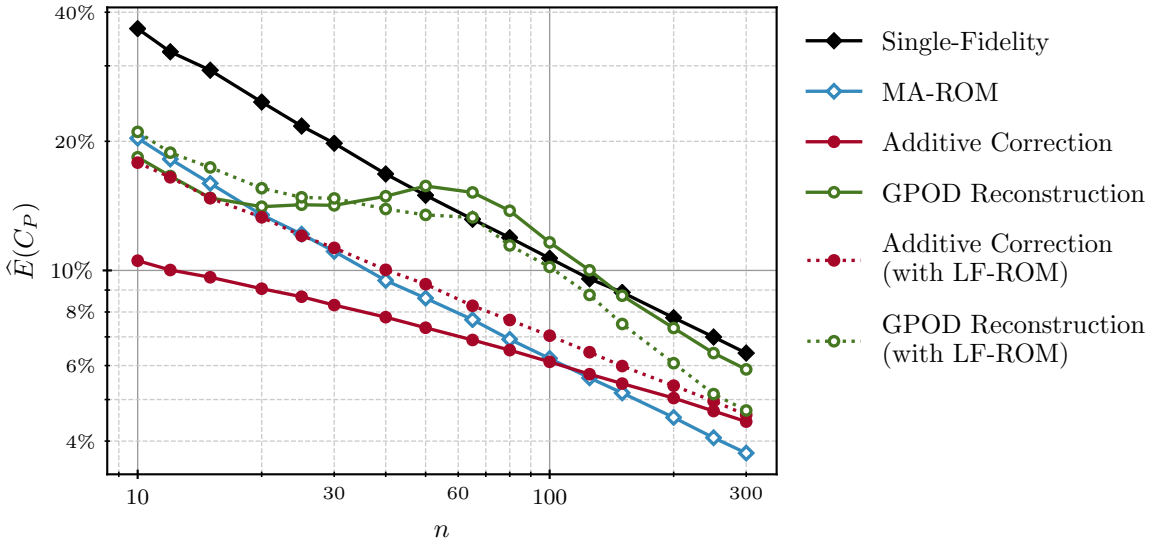


**Figure 5.26:** Field prediction error of the MA-ROM method compared to existing adaptation-based methods applied to ROM predictions of the low-fidelity results (LF-ROM). Results correspond to the RAE test case with the A1 + A2 fidelity combinations, $\tau = 4$, and $b = 3$.

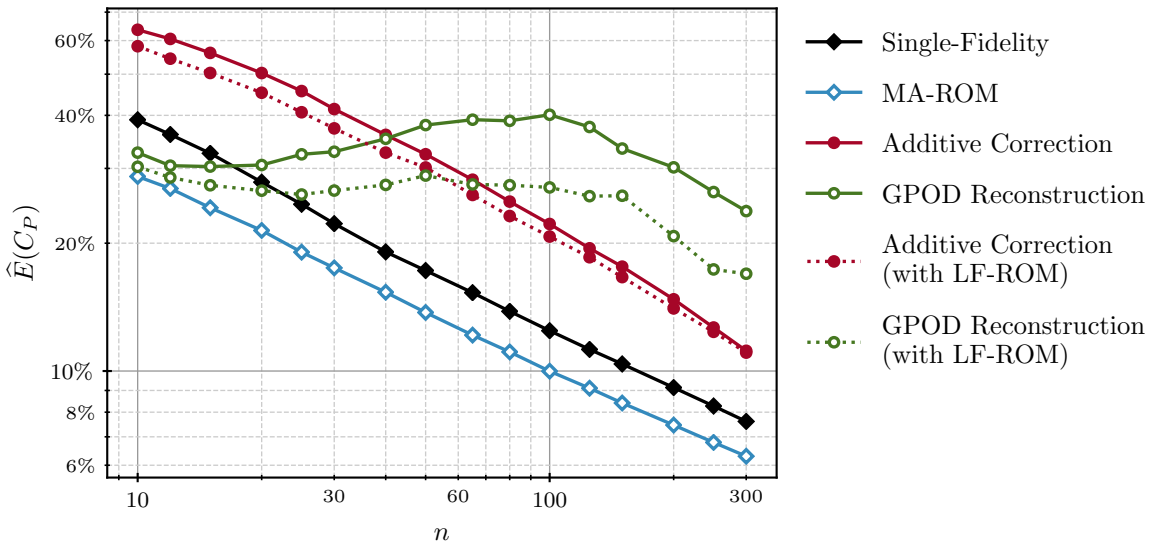


**Figure 5.27:** Field prediction error of the MA-ROM method compared to existing adaptation-based methods applied to ROM predictions of the low-fidelity results (LF-ROM). Results correspond to the RAE test case with the A1 + A3 fidelity combinations, $\tau = 4$, and $b = 3$.

as shown in Figure 5.25, yet their $\widehat{E}(C_P)$ values were still slightly lower than those of a single-fidelity method. Interestingly, the $\widehat{E}(C_P)$ for the adaptation-based methods applied to the exact low-fidelity fields is higher than for methods using the prediction of a low-fidelity ROM. Although, in both cases the errors are still noticeably higher than for a single-fidelity approach. It is also worth noting that while the adaptation-based methods have disappointing performance in the current scenario, the proposed MA-ROM method still offers an appreciable reduction in $\widehat{E}(C_P)$ compared to a conventional ROM.

### 5.4.4 Summary

The purpose of this experiment was to compare the prediction accuracy of the developed MA-ROM method to those of existing multi-fidelity ROM methods previously identified in Section 2.5. As stated in Hypothesis 3, the formulation of the MA-ROM method can be categorized as a fusion-based method, and its performance is expected to be similar to the Common POD and the Extended POD methods in scenarios combining fields with consistent representations. This was corroborated in Section 5.4.2 where the fusion-based methods were used to combined results of RANS CFD simulations using different grid sizes. While the Common POD methods had slightly lower prediction errors with small training datasets, the MA-ROM was superior with additional training data. However, when combining RANS and inviscid results, the existing fusion-based methods generally performed poorly, and their accuracy was on par with that of a single-fidelity approach. This is because the RANS and inviscid flow fields have slightly different features, and the Common and Extended POD methods have no mechanism to address this inconsistency. The MA-ROM method resolves this inconsistency with the manifold alignment and was still able to produce more accurate results than a single-fidelity ROM.

As for adaptation-based methods, the results of Section 5.4.3 showed that only the

Additive Correction method was able to produce better results than the MA-ROM method. However, the developed method was only outperformed by the Additive Correction method applied to exact low-fidelity solutions and with the A1 + A2 fidelity combination. In other cases using the low-fidelity ROM predictions or the A1 + A3 fidelity combinations, the MA-ROM method was overall superior to the existing adaptation-based methods. Additionally, comparing the results of Sections 5.4.2 and 5.4.3, we note that the fusion-based methods generally have better predictions than adaptation-based methods as it is the cases with multi-fidelity data-fit models (see Section 2.3).

All in all, this experiment has demonstrated that the MA-ROM method developed in this work is a viable solution for multi-fidelity problems even in the absence of field inconsistencies. Even though the MA-ROM method was outperformed by some of the alternative multi-fidelity ROMs in a handful of the considered cases, its accuracy was generally as good or better than existing methods.

## 5.5 Supplementary Observations

This last section presents additional observations regarding the MA-ROM method obtained from the results of the previous experiments. While these observations do not directly answer the research questions outlined in Chapter 4, they remain insightful and are provided here for completeness.

### 5.5.1 Benefits of the Manifold Alignment

In Section 3.2.1, we explained that in a non-intrusive ROM, the components of a predicted latent variable $\widetilde{\mathbf{z}} \in \mathbb{R}^k$ are obtained using a set of $k$ regression models $\widetilde{\mathbf{g}}(\mathbf{p}) = [\widetilde{g}_1(\mathbf{p}), \ldots, \widetilde{g}_k(\mathbf{p})]$. With the MA-ROM method, $\widetilde{\mathbf{g}}(\mathbf{p})$ is instead comprised of multi-fidelity regression models trained with the high-fidelity latent variables $\mathbf{Z}_{\text{hi}} \in \mathbb{R}^{k \times n}$ and the aligned low-fidelity latent variables $\mathbf{Z}_{\text{lo}} \in \mathbb{R}^{k \times m}$. Since each component

of $\widetilde{\mathbf{z}} \in \mathbb{R}^k$ is predicted separately, $\mathbf{Z}_{\text{hi}}$ and $\mathbf{Z}_{\text{lo}}$ are fused component-wise (i.e., row-wise) by the multi-fidelity regression models. The purpose of the Procrustes manifold alignment is thus to correctly match the components of the high- and low-fidelity latent variables. In other words, the alignment ensures that the $i$-th component of $\mathbf{Z}_{\text{lo}}$ is best correlated to the $i$-th component of $\mathbf{Z}_{\text{hi}}$. As a result, each multi-fidelity regression model within $\widetilde{\mathbf{g}}(\mathbf{p})$ can fully leverage the additional information available within the low-fidelity data.

To demonstrate the role of the Procrustes manifold alignment in the MA-ROM method, we show in Figures 5.28 and 5.29 the consequences of omitting the alignment step during the training of multi-fidelity models. These figures reuse the results of Section 5.1.2 related to Experiment 1 with the RAE 2822 airfoil test case. Figure 5.28 shows $\widehat{E}(C_P)$ as a function of $n$ for the A1 and A2 fidelity combination, while Figure 5.29 presents the errors for the A1 and A3 combination. The left side of these figures shows the original MA-ROM results, and the right side gives the prediction errors for multi-fidelity ROMs without the manifold alignment. The latter models are trained with an approach similar to MA-ROM except that the multi-fidelity regression models $\widetilde{\mathbf{g}}(\mathbf{p})$ are using $\mathbf{W}$ instead $\mathbf{Z}_{\text{lo}}$ as the low-fidelity dataset, where $\mathbf{W}$ contains the low-fidelity latent variables prior to the manifold alignment (see Section 3.2.2).

From the results of Figures 5.28 and 5.29, we note that multi-fidelity ROMs trained with the manifold alignment are clearly superior to models trained without it. For instance, with the A1 + A2 fidelity combination, $n = 100$, and $\tau = 4$, the prediction error of a MA-ROM as shown in Figure 5.28a is roughly half the error of a single-fidelity ROM. In comparison, the error in Figure 5.28b for an equivalent multi-fidelity ROM without the manifold alignment is barely lower than the single-fidelity result. With the A1 and A3 fidelity combination instead, the results of Figure 5.29b suggest that without the manifold alignment, the accuracies of single- and multi-fidelity ROMs are more or less the same. Therefore, the current results provide evidence

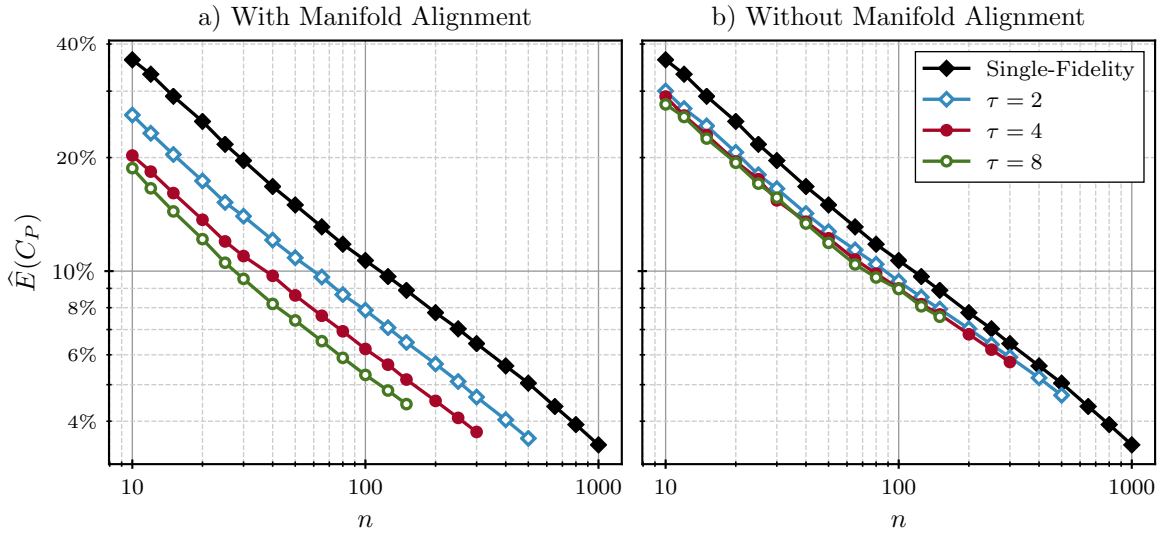


**Figure 5.28:** Field prediction errors of multi-fidelity ROMs generated with (a) and without (b) manifold alignment. Models are trained with the A1 + A2 fidelity combinations for the RAE 2822 test case and with $b = 3$.

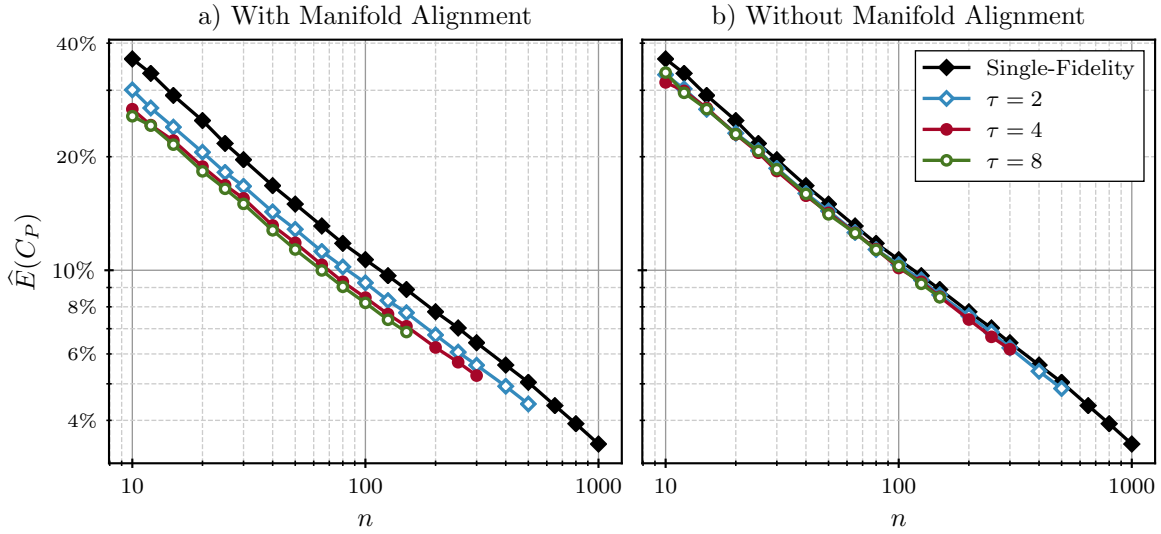


**Figure 5.29:** Field prediction errors of multi-fidelity ROMs generated with (a) and without (b) manifold alignment. Models are trained with the A1 + A3 fidelity combinations for the RAE 2822 test case and with $b = 3$.

supporting the inclusion of the Procrustes manifold alignment within the developed method. Without the alignment step, even though the $\mathbf{Z}_{\text{hi}}$ and $\mathbf{W}$ datasets are related, their individual components (i.e., rows) are not necessarily correlated. In turn, the effectiveness of $\widetilde{\mathbf{g}}(\mathbf{p})$ is reduced and new latent variables cannot be predicted with greater accuracy.

### 5.5.2 Low-Fidelity vs. Multi-Fidelity ROMs

An important assumption used throughout this thesis is that the accuracy of the low-fidelity simulation is inadequate for a given design task. Indeed, we focused on the prediction of the high-fidelity field, and we proposed the MA-ROM method to achieve this at a lower computational cost. However, if limited computing resources are available or if the accuracy of the field prediction is not critical, an argument could be made for simply predicting the low-fidelity field instead of the high-fidelity one.

For instance, let us consider the simulation error as the difference between the high- and low-fidelity fields. Following the error definitions of Section 4.3, this error can be defined as

$$E_{\text{sim}}(\mathbf{y}) = \sqrt{\frac{\sum_{j=1}^{n} \|\mathbf{x}_j - \mathbf{y}_j\|_2^2}{n}} \tag{5.1}$$

where $\mathbf{x}_j \in \mathbb{R}^d$ and $\mathbf{y}_j \in \mathbb{R}^d$ are fields produced by the high- and low-fidelity simulation respectively. Note that $E_{\text{sim}}(\mathbf{y})$ can only be calculated if the high- and low-fidelity fields share the same representation. Also, the value of $E_{\text{sim}}(\mathbf{y})$ solely depends on the fidelity difference between the considered simulations. Assuming that the high- and low-fidelity fields are consistent, one could potentially use a ROM trained with low-fidelity samples only to approximate the high-fidelity simulation. In which case, the error of this low-fidelity ROM would combine the simulation error of Eq. (5.1) and the prediction error of the surrogate model. Since the low-fidelity simulation should be relatively cheap to evaluate, one can reasonably train a ROM with a small

prediction error at a relatively low cost. If $E_{\text{sim}}(\mathbf{y})$ is also sufficiently small, then using a ROM of the low-fidelity data could be a computationally cheaper substitute for the high-fidelity simulation.

To demonstrate how a ROM of the low-fidelity data could be a viable option, Figure 5.30 shows the prediction errors for ROMs trained with A1 data, ROMs trained with A2 data, and MA-ROMs trained with the A1 + A2 fidelity combination. These results use the RAE 2822 test case with the $b = 3$ parametrization as presented previously in Section 5.1.2. For the ROMs trained with A2 data, the error values represent the discrepancy between the actual high-fidelity and the predicted low-fidelity $C_P$ fields. Since the A1 and A2 fidelity levels use different grid sizes, the A2 ROM predictions are mapped to the high-fidelity grid to compute the error. From Figure 5.30, we see that for small $n$, the A2 ROM error is dominated by the surrogate error, and its $\widehat{E}(C_P)$ value is similar to the A1 ROM results. With additional training data, the A2 ROM error asymptotically converges to roughly 16%, which corresponds to the simulation error of the A2 fidelity level. This demonstrates that approximating the high-fidelity solutions with low-fidelity predictions will produce an error bounded from below by the simulation error. However, if we take the computational cost into account, the right side of Figure 5.30 shows that for a very small computational budget, a ROM using A2 data provides a lower overall error than either a ROM using A1 data or a multi-fidelity ROM combining both fidelity levels. At this lower limit, the accuracy of the A2 ROM is still low but could be sufficient for some design scenarios.

We can also extend this demonstration to a different fidelity combination and the results of Figure 5.31 shows the prediction error for ROMs trained with A1 data, ROMs trained with A3 data, and MA-ROMs trained with the A1 + A3 fidelity combination. These results are obtained similarly to Figure 5.30 except that the A3 fidelity level is used instead of the A2. In this scenario, the errors of ROMs

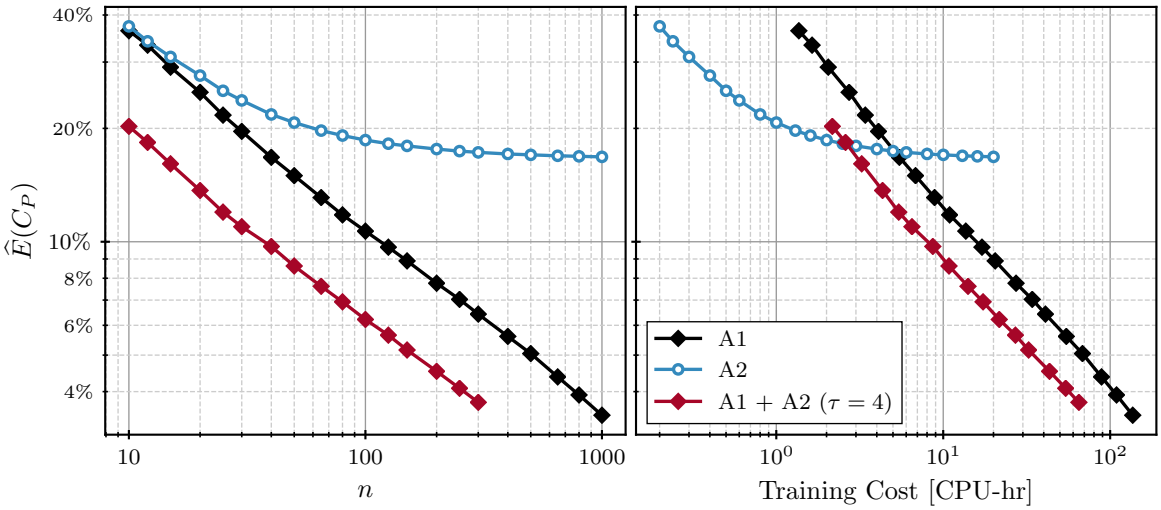


**Figure 5.30:** Normalized errors for single- and multi-fidelity ROMs trained with the A1, A2, or A1 + A2 fidelity levels. Models are trained using the RAE 2822 test case with $b = 3$, and all errors are with respect to the A1 fidelity level.

trained with only A3 data are constant at roughly 90%, which corresponds to the simulation error between the A1 and A3 fidelity levels. This suggests that for this fidelity combination, the low-fidelity fields are not an adequate replacement for the high-fidelity solutions regardless of its lower computational cost. However, the A3 data can still be combined with the A1 data using a multi-fidelity ROM and produce a more accurate model than a single-fidelity ROM trained with A1 data only.

In summary, the results of Figures 5.30 and 5.31 illustrates that one should not necessarily assume that the low-fidelity results are inadequate. While training an accurate ROM with either a single- or multi-fidelity method will require high-fidelity data, this accuracy might not be needed for every design task. Alternatively, the limited availability of computational resources could be such that producing enough high-fidelity data is impractical, even with a multi-fidelity approach. Ultimately, the adequate surrogate modeling option will depend on what trade-off between accuracy and training cost is admissible for a given task. We argue that in many design problems, the MA-ROM method is likely the better solution, but we also acknowledge that simpler alternatives are sufficient in some scenarios. However, it is important

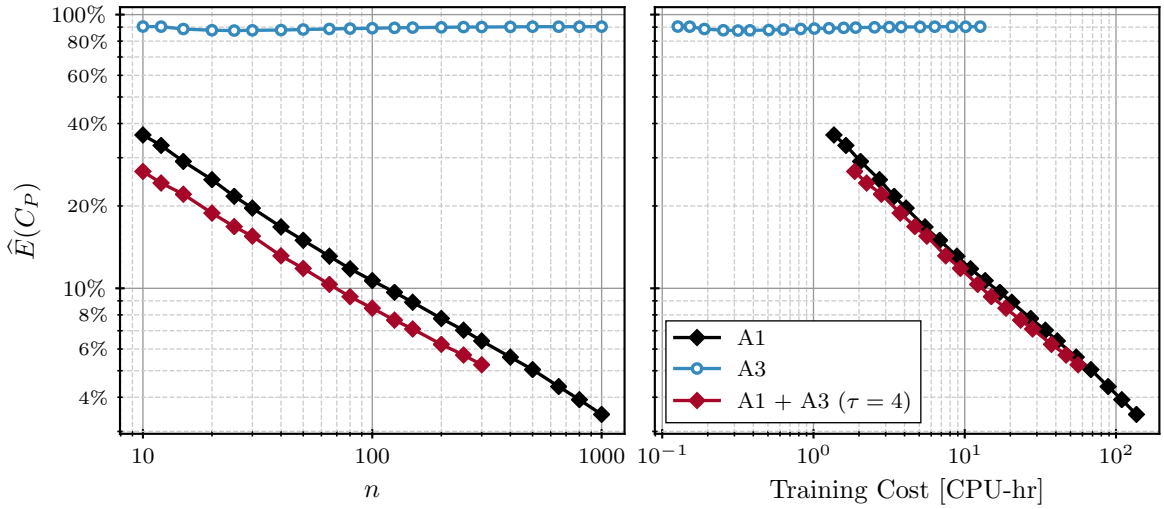


**Figure 5.31:** Normalized errors for single- and multi-fidelity ROMs trained with the A1, A3, or A1 + A3 fidelity levels. Models are trained using the RAE 2822 test case with $b = 3$, and all errors are with respect to the A1 fidelity level.

to point out that the current demonstration assumes that the high- and low-fidelity fields have a consistent representation. Using only the low-fidelity results could be infeasible simply because the fields might not have the correct representation, in which case the MA-ROM method should be considered.

### 5.5.3 Error Distribution within Design Space

The prediction errors presented in the previous experiments of this chapter represent the overall accuracy of a single- or multi-fidelity ROM across the design space. Considering for instance the $C_P$ field, the error $e(C_P)$ of each test samples is combined into the normalized RMS error $\widehat{E}(C_P)$ as defined in Section 4.3.1. While a global error metric is a helpful indicator of a ROM performance, individual test samples can have a higher and lower prediction error depending on their design parameters values. As such, the following section demonstrates what factors can affect the prediction error distribution within the design space.

To illustrate the error variation across the design space, Figure 5.32 shows the distribution of the sample error $e(C_P)$ for a single-fidelity ROM of the CRM wing

as defined in Section 5.2.2. This ROM is trained using $n = 50$ samples from the W1 fidelity datasets and considers $b = 2$ design parameters, which corresponds to the wing root and tip twists. We choose this scenario specifically for its low input space dimensionality, which facilitates the visualization. To complement the results of Figure 5.32, Figure 5.33 presents the $e(C_P)$ distribution for a MA-ROM trained with the same high-fidelity samples, and enhanced with $m = 200$ additional low-fidelity samples from the W2 fidelity dataset.

From Figure 5.32, we observe that the sample error is highest in the upper right region of the design space, which corresponds to the maximum root and tip twist values. Twisting the wing root or tip upward raises the local angle of attack, and in turn, increases the sectional lift of the wing. In transonic flow conditions, a higher lift is typically associated with the presence of stronger shocks. As mentioned previously, POD-based ROMs tend to struggle in situations involving strong discontinuities [92], which would explain the increased error at larger twist values. This demonstrates that the accuracy of a ROM is likely to be lower in regions of the design space having more challenging physics. The results of Figure 5.32 also shows that the error is lower in the vicinity of the training samples. This implies that the predictions are less accurate in large unexplored regions of the design space. This behavior can be attributed to the regression models within the ROM, which are Kriging models in this work. As defined in Section 3.3.1, the Kriging predictor depends on the spatial correlation between existing observations. Since this correlation is based on the distance between points in the design space, the prediction uncertainty is higher when the point of interest is far from existing observations, which explain the results of Figure 5.32. Additionally, the results of Figure 5.33 show that enhancing the high-fidelity data with low-fidelity samples produces a similar trend in the error distribution. The prediction error for a MA-ROM is indeed highest at the maximum twist values and away from existing high-fidelity samples. However, compared to Figure 5.32, the error is overall lower for

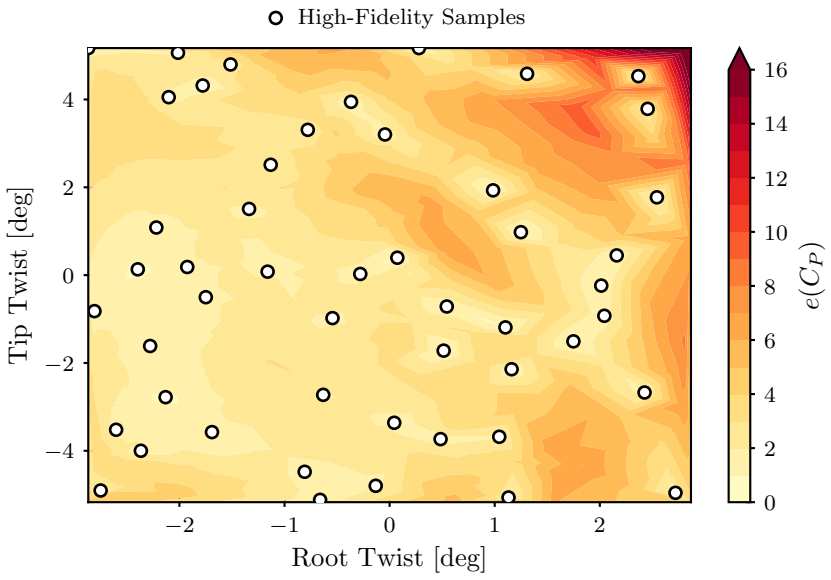


**Figure 5.32:** Prediction error distribution within the design space for a single-fidelity ROM of the W1 fidelity level. The results correspond to the CRM wing test case with the $b = 2$ parametrization.

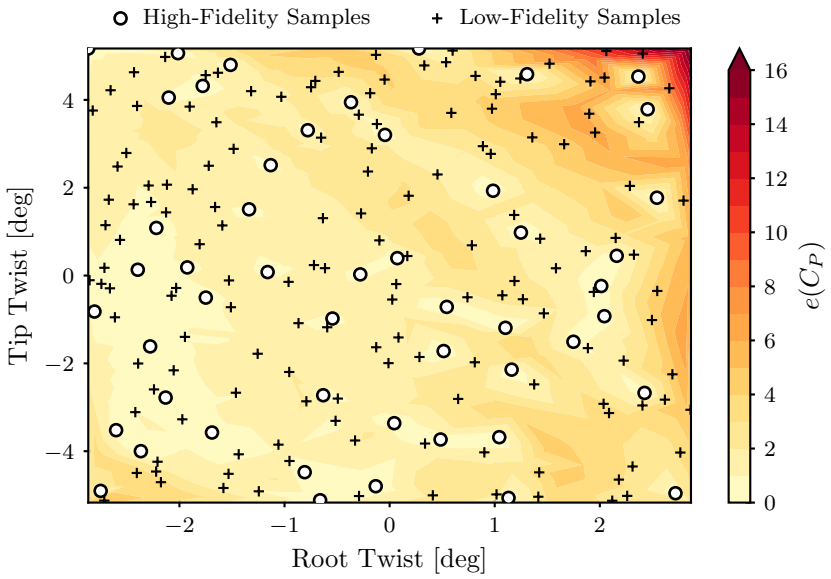


**Figure 5.33:** Prediction error distribution within the design space for a MA-ROM combining the A1 and A2 fidelity levels with $\tau = 4$. The results correspond to the CRM wing test case with the $b = 2$ parametrization.

the multi-fidelity than for the single-fidelity ROM. This indicates that the benefits of a multi-fidelity approach are more or less uniform across the design space as we previously discussed in Section 1.4.3.

To summarize, this demonstration has established that the accuracy of a surrogate is not constant within the design space. With the current single- and multi-fidelity ROM methods, one can expect higher prediction errors in the presence of challenging physics and in under-sampled regions of the design space. However, despite the prediction error being non-uniformly distributed, a multi-fidelity method will reduce it globally.

# CHAPTER 6
# CONCLUSION

This dissertation has explored the use of ROMs as a replacement of high-fidelity simulations for preliminary aircraft design and the many-query context. Although these models can predict high-dimensional fields results with relative ease, their accuracy is conditional on the amount of data used for their construction. Gathering such datasets of high-fidelity solutions can incur a prohibitive cost, and we address this limitation by seeking a multi-fidelity variant of reduced-order modeling. Moreover, field results of different fidelity can have disparate representations, which we identified as a major obstacle to the construction of multi-fidelity ROMs. We proposed a novel multi-fidelity ROM method based on the Procrustes manifold alignment that is capable of merging fields with inconsistent dimensionalities, topologies, and features. An experimental approach with practical problems was then used to assess the performance and limitations of the proposed method. The following chapter discusses the main findings of this work and presents some avenues for future research.

## 6.1 Summary of Research Questions and Findings

The research formulation presented in Chapter 4 was the foundation of the experimental approach taken in Chapter 5. This research focused on three main areas, i.e., the multi-fidelity performance of the MA-ROM method, the effects of field inconsistencies on the multi-fidelity predictions, and a comparison between the proposed method and existing alternatives. The subsequent sections review the formulated research questions and hypotheses considering the experimental results.

### 6.1.1 Multi-Fidelity Performance

For the MA-ROM method to be a successful multi-fidelity solution, it must be able to provide some benefits, in terms of accuracy and cost, when compared to a single-fidelity approach. As such, we formulated the first research question of this work as follows:

**Research Question 1**

Compared to an equivalent single-fidelity ROM, can the proposed multi-fidelity method improve the overall performance of the model, in terms of accuracy and training cost, by augmenting high-fidelity data with low-fidelity results?

From the literature on multi-fidelity surrogate modeling, it was determined that the performance of a multi-fidelity method would depend on the fidelity gap between the high- and low-fidelity results. Since low-fidelity fields augment the high-fidelity results, the proportion of training samples coming from each dataset would also affect the performance of the method. This led to the following hypothesis:

**Hypothesis 1.1**

Similarly to multi-fidelity data-fit models, the performance of a MA-ROM, in terms of accuracy and training costs, should be superior to an equivalent single-fidelity model. Furthermore, the performance improvement between a multi- and single-fidelity model, if any, should depend on the ratio of high- and low-fidelity results, and the fidelity difference between both sources of data.

The above hypothesis was verified with Experiments 1 and 2 (see Sections 5.1 and 5.2) that applied the MA-ROM method on test cases using the RAE 2822 airfoil

and the CRM wing. These experiments tested multiple model configuration using different fidelity combinations, training data sizes, and ratios between high- and low-fidelity results. The outcomes showed that the developed method could reduce the training cost by up to 78% when compared to a single-fidelity ROM with the same prediction error. Similarly, the field prediction error given by the MA-ROM method could be up to 42% lower than a conventional ROM training with the same computational budget. The potential improvement of the proposed method was also found to depend on the fidelity combination being used. We observed that the MA-ROM performed best when using high- and low-fidelity solutions obtained from similar simulations, yet with different discretizations. When combining fields issued from different governing equations, such as the RANS and Euler equations, the performance of the MA-ROM method was still superior to a single-fidelity ROM, but by a smaller margin. At worst, if the high- and low-fidelity data are fundamentally different, the results show that the MA-ROM will perform similarly to a single-fidelity ROM. It was also observed from Experiments 1 and 2 that for a set of high-fidelity samples, the proposed method would become more accurate with additional low-fidelity results, but only up to a limit. In many cases, no appreciable benefits were observed from using a ratio of low- to high-fidelity samples of four or more, especially when considering the compounded cost of generating the data. Therefore, one cannot solely rely on the low-fidelity simulation to generate an accurate model.

Additionally, we identified that the high training cost of ROMs is mostly problematic for design problems involving many design parameters. A multi-fidelity approach was proposed specifically because it does not directly depend on the input dimensionality. This observation produced the following hypothesis:

**Hypothesis 1.2**

Similarly to multi-fidelity data-fit models, the relative benefits of a MA-ROM compared to an equivalent single-fidelity ROM, in terms of cost and accuracy, should be preserved in situations with many design parameters.

As part of Experiments 1 and 2, the MA-ROM method was also applied to design problems with parametrizations of different sizes. For cases involving the RAE 2822 airfoil, the absolute prediction error of both single- and multi-fidelity ROMs was shown to degrade with additional design parameters. Nevertheless, the relative difference between the prediction errors of the MA-ROM and an equivalent single-fidelity method was roughly the same for all the parametrization sizes. With the CRM wing test case, an improvement in the relative performance of the MA-ROM method was observed with additional design parameters instead. This behavior was attributed to the smaller proportion of regression error associated with the lower-dimensional parametrization.

Overall, the results of both Experiments 1 and 2 confirms our Hypotheses 1.1 and 1.2. This establishes that the developed method can indeed be used to improve the prediction of models by augmenting high-fidelity data with low-fidelity results.

### 6.1.2 Effect of Field Inconsistencies

The development of the MA-ROM method was predominantly motivated by the issue of field inconsistencies between solutions of different fidelity levels. As such, it is necessary to verify that the proposed method is capable of fusing fields with disparate representations and assess how these inconsistencies affect the method. In other words:

**Research Question 2**

Is the multi-fidelity performance of the proposed MA-ROM method affected by inconsistencies between the high- and low-fidelity field representations in terms of dimensionality, topology, and feature?

The formulation of the MA-ROM method is such that the high- and low-fidelity data are individually projected in distinct subspaces. Once embedded in their respective latent spaces, their coordinates are aligned with the Procrustes analysis. The MA-ROM method fuses the latent representation of the high- and low-fidelity data, which bypasses any inconsistencies in their original representation. From this reasoning, the following hypothesis was formulated:

**Hypothesis 2**

Aside from differences in terms of fidelity levels, inconsistencies between the field representations of the high- and low-fidelity results should not directly affect the performance of the MA-ROM method since the multi-fidelity datasets are fused after being projected onto a shared latent space.

As defined in Section 5.3, Experiment 3 verifies Hypothesis 3 by comparing side-by-side multi-fidelity cases with and without consistent field representations among the high- and low-fidelity data. These multi-fidelity problems would also use equivalent fidelity combinations to isolate the effect of field inconsistencies on the performance of MA-ROM. Since the inconsistencies between fields can either be in terms of dimensionality, topology, or features, Experiment 3 was subdivided into three sub-experiments, each testing a specific type of inconsistency. The results of Experiment 3.1 demonstrated that fields using disparate discretizations, i.e., having

different dimensionality, can be combined with the MA-ROM method without adverse effect. Unlike other multi-fidelity ROM methods, the developed method can be applied without mapping all the results onto a common grid beforehand. Similarly, the results of Experiment 3.2 established that differences in topology did not appreciably affect the performance of the MA-ROM method. In Experiment 3.3, we used the proposed method to combine high- and low-fidelity results representing different physical quantities, and as such, having different features. Specifically, the high-fidelity $C_F$ distribution over the CRM wing was augmented by the low-fidelity $C_P$ distribution. In this instance, the results showed that models fusing the $C_F$ and $C_P$ fields had inferior performance when compared to equivalent models using the $C_F$ fields for both the high- and low-fidelity data. Nonetheless, despite joining different physical quantities, the prediction of the MA-ROM method was better than an equivalent single-fidelity model.

In summary, the results of Experiment 3 partially confirm Hypothesis 2. While combining fields with different features did have an impact on the MA-ROM method, the loss in performance remained reasonably low, and the method could still provide some benefits. At the very least, the results of Experiment 3 demonstrate that the proposed method can successfully fuse multi-fidelity fields with disparate representations in practical applications.

### 6.1.3 Comparison with Existing Multi-Fidelity Methods

As described in Section 2.5, other researchers have previously developed for multi-fidelity methods for reduced-order modeling. While most of these existing solutions do not directly address the issue of field inconsistencies, they were shown to have better performance than a single-fidelity model on practical problems. As such, it is reasonable to compare the MA-ROM method of this work to these alternative multi-fidelity methods, which motivated the following question:

**Research Question 3**

In situations where high- and low-fidelity results have a consistent field representation, is the performance of the MA-ROM method comparable to other multi-fidelity ROM methods existing in the literature?

Since the MA-ROM combines both high- and low-fidelity results into a single self-contained surrogate model, it can be qualified as a fusion-based method. For that reason, the formulation of the developed method is comparable to other fusion-based methods, e.g., the Common POD and the Extended POD methods of Mifsud et al. [110, 111] and Benamara et al. [12, 14]. The main difference between the MA-ROM method and existing fusion-based methods is the manifold alignment step that should be superfluous in scenarios with no field inconsistency. This leads to the following hypothesis:

**Hypothesis 3**

In problems involving high- and low-fidelity results with a consistent field representation, the MA-ROM method should perform comparably to existing fusion-based multi-fidelity ROM methods on the basis that their formulations are alike.

The above hypothesis is verified with Experiment 4 where the MA-ROM and the existing multi-fidelity ROM methods were all applied to the same multi-fidelity problems. To allow a fair comparison between the various methods, the high- and low-fidelity results were interpolated onto a common grid to eliminate any differences in field dimensionality as described in Section 5.4. When combining high- and low-fidelity RANS solutions, the results of Experiment 4 showed that for a given model configuration, the prediction errors of the MA-ROM method was indeed comparable

to those of existing fusion-based methods. More specifically, the Common POD and Extended POD methods exhibited a lower reconstruction error while the MA-ROM had a reduced regression error. However, when applied to high- and low-fidelity fields with slightly different features, i.e., RANS and inviscid CFD solutions, the results of Experiment 4 showed that the accuracies of existing fusion-based methods were not significantly better than a single-fidelity approach. The MA-ROM method, on the other hand, could still provide a substantial reduction in prediction errors in similar circumstances. As for existing adaptation-based methods, we observed that the MA-ROM and other fusion-based methods generally provide better performance.

All in all, the results of Experiment 4 confirm our Hypothesis 3 and establish the MA-ROM as a competitive alternative to existing multi-fidelity ROM methods, even in a situation with fields having a consistent representation.

## 6.2 Opportunities for Future Research

This dissertation has focused on high-fidelity aerodynamic applications due to their complex physics are their relatively higher computational cost when compared to other disciplines. While the RAE 2822 and CRM wing test case yielded positive results, the MA-ROM is also relevant to other applications with unique multi-fidelity challenges. For instance, in structural modeling, the solutions of beam, shell, and solid models each have distinct representations and cannot be trivially combined. Yet, the developed method could be employed to fuse such multi-fidelity results. Demonstrating the benefits of the MA-ROM method on structural applications would also lay the groundwork for the development of multi-fidelity ROMs in the context of tightly coupled aero-structural problems.

Furthermore, this work has focused on POD-based ROM methods due to their ease of use and their predominance in engineering applications. As illustrated by the results of Figures 5.3 and 5.11, such methods tend to struggle in problems involv-

ing strong discontinuities such as shock waves. To address this issue, some authors have considered the use of non-linear ROM methods developed around more complex dimensionality reduction methods, such as Isomap and LLE. Fundamentally, the Procrustes manifold alignment, which is at the core of this work, can be applied to latent variables produced by any dimensionality reduction methods. One could then modify the linear formulation of the MA-ROM method into a non-linear one by using the Isomap or LLE methods to find the latent representations of the high- and low-fidelity fields. Alternatively, one could examine other forms of manifold alignment that are inherently non-linear, such as the semi-supervised method proposed Wang and Mahadevan [167, 169]. Such an approach would join together the dimensionality reduction and the manifold alignment steps of the MA-ROM method.

Lastly, the prediction of field quantities has been at the forefront of this work, and we have shown that integrated quantities could still be computed using field predictions. We demonstrated that the improved accuracy of the proposed multi-fidelity method could also benefit the computation of integrated results. However, both single- and multi-fidelity ROMs constructed in this work were not necessarily optimized for the accurate computation of integrated quantities. Since many design problems specifically revolve around performance metrics such as the lift, drag, or take-off gross weight, a ROM formulation that minimizes the errors on both the field predictions and some integrated results could be beneficial. One could potentially formulate a model that would provide both field and scalar predictions at once, thus circumventing the integration of a physical field.

# Appendices

# APPENDIX A

# PROOFS

## A.1 Breakdown of the Field Prediction Error

In Section 4.3.1, we stated that the field prediction error $E(\mathbf{x})$ of some field $\mathbf{x} \in \mathbb{R}^d$ can be decomposed as follows

$$E(\mathbf{x}) = \sqrt{E_{\text{rc}}(\mathbf{x})^2 + E_{\text{rg}}(\mathbf{x})^2} \tag{A.1}$$

where $E_{\text{rc}}(\mathbf{x})$ and $E_{\text{rg}}(\mathbf{x})$ are the reconstruction and regression components of $E(\mathbf{x})$ respectively.

To demonstrate the above relation, let us consider the data matrix $\mathbf{X}^* \in \mathbb{R}^{d \times n_t}$ whose $j$-th column contains the test sample $\mathbf{x}_j^* \in \mathbb{R}^d$. Also, let $\widetilde{\mathbf{X}} \in \mathbb{R}^{d \times n_t}$ be a matrix whose $j$-th column contains the predicted field $\widetilde{\mathbf{x}}_j \in \mathbb{R}^d$ corresponding to the test sample $\mathbf{x}_j^*$. Using the definition of the Frobenius norm, the expression of $E(\mathbf{x})$ given by Eq. (4.2) can then be redefined as

$$E(\mathbf{x})^2 = \frac{1}{n_t} \sum_{j=1}^{n_t} \|\mathbf{x}_j^* - \widetilde{\mathbf{x}}_j\|_2^2 = \frac{1}{n_t} \left\| \mathbf{X}^* - \widetilde{\mathbf{X}} \right\|_F^2 \tag{A.2}$$

Similarly, the definition of Eq. (4.4) and Eq. (4.5) for $E_{\text{rc}}(\mathbf{x})$ and $E_{\text{rg}}(\mathbf{x})$ respectively can be reformulated as

$$E(\mathbf{x})_{\text{rc}}^2 = \frac{1}{n_t} \left\| (\mathbf{I} - \mathbf{\Phi}_k \mathbf{\Phi}_k^T) \mathbf{X}^* \right\|_F^2 \tag{A.3}$$

$$E(\mathbf{x})_{\text{rg}}^2 = \frac{1}{n_t} \left\| \mathbf{\Phi}_k (\mathbf{\Phi}_k^T \mathbf{X}^* - \widetilde{\mathbf{Z}}) \right\|_F^2 \tag{A.4}$$

where $\widetilde{\mathbf{Z}} = \mathbf{\Phi}_k^T \widetilde{\mathbf{X}} \in \mathbb{R}^{k \times n_t}$ is a matrix whose $j$-th column contains the predicted latent

variable $\widetilde{\mathbf{z}}_j \in \mathbb{R}^k$ used to construct $\widetilde{\mathbf{x}}_j$.

To separate the reconstruction and regression components of $E(\mathbf{x})$, we manipulate Eq. (A.2) such that

$$\begin{aligned} E(\mathbf{x})^2 &= \frac{1}{n_t} \left\| \mathbf{X}^* - \widetilde{\mathbf{X}} \right\|_F^2 \\ &= \frac{1}{n_t} \left\| \mathbf{X}^* - \mathbf{\Phi}_k \mathbf{\Phi}_k^T \mathbf{X}^* + \mathbf{\Phi}_k \mathbf{\Phi}_k^T \mathbf{X}^* - \widetilde{\mathbf{X}} \right\|_F^2 \\ &= \frac{1}{n_t} \left\| (\mathbf{I} - \mathbf{\Phi}_k \mathbf{\Phi}_k^T) \mathbf{X}^* + \mathbf{\Phi}_k (\mathbf{\Phi}_k^T \mathbf{X}^* - \widetilde{\mathbf{Z}}) \right\|_F^2 \end{aligned} \tag{A.5}$$

We also consider the following property of the Frobenius norm

$$\|\mathbf{A} + \mathbf{B}\|_F^2 = \|\mathbf{A}\|_F^2 + \|\mathbf{B}\|_F^2 + 2\,\mathrm{tr}(\mathbf{A}^T \mathbf{B}) \tag{A.6}$$

In the context of Eq. (A.5), the matrices $\mathbf{A}$ and $\mathbf{B}$ are substituted by

$$\mathbf{A} = (\mathbf{I} - \mathbf{\Phi}_k \mathbf{\Phi}_k^T) \mathbf{X}^* \tag{A.7}$$

$$\mathbf{B} = \mathbf{\Phi}_k (\mathbf{\Phi}_k^T \mathbf{X}^* - \widetilde{\mathbf{Z}}) \tag{A.8}$$

Furthermore, we note that with the current formulation, the columns or $\mathbf{A}$ and $\mathbf{B}$ are orthogonal to each other such that

$$\begin{aligned} \mathbf{A}^T \mathbf{B} &= (\mathbf{X}^*)^T (\mathbf{I} - \mathbf{\Phi}_k \mathbf{\Phi}_k^T) \mathbf{\Phi}_k (\mathbf{\Phi}_k^T \mathbf{X}^* - \widetilde{\mathbf{Z}}) \\ &= (\mathbf{X}^*)^T (\mathbf{\Phi}_k - \mathbf{\Phi}_k)(\mathbf{\Phi}_k^T \mathbf{X}^* - \widetilde{\mathbf{Z}}) \\ &= \mathbf{0} \end{aligned} \tag{A.9}$$

Combining Eq. (A.5) with Eq. (A.6) provides the following expression

$$E(\mathbf{x})^2 = \frac{1}{n_t} \left\| (\mathbf{I} - \mathbf{\Phi}_k \mathbf{\Phi}_k^T) \mathbf{X}^* \right\|_F^2 + \frac{1}{n_t} \left\| \mathbf{\Phi}_k (\mathbf{\Phi}_k^T \mathbf{X}^* - \widetilde{\mathbf{Z}}) \right\|_F^2 \tag{A.10}$$

Using the definitions of Eq. (A.3) and (A.4), we then obtain

$$E(\mathbf{x})^2 = E_{\mathrm{rc}}(\mathbf{x})^2 + E_{\mathrm{rg}}(\mathbf{x})^2 \tag{A.11}$$

which corresponds to the relation given in Eq. (A.1).

# APPENDIX B
# SUPPLEMENTARY RESULTS

## B.1 Pressure Visualization for the Transonic Airfoil Test Case

In Section 5.1.2, the visualization of Figure 5.3 provided an example of the $C_P$ field and the associated error field generated by a single-fidelity ROM and MA-ROMs applied to the RAE 2822 airfoil test case. The results shown represented a test sample with a prediction error comparable to the results presented in Table 5.1 for similar model configurations. To complement Figure 5.3, Figures B.1 and B.2 present instead visualizations for the samples having the lowest and highest prediction error respectively among the test dataset. Specifically, these figures show the predicted $C_P$ field around the RAE 2822 airfoil with $b = 3$ and $n = 100$. For the MA-ROM results, both the A1 +A2 and the A1 + A3 fidelity combinations are considered with $\tau = 4$.

## B.2 Pressure Visualization for the Transonic Wing Test Case

As with the airfoil test case, Figure 5.11 of Section 5.2.2 compared the predicted $C_P$ field and its associated error for a single-fidelity ROM and MA-ROMs applied to the CRM wing test cases. The test sample selected for these figures had a prediction error on par with the results presented in Table 5.8 for similar model configurations. For completeness, Figures B.5 and B.6 shows the results for the test samples with the lowest and highest prediction error respectively. These results are for a multi-fidelity scenario with $b = 2$ and $n = 100$. Also, the multi-fidelity models consider the W1 + W2 and the W1 + W3 fidelity combinations with $\tau = 4$. For comparison, Figures B.3 and B.4 shows the actual $C_P$ fields associated with Figures B.5 and B.6.

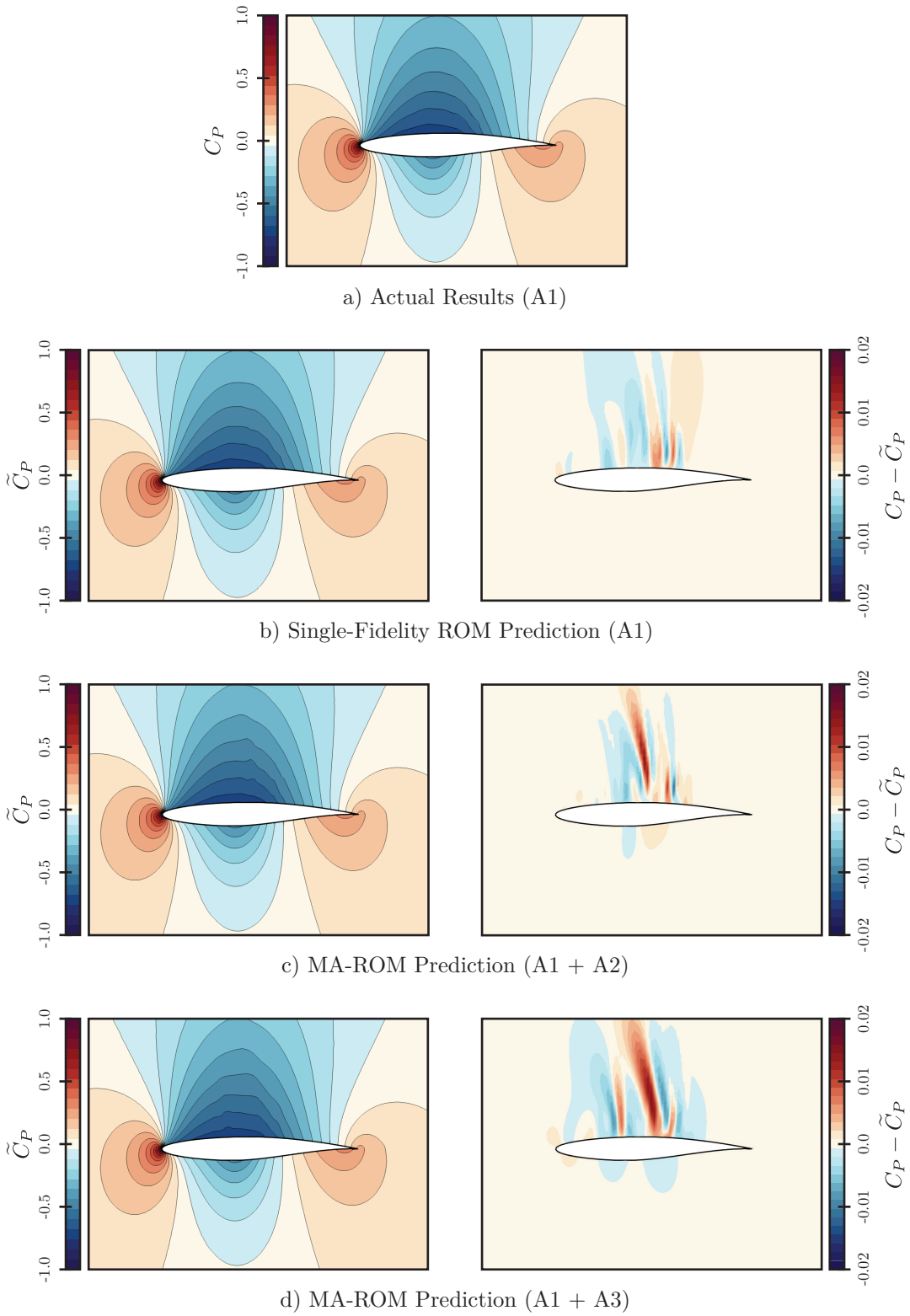


**Figure B.1:** Predicted $C_P$ fields (left) of the RAE 2822 airfoil test case and the associated error fields (right) for the test sample with the *lowest* prediction error. Results are for both single- and multi-fidelity ROMs with $n = 100$, $\tau = 4$ (MA-ROM only), and $b = 3$.

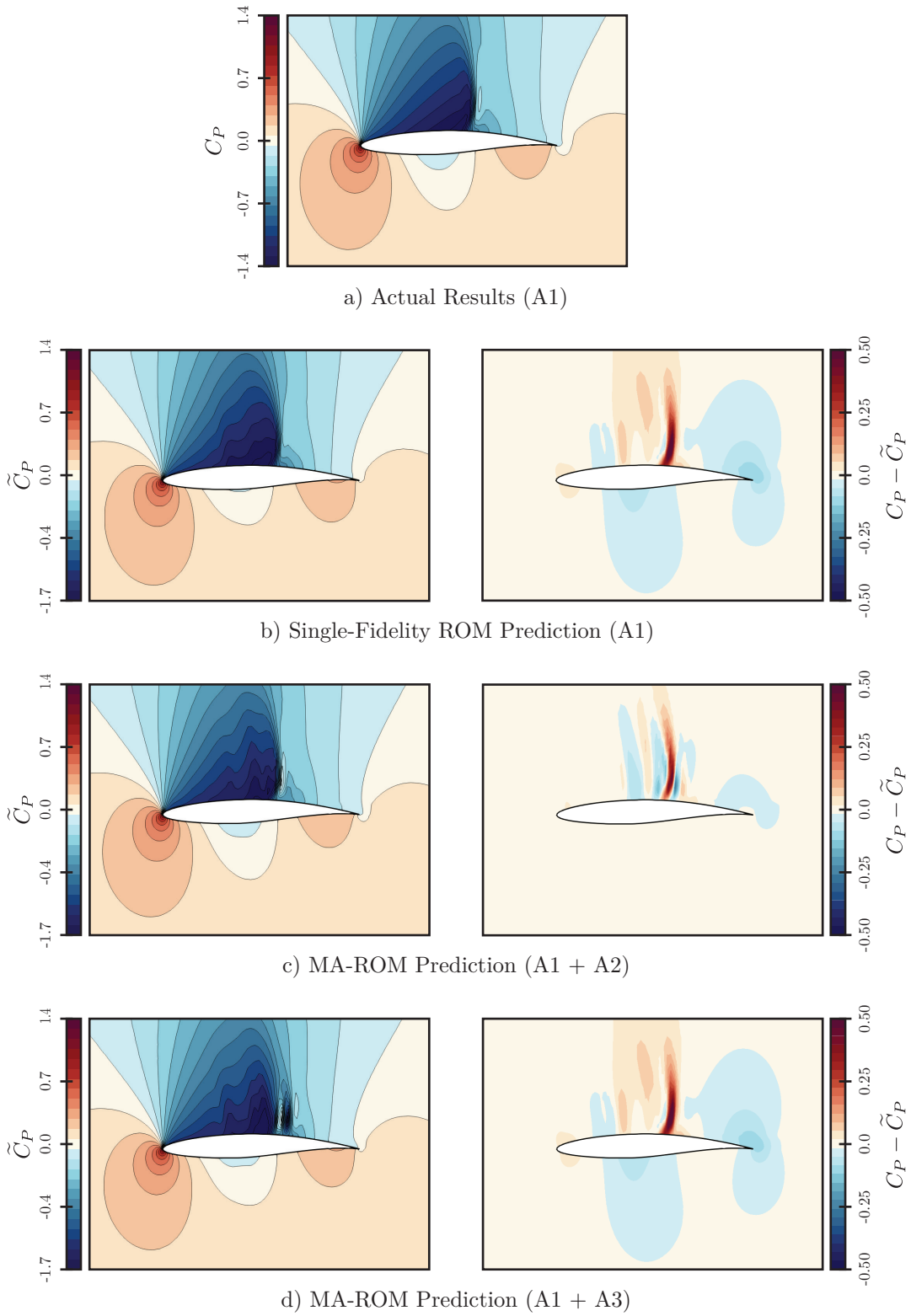


**Figure B.2:** Predicted $C_P$ fields (left) of the RAE 2822 airfoil test case and the associated error fields (right) for the test sample with the *highest* prediction error. Results are for both single- and multi-fidelity ROMs with $n = 100$, $\tau = 4$ (MA-ROM only), and $b = 3$.

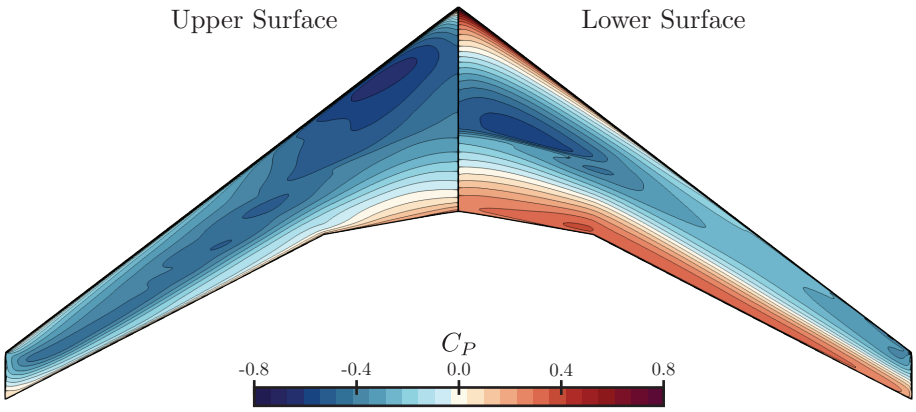


**Figure B.3:** Actual $C_P$ field over the CRM wing upper (left) and lower (right) surfaces for the test sample with the *lowest* prediction error. Results are for the $b = 2$ parametrization and the W1 fidelity level.

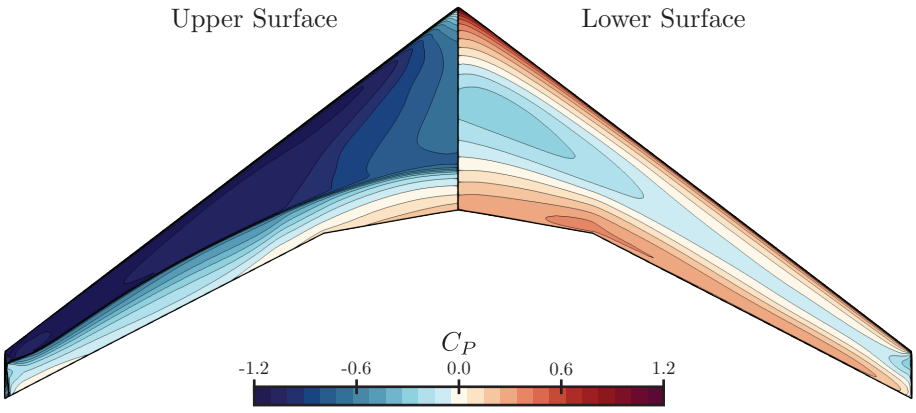


**Figure B.4:** Actual $C_P$ field over the CRM wing upper (left) and lower (right) surfaces for the test sample with the *highest* prediction error. Results are for the $b = 2$ parametrization and the W1 fidelity level.

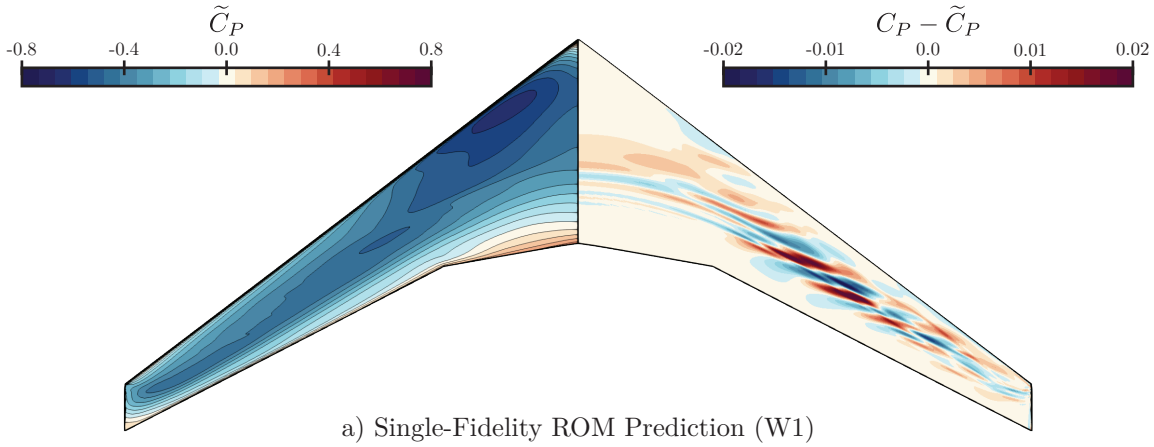


a) Single-Fidelity ROM Prediction (W1)

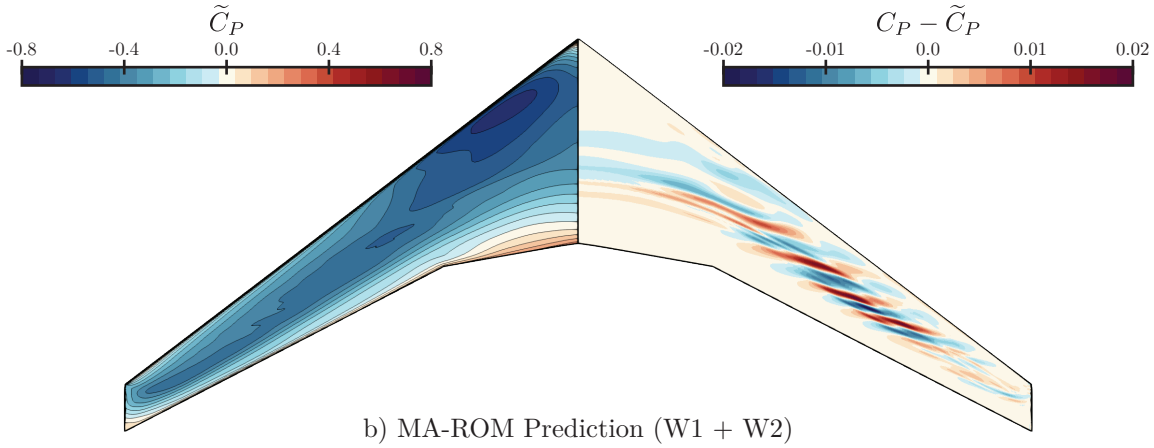


b) MA-ROM Prediction (W1 + W2)

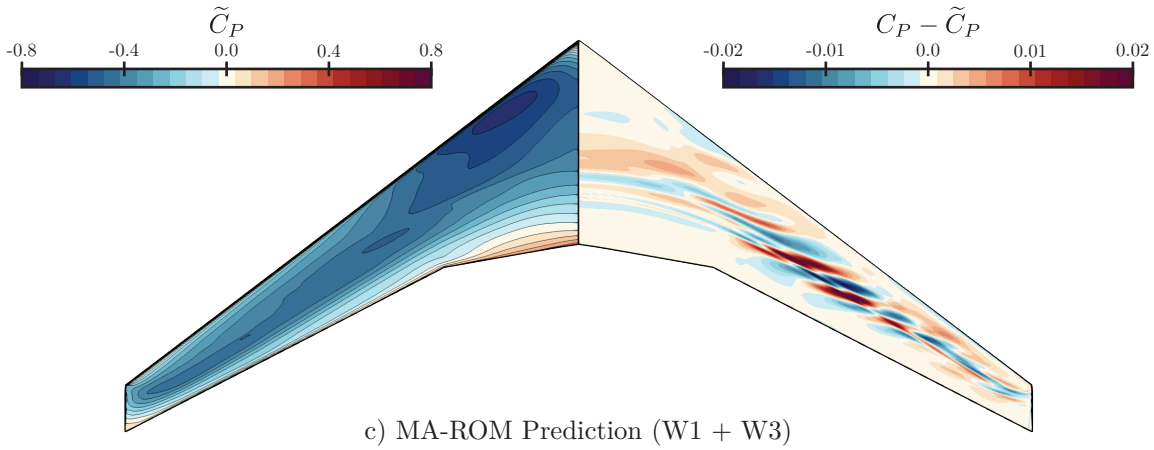


c) MA-ROM Prediction (W1 + W3)

**Figure B.5:** Predicted $C_P$ distributions (left) of the CRM wing and the associated error fields (right) for the test sample with the *lowest* prediction error (See Figure B.3). Results are for both single- and multi-fidelity ROMs with $n = 100$, $\tau = 4$ (MA-ROM only), and $b = 2$.

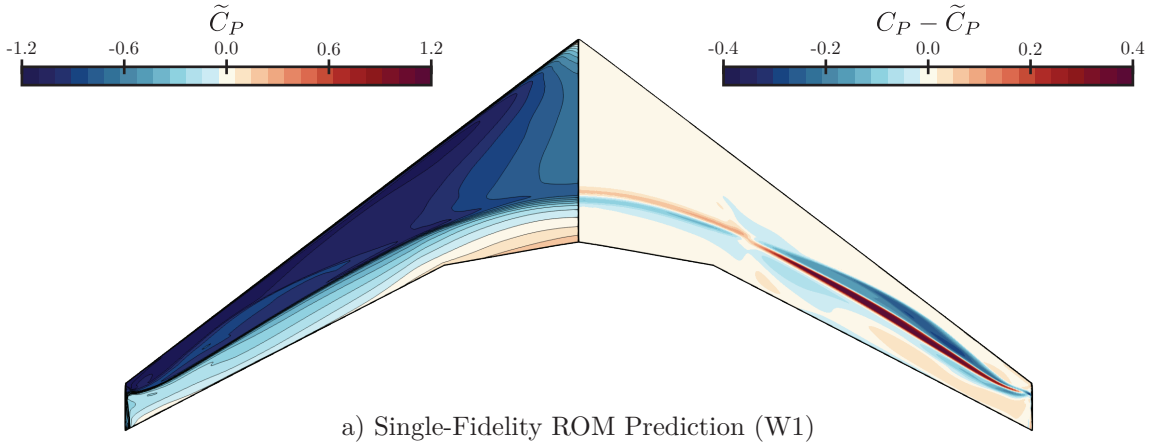


a) Single-Fidelity ROM Prediction (W1)

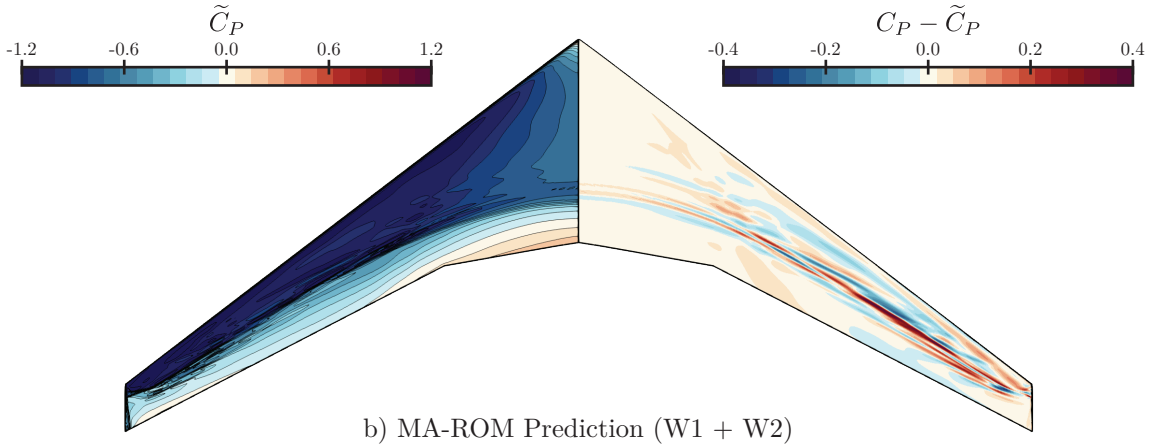


b) MA-ROM Prediction (W1 + W2)

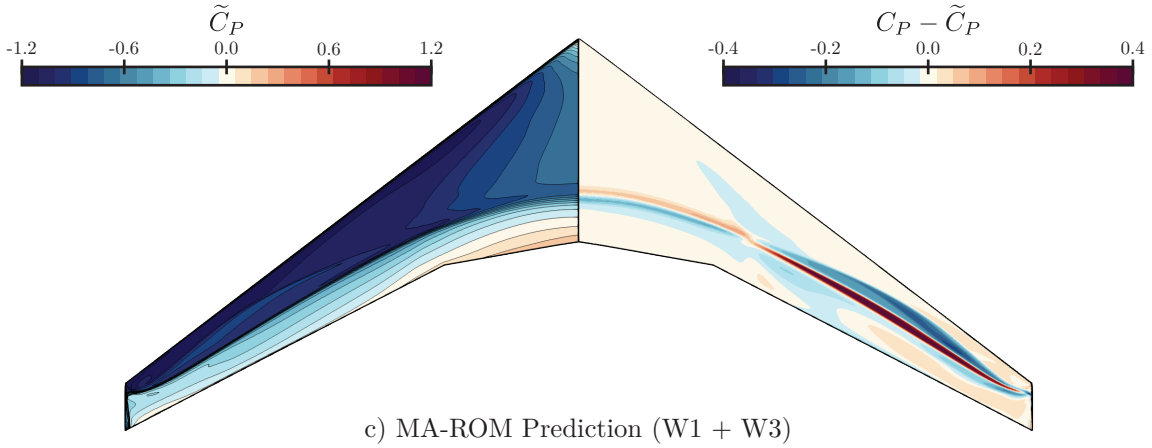


c) MA-ROM Prediction (W1 + W3)

**Figure B.6:** Predicted $C_P$ distributions (left) of the CRM wing and the associated error fields (right) for the test sample with the *highest* prediction error (See Figure B.3). Results are for both single- and multi-fidelity ROMs with $n = 100$, $\tau = 4$ (MA-ROM only), and $b = 2$.

## REFERENCES


[1] N. M. Alexandrov, J. E. Dennis, R. M. Lewis, and V. Torczon, "A trust-region framework for managing the use of approximation models in optimization," *Structural Optimization*, vol. 15, no. 1, pp. 16–23, 1998.

[2] N. M. Alexandrov and R. M. Lewis, "An Overview of First-Order Model Management for Engineering Optimization," *Optimization and Engineering*, vol. 2, no. 4, pp. 413–430, 2001.

[3] N. M. Alexandrov, R. M. Lewis, C. R. Gumbert, L. L. Green, and P. a. Newman, "Approximation and Model Management in Aerodynamic Optimization with Variable-Fidelity Models," *Journal of Aircraft*, vol. 38, no. 6, pp. 1093–1101, 2001.

[4] D. Allaire and K. Willcox, "Surrogate Modeling for Uncertainty Assessment with Application to Aviation Environmental System Models," *AIAA Journal*, vol. 48, no. 8, pp. 1791–1803, 2010.

[5] Amazon Web Services, *Amazon EC2 On-Demand Pricing*, `https://aws.amazon.com/ec2/pricing/on-demand/`, last accessed: 09-09-2020.

[6] D. Amsallem and C. Farhat, "Interpolation Method for Adapting Reduced-Order Models and Application to Aeroelasticity," *AIAA Journal*, vol. 46, no. 7, pp. 1803–1813, 2008.

[7] D. Amsallem, J. Cortial, and C. Farhat, "On-Demand CFD-Based Aeroelastic Predictions Using a Database of Reduced-Order Bases and Models," *47th AIAA Aerospace Sciences Meeting Including The New Horizons Forum and Aerospace Exposition*, no. January, Orlando, Florida, 2009.

[8] G. R. Anderson, M. Nemec, and M. J. Aftosmis, "Aerodynamic Shape Optimization Benchmarks with Error Control and Automatic Parameterization," in *53rd AIAA Aerospace Sciences Meeting*, Reston, Virginia: American Institute of Aeronautics and Astronautics, 2015, pp. 1–18.

[9] U. Ayachit, *The paraview guide: a parallel visualization application*. Kitware, Inc., 2015.

[10] M. Belkin and P. Niyogi, "Laplacian eigenmaps and spectral techniques for embedding and clustering," in *Advances in neural information processing systems*, 2002, pp. 585–591.

[11] J. Bell, "Pressure-Sensitive Paint Measurements on the NASA Common Research Model in the NASA 11-ft Transonic Wind Tunnel," in *49th AIAA Aerospace Sciences Meeting including the New Horizons Forum and Aerospace Exposition*, Reston, Virigina: American Institute of Aeronautics and Astronautics, 2011.

[12] T. Benamara, P. Breitkopf, I. Lepot, and C. Sainvitu, "Multi-Fidelity Extension To Non-Intrusive Proper Orthogonal Decomposition Based Surrogates," *Proceedings of the VII European Congress on Computational Methods in Applied Sciences and Engineering (ECCOMAS Congress 2016)*, no. January 2016, pp. 4129–4145, 2016.

[13] T. Benamara, P. Breitkopf, I. Lepot, and C. Sainvitu, "Adaptive infill sampling criterion for multi-fidelity optimization based on Gappy-POD," *Structural and Multidisciplinary Optimization*, vol. 54, no. 4, pp. 843–855, 2016.

[14] T. Benamara, P. Breitkopf, I. Lepot, C. Sainvitu, and P. Villon, "Multi-fidelity POD surrogate-assisted optimization: Concept and aero-design study," *Structural and Multidisciplinary Optimization*, vol. 56, no. 6, pp. 1387–1412, 2017.

[15] P. Benner, S. Gugercin, and K. Willcox, "A survey of model reduction methods for parametric systems," *MPI Magdeburg Preprints*, vol. MPIMD, no. 13-14, pp. 1–36, 2013.

[16] S. H. Berguin, A. Renganathan, M. Chen, J. Ahuja, J. C. Tai, D. N. Mavris, and D. Hills, "Sensitivity Analysis of Aero-Propulsive Coupling for Over-Wing-Nacelle Concepts," *2018 AIAA Aerospace Sciences Meeting*, no. January, pp. 1–17, 2018.

[17] A. Bertram, C. Othmer, and R. Zimmermann, "Towards Real-time Vehicle Aerodynamic Design via Multi-fidelity Data-driven Reduced Order Modeling," *2018 AIAA/ASCE/AHS/ASC Structures, Structural Dynamics, and Materials Conference*, no. January, 2018.

[18] A. Bhosekar and M. Ierapetritou, "Advances in surrogate based modeling, feasibility analysis, and optimization: A review," *Computers & Chemical Engineering*, vol. 108, pp. 250–267, 2018.

[19] C. M. Bishop, *Pattern Recognition and Machine Learning (Information Science and Statistics)*. Berlin, Heidelberg: Springer-Verlag, 2006.

[20] M Björkman and K Holmström, "Global Optimization of Costly Nonconvex Functions Using Radial Basis Functions," *Optimization and Engineering*, vol. 1, no. 4, pp. 373–397, 2000.

[21] M. A. Bouhlel and J. R. Martins, "Gradient-enhanced kriging for high-dimensional problems," *Engineering with Computers*, vol. 0, no. 0, pp. 1–17, 2018. arXiv: 1708.02663.

[22] G. E. P. Box, "The Exploration and Exploitation of Response Surfaces: Some General Considerations and Examples," *Biometrics*, vol. 10, no. 1, p. 16, 1954.

[23] T. Bui-Thanh, M. Damodaran, and K. Willcox, "Proper Orthogonal Decomposition Extensions for Parametric Applications in Compressible Aerodynamics," *21st AIAA Applied Aerodynamics Conference*, no. June, pp. 1–11, 2003.

[24] T. Bui-Thanh, K. Willcox, and O. Ghattas, "Parametric Reduced-Order Models for Probabilistic Analysis of Unsteady Aerodynamic Applications," *AIAA Journal*, vol. 46, no. 10, pp. 2520–2529, 2008.

[25] T. Bui-Thanh, M. Damodaran, and K. E. Willcox, "Aerodynamic Data Reconstruction and Inverse Design Using Proper Orthogonal Decomposition," *AIAA Journal*, vol. 42, no. 8, pp. 1505–1516, 2004.

[26] R. E. Caflisch, "Monte Carlo and quasi-Monte Carlo methods," *Acta Numerica*, vol. 7, p. 1, 1998.

[27] K. J. Chang, R. T. Haftka, G. L. Giles, and I.-J. Kao, "Sensitivity-based scaling for approximating structural response," *Journal of Aircraft*, vol. 30, no. 2, pp. 283–288, 1993.

[28] A. Chaudhuri and R. T. Haftka, "Efficient Global Optimization with Adaptive Target Setting," *AIAA Journal*, vol. 52, no. 7, pp. 1573–1578, 2014.

[29] W. Chen, B. Junqiang, and J. S. Hesthaven, "An iterative approach to improve non-intrusive reduced-order models efficiency for parameterized problems," *21st AIAA International Space Planes and Hypersonics Technologies Conference, Hypersonics 2017*, no. March, 2017.

[30] S. Choi, J. J. Alonso, and I. M. Kroo, "Two-Level Multifidelity Design Optimization Studies for Supersonic Jets," *Journal of Aircraft*, vol. 46, no. 3, pp. 776–790, 2009.

[31] S. M. Clarke, J. H. Griebsch, and T. W. Simpson, "Analysis of Support Vector Regression for Approximation of Complex Engineering Analyses," *Journal of Mechanical Design*, vol. 127, no. 6, p. 1077, 2005.

[32] P. Cook, M. Mcdonald, and M. Firmin, "Experimental data base for computer program assessment," *AGARD AR-138*, 1979.

[33] M. A. A. Cox and T. F. Cox, "Multidimensional Scaling," in *Handbook of Data Visualization*, Berlin, Heidelberg: Springer Berlin Heidelberg, 2008, pp. 315–347.

[34] K. Cutajar, M. Pullin, A. Damianou, N. Lawrence, and J. González, "Deep Gaussian Processes for Multi-fidelity Modeling," vol. 1, no. 2, 2019. arXiv: 1903.07320.

[35] T. De Bie, N. Cristianini, and R. Rosipal, "Eigenproblems in Pattern Recognition," in *Handbook of Geometric Computing*, vol. 10, 2005, pp. 129–167.

[36] K. Decker, H. D. Schwartz, and D. Mavris, "Dimensionality Reduction Techniques Applied to the Design of Hypersonic Aerial Systems," pp. 1–24, 2020.

[37] D. DeMers and G. W. Cottrell, "Non-linear dimensionality reduction," in *Advances in neural information processing systems*, 1993, pp. 580–587.

[38] R. P. Dwight, "Robust Mesh Deformation using the Linear Elasticity Equations," in *Computational Fluid Dynamics 2006*, Berlin, Heidelberg: Springer Berlin Heidelberg, 2009, pp. 401–406.

[39] T. D. Economon, F. Palacios, S. R. Copeland, T. W. Lukaczyk, and J. J. Alonso, "SU2: An Open-Source Suite for Multiphysics Simulation and Design," *AIAA Journal*, vol. 54, no. 3, pp. 1–19, 2015.

[40] M. Eldred, A. Giunta, and S Collis, "Second-Order Corrections for Surrogate-Based Optimization with Model Hierarchies," *10th AIAA/ISSMO Multidisciplinary Analysis and Optimization Conference*, no. September, pp. 1–15, 2004.

[41] R. Everson and L. Sirovich, "Karhunen–Loève procedure for gappy data," *Journal of the Optical Society of America A*, vol. 12, no. 8, p. 1657, 1995.

[42] R. A. Fisher, "The statistical utilization of multiple measurements," *Annals of eugenics*, vol. 8, no. 4, pp. 376–386, 1938.

[43] A. Flaig, "Airbus A380: Solutions to the Aerodynamic Challenges of Designing the World's Largest Passenger Aircraft," Airbus, Hamburg, Tech. Rep., 2008.

[44] A. I. Forrester and A. J. Keane, "Recent advances in surrogate-based optimization," *Progress in Aerospace Sciences*, vol. 45, no. 1-3, pp. 50–79, 2009. arXiv: 1106.2697.

[45] A. I. Forrester, A. Sóbester, and A. J. Keane, "Multi-fidelity optimization via surrogate modelling," *Proceedings of the Royal Society A: Mathematical, Physical and Engineering Sciences*, vol. 463, no. 2088, pp. 3251–3269, 2007.

[46] M. Fossati, "Evaluation of Aerodynamic Loads via Reduced-Order Methodology," *AIAA Journal*, vol. 53, no. 8, pp. 2389–2405, 2015.

[47] T. Franz, R. Zimmermann, S. Görtz, and N. Karcher, "Interpolation-based reduced-order modelling for steady transonic flows via manifold learning," *International Journal of Computational Fluid Dynamics*, vol. 28, no. 3-4, pp. 106–121, 2014.

[48] T. Franz, R. Zimmermann, and S. Görtz, *Adaptive Sampling for Nonlinear Dimensionality Reduction Based on Manifold Learning*, P. Benner, M. Ohlberger, A. Patera, G. Rozza, and K. Urban, Eds., ser. MS&A. Cham: Springer International Publishing, 2017, vol. 17, pp. 255–269.

[49] M. Fujino and Y. Kawamura, "Wave-Drag Characteristics of an Over-the-Wing Nacelle Business-Jet Configuration," *Journal of Aircraft*, vol. 40, no. 6, pp. 1177–1184, 2003.

[50] S. Gano, B. Sanders, and J. Renaud, "Variable Fidelity Optimization Using a Kriging Based Scaling Function," *10th AIAA/ISSMO Multidisciplinary Analysis and Optimization Conference*, no. September, pp. 1–19, 2004.

[51] S. E. Gano, J. E. Renaud, and B. Sanders, "Hybrid Variable Fidelity Optimization by Using a Kriging-Based Scaling Function," *AIAA Journal*, vol. 43, no. 11, pp. 2422–2433, 2005.

[52] A. Garbaruk, M. Shur, M. Strelets, and P. R. Spalart, "Numerical study of wind-tunnel walls effects on transonic airfoil flow," *AIAA Journal*, vol. 41, no. 6, pp. 1046–1054, 2003.

[53] M. Giselle Fernández-Godino, C. Park, N. H. Kim, and R. T. Haftka, "Issues in deciding whether to use multifidelity surrogates," *AIAA Journal*, vol. 57, no. 5, pp. 2039–2054, 2019.

[54] J. C. Gower, "Procrustes methods," *Wiley Interdisciplinary Reviews: Computational Statistics*, vol. 2, no. 4, pp. 503–508, 2010.

[55] J. C. Gower and G. B. Dijksterhuis, *Procrustes Problems*. Oxford University Press, 2004.

[56] R. Guerrero, C. Ledig, and D. Rueckert, "Manifold Alignment and Transfer Learning for Classification of Alzheimer's Disease," in, 2014, pp. 77–84.

[57] O. Gur, M. Bhatia, J. A. Schetz, W. H. Mason, R. K. Kapania, and D. N. Mavris, "Design Optimization of a Truss-Braced-Wing Transonic Transport Aircraft," *Journal of Aircraft*, vol. 47, no. 6, pp. 1907–1917, 2010.

[58] H.-M. Gutmann, "A Radial Basis Function Method for Global Optimization," *Journal of Global Optimization*, vol. 19, no. 3, pp. 201–227, 2001.

[59] R. T. Haftka, D. Villanueva, and A. Chaudhuri, "Parallel surrogate-assisted global optimization with expensive functions – a survey," *Structural and Multidisciplinary Optimization*, vol. 54, no. 1, pp. 3–13, 2016.

[60] J. H. Ham, D. D. Lee, and L. K. Saul, "Learning high dimensional correspondences from low dimensional manifolds," in *Proceedings of the Twentieth International Conference on Machine Learning (ICML-2003) Workshop: The Continuum from Labeled to Unlabeled Data in Machine Learning and Data Mining*, Washington DC, 2003, pp. 34–41.

[61] J. Ham, D. D. Lee, and L. K. Saul, "Semisupervised alignment of manifolds," *Proceedings of the Tenth International Workshop on Artificial Intelligence and Statistics*, vol. 10, pp. 120–127, 2005.

[62] Z.-H. Han and S. Görtz, "Hierarchical Kriging Model for Variable-Fidelity Surrogate Modeling," *AIAA Journal*, vol. 50, no. 9, pp. 1885–1896, 2012.

[63] Z. H. Han, S. Görtz, and R. Zimmermann, "Improving variable-fidelity surrogate modeling via gradient-enhanced kriging and a generalized hybrid bridge function," *Aerospace Science and Technology*, vol. 25, no. 1, pp. 177–189, 2013.

[64] Z. Han, R. Zimmerman, and S. Görtz, "Alternative Cokriging Method for Variable-Fidelity Surrogate Modeling," *AIAA Journal*, vol. 50, no. 5, pp. 1205–1210, 2012.

[65] T. Hastie, R. Tibshirani, and J. Friedman, *The Elements of Statistical Learning*, ser. Springer Series in Statistics. New York, NY: Springer New York, 2009.

[66] X. He, D. Cai, S. Yan, and H.-J. Zhang, "Neighborhood preserving embedding," in *Tenth IEEE International Conference on Computer Vision (ICCV'05) Volume 1*, IEEE, 2005, 1208–1213 Vol. 2.

[67] X. He and P. Niyogi, "Locality Preserving Projections," in *Advances in Neural Information Processing Systems 16*, S Thrun, L. K. Saul, and B Schölkopf, Eds., MIT Press, 2004, pp. 153–160.

[68] J. S. Hesthaven and S. Ubbiali, "Non-intrusive reduced order modeling of nonlinear problems using neural networks," *Journal of Computational Physics*, vol. 363, pp. 55–78, 2018.

[69] J. R. Hooker, A. Wick, C. H. Zeune, and A. Agelastos, "Over Wing Nacelle Installations for Improved Energy Efficiency," in *31st AIAA Applied Aerody-*

*namics Conference*, Reston, Virginia: American Institute of Aeronautics and Astronautics, 2013.

[70] S.-Y. Huang, M.-H. Lee, and C. K. Hsiao, "Nonlinear measures of association with kernel canonical correlation analysis and applications," *Journal of Statistical Planning and Inference*, vol. 139, no. 7, pp. 2162–2174, 2009.

[71] E. Iuliano, "Global optimization of benchmark aerodynamic cases using physics-based surrogate models," *Aerospace Science and Technology*, vol. 67, pp. 273–286, 2017.

[72] A. Jameson, W. Schmidt, and E. Turkel, "Numerical solution of the Euler equations by finite volume methods using Runge Kutta time stepping schemes," in *14th Fluid and Plasma Dynamics Conference*, Reston, Virigina: American Institute of Aeronautics and Astronautics, 1981.

[73] J. P. Jasa, J. T. Hwang, and J. R. R. A. Martins, "Open-source coupled aerostructural optimization using Python," *Structural and Multidisciplinary Optimization*, vol. 57, no. 4, pp. 1815–1827, 2018.

[74] I. Jolliffe, *Principal Component Analysis*, 2nd ed., ser. Springer Series in Statistics. New York: Springer-Verlag, 2002, p. 488.

[75] D. Jones, "A Taxonomy of Global Optimization Methods Based on Response Surfaces," *Journal of Global Optimization*, vol. 21, no. 4, pp. 345–383, 2001.

[76] D. R. Jones, M. Schonlau, and J William, "Efficient Global Optimization of Expensive Black-Box Functions," *Journal of Global Optimization*, vol. 13, pp. 455–492, 1998.

[77] V. R. Joseph, E. Gul, and S. Ba, "Maximum projection designs for computer experiments," *Biometrika*, vol. 102, no. 2, pp. 371–380, 2015.

[78] H. Kato and K.-i. Funazaki, "POD-Driven Adaptive Sampling for Efficient Surrogate Modeling and its Application to Supersonic Turbine Optimization," in *Volume 2B: Turbomachinery*, ASME, 2014, V02BT45A023.

[79] J. Katz and A. Plotkin, *Low-Speed Aerodynamics*. Cambridge University Press, 2001.

[80] M. Kennedy and A. O'Hagan, "Predicting the output from a complex computer code when fast approximations are available," *Biometrika*, vol. 87, no. 1, pp. 1–13, 2000.

[81] G. Kenway, G. Kennedy, and J. Martins, "A CAD-Free Approach to High-Fidelity Aerostructural Optimization," in *13th AIAA/ISSMO Multidisciplinary Analysis Optimization Conference*, Reston, Virigina: American Institute of Aeronautics and Astronautics, 2010, pp. 1–18.

[82] C. Klingenberg, "Analyzing Fluctuating Asymmetry with Geometric Morphometrics: Concepts, Methods, and Applications," *Symmetry*, vol. 7, no. 2, pp. 843–934, 2015.

[83] E. Kokiopoulou, J. Chen, and Y. Saad, "Trace optimization and eigenproblems in dimension reduction methods," *Numerical Linear Algebra with Applications*, vol. 18, no. 3, pp. 565–602, 2011. arXiv: `arXiv:1112.5346v3`.

[84] D. G. Krige, "A statistical approach to some basic mine valuation problems on the Witwatersrand," *Journal of the Southern African Institute of Mining and Metallurgy*, vol. 52, no. 6, pp. 119–139, 1951.

[85] N. Kroll, M. Abu-Zurayk, D. Dimitrov, T. Franz, T. Führer, T. Gerhold, S. Görtz, R. Heinrich, C. Ilic, J. Jepsen, J. Jägersküpper, M. Kruse, A. Krumbein, S. Langer, D. Liu, R. Liepelt, L. Reimer, M. Ritter, A. Schwöppe, J. Scherer, F. Spiering, R. Thormann, V. Togiti, D. Vollmer, and J. H. Wendisch, "DLR project Digital-X: towards virtual aircraft design and flight testing based on high-fidelity methods," *CEAS Aeronautical Journal*, vol. 7, no. 1, pp. 3–27, 2016.

[86] Y. Kuya, K. Takeda, X. Zhang, and A. I. J. Forrester, "Multifidelity Surrogate Modeling of Experimental and Computational Aerodynamic Data Sets," *AIAA Journal*, vol. 49, no. 2, pp. 289–298, 2011.

[87] R. Lam, D. L. Allaire, and K. E. Willcox, "Multifidelity Optimization using Statistical Surrogate Modeling for Non-Hierarchical Information Sources," in *56th AIAA/ASCE/AHS/ASC Structures, Structural Dynamics, and Materials Conference*, vol. 1093, Reston, Virginia: American Institute of Aeronautics and Astronautics, 2015, pp. 1093–1101.

[88] J. Laurenceau and P. Sagaut, "Building Efficient Response Surfaces of Aerodynamic Functions with Kriging and Cokriging," *AIAA Journal*, vol. 46, no. 2, pp. 498–507, 2008.

[89] L. Le Gratiet and J. Garnier, "Recursive Co-Kriging Model for Design of Computer Experiments With Multiple Levels of Fidelity," *International Journal for Uncertainty Quantification*, vol. 4, no. 5, pp. 365–386, 2014. arXiv: `Int.J.UncertaintyQuantification.2014006914 [10.1615]`.

[90] C. Lee, D. Koo, K. Telidetzki, H. Buckley, H. Gagnon, and D. W. Zingg, "Aerodynamic Shape Optimization of Benchmark Problems Using Jetstream," in *53rd AIAA Aerospace Sciences Meeting*, Reston, Virginia: American Institute of Aeronautics and Astronautics, 2015.

[91] K. Lee, T. Nam, C. Perullo, and D. N. Mavris, "Reduced-Order Modeling of a High-Fidelity Propulsion System Simulation," vol. 49, no. 8, 2011.

[92] J. Li and W. Zhang, "The performance of proper orthogonal decomposition in discontinuous flows," *Theoretical and Applied Mechanics Letters*, vol. 6, no. 5, pp. 236–243, 2016.

[93] D. Liao, Y. Qian, and J. Zhou, "Visualization of hyperspectral imaging data based on manifold alignment," *Proceedings - International Conference on Pattern Recognition*, pp. 70–75, 2014.

[94] R. H. Liebeck, "Design of the Blended Wing Body Subsonic Transport," *Journal of Aircraft*, vol. 41, no. 1, pp. 10–25, 2004.

[95] T. Lieu, C. Farhat, and M. Lesoinne, "Reduced-order fluid/structure modeling of a complete aircraft configuration," *Computer Methods in Applied Mechanics and Engineering*, vol. 195, no. 41-43, pp. 5730–5742, 2006.

[96] D. J. Linse and R. F. Stengel, "Identification of aerodynamic coefficients using computational neural networks," *Journal of Guidance, Control, and Dynamics*, vol. 16, no. 6, pp. 1018–1025, 1993.

[97] H. Liu, Y. S. Ong, and J. Cai, "A survey of adaptive sampling for global metamodeling in support of simulation-based complex engineering design," *Structural and Multidisciplinary Optimization*, vol. 57, no. 1, pp. 393–416, 2018.

[98] D. J. Lucia, P. S. Beran, and W. A. Silva, "Reduced-order modeling: New approaches for computational physics," *Progress in Aerospace Sciences*, vol. 40, no. 1-2, pp. 51–117, 2004.

[99] J. L. Lumley, "The Structure of Inhomogeneous Turbulent Flows," in *Atmospheric turbulence and radio propagation*, A. M. Yaglom and V. I. Tatarski, Eds., Moscow: Nauka, 1967, pp. 166–178.

[100] Z. Lyu, G. K. Kenway, and J. Martins, "RANS-based Aerodynamic Shape Optimization Investigations of the Common Research Model Wing," *52nd Aerospace Sciences Meeting*, vol. 2014, no. 4, pp. 1–19, 2014.

[101] Z. Lyu, G. K. Kenway, and J. R. Martins, "Aerodynamic shape optimization investigations of the common research model wing benchmark," *AIAA Journal*, vol. 53, no. 4, pp. 968–985, 2015.

[102] Z. Lyu and J. Martins, "Strategies for Solving High-Fidelity Aerodynamic Shape Optimization Problems," in *15th AIAA/ISSMO Multidisciplinary Analysis and Optimization Conference*, Reston, Virginia: American Institute of Aeronautics and Astronautics, 2014, pp. 1–15.

[103] L. van der Maaten and G. Hinton, "Visualizing data using t-SNE," *Journal of machine learning research*, vol. 9, no. Nov, pp. 2579–2605, 2008.

[104] B. Magnus, T. Landelius, and H. Knutsson, *A Unified Approach to PCA , PLS , MLR and CCA*. Linköping University, Department of Electrical Engineering, 1997.

[105] B. Malouin, J.-Y. Trépanier, and M. Gariépy, "Interpolation of Transonic Flows Using a Proper Orthogonal Decomposition Method," *International Journal of Aerospace Engineering*, vol. 2013, pp. 1–11, 2013.

[106] J. D. Martin and T. W. Simpson, "Use of Kriging Models to Approximate Deterministic Computer Models," *AIAA Journal*, vol. 43, no. 4, pp. 853–863, 2005.

[107] J. R. R. A. Martins and J. T. Hwang, "Review and Unification of Methods for Computing Derivatives of Multidisciplinary Computational Models," *AIAA Journal*, vol. 51, no. 11, pp. 2582–2599, 2013.

[108] J. R. R. A. Martins and A. B. Lambe, "Multidisciplinary Design Optimization: A Survey of Architectures," *AIAA Journal*, vol. 51, no. 9, pp. 2049–2075, 2013.

[109] M. R. Meireles, P. E. Almeida, and M. G. Simões, "A comprehensive review for industrial applicability of artificial neural networks," *IEEE Transactions on Industrial Electronics*, vol. 50, no. 3, pp. 585–601, 2003.

[110] M. J. Mifsud, D. G. MacManus, and S. T. Shaw, "A variable-fidelity aerodynamic model using proper orthogonal decomposition," *International Journal for Numerical Methods in Fluids*, vol. 82, no. 10, pp. 646–663, 2016.

[111] M. Mifsud, "Reduced-order modelling for high-speed aerial weapon aerodynamics," Ph.D. Thesis, Cranfield University, 2008, p. 260.

[112] S. Mika, G. Ratsch, J. Weston, B. Scholkopf, and K. Mullers, "Fisher discriminant analysis with kernels," in *Neural Networks for Signal Processing*

*IX: Proceedings of the 1999 IEEE Signal Processing Society Workshop*, IEEE, 1999, pp. 41–48.

[113] Multidisciplinary Design Optimization Laboratory, *Aerodynamic Design Optimization Discussion Group (ADODG)*, `http://mdolab.engin.umich.edu/wiki/aerodynamic-design-optimization-workshop.html`, last accessed: 09-05-2020.

[114] D. E. Myers, "Matrix formulation of co-kriging," *Journal of the International Association for Mathematical Geology*, vol. 14, no. 3, pp. 249–257, 1982.

[115] J. Ollar, C. Mortished, R. Jones, J. Sienz, and V. Toropov, "Gradient based hyper-parameter optimisation for well conditioned kriging metamodels," *Structural and Multidisciplinary Optimization*, vol. 55, no. 6, pp. 2029–2044, 2017.

[116] C. Park, R. T. Haftka, and N. H. Kim, "Remarks on multi-fidelity surrogates," *Structural and Multidisciplinary Optimization*, vol. 55, no. 3, pp. 1029–1050, 2017.

[117] K. H. Park, S. O. Jun, S. M. Baek, M. H. Cho, K. J. Yee, and D. H. Lee, "Reduced-Order Model with an Artificial Neural Network for Aerostructural Design Optimization," *Journal of Aircraft*, vol. 50, no. 4, pp. 1106–1116, 2013.

[118] B. Peherstorfer, K. Willcox, and M. Gunzburger, "Optimal Model Management for Multifidelity Monte Carlo Estimation," *SIAM Journal on Scientific Computing*, vol. 38, no. 5, A3163–A3194, 2016. arXiv: `arXiv:0904.1950`.

[119] ——, "Survey of Multifidelity Methods in Uncertainty Propagation, Inference, and Optimization," *SIAM Review*, vol. 60, no. 3, pp. 550–591, 2018. arXiv: `1806.10761`.

[120] R. Pinnau, "Model Reduction via Proper Orthogonal Decomposition," in *Model Order Reduction: Theory, Research Aspects and Applications*, Springer, 2008, pp. 95–109.

[121] D. J. Poole, C. B. Allen, and T. Rendall, "Control Point-Based Aerodynamic Shape Optimization Applied to AIAA ADODG Test Cases," *53rd AIAA Aerospace Sciences Meeting*, no. January, pp. 1–20, 2015.

[122] N. V. Queipo, R. T. Haftka, W. Shyy, T. Goel, R. Vaidyanathan, and P. Kevin Tucker, "Surrogate-based analysis and optimization," *Progress in Aerospace Sciences*, vol. 41, no. 1, pp. 1–28, 2005. arXiv: `arXiv:1011.1669v3`.

[123] M. Raissi and G. Karniadakis, "Deep Multi-fidelity Gaussian Processes," no. 1, pp. 1–14, 2016. arXiv: `1604.07484`.

[124] D. Rajaram, C. Perron, T. G. Puranik, and D. N. Mavris, "Randomized Algorithms for Non-Intrusive Parametric Reduced Order Modeling," *AIAA Journal*, pp. 1–19, 2020.

[125] D. Rajaram, T. G. Puranik, C. Perron, and D. N. Mavris, "Non-Intrusive Parametric Reduced Order Modeling using Randomized Algorithms," in *AIAA Scitech 2020 Forum*, Reston, Virginia: American Institute of Aeronautics and Astronautics, 2020, pp. 1–23.

[126] C. E. Rasmussen and C. K. I. Williams, *Gaussian Processes for Machine Learning*. Cambridge, UNITED STATES: MIT Press, 2005.

[127] R. G. Regis, "Multi-objective constrained black-box optimization using radial basis function surrogates," *Journal of Computational Science*, vol. 16, pp. 140–155, 2016.

[128] R. G. Regis and C. A. Shoemaker, "Constrained global optimization of expensive black box functions using radial basis functions," *Journal of Global Optimization*, vol. 31, no. 1, pp. 153–171, 2005.

[129] ——, "Improved strategies for radial basis function methods for global optimization," *Journal of Global Optimization*, vol. 37, no. 1, pp. 113–135, 2007.

[130] ——, "Parallel radial basis function methods for the global optimization of expensive functions," *European Journal of Operational Research*, vol. 182, no. 2, pp. 514–535, 2007.

[131] ——, "A quasi-multistart framework for global optimization of expensive functions using response surface models," *Journal of Global Optimization*, vol. 56, no. 4, pp. 1719–1753, 2013.

[132] T. D. Robinson, M. S. Eldred, K. E. Willcox, and R. Haimes, "Surrogate-Based Optimization Using Multifidelity Models with Variable Parameterization and Corrected Space Mapping," *AIAA Journal*, vol. 46, no. 11, pp. 2814–2822, 2008.

[133] T. Robinson, K. Willcox, M. Eldred, and R. Haimes, "Multifidelity Optimization for Variable-Complexity Design," *Proceedings of the 11th AIAA/ISSMO Multidisciplinary Analysis and Optimization Conference*, no. September, pp. 1–18, 2006.

[134] T. Robinson, M. Eldred, K. Willcox, and R. Haimes, "Strategies for Multifidelity Optimization with Variable Dimensional Hierarchical Models," *47th AIAA/ASME/ASCE/AHS/ASC Structures, Structural Dynamics, and Materials Conference*, no. May, pp. 1–20, 2006.

[135] R. Rosipal, "Nonlinear Partial Least Squares An Overview," in *Chemoinformatics and Advanced Machine Learning Perspectives*, IGI Global, 2011, pp. 169–189.

[136] S. T. Roweis, "Nonlinear Dimensionality Reduction by Locally Linear Embedding," *Science*, vol. 290, no. 5500, pp. 2323–2326, 2000.

[137] S. Roweis, "EM Algorithms for PCA and SPCA," *Computing*, vol. 10, no. 13, pp. 626–632, 1997. arXiv: `arXiv:1011.1669v3`.

[138] G. Rozza, D. B. P. Huynh, and A. T. Patera, "Reduced Basis Approximation and a Posteriori Error Estimation for Affinely Parametrized Elliptic Coercive Partial Differential Equations," *Archives of Computational Methods in Engineering*, vol. 15, no. 3, pp. 229–275, 2008.

[139] T. J. Santner, B. J. Williams, and W. I. Notz, "Space-Filling Designs for Computer Experiments," in *The Design and Analysis of Computer Experiments*, New York, NY: Springer, 2003, pp. 121–161.

[140] R. Schaller, "Moore's law: past, present and future," *IEEE Spectrum*, vol. 34, no. 6, pp. 52–59, 1997.

[141] B. Schölkopf, A. Smola, and K.-R. Müller, "Nonlinear Component Analysis as a Kernel Eigenvalue Problem," *Neural Computation*, vol. 10, no. 5, pp. 1299–1319, 1998.

[142] N. R. Secco and J. R. R. A. Martins, "RANS-Based Aerodynamic Shape Optimization of a Strut-Braced Wing with Overset Meshes," *Journal of Aircraft*, pp. 1–11, 2018.

[143] R. Sellar, S. Batill, and J. Renaud, "Response surface based, concurrent subspace optimization for multidisciplinary system design," in *34th Aerospace Sciences Meeting and Exhibit*, Reston, Virigina: American Institute of Aeronautics and Astronautics, 1996.

[144] L. Sirovich, "Turbulence and the dynamics of coherent structures. II. Symmetries and transformations," *Quarterly of Applied Mathematics*, vol. 45, no. 3, pp. 573–582, 1987.

[145] ——, "Turbulence and the dynamics of coherent structures. III. Dynamics and scaling," *Quarterly of Applied Mathematics*, vol. 45, no. 3, pp. 583–590, 1987.

[146] S. N. Skinner and H. Zare-Behtash, "State-of-the-art in aerodynamic shape optimisation methods," *Applied Soft Computing Journal*, vol. 62, pp. 933–962, 2018.

[147] J. Slotnick, A. Khodadoust, J. Alonso, D. Darmofal, W. Gropp, E. Lurie, and D. Mavriplis, "CFD Vision 2030 Study: A Path to Revolutionary Computational Aerosciences," NASA Langley Research Center, Hampton, VA, United States, Tech. Rep. March 2014, 2014.

[148] A. J. Smola and B. Schölkopf, "A tutorial on support vector regression," *Statistics and Computing*, vol. 14, no. 3, pp. 199–222, 2004. arXiv: `arXiv:1011.1669v3`.

[149] I. P. Sobieski and I. M. Kroo, "Collaborative Optimization Using Response Surface Estimation," *AIAA Journal*, vol. 38, no. 10, pp. 1931–1938, 2000.

[150] P. Spalart and S. Allmaras, "A one-equation turbulence model for aerodynamic flows," in *30th Aerospace Sciences Meeting and Exhibit*, Reston, Virigina: American Institute of Aeronautics and Astronautics, 1992.

[151] B. Sudret, S. Marelli, and J. Wiart, "Surrogate models for uncertainty quantification: An overview," *2017 11th European Conference on Antennas and Propagation, EUCAP 2017*, pp. 793–797, 2017.

[152] R. Swischuk, L. Mainini, B. Peherstorfer, and K. Willcox, "Projection-based model reduction: Formulations for physics-based machine learning," *Computers and Fluids*, vol. 179, pp. 704–717, 2019.

[153] C. Tang, K. Gee, and S. Lawrence, "Generation of Aerodynamic Data using a Design Of Experiment and Data Fusion Approach," *43rd AIAA Aerospace Sciences Meeting and Exhibit*, no. January, pp. 1–9, 2005.

[154] J. B. Tenenbaum, "A Global Geometric Framework for Nonlinear Dimensionality Reduction," *Science*, vol. 290, no. 5500, pp. 2319–2323, 2000. arXiv: `arXiv:1011.1669v3`.

[155] J. P. Thomas, E. H. Dowell, and K. C. Hall, "Three-Dimensional Transonic Aeroelasticity Using Proper Orthogonal Decomposition-Based Reduced-Order Models," *Journal of Aircraft*, vol. 40, no. 3, pp. 544–551, 2003.

[156] M. E. Tipping and C. M. Bishop, "Probabilistic Principal Component Analysis," *Journal of the Royal Statistical Society: Series B (Statistical Methodology)*, vol. 61, no. 3, pp. 611–622, 1999.

[157] D. J. J. Toal, "On the potential of a multi-fidelity G-pod based approach for optimization & uncertainty quantification," *Turbine technical conference and exposition*, 2014.

[158] D. J. J. Toal, "Some considerations regarding the use of multi-fidelity Kriging in the construction of surrogate models," *Structural and Multidisciplinary Optimization*, vol. 51, no. 6, pp. 1223–1245, 2015.

[159] D. J. J. Toal, A. J. Keane, D. Benito, J. A. Dixon, J. Yang, M. Price, T. Robinson, A. Remouchamps, and N. Kill, "Multifidelity Multidisciplinary Whole-Engine Thermomechanical Design Optimization," *Journal of Propulsion and Power*, vol. 30, no. 6, pp. 1654–1666, 2014.

[160] D. J. Toal, A. I. Forrester, N. W. Bressloff, A. J. Keane, and C. Holden, "An adjoint for likelihood maximization," *Proceedings of the Royal Society A: Mathematical, Physical and Engineering Sciences*, vol. 465, no. 2111, pp. 3267–3287, 2009.

[161] D. Tuia, M. Volpi, M. Trolliet, and G. Camps-Valls, "Semisupervised manifold alignment of multimodal remote sensing images," *IEEE Transactions on Geoscience and Remote Sensing*, vol. 52, no. 12, pp. 7708–7720, 2014.

[162] E. Ulu, R. Zhang, and L. B. Kara, "A data-driven investigation and estimation of optimal topologies under variable loading configurations," *Computer Methods in Biomechanics and Biomedical Engineering: Imaging & Visualization*, vol. 4, no. 2, pp. 61–72, 2016.

[163] L. Van Der Maaten, E. Postma, and J. Van Den Herik, "Dimensionality Reduction : A Comparative Review," *October*, pp. 1–35, 2009.

[164] J. Vassberg, M. Dehaan, M. Rivers, and R. Wahls, "Development of a common research model for applied CFD validation studies," in *26th AIAA Applied Aerodynamics Conference*, 2008, p. 6919.

[165] J. C. Vassberg, E. N. Tinoco, M. Mani, B. Rider, T. Zickuhr, D. W. Levy, O. P. Brodersen, B. Eisfeld, S. Crippa, R. A. Wahls, J. H. Morrison, D. J. Mavriplis, and M. Murayama, "Summary of the fourth AIAA CFD drag prediction workshop," *28th AIAA Applied Aerodynamics Conference*, vol. 1, no. July, pp. 1–29, 2010.

[166] A. Vendl and H. Faßbender, "Projection-Based Model Order Reduction for Steady Aerodynamics," in *Computational Flight Testing: Results of the Closing Symposium of the German Research Initiative ComFliTe, Braunschweig, Germany, June 11th-12th, 2012*, N. Kroll, R. Radespiel, J. W. Burg, and K. Sørensen, Eds., Berlin, Heidelberg: Springer Berlin Heidelberg, 2013, pp. 151–166.

[167] C. Wang, "A geometric framework for transfer learning using manifold alignment," *Ph.D thesis*, no. September, 2010.

[168] C. Wang and S. Mahadevan, "Manifold alignment using Procrustes analysis," *Proceedings of the 25th international conference on Machine learning*, pp. 1120–1127, 2008.

[169] ——, "A general framework for manifold alignment," in *AAAI Fall Symposium Series*, 2009, pp. 53–58.

[170] ——, "Manifold Alignment," in *Manifold Learning: Theory and Applications*, 1st, CRC press, 2011, pp. 95–120.

[171] X. Wang, J. Kou, and W. Zhang, "Multi-fidelity surrogate reduced-order modeling of steady flow estimation," *International Journal for Numerical Methods in Fluids*, no. April, pp. 1–19, 2020.

[172] R. Webster and M. A. Oliver, *Geostatistics for Environmental Scientists*. Chichester, UNITED KINGDOM: John Wiley & Sons, Incorporated, 2007.

[173] K. Willcox and J. Peraire, "Balanced Model Reduction via the Proper Orthogonal Decomposition," *AIAA Journal*, vol. 40, no. 11, pp. 2323–2330, 2002.

[174] R. Yondo, E. Andrés, and E. Valero, "A review on design of experiments and surrogate models in aircraft real-time and many-query aerodynamic analyses," *Progress in Aerospace Sciences*, vol. 96, no. November 2017, pp. 23–61, 2018.

[175] S. Yu, K. Yu, V. Tresp, H.-P. Kriegel, and M. Wu, "Supervised probabilistic principal component analysis," in *Proceedings of the 12th ACM SIGKDD international conference on Knowledge discovery and data mining - KDD '06*, New York, New York, USA: ACM Press, 2006, p. 464.

[176] Y. Yu, Z. Lyu, Z. Xu, and J. R. Martins, "On the influence of optimization algorithm and initial design on wing aerodynamic shape optimization," *Aerospace Science and Technology*, vol. 75, pp. 183–199, 2018.

[177] Y. Zhang, W. J. Sung, and D. N. Mavris, "Application of Convolutional Neural Network to Predict Airfoil Lift Coefficient," in *2018 AIAA/ASCE/AHS/ASC Structures, Structural Dynamics, and Materials Conference*, Reston, Virginia: American Institute of Aeronautics and Astronautics, 2018, pp. 1–9. arXiv: 1712.10082.

[178] Y. Zhang, N. H. Kim, C. Park, and R. T. Haftka, "Multifidelity surrogate based on single linear regression," *AIAA Journal*, vol. 56, no. 12, pp. 4944–4952, 2018.

[179] Z. Zhang and H. Zha, "Principal Manifolds and Nonlinear Dimensionality Reduction via Tangent Space Alignment," *SIAM Journal on Scientific Computing*, vol. 26, no. 1, pp. 313–338, 2004.

[180] R. Zimmermann, "Gradient-enhanced surrogate modeling based on proper orthogonal decomposition," *Journal of Computational and Applied Mathematics*, vol. 237, no. 1, pp. 403–418, 2013.

[181] D. W. Zingg, M. Nemec, and T. H. Pulliam, "A comparative evaluation of genetic and gradient-based algorithms applied to aerodynamic optimization," *Revue européenne de mécanique numérique*, vol. 17, no. 1-2, pp. 103–126, 2008.